(JPL-DSN-PR-42-49) THE DEEP SPACE NETWORK Progress Report, Nov. 1978 - Dec. 1978 (Jet Propulsion Lab.) 189 p HC A09/MF A01
CSCL 14B
G3/12

N79-19045
THRU
N79-19064
Unclas
18124

The Deep Space Network Progress Report 42-49

November and December 1978

February 15, 1979

National Aeronautics and Space Administration

Jet Propulsion Laboratory
California Institute of Technology
Pasadena, California

The Deep Space Network Progress Report 42-49

November and December 1978

February 15, 1979

National Aeronautics and
Space Administration

Jet Propulsion Laboratory
California Institute of Technology
Pasadena, California

The research described in this publication was carried out by the Jet Propulsion Laboratory, California Institute of Technology, under NASA Contract No NAS7-100

Preface

Beginning with Volume XX, the Deep Space Network Progress Report changed from the Technical Report 32- series to the Progress Report 42- series. The volume number continues the sequence of the preceding issues. Thus, Progress Report 42-20 is the twentieth volume of the Deep Space Network series, and is an uninterrupted follow-on to Technical Report 32-1526, Volume XIX.

This report presents DSN progress in flight project support, tracking and data acquisition (TDA) research and technology, network engineering, hardware and software implementation, and operations. Each issue presents material in some, but not all, of the following categories in the order indicated.

Description of the DSN

Mission Support
- Ongoing Planetary/Interplanetary Flight Projects
- Advanced Flight Projects

Radio Astronomy

Special Projects

Supporting Research and Technology
- Tracking and Ground-Based Navigation
- Communications—Spacecraft/Ground
- Station Control and Operations Technology
- Network Control and Data Processing

Network and Facility Engineering and Implementation
- Network
- Network Operations Control Center
- Ground Communications
- Deep Space Stations
- Quality Assurance

Operations
- Network Operations
- Network Operations Control Center
- Ground Communications
- Deep Space Stations

Program Planning
- TDA Planning

In each issue, the part entitled "Description of the DSN" describes the functions and facilities of the DSN and may report the current configuration of one of the seven DSN systems (Tracking, Telemetry, Command, Monitor & Control, Test & Training, Radio Science, and Very Long Baseline Interferometry).

The work described in this report series is either performed or managed by the Tracking and Data Acquisition organization of JPL for NASA.

Contents

DESCRIPTION OF THE DSN

MISSION SUPPORT

Ongoing Planetary/Interplanetary Flight Projects

SUPPORTING RESEARCH AND TECHNOLOGY

Tracking and Ground-Based Navigation

Station Control and Operations Technology

Network Control and Data Processing

NETWORK AND FACILITY ENGINEERING AND IMPLEMENTATION

Network

Deep Space Stations

OPERATIONS

Deep Space Stations

Network Functions and Facilities

N. A. Renzetti
Office of Tracking and Data Acquisition

The objectives, functions, and organization of the Deep Space Network are summarized; deep space station, ground communication, and network operations control capabilities are described.

The Deep Space Network was established by the National Aeronautics and Space Administration (NASA) Office of Space Tracking and Data Systems and is under the system management and technical direction of the Jet Propulsion Laboratory (JPL). The network is designed for two-way communications with unmanned spacecraft traveling approximately 16,000 km (10,000 miles) from Earth to the farthest planets and to the edge of our solar system. It has provided tracking and data acquisition support for the following NASA deep space exploration projects: Ranger, Surveyor, Mariner Venus 1962, Mariner Mars 1964, Mariner Venus 1967, Mariner Mars 1969, Mariner Mars 1971, and Mariner Venus-Mercury 1973, for which JPL has been responsible for the project management, the development of the spacecraft, and the conduct of mission operations; Lunar Orbiter, for which the Langley Research Center carried out the project management, spacecraft development, and conduct of mission operations; Pioneer, for which Ames Research Center carried out the project management, spacecraft development, and conduct of mission operations; and Apollo, for which the Lyndon B. Johnson Space Center was the project center and the Deep Space Network supplemented the Manned Space Flight Network, which was managed by the Goddard Space Flight Center. The network is currently providing tracking and data acquisition support for Helios, a joint U.S./West German project; Viking, for which Langley Research Center provided the Lander spacecraft and project management until May, 1978, at which time project management and mission operations were transferred to JPL, and for which JPL provided the Orbiter spacecraft; Voyager, for which JPL provides project management, spacecraft development, and is conducting mission operations; and Pioneers, for which the Ames Research Center provides project management, spacecraft development, and conduct of mission operations. The network is adding new capability to meet the requirements of the Galileo mission to Jupiter, for which JPL is providing the Orbiter spacecraft, and the Ames Research Center the probe. In addition, JPL will carry out the project management and the conduct of mission operations.

The Deep Space Network (DSN) is one of two NASA networks. The other, the Spaceflight Tracking and Data Network (STDN), is under the system management and technical direction of the Goddard Space Flight Center (GSFC). Its function is to support manned and unmanned Earth-orbiting satellites. The Deep Space Network supports lunar, planetary, and interplanetary flight projects.

From its inception, NASA has had the objective of conducting scientific investigations throughout the solar system. It was recognized that in order to meet this objective, significant supporting research and advanced technology development must be conducted in order to provide deep space telecommunications for science data return in a cost effective

manner. Therefore, the Network is continually evolved to keep pace with the state of the art of telecommunications and data handling. It was also recognized early that close coordination would be needed between the requirements of the flight projects for data return and the capabilities needed in the Network. This close collaboration was effected by the appointment of a Tracking and Data Systems Manager as part of the flight project team from the initiation of the project to the end of the mission. By this process, requirements were identified early enough to provide funding and implementation in time for use by the flight project in its flight phase.

As of July 1972, NASA undertook a change in the interface between the Network and the flight projects. Prior to that time, since 1 January 1964, in addition to consisting of the Deep Space Stations and the Ground Communications Facility, the Network had also included the mission control and computing facilities and provided the equipment in the mission support areas for the conduct of mission operations. The latter facilities were housed in a building at JPL known as the Space Flight Operations Facility (SFOF). The interface change was to accommodate a hardware interface between the support of the network operations control functions and those of the mission control and computing functions. This resulted in the flight projects assuming the cognizance of the large general-purpose digital computers which were used for both network processing and mission data processing. They also assumed cognizance of all of the equipment in the flight operations facility for display and communications necessary for the conduct of mission operations. The Network then undertook the development of hardware and computer software necessary to do its network operations control and monitor functions in separate computers. A characteristic of the new interface is that the Network provides direct data flow to and from the stations; namely, metric data, science and engineering telemetry, and such network monitor data as are useful to the flight project. This is done via appropriate ground communication equipment to mission operations centers, wherever they may be.

The principal deliverables to the users of the Network are carried out by data system configurations as follows:

(1) The DSN Tracking System generates radio metric data, i.e., angles, one- and two-way doppler and range, and transmits raw data to Mission Control.

(2) The DSN Telemetry System receives, decodes, records, and retransmits engineering and scientific data generated in the spacecraft to Mission Control.

(3) The DSN Command System accepts spacecraft commands from Mission Control and transmits the commands via the Ground Communication Facility to a Deep Space Station. The commands are then radiated to the spacecraft in order to initiate spacecraft functions in flight.

(4) The DSN Radio Science System generates radio science data, i.e., the frequency and amplitude of spacecraft transmitted signals affected by passage through media such as the solar corona, planetary atmospheres, and plantetary rings, and transmits this data to Mission Control.

(5) The DSN Very Long Baseline Interferometry System generates time and frequency data to synchronize the clocks among the three Deep Space Communications complexes. It will generate universal time and polar motion and relative Deep Space Station locations as by-products of the primary data delivery function.

The data system configurations supporting testing, training, and network operations control functions are as follows:

(1) The DSN Monitor and Control System instruments, transmits, records, and displays those parameters of the DSN necessary to verify configuration and validate the Network. It provides the tools necessary for Network Operations personnel to control and monitor the Network and interface with flight project mission control personnel.

(2) The DSN Test and Training System generates and controls simulated data to support development, test, training and fault isolation within the DSN. It participates in mission simulation with flight projects.

The capabilities needed to carry out the above functions have evolved in the following technical areas:

(1) The Deep Space Stations, which are distributed around Earth and which, prior to 1964, formed part of the Deep Space Instrumentation Facility. The technology involved in equipping these stations is strongly related to the state of the art of telecommunications and flight-ground design considerations, and is almost completely multimission in character.

(2) The Ground Communications Facility provides the capability required for the transmission, reception, and monitoring of Earth-based, point-to-point communications between the stations and the Network Operations Control Center at JPL, Pasadena, and to the JPL Mission Operations Centers. Four communications disciplines are provided: teletype, voice, high-speed, and wideband. The Ground Communications Facility uses the capabilities provided by common carriers throughout the world, engineered into an integrated system by Goddard Space Flight Center, and controlled from the

communications Center located in the Space Flight Operations Facility (Building 230) at JPL.

The Network Operations Control Center is the functional entity for centralized operational control of the Network and interfaces with the users. It has two separable functional elements; namely, Network Operations Control and Network Data Processing. The functions of the Network Operations Control are:

(1) Control and coordination of Network support to meet commitments to Network users.

(2) Utilization of the Network data processing computing capability to generate all standards and limits required for Network operations.

(3) Utilization of Network data processing computing capability to analyze and validate the performance of all Network systems.

The personnel who carry out the above functions are located in the Space Flight Operations Facility, where mission operations functions are carried out by certain flight projects. Network personnel are directed by an Operations Control Chief. The functions of the Network Data Processing are:

(1) Processing of data used by Network Operations Control for control and analysis of the Network.

(2) Display in the Network Operations Control Area of data processed in the Network Data Processing Area.

(3) Interface with communications circuits for input to and output from the Network Data Processing Area.

(4) Data logging and production of the intermediate data records.

The personnel who carry out these functions are located approximately 200 meters from the Space Flight Operations Facility. The equipment consists of minicomputers for real-time data system monitoring, two XDS Sigma 5s, display, magnetic tape recorders, and appropriate interface equipment with the ground data communications.

D2

N79-19047

DSN Telemetry System Mark III-77

E. C. Gatz
TDA Engineering Office

This article provides a description of the DSN Telemetry System, Mark III-77, and the recent improvements. Telemetry functions and performance are identified.

I. Introduction

The Deep Space Network Telemetry System has been described in Ref. 1. The current system configuration described below has been implemented by incremental changes and upgrades to existing equipment configurations. The system is now configured to provide support for the following missions:

(1) Voyager.

(2) Pioneers 6 through 11.

(3) Pioneer Venus 78 Orbiter and Multiprobe.

(4) Helios.

(5) Viking.

(6) Galileo.

II. System Definition

The DSN Telemetry System provides the capability to acquire, process, decode, and distribute deep space probe telemetry data. Telemetry data are defined as consisting of science and engineering information modulated on radio signals transmitted from the spacecraft.

The DSN Telemetry System, Mark III-77, performs three main functions:

(1) Telemetry data acquisition.

(2) Telemetry data conditioning and transmission.

(3) Telemetry system validation.

Telemetry data acquisition consists of those functions necessary to extract the telemetry information modulated on the downlink carrier(s) of the spacecraft. Telemetry data conditioning and transmission consist of those functions necessary to decode, format, record, and transmit the data to users. Telemetry System validation consists of those functions necessary to validate the performance of the Network in the acquisition, conditioning, and transmission of telemetry data. Verification of correct system performance is made and corrective action is taken when such performance does not meet specifications.

III. Key Characteristics

The key characteristics of the DSN Telemetry System, Mark III-77, consist of:

(1) High-rate (up to 250 ksps) X-band telemetry capability at both a 34- and a 64-meter subnet, in addition to S-band telemetry at all subnets.

(2) Maximum likelihood decoding of short constraint length convolutional codes at all Deep Space Stations (DSS). Deletion of block decoding after completion of Viking Mission.

(3) Replacement of the Telemetry and Command Processor with a dedicated processor for telemetry, the Telemetry Processor Assembly (TPA).

(4) Centralized monitoring and control of the DSN Telemetry System by the Network Operations Control Center (NOCC).

(5) Precise measurement of received signal level and system noise temperature.

(6) Real-time reporting of DSN Telemetry System status through the DSN Monitor and Control System.

(7) Low-loss onsite recording of predetection analog/digital records with non-real-time playback.

(8) Production of a digital Telemetry Original Data Record (ODR) at each DSS with playback via local manual control or in automatic response to GCF inputs.

(9) Simultaneous reception of five carriers at selected DSS for Pioneer Venus (to be deleted after the mission).

(10) Replacement of the Data Decoder Assembly (DDA) and incorporation of its functions into the TPA.

(11) Increased high-speed data (HSD) line rate to 7200 b/s, and wideband capability standard of 56 kb/s, up to 230 kb/s at selected DSS.

(12) Generation of a Telemetry Intermediate Data Record (IDR), a time-merged record of all received telemetry data.

(13) Real-time arraying of signals received from two DSSs at the same longitude.

IV. Functional Description

A simplified block diagram of the system is shown in Fig. 1. Predicts messages are initially generated at the NOCC for high-speed data line (HSDL) transmission to the DSS for the purpose of selecting the proper data modes and configurations. Such messages consist of predicted signal levels and tolerances.

At the Deep Space Station, the received spacecraft signal is amplified by the Antenna Microwave Subsystem (UWV). The RF carrier is tracked by the Receiver-Exciter Subsystem (RCV), and the telemetry spectrum is routed to the Subcarrier Demodulator Assembly (SDA). The subcarrier is regenerated by the SDA and the symbol stream is demodulated. The resulting demodulated symbol stream is passed to the Symbol Synchronizer Assembly (SSA), where it is digitized. The digitized stream for convolutional encoded data is then routed to (1) the Maximum Likelihood Convolutional Decoder (MCD) for decoding of short-constraint-length convolutional codes, or (2) the TPA for decoding of long-constraint-length convolutional codes or uncoded data. The digitized symbol stream for block encoded data is sent to either the TPA or the Block Decoder Assembly (BDA), depending on the rate. All data are formatted for high-speed or wideband data line transmission by the TPA.

A special configuration at DSS 14 and DSS 43 for the Pioneer Venus 78 entry mission allows simultaneous reception of five carriers and for the processing of four carriers in real-time. For backup purposes, four open-loop receivers are used with bandpass filters and an analog recorder. This combination allows for recording a wideband spectrum around the anticipated carrier frequencies of the four atmospheric probes. In non-real-time, at CTA-21, these data can be played back and converted up to S-band for reception and processing by conventional receiver/SDA/SSA/TPA telemetry equipment.

At each DSS, an ODR of the decoded data is written in GCF blocks by either the TPA for high-rate data or the Communications Monitor and Formatter Assembly (CMF) for low-rate data. The data are passed to the high-speed or wideband buffer, depending upon the data rate. All data are formatted by the TPA for high-speed or wideband data line transmission.

The data are then transmitted to the Mission Control and Computing Center (MCCC) or Remote Mission Operations Centers (RMOC) and, in parallel, to the NOCC. At the NOCC, a limited amount of decommutation of engineering telemetry data is performed to analyze system performance and to obtain certain spacecraft parameters useful in controlling the Network. The NOCC also receives and displays DSN Telemetry System parameters.

A log tape containing all data received at the NOCC, either in real-time or by recall, is generated by the Network Log Processor (NLP). This log is the Network Data Log (NDL). The Data Records Assembly provides for the recall of data from the station ODRs, and for merging the recalled data with data on the NDL. It also provides for the generation of the IDR.

DSN Telemetry System performance is validated by the NOCC Telemetry Subsystem Real-Time Monitor (RTM) Processor in response to the controls and standards and limits applied from DSN Operations personnel in the Network

Operations Control Area (NOCA). Telemetry System alarms, status, and data are transmitted from the NOCC Telemetry RTM to the NOCC Display Subsystem. DSN Telemetry System alarms and status are also transmitted to the DSN Monitor and Control System and are included in the Network Performance Record (NPR). A DSN Telemetry System Performance Record (SPR), containing status and alarms, is maintained for non-real-time analysis. The SPR also contains a list of all telemetry data gaps. This list is used by the Data Records Assembly to compose recall requests from the station ODRs.

The DSN Test and Training System is used to provide simulated DSN Telemetry System data and test signals for the checkout of the system and for the training of DSN personnel.

V. System Configuration

The current configuration of equipment comprising the DSN Telemetry System is shown in Fig. 2. One 26-meter subnet—DSS 12, 42, and 61—is being upgraded to 34-meter diameter and converted to X-band Operation. DSS 12 conversion has been completed; the conversions of DSS 42 and 61 are now being implemented and will be complete by April 1980.

A. System Performance

1. **Output delay.** All spacecraft telemetry data received at the DSS are delivered in real-time to the flight project interface. The data are delayed only for (1) the time to fill on GCF data block, and (2) the ground communications transmission time.

2. **Reliability.** The DSN Telemetry System is designed to perform continuously with outages for a given telemetry stream not to exceed the following counts:

(1) Not more than one outage exceeding 15 minutes in 12 hours.

(2) Not more than 10 outages exceeding 1 minute in 24 hours.

(3) Not more than 2% total outage time in one year of scheduled operation.

Outages are defined as failures resulting in total loss of signal and requiring reconfiguration, reinitialization, or replacement of an element in the system, not the introduction of a random bit error or burst of errors.

3. **Restoration of service.** The DSN Telemetry System is capable of physical repair or replacement of failed elements within 15 minutes of the detection of a failure (provided redundant elements are available). When redundant elements are energized, configured and initialized, switching from failed elements to backup elements can be accomplished in 6 minutes.

4. **Initiation time.** After configuration of the DSN Telemetry System (connection, application of power, programs loaded on all online assemblies) for a particular operation, the System is capable of initialization within 10 minutes. Within a facility, this initialization is possible by a single operator for the facility.

5. **Reconfiguration time.** Scheduled reconfiguration of the DSN Telemetry System from support of one flight project to another can be performed within 15 minutes without prepass or postpass calibration. The capability exists for a single operator to accomplish this reconfiguration at each facility. Scheduled changes in operating mode (data rate, format, etc.) for one flight project are accomplished in 5 minutes; these changes are capable of being accomplished by a single operator for the facility.

B. DSS Modification

The following telemetry system modifications are being installed in addition to the capability defined in Ref. 1.

1. **Telemetry arraying.** At each complex (i.e. Goldstone, Spain, and Australia), capability is being provided for combining subcarrier spectrum outputs from 64- and 34-meter DSS to provide a single enhanced stream. This arraying includes automatic acquisition and synchronization not to exceed 5 minutes. The arraying accommodates subcarrier frequencies of 24 to 500 kHz and symbol rates from 2 ksps up to 250 kdps. The combining process introduces less than 0.2 dB degradation, and operates at received signal levels as low as

$$\text{STs/No} = -5.2 \text{ dB} \quad \text{34-m DSS}$$

$$\text{STs/No} = 0.8 \text{ dB} \quad \text{64-m DSS}$$

2. **Precision signal power measurement.** Capability is being provided at each DSS to measure precisely the received power in each carrier and the system noise temperature. This capability will be implemented in late 1979 at 64-meter DSSs, and in subsequent years for the other stations. The basic accuracy of these measurements will be 0.1 dB, with some degradation at strong and weak signals.

C. Planned Improvements

This article describes the current configuration and improvements being implemented. Future improvements are also planned in two areas:

(1) Enhancing the microwave performance to provide increased gain and lower noise temperature for the Voyager Saturn encounters.

(2) Addition of megabit (up to 30 Mbps) telemetry reception and detection for the Venus Orbiting Imaging Radar (VOIR) project.

Reference

1. Gatz, E. C., "DSN Telemetry System, Mark III-77," in *The Deep Space Network Progress Report, 42-42,* pp. 4-11, Jet Propulsion Laboratory, Pasadena, Calif., Dec. 15, 1977.

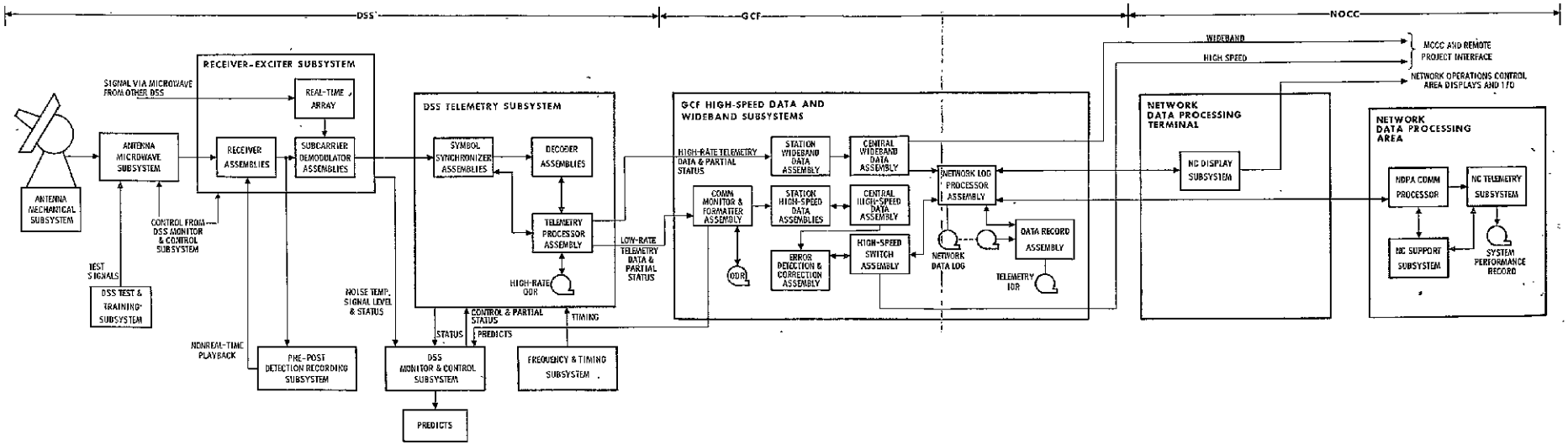

Fig. 1. DSN Telemetry System, Mark III-77, block diagram

PAGE INTENTIONALLY BLANK

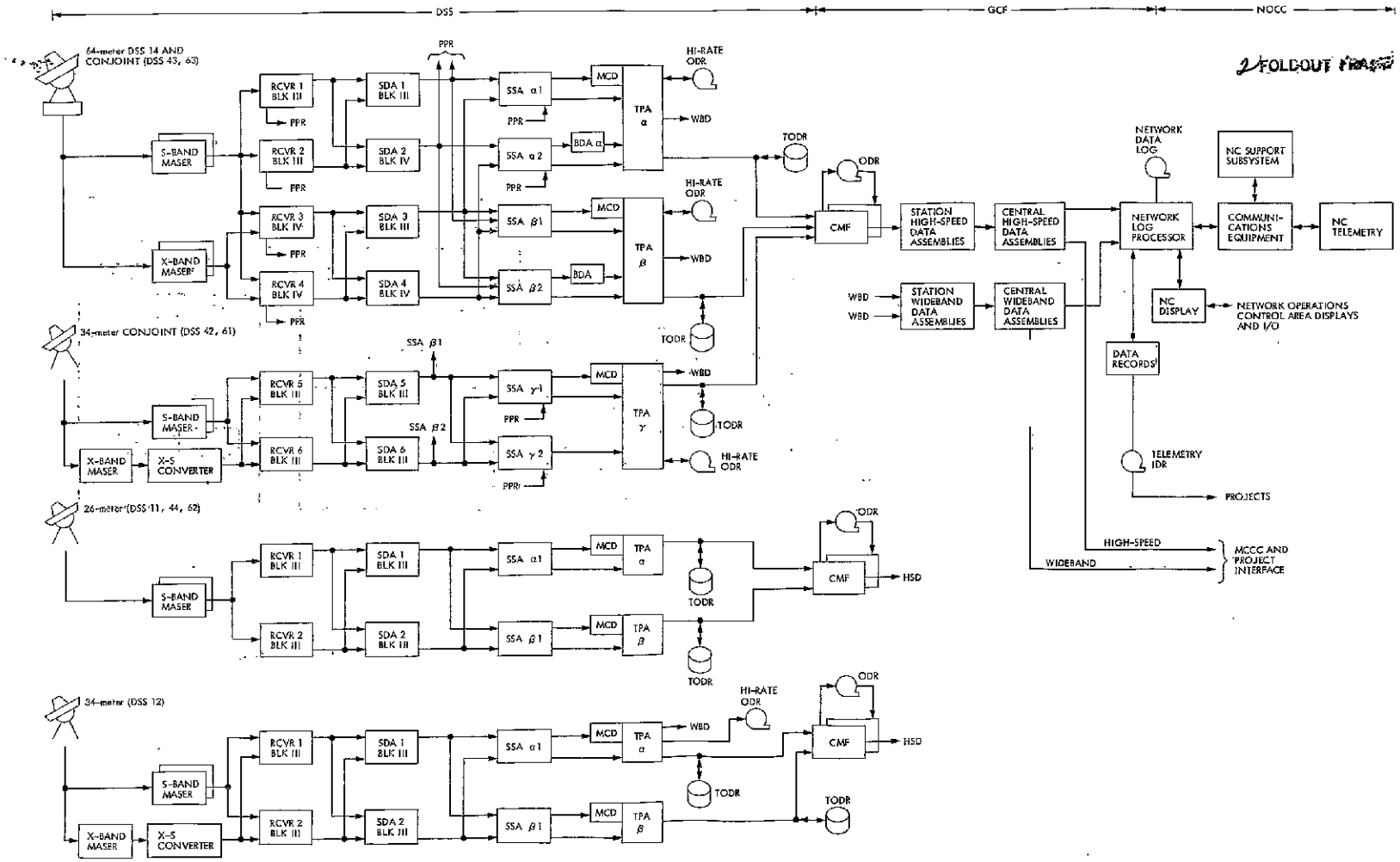

Fig. 2. DSN Telemetry System, Mark III-77 configuration

DSN Command System Mark III-78

H. C. Thorman
TDA Engineering Office

DSN Command System Mark III-78 implementation and functional operation are described. Recent software upgrade enables expanded storage capacity in the DSS Command Processor Assembly. Store-and-forward command data handling is operational for Voyager and Helios. Near-real-time command data handling has been retained for Viking and Pioneer.

I. System Functional Description

End-to-end command system operations are represented functionally in Fig. 1. Command sequences for one or more spacecraft are generated and stored at a Mission Operations Center (MOC). Commands for a particular spacecraft are selected from the command files, formatted into messages, and stored for transmittal to a specified Deep Space Station (DSS). Command data is extracted from the messages received at the DSS and stored until radiated. Finally, the commands arrive at the spacecraft and are either executed immediately or stored onboard for later execution.

The functions of the DSN Command System in this process include the following:

(1) Establishing the DSS configuration for the specified spacecraft.

(2) Receiving and storing command data at the DSS.

(3) Queuing command data to be radiated to the spacecraft.

(4) Radiating the command data to the spacecraft.

(5) Monitoring and reporting system status and events.

The Network Operations Control Center (NOCC) provides control and monitoring of the DSN Command System. Instructions from NOCC and command data from MOC are communicated to the DSS via the Ground Communication Facility (GCF) High-Speed Data subsystem (GHS), as shown in Fig. 2.

A detailed diagram of the DSN Command System Mark III-78 is presented in Fig. 3.

II. System Implementation

The equipment configuration for the DSN Command System Mark III-78 (Fig. 3) is the same as the Mark III-77 configuration described in Refs. 1 and 2, except that the DSS pre-and-post detection analog recording (PPR) subsystem has been eliminated. The DSN Mark III data subsystems implementation project was completed with the reconfiguration of the final Deep Space Station, DSS 11, at Goldstone, California, in early 1978. The GCF High-Speed Data Subsystem (GHS) conversion from line-switching to programmable message-switching was completed in mid-1978. The GHS upgrade included implementation of the required interfaces.

with the Network Operations Control Center (NOCC) and the Mission Control and Computing Center (MCCC). High-speed data for all missions, except Viking, are routed by the message-switching processors. The line-switching interface for Viking data will be maintained until March 1979.

During 1978 the DSS Command Processor Assembly (CPA) software program was upgraded to include the "store-and-forward" data-handling method and increased command storage capacity described in Ref. 3. The JPL Mission Control and Computing Center was reconfigured to provide the required processing functions to utilize the store-and-forward technique for Voyager and Helios spacecraft command operations. The Pioneer and Viking mission operations organizations have chosen to continue to use the older, near-real-time method of command data handling.

Command System testing with the new CPA software was conducted during the period of July through October. The testing included subsystem acceptance tests, system acceptance tests, system performance tests, DSN operational verification tests, interface tests, flight project ground data system tests, and command demonstrations with in-flight spacecrafts. The CPA software was transferred to DSS operational use at the beginning of November.

The testing identified many minor anomalies (which can be avoided by using operational restraints). These remain to be corrected by future program modifications. The anomalies are documented as liens against the development-to-operations transfer agreement. The next update of the CPA software is planned to be operational after the Voyager 2 Jupiter encounter and the Pioneer 11 Saturn encounter.

III. Pretrack System Preparation

DSS pretrack operations performed by station personnel include initializing the CPA software for "phase 1" or "phase 2" operation so that the CPA will be prepared to recognize the content of the high-speed data blocks to be received from NOCC and the flight project command center. Phase 1 initialization is required for the older type of command data messages (Ref. 1); phase 2 initialization is required for the new (store-and-forward) type (Ref. 3). Additional on-site initialization inputs to the CPA specify the flight project name and the spacecraft identification number. These inputs cause the software to transfer a specific configuration and standards and limits table from disk storage to memory and to configure the Command Modulator Assembly (CMA) and CPA according to the table. Changes may later be made by high-speed data messages from NOCC or by keyboard entries at the Data System Terminal (DST) in the station.

Upon initialization, the CPA sends DSS Command Subsystem (DCD) configuration and status information across the star switch controller (SSC) to the DSS Monitor and Control Subsystem (Fig. 4) for inclusion in the monitor data blocks that are periodically transmitted to the NOCC to provide station status displays in the Network Operations Control Area (NOCA). The subsystem configuration and status information are also sent from the CPA to the DST for station display.

Prior to the beginning of the scheduled spacecraft track the control of the station command functions is transferred to the NOCC. Configuration and standards and limits are updated by transmission of high-speed data messages from the NOCC command subsystem (NCD) real-time monitor (RTM) processor. The configuration and standards and limits are derived from files maintained in the Network Support Computer (NSC). Spacecraft-dependent parameters, such as symbol period, command subcarrier frequency, exciter frequency, and appropriate abort limits, are established via these messages. After the proper configuration and standards and limits have been established, test commands are transmitted through the system to ensure that the system can accept spacecraft commands via high-speed data messages, temporarily store the commands, and properly confirm transmission. After NOCC operations personnel have established that the system is operating properly, the system control is transferred to the flight project for transmission of actual spacecraft command sequences during the spacecraft track period.

IV. Command Data Handling

A. Phase 1 Method – Near-Real-Time

With the CPA initialized for phase 1 operation, the data handling method is functionally the same as has been used since 1973. A command stack provides storage of high-speed data blocks (stack modules) of command data. Each stack module consists of up to six command elements. Each command element contains up to 71 bits of command data and, at project option, can be either timed or nontimed.

The top command element in the first stack module is eligible for radiation to the spacecraft. Nontimed commands are radiated immediately after eligibility. Timed commands are radiated after becoming eligible at the time specified in the high-speed data block. At the time for radiation of the command element, the CPA establishes the proper mode (see Fig. 5 for description of the various modes) and configuration of the CMA; then the command is transferred to the CMA for immediate radiation via the Receiver-Exciter, Transmitter, Microwave, and Antenna Subsystems. Related verification, confirmation, and abort criteria (if required) are established by the CPA.

During these command operations, events may occur in which high-speed data message transmission to the NOCC and MOC becomes necessary. The following events initiate message transmission:

(1) Acknowledged receipt of a high-speed data block.

(2) High-speed data block rejection by the CPA.

(3) DSS alarm or alarm clear.

(4) Response to a recall request.

(5) Confirmed command element.

(6) Aborted command element.

B. Phase 2 Method – Store-and-Forward

The new data-handling method associated with phase 2 initialization of the CPA utilizes the CPA disk to provide expanded storage of command data. This method is designed to allow mission operations to prepare large files of spacecraft commands in advance and then to forward several files to the DSS at the beginning of a spacecraft track.

1. Command files. Each file may consist of 2 to 256 high-speed data blocks. The content of each of these data blocks is a file *element.* The first block of each file contains the *header element* and the remaining blocks each contain a *command element.* Each command element may consist of up to 800 bits of spacecraft command data. Up to 8 files for a given mission can be stored by the CPA. Thus, the available storage is greater than 1.6 million command bits.

The header element contains file identification information, file processing instruction, and a file checksum for error protection. The file identification information consists of a file time ID, a file text name, and a project reference number. Once generated (normally by project command generation software), the information is unchanged throughout the ground system. The file processing instructions consist of optional file radiation open and close window times, and an optional file bit 1 radiation time. File open and close window times specify the only time interval during which command elements in the file may begin radiation (i.e., a mission sequence may demand that specific commands *not* be sent before or after certain times). The bit 1 radiation time allows the project to specify the exact time at which the file is to begin radiation to the spacecraft. The file checksum is intended to provide error protection for the end-to-end ground command system. It is created at the time of file generation and is passed intact to the DSS. It adds reliability to insure that no data were dropped or altered in the transfer from one facility to another.

The command elements contain the actual command bits to be radiated to the spacecraft, identification information, and processing-control information. The identification information includes the file time ID and the file text name (same as the header element), project reference number, and element number (1-255). The processing-control information consists of an optional delay time. If the project wants to delay radiation of a command element (delay from the previous command), this delay time would be used.

2. Receiving and storing command data at a DSS. Normally, the file(s) of commands to be radiated to the spacecraft are sent to a DSS during the first few minutes of a spacecraft track (i.e., just after spacecraft signal acquisition). The first step in receiving and storing command data at a DSS is the process of opening a file area on the CPA disk at a DSS. This is accomplished by the Mission Control Center sending a file header element to the DSS CPA. The CPA acknowledges receipt of this *file-open* instruction. The Mission Control Center immediately sends a command file (up to 255 command elements per file). Command element blocks are normally sent at a rate of 3 per second; however, the rate can be increased to a maximum of 5.4 per second if necessary. The Mission Control Center then follows with a *file-close* instruction. The CPA acknowledges the close instruction and indicates file loading successful or unsuccessful. If successful, the Mission Control Center proceeds to send any remaining files (up to 8 total). If unsuccessful, the CPA specifies (in the acknowledge to the Mission Control Center) the reason for the failure and from what point in the file the command elements are to be retransmitted.

There are numerous reasons the CPA rejects the close instruction, but the prime one would be an error occurring in the transmission link between the Mission Control Center and the DSS. The Mission Control Center retransmits the data and again attempts to close the file. Again, after a successful file close, the Mission Control Center proceeds to send any remaining files. Upon successful closing of all files, the loading and storing process is complete. This process will normally take less than 10 minutes to complete. The command data is then available for radiation to the spacecraft.

3. Queuing the command data for radiation. After having loaded the file(s) at the CPA, files may be selected for radiation to the spacecraft. This process is called *attaching.* A five-entry *queue* of file names is provided. The Mission Control Team determines in which order the files are to be attached, normally in the order in which they were sent to a DSS. The order in which they are attached determines the sequence in which they will be radiated: that is, first attached, first to radiate to the spacecraft. Attaching a file to the queue is accomplished by the Mission Control Center sending an attach

directive to the DSS CAP. Each file, as it is attached, is placed at the bottom of the queue. After attaching the files, the top file in the queue is eligible for radiation to the spacecraft.

4. **Command radiation to the spacecraft.** The first command element in the top (prime) file in the queue begins radiation to the spacecraft immediately after attachment or as soon as all optional file instructions are satisfied. As previously stated, a file can have optional instructions – Bit 1 radiation time and file open and close window times. If used, these instructions control when the first command element in the file begins radiation to the spacecraft. The file is defined to be active when the first command element begins radiation. Upon completion of radiation of the first command element, the CPA radiates the second command element either immediately or when the optional instruction delay time has been satisified. The CPA continues to radiate all command elements in the file until complete. After the first file completes the radiation process, the second file in the queue automatically becomes the prime file and the file radiation process is repeated. After the second file completes radiation, the third file becomes prime, etc. This process is repeated until all files in the queue are exhausted. The Mission Control Center can attach new files to the queue whenever space becomes available (i.e., after the first file radiates).

As the radiation of command elements in a file is in process, periodic reporting via high-speed data line messages to the Mission Control Center is accomplished. Transmission of these messages to the Mission Control Center occurs every three minutes, or after five elements have been radiated, whichever occurs first.

5. **Additional Data Processing.** The functions of storing the command files at a DSS, attaching the files to the queue, and radiating the commands to the spacecraft are rather straightforward and the above descriptions assumed nominal-standard operation of the data processing functions. However, the complexity of the total data processing capabilities is a result of assuming worst case, failure-recovery, or non-nominal operating conditions. Numerous data processing capabilities exist to accommodate these conditions. Below is a list of the optional or non-nominal data processing functions.

a. File erase. The capability exists to delete a file from storage at the DSS CPA. This *erase* function can be accomplished either locally at a DSS or via high-speed data message from the Mission Control Center. It is expected that files will be stored on disk at the CPA that are not intended to be radiated to the spacecraft. Examples: Test files left from pretrack testing or the Mission Control Center sends wrong files to DSS. The file erase function is provided so that unnecessary files stored at the DSS can be deleted to make room for files intended for radiation to the spacecraft.

b. Clearing the queue. Files could be attached to the queue out of order. As previously stated, the order of file radiation to the spacecraft is dependent on the order of files in the queue. The queue can be cleared by a high-speed data *clear-queue* message from the Mission Control Center.

c. Suspend radiation. If for some reason, Mission Control desires to stop command radiation, a *suspend* message can be sent from the Mission Control Center. This message stops command radiation to the spacecraft. The file is defined as being in the suspended state.

d. Resume command radiation. To *resume* radiation of a suspended file (either suspended intentionally or from an abort), a message can be sent from the Mission Control Center to resume radiation at a specific element in the file.

e. Command abort. As each command bit is radiated to the spacecraft, numerous checks are made to insure validity of the command data. If a failure is detected during radiation, the command element is *aborted.* Optional methods of treating an abort are provided. Automatic recovery can be attempted (resend the command element) or radiation is terminated until operator intervention occurs. If radiation ceases, again the file is said to be suspended.

f. Close window time override. The close window time (previously discussed) can cause an actively radiating file to become suspended. If this occurs, Mission Control can send a message to the DSS CPA to *override* this time. The close window time override directs the CPA to ignore the close window time and proceed to radiate the complete file.

Most of the imperfections that exist in the currently operational CPA software program are in this area of real-time file manipulation and in the details of status and event reporting. The known discrepancies will be corrected in a future CPA software upgrade.

V. Data Records

All high-speed data blocks received by the CPA and all high-speed data blocks sent from the CPA are logged at the

DSS on the Original Data Record (ODR) by the Communications Monitor and Formatter (CMF). The CPA has the capability to record a temporary ODR on disk, if the CMF ODR is disabled.

High-speed data blocks received at the GCF central communications terminal, from all DSSs, are recorded on the Network Data Log (NDL) at the Network Log Processor (NLP). The NLP also logs all command system high-speed data blocks transmitted to the DSS from NOCC or any MOC.

The ODR and the NDL provide a source of information for fault isolation in case of system failure.

References

1. Stinnett, W. G., "DSN Command System Mark III-75," in *The Deep Space Network Progress Report 42-29*, pp. 5-9, Jet Propulsion Laboratory, Pasadena, Calif., Oct. 15, 1975.
2. Stinnett, W. G., "Mark III-77 DSN Command System," in *The Deep Space Network Progress Report 42-37*, pp. 4-11, Jet Propulsion Laboratory, Pasadena, Calif., Feb. 15, 1977.
3. Stinnett, W. G., "DSN Command System Mark III-78," in *The Deep Space Network Progress Report 42-43*, pp. 4-8, Jet Propulsion Laboratory, Pasadena, Calif., Feb. 15, 1978.

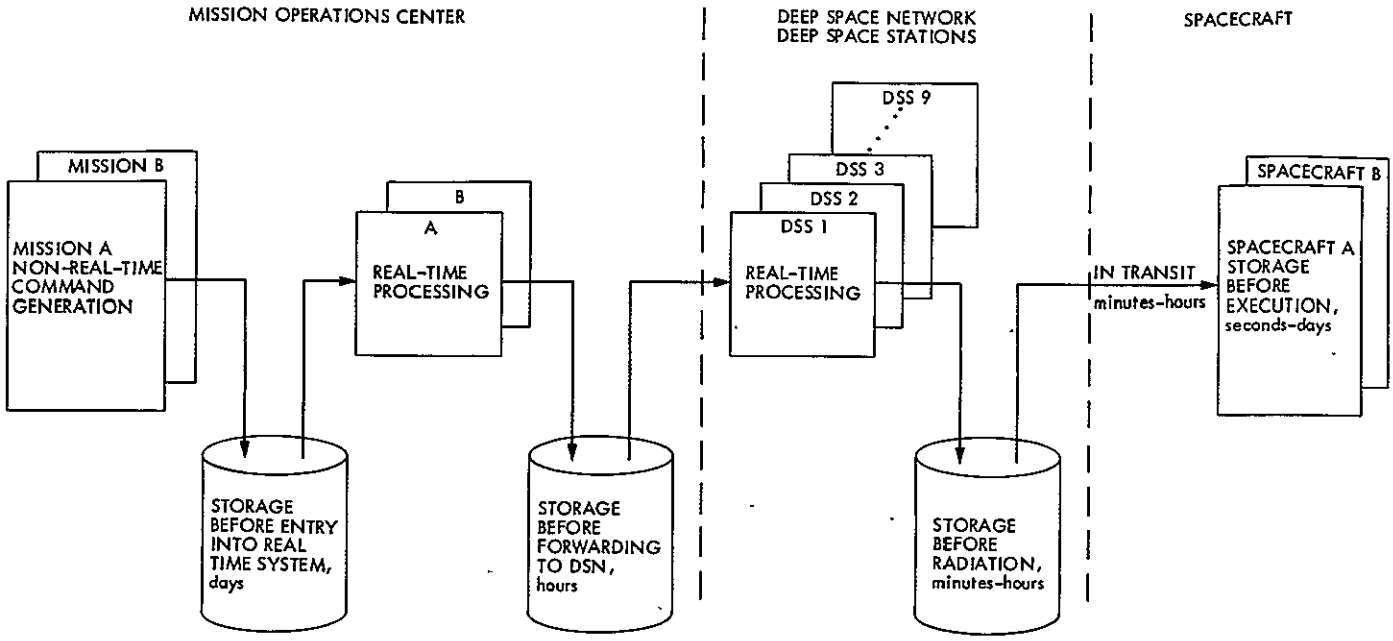

Fig. 1. End-to-end command data flow – typical storage times

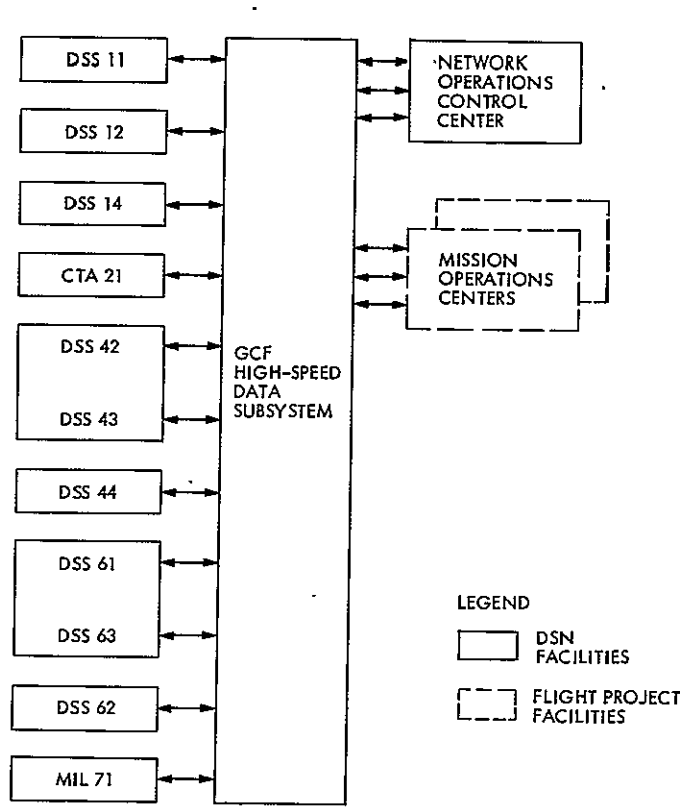

Fig. 2. Facilities which participate in command operations

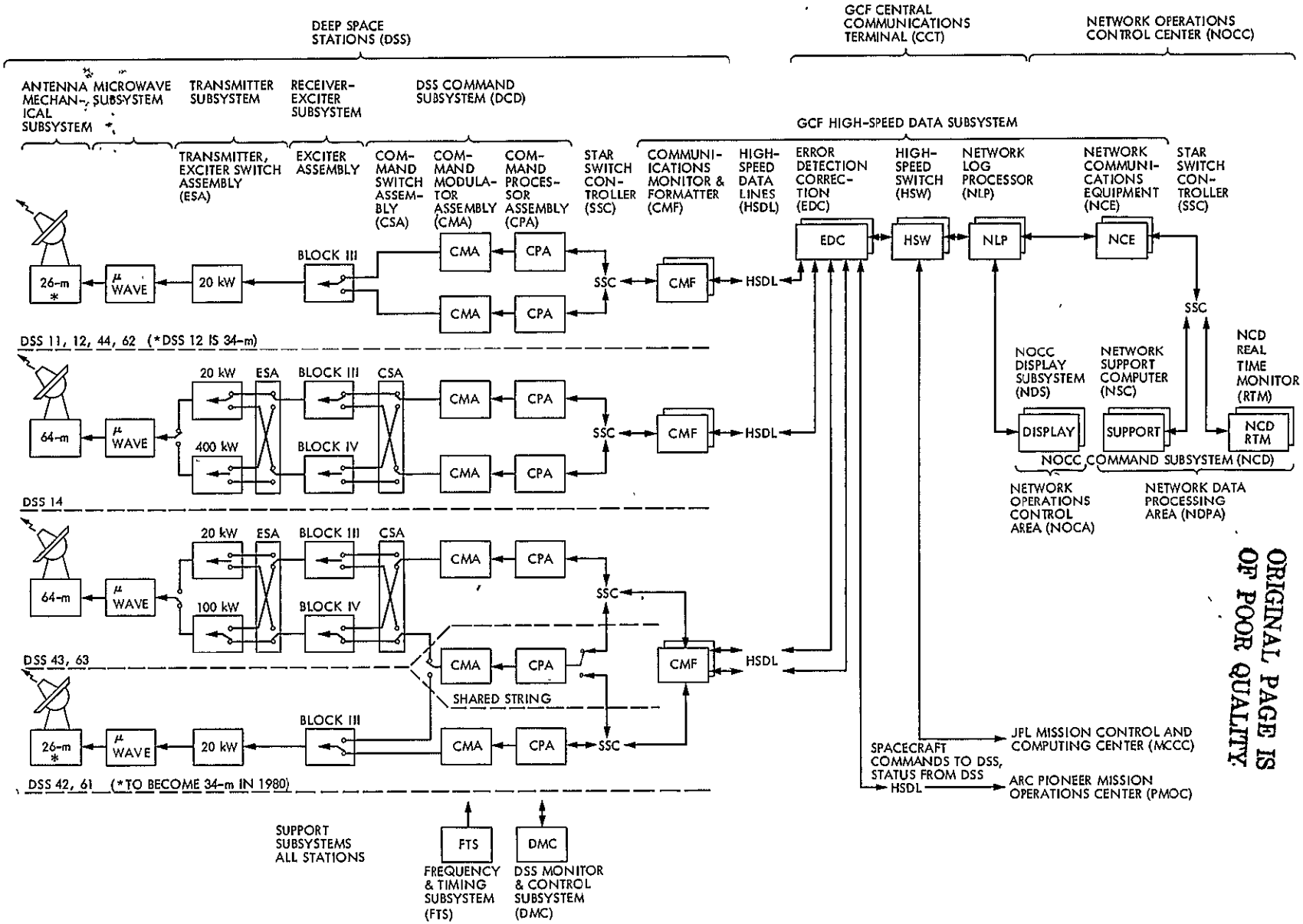

ORIGINAL PAGE IS OF POOR QUALITY

Fig. 3. DSN Command System Mark III-78

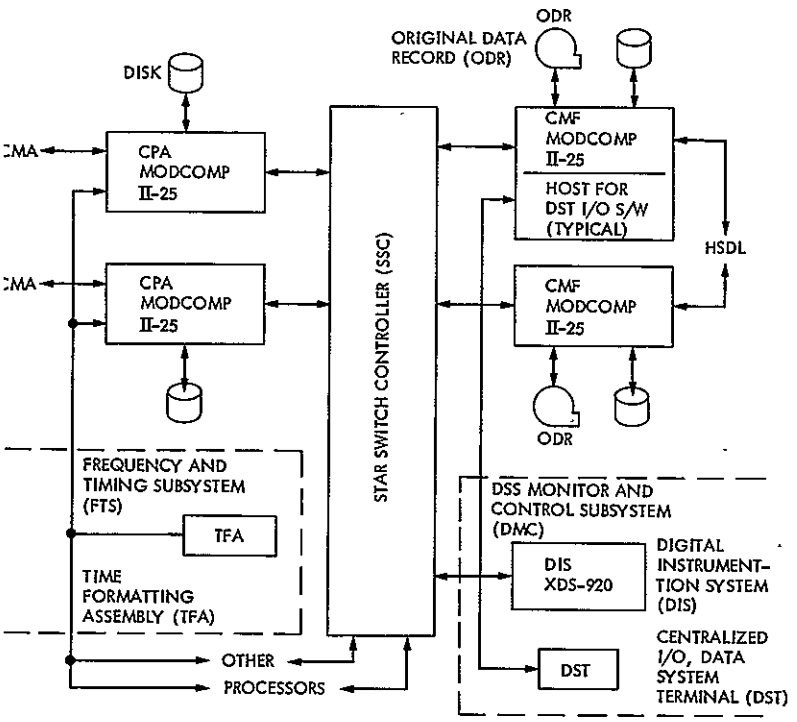

Fig. 4. Deep Space Station implementation details

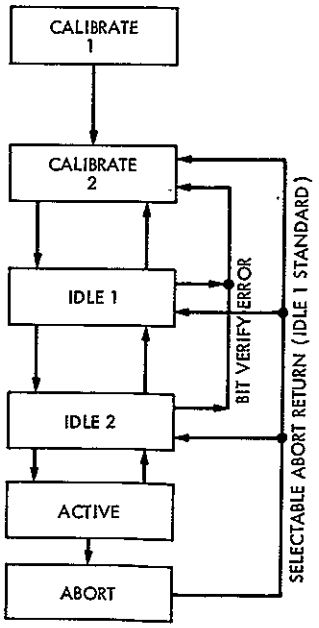

CPA MODE	PRIME PURPOSE	DATA ACCEPTED VIA HIGH SPEED	COMMENTS
CALIBRATE 1	ALLOWS DSS OPS PERSONNEL TO PERFORM INITIALIZATION TASKS	CONFIGURATION, STANDARDS AND LIMITS, MODE CONTROL, RECALL	UPON RECEIPT OF A STANDARDS AND LIMITS AND CONFIGURATION HSD BLOCK, THE CALIBRATE 2 MODE WILL BE ENTERED
CALIBRATE 2	STANDARD MODE FOR UPDATING STANDARDS AND LIMITS AND CONFIGURATION DATA VIA HIGH SPEED PRIOR TO SPACECRAFT ACQUISITION	CONFIGURATION, STANDARDS AND LIMITS, MODE CONTROL, RECALL	MULTIMISSION STANDARD PROCEDURES SHOULD STATE THAT THIS MOD IS TO BE ENTERED FOR CHANGING SUBCARRIER FREQUENCY, BIT RATE
IDLE 1	SAFE MODE - CANNOT COMMAND. PROVISION FOR IDLE/ACQUISITION SEQUENCE. ALLOWS CONFIGURATION AND STANDARDS AND LIMITS TO BE CHANGED	CONFIGURATION, STANDARDS AND LIMITS, MODE CONTROL, RECALL	ALL STANDARDS AND LIMITS AND CONFIGURATION DATA PARAMETERS WILL TAKE IMMEDIATE EFFECT IN THIS MODE
IDLE 2	ALLOWS ENTRY INTO ACTIVE MODE. PROVIDES IDLE/ACQUISITION SEQUENCE DURING COMMAND PERIODS	RECALL AND MODE CONTROL DATA ONLY	MODE CONTROL DATA CONTAINED IN THE COMMAND ELEMENT BLOCK
ACTIVE	COMMAND TRANSMISSION	RECALL AND MODE CONTROL DATA ONLY	
ABORT	PROVIDES ABORT INSTRUCTION TO CMA	RECALL AND MODE CONTROL DATA ONLY	

NOTES: 1. COMMAND DATA MESSAGES WILL BE ACCEPTED IN ALL MODES
2. ALARM MESSAGES/ALARM DATA WILL BE TRANSMITTED TO THE MOC IN ALL MODES EXCEPT ABORT

Fig. 5. DSN Command System mode descriptions

DSN Ground Communications Facility

R. H. Evans
TDA Engineering Section

A functional description of the GCF and its relationships with other elements of the DSN and NASCOM is presented together with development objectives and goals and comments on implementation activities in support of flight projects.

I. Introduction

The Ground Communications Facility (GCF) is one of the three elements of the DSN. The GCF provides for transmission, reception, and monitoring of Earth-based point-to-point communications between the Deep Space Stations (DSSs) (one of the DSN elements), the Network Operations Control Center (NOCC) (the other element) located at JPL, Pasadena, and the Mission Operations Control Center (MOC) at JPL. Voice, teletype, high-speed data, and wideband data channels of the world-wide NASA Communications Network (NASCOM) are utilized for all long-distance circuits, except those between JPL and the Goldstone Deep Space Communications Complex (GCSCC). Goddard Space Flight Center (GSFC) NASCOM Engineering has delegated the responsibilities for planning, budgeting, design, implementation, operation, and maintenance of the communications requirements between Goldstone and JPL to the DSN GCF. Additionally, the GCF provides communications services between the DSSs at each geographic communications complex (Madrid, Australia and Goldstone, Calif.) via intersite microwave system capabilities, and between separated areas of the NOCC at JPL via 230 kbit/s wideband data channels. Also, voice communications are provided within the stations, between the stations, within the complexes, and within the NOCC. The GCF is comprised of eight subsystems; Voice, Teletype, High-Speed Data, Wideband Data, Monitor and Control, Data Records, Network Log Processor, and Network Communications Equipment. The DSN Tracking and Data Acquisition Engineering Office of JPL provides the technical direction and systems management of the GCF and acts as the representative of NASCOM for switching and interconnect functions on the West Coast.

II. GCF-NASCOM Interrelationships

The interrelationships at the programmatic level between JPL's DSN GCF and the NASCOM network, managed, engineered, and controlled at GSFC, are characterized as follows:

NASCOM

(1) Provides long-haul operational ground communications in support of all NASA projects and mission activities including those supported by the DSN.

(2) Accepts and supports communications requirements established by the DSN and validated through continuing consultation and review.

(3) Establishes in consultation with the users the basic characteristics of the NASCOM systems, such as tele-

type line rate and block header formats for switching, and the user electrical interfaces.

GCF

(1) Provides ground communications for all DSN missions and uses the services of NASCOM.

(2) Establishes additional characteristics of all GCF subsystems on an end-to-end basis such as block multiplexing, error correction, monitoring and control, and data records capabilities.

III. Objectives and Goals

The primary objectives of the GCF are to provide highest quality point-to-point transfer of operational data within the DSN and provide simple user and NASCOM electrical and operational interfaces. These objectives are being met by:

(1) Providing automatic message switching and routing.

(2) Providing data transmission subsystems that are as transparent to the user as possible.

(3) Minimizing project-dependent equipment within the GCF.

(4) Providing a centralized common user data records capability.

The goals of the GCF are to provide highly reliable and cost-effective data transmission while continuing an adequate capability balance for multiple mission users. These goals include the following:

(1) Equipment and routing redundancy to minimize single-point-of-failure impact.

(2) Error performance which provides essentially block-error-free throughput.

(3) Design coordinated and consistent with the NASCOM Development Program.

IV. Configuration and Functional Subsystem

The current GCF configuration, including the related NASCOM interfaces and functions, is illustrated in Fig. 1. This configuration illustrates the long-haul communication circuit services external to JPL and Deep Space Communications Complexes (except circuits between the Goldstone Complex and JPL) which are the responsibility of NASCOM. The voice, teletype, high-speed data, wideband data, and monitor and control subsystems point-to-point communications are serviced by this Fig. 1 configuration.

A. High-Speed Data Subsystem

This subsystem shall consist of GCF assemblies that switch, transmit, record, process, distribute, test, and monitor digital data and is used for transmission of:

(1) All digital data for the DSN command, tracking, and monitor control systems.

(2) All low or medium rate data of the DSN Telemetry, Radio Science, Very Long Baseline Interferometry (VLBI), and the DSN Test and Training System.

The High-Speed Data Subsystem provides a capability for transmitting and receiving the serial bit stream formatted data over a single four-wire properly conditioned alternate voice/data channel having a 3.0-kHz bandwidth. This serial bit stream is impressed on communication circuits at a continuous line bit rate divided into message segments referred to as high-speed data blocks.

Two types of data blocks are used:

(1) Data blocks containing user data bits to be transmitted.

(2) Filler blocks containing filler data bits provided GCF when the user data bit/block rate is insufficient to maintain the contiguous bit/block rate required for continuous line monitoring and error control.

Current capabilities for the GCF Mark III period provide the functional capabilities illustrated in Fig. 2. The GCF High-Speed Data Subsystem is standardized on a 1200-bit block size (message segment) and a line bit rate of 7200 bit/s. Subsystem changes to bring about the Mark III capabilities included conversion from a 33-bit to a 22-bit error detection encoding/decoding polynomial code and increasing the number of bits reserved in the data block ending from 36 to 40 bits. The 40-bit block ending with the 22-bit code facilitates numerical serialization and acknowledgement numbers for error correction by retransmission for short outages or errors in GCF end-to-end data transmission.

The error correction capability has significantly reduced the post-pass time required for non-real-time replay of blocks received in error to complete the intermediate data record. Figure 3 illustrates the High-Speed Data Subsystem transitional configuration that was planned for the CY 1977 and CY 1978 time period. The transititional configuration (old and new configurations and interfaces separately or in combinations operational and usable) was required to provide continuous support for ongoing and new projects starting up until the conversion from the old Ground Data System to the new one was completed for support of Voyager and Pioneer Venus Projects and to support the continued extended mission of the

Viking Project through early CY 1979. The dual-mode configuration became operable and usable to support DSN System Testing in November 1977. The added new computer-to-computer switched interface became operational in limited form in early CY 1978 serving the Pioneer Venus Project, other ongoing Pioneer Projects, and the Helios Project with the new Ames Research Center and DSN-NOCC interface in the 22-bit polynomial error detection mode. This new computer switched interface to the Mission Control and Computing Center (MCCC) became operational supporting the Voyager Project in September 1978. The Voyager Project began using the high-speed data subsystem in the error correction mode on November 11, 1978, with the Helios and Pioneer Project following suit shortly thereafter.

The high-speed data subsystem CCT equipment will be reconfigured beginning in early CY 1979 at the termination of the Viking Extended Mission to eliminate the transitional configuration and old 33-bit error detection encoding/decoding equipment and hardware interfaces to the NOCC and MCCC. Other changes are also planned in the interest of cost savings and improved reliability.

B. Wideband Data Subsystem

The Wideband Data Subsystem consists of assemblies that switch, transmit, receive, process, distribute, test and monitor data requiring the use of bandwidths greater than those provided by standard high-speed data channels. The GCF Wideband Data Subsystem functionally illustrated in Fig. 4, together with a listing of functional capabilities provided, includes standard wideband circuits as well as all intersite-microwave (area microwave) capabilities. The Wideband Data Subsystem is used for the transmission of:

(1) All DSN Telemetry System high-rate data that exceed High-Speed Data Subsystem capabilities.

(2) Data interchange between the NOCC and GCF Comm Terminal at JPL.

(3) Data interchange between DSSs within a complex via intersite microwave, including critical timing signals.

(4) Simulation System Data from the Mission Control and Computing Center/Mission Operations Center to the DSSs.

(5) DSN Test and Training System data from the Network Operations Control Center to the DSSs.

The wideband data circuits for interchange of data between the DSSs and JPL are impressed with serial bit streams at a continuous line rate typically 56,168, or 230.4 kbits/s, divided into 2400 or 4800 bit message segments (data blocks). (Line rates of 27.6, 28.5 and 50 kbits/s previously used were deleted in early CY 1978. The 2400-bit data block size will not be used after Viking Extended Mission terminates in early CY 1979.) Similar to the high-speed data subsystem, the blocks are either data blocks or filler blocks inserted when the user data load is insufficient to maintain contiguous data blocks on line.

Engineering planning and design effort is under way beginning this FY 1979 to implement error correction capability into the wideband data subsystem for inbound data from the DSSs to JPL.

C. Voice Subsystem

The Voice Subsystem consists of GCF assemblies that switch, transmit, receive, distribute, test, and monitor transmissions originally generated in vocal form, and includes internal voice communications within the Deep Space Station Communications Complexes, DSSs, and the NOCC. The subsystem service provides capabilities between those areas and to non-DSN area interfaces as follows:

(1) NOCC and DSS.

(2) NOCC and MCCC/MOC (or remote MOC).

(3) MOC and DSS for Command System backup.

The Voice Subsystem functional capabilities and key characteristics include:

(1) Standard voice-data grade circuits for all traffic.

(2) Conferencing capability on one intercontinental circuit during noncritical periods for all deep space stations supporting a single project (individual circuits for each DSS during critical periods, resources permitting).

(3) User-controlled intercomm switching.

(4) Circuits used for high-speed data transmission (backup) if required.

(5) Voice traffic recording in the central communications terminal upon request.

D. Teletype Subsystem

This subsystem consists of assemblies that switch, transmit, receive, distribute, test and monitor digital signals originally generated in 5-level Baudot format at a teletype (TTY) line rate of 100 words per minute. The operational use of teletype continues to be de-emphasized and is used primarily for emergency backup operational transmissions and administrative communications. Service functions and key characteristics include:

(1) Handling Air Force Eastern Test Range (AFETR) generated predicts for DSN initial acquisition.

(2) Transmitting nonoperational messages between the JPL Message Center and other locations.

(3) Use of standard NASCOM format and the NASCOM communications processor for message switching.

(4) Employment of time division multiplexing techniques to reduce trunk circuit costs.

GCF and NASCOM engineering work has begun to convert the TTY subsystem to the new eight-level ASCII (American Standard Code for Information Interchange) national standard. Plans are to complete the conversion in CY 1979.

E. Monitor and Control Subsystem

The Monitor and Control Subsystem consists of assemblies that collect, process, and display the status and performance of the GCF Subsystems in real-time. The Monitor and Control Subsystem with a listing of functional capabilities illustrated in Fig. 5 include minor subassemblies located at each DSS in the CMF to interface station GCF function status and performance indicators to the CMF for monitor block formatting and transfer to the Central Communications Monitor (CCM) Processor at JPL. The CCM also receives real-time status and performance information from local GCF subsystems. All real-time status and performance information received by the CCM is processed and displayed relative to preset standards and limits to facilitate operations monitoring and technical control. Information and alarms are displayed on continuous line performance and data flow throughput error control.

F. Data Records Subsystem

The DSN requirements for the data record processing and production functions are implemented in the GCF Data Records Subsystem. The Data Records Subsystem consists of assemblies in the CCT that log in real-time, monitor, identify gaps, provide for processing and editing of data gap lists, control data gap recalls from the DSSs and the generation and accounting for Intermediate Data Records (IDRs) and fill data records selected from records of the GCF real-time log.

The existing Data Records capability is a collection of functions distributed through the Data Records Processor, the GCF Network Log and Network Communications Equipment Subsystems, which uses the NOCC Real-Time Monitor and Network Support Processors to identify process and edit the gap lists.

G. Network Log Processor Subsystem

The Network Log Processor (NLP) Subsystem consists of GCF miniprocessors, multiple mag tape units, and peripheral I/O assemblies that switch, transmit, receive, process, and record data. The NLP Subsystem assemblies are located in the Central Communications Terminal (CCT) for interfacing the CCT with the remote-located DSN Network Data Processing Area (NDPA), and the NDPA with the Network Operations Control Area (NOCA) (See Fig. 6).

The NLP Subsystem provides a Deep Space Network Operations Control interface to monitor and log all data transferred between the DSSs and the local and remote MOCs, receive all inbound DSS Monitor and Control Response Data, and transmit all predicts and control messages from the NOCA to the DSSs.

H. Network Communications Equipment Subsystem

The Network Communications Equipment (NCE) Subsystem consists of GCF miniprocessors and peripheral I/O assemblies that switch, transmit and receive data. The NCE Subsystem assemblies are located in the Remote NDPA (roughly three-quarters of a cable mile distant from the CCT). The NCE assemblies comprise a GCF Area Communications Terminal located adjacent to the NDPA (in Building 202 at JPL).

The NCE interchanges multiplexed block formatted data with the NLP subsystem processors located in the CCT over three full-duplex 230-kbit/s wideband data channels extending the GCF interface to the NDPA (See Fig. 6). This GCF-NDPA interface function provides:

(1) Process data for transmission to and accept data from the GCF CCT.

(2) Multiplex/demultiplex and buffer data for all NDPA processors.

(3) Route data to and from all NDPA processors.

V. Typical Configuration

The DSN GCF is designed for multiple mission support. Improvements and additions are integrated to meet new era and project requirements (Voyager and Pioneer-Venus requirements were completed in CY 1978) while continuing to support the Viking, Helios, and Pioneer 6 through 11 Projects. Figure 7 illustrates, in general, the GCF configuration for support of these projects. Additionally, remote information centers and other non-DSN NASCOM-serviced installations on the West Coast are serviced through the NASCOM West Coast Switching Center, an integral part of the GCF 20/Central Communications Terminal at JPL.

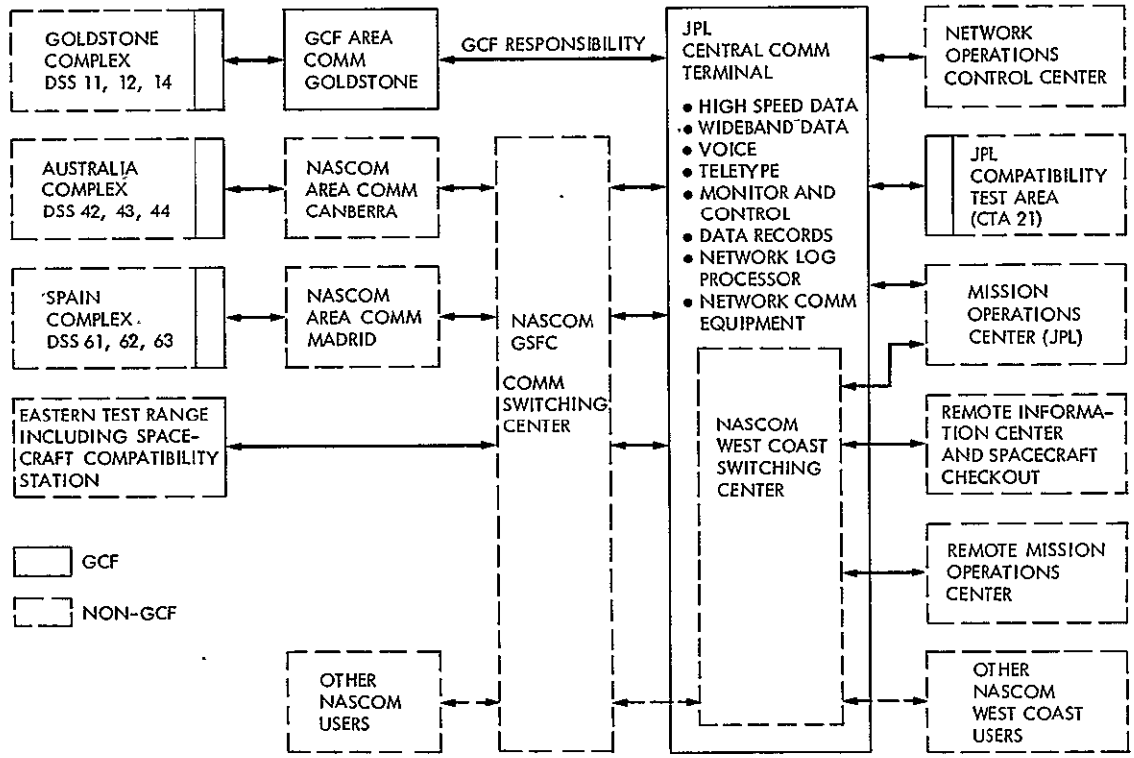

Fig. 1. GCF configuration

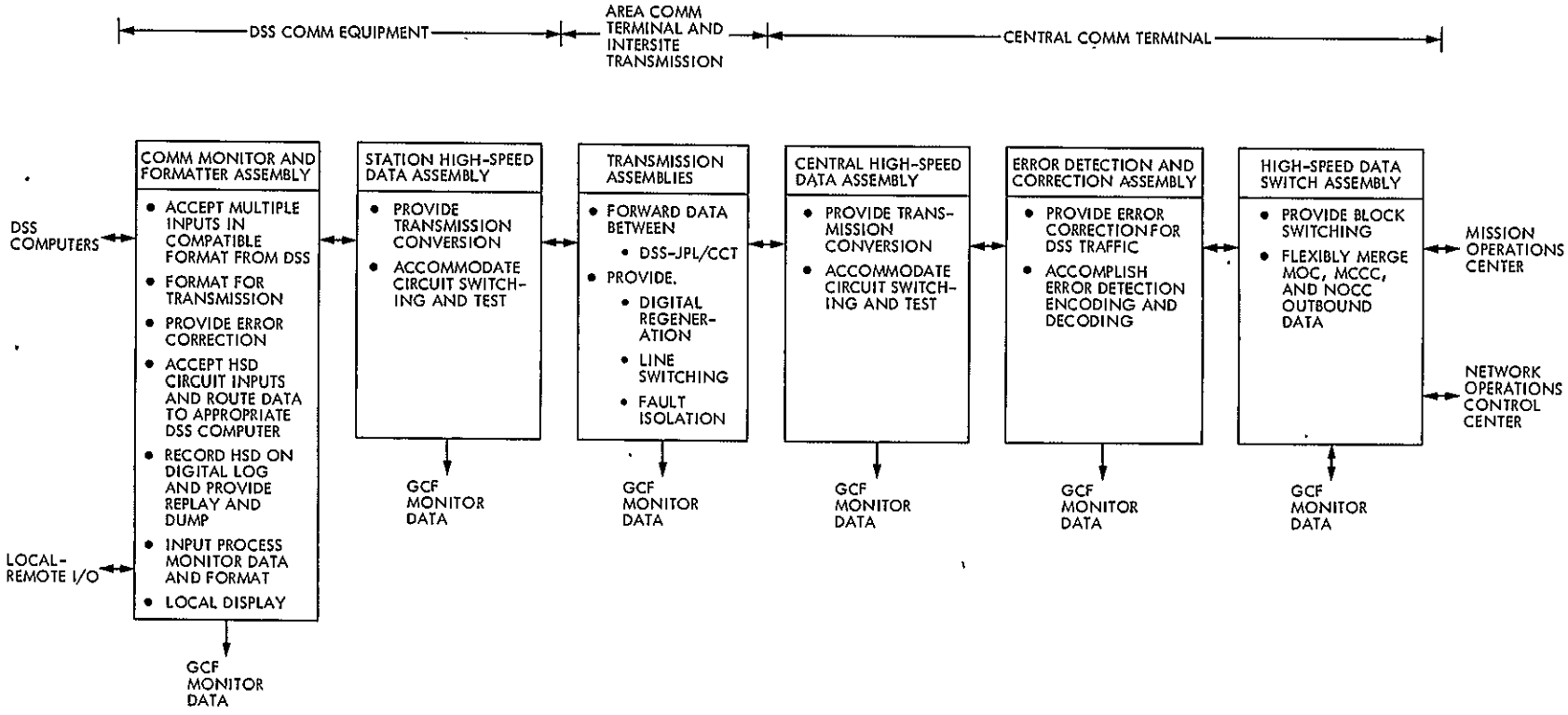

Fig. 2. GCF high-speed data subsystem functional capabilities

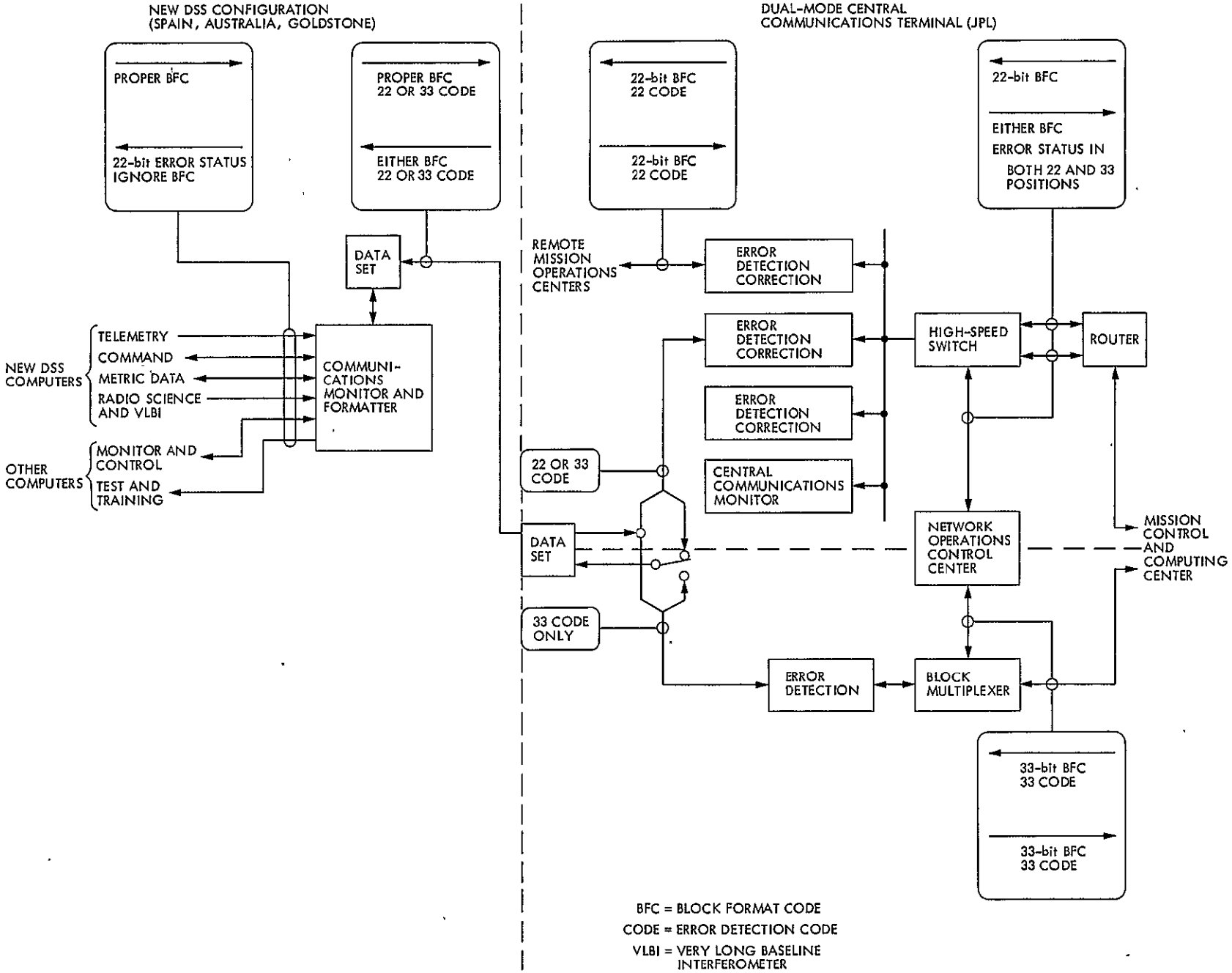

Fig. 3. GCF high-speed subsystem configuration and interface through Viking Extended Mission, ending March 31, 1979

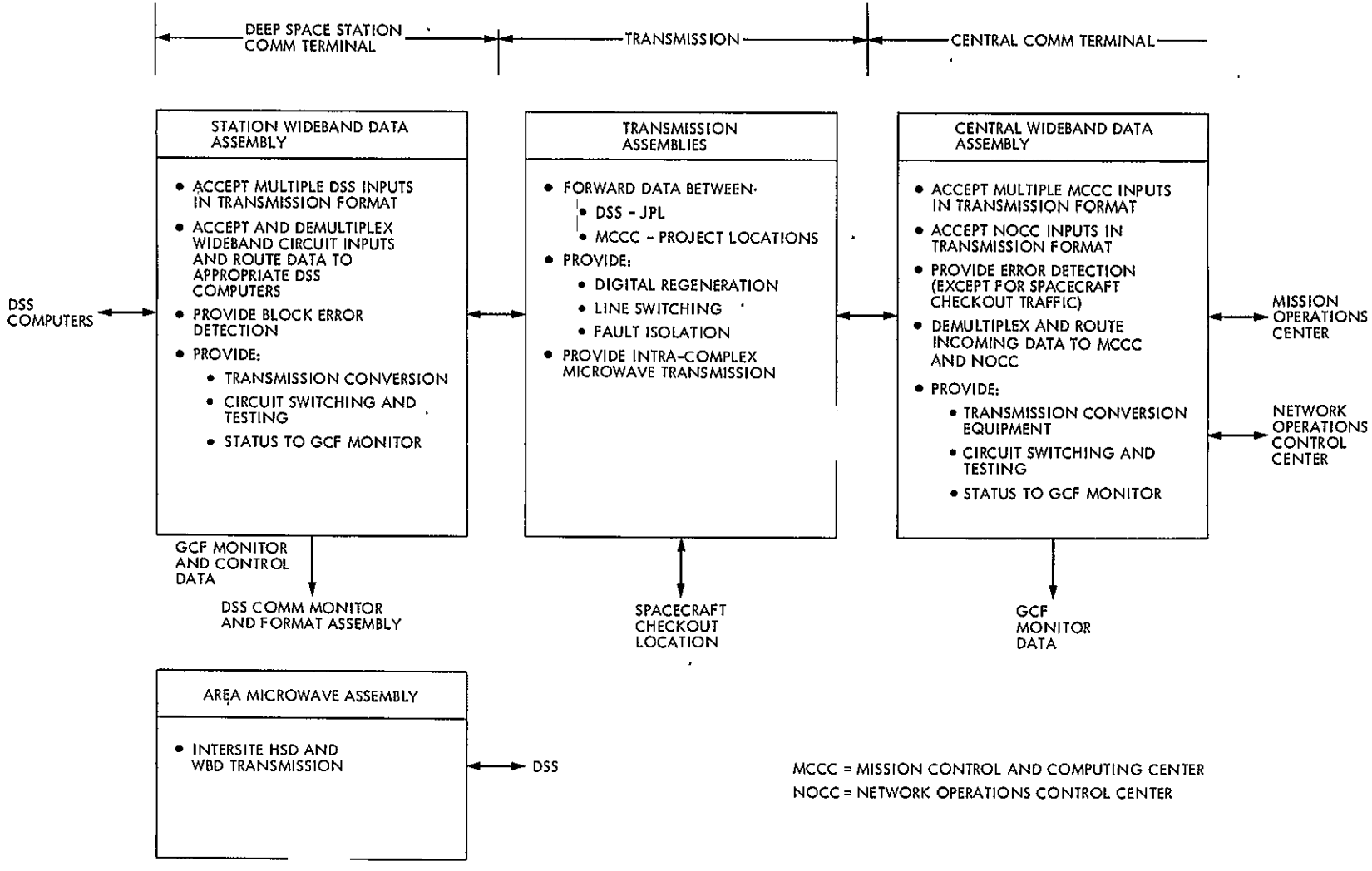

Fig. 4. GCF wideband subsystem

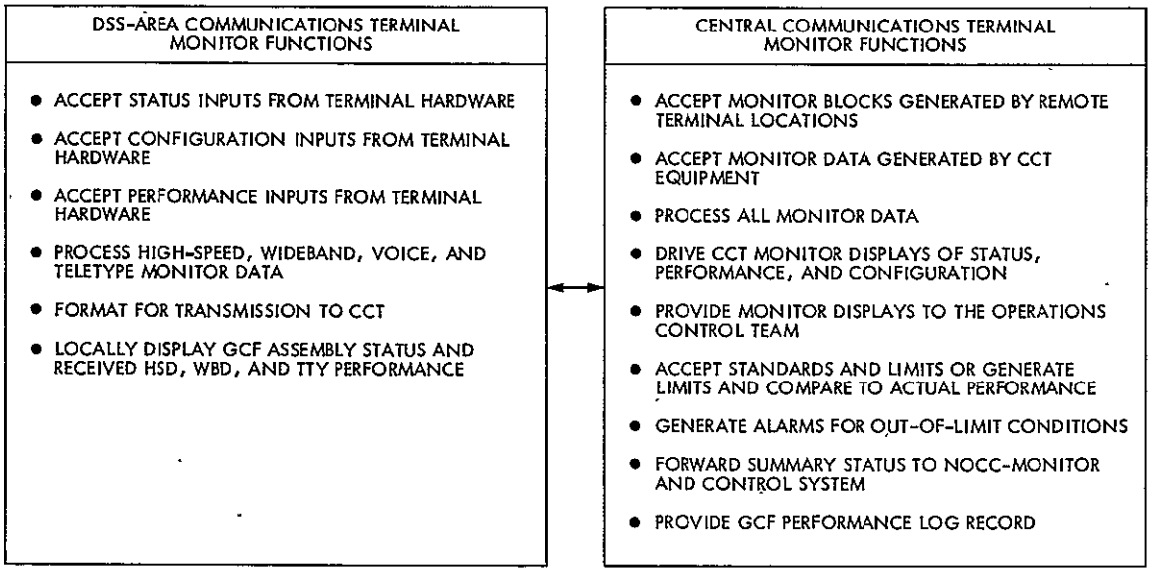

Fig. 5. GCF Monitor and Control Subsystem functional requirements

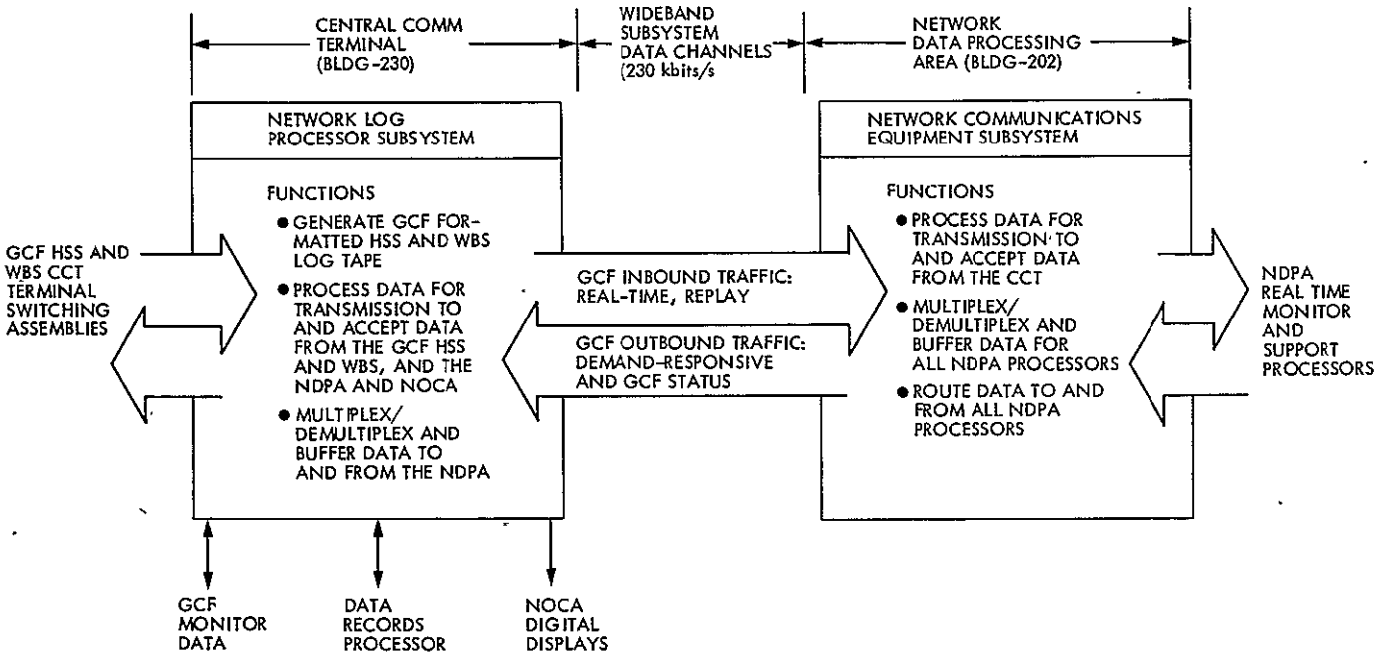

Fig. 6. GCF network logging and interface network operation and control subsystems

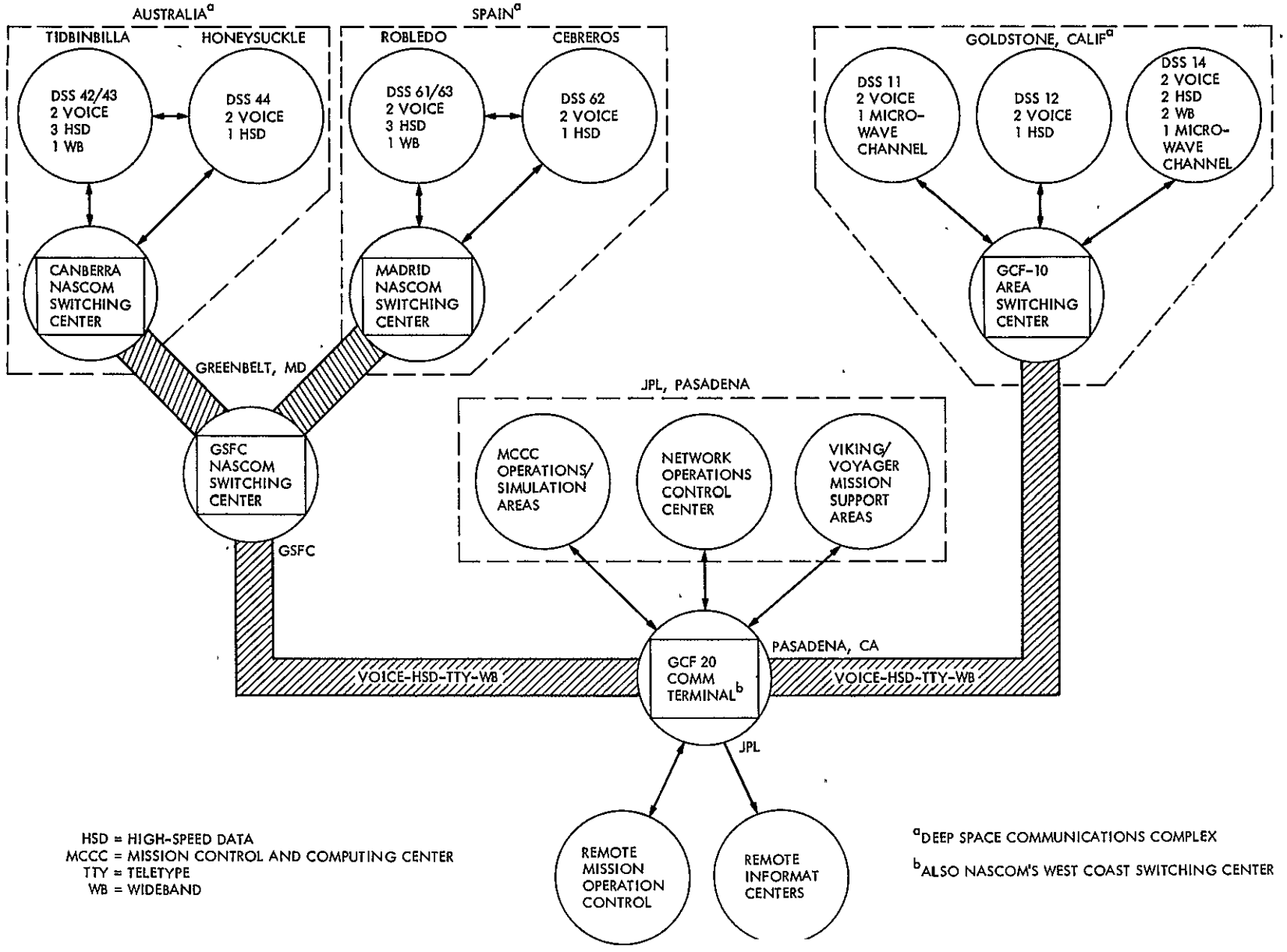

Fig. 7. DSN support locations and GCF-NASCOM circuit requirements

Voyager Support

J. Allen and H. Nance
Deep Space Network Operations Section

This is a continuing Deep Space Network report on tracking and data acquisition for Project Voyager. This report covers the period from January through May 1978.

I. Voyager Operation

A. Status

Both spacecraft successfully passed through the asteroid belt which lies between the orbits of Mars and Jupiter. As of May 1978, Voyager 1 was 555 million kilometers (348 million miles) from Earth, traveling with a velocity of about 19.9 kilometers (12.4 miles) per second relative to the sun with one-way communications time of 30 minutes and 45 seconds. Voyager 2 was more than 535 million kilometers (332 million miles) from Earth, traveling at about 18.8 kilometers (11.7 miles) per second relative to the sun, with one-way signal time of 29 minutes and 52 seconds.

Both spacecraft have experienced problems that required special support effort by the Deep Space Network (DSN) personnel. DSN personnel worked closely with project personnel in determining the best way to extract the maximum capability of equipment and facilities to enhance the probability of meeting project mission objectives.

B. Spacecraft Problems

1. Voyager 1. On February 17, when DSS 63 acquired the Voyager 1 spacecraft, it was discovered that 40 b/s of engineering data was being transmitted through the low-gain antenna (LGA) instead of the 1280 b/s through the high-gain antenna (HGA) as expected. This mode indicated that the failure protection algorithm had been entered. The data was erratic because the link performance was at threshold; to strengthen the downlink signal, it was decided that the S-band ranging would be turned *off*. It was determined that the spacecraft was in roll inertial, sun acquired, but not in celestial cruise. Commands were sent to capture Canopus, and the HGA was automatically selected. A programed Cruise Science Maneuver (CRSMVR) had been aborted, apparently caused by some form of gyro-induced error since sun sensor data obtained from the playback indicated a displacement in solar position at the culmination of each of ten 360-degree yaw turns. A group of analysts examined the data in detail and determined that the spacecraft attitude at the end of the 3600-degree yaw turn was about 24.50 deg short of the predicted orientation. This resulted in the sun being outside the sun sensor field of view, causing the CCS to abort the remaining portion of the maneuver. A sun search was automatically initiated and the sun was reacquired.

The attitude error was caused by the use of the design value of the gyro scale factor in the Maneuver Analysis Program SET (MAPS) instead of the actual measured scale factor values of the gyros. It was noted that the 24.50-deg turn error represents a deviation in scale factor values from the design value of approximately 0.37%, which is well within the allowed tolerance and in no way associated with substandard gyro performance. The improper gyro scale factor conversion values in the

ground software that caused the problem has been corrected by including the appropriate value for each gyro in the generation program.

On February 17 the Plasma Science principal investigator indicated that the sensitivity of the main cluster of the three plasma detectors had degraded significantly and the instrument was not able to detect positive ions to a level as low as before. Real-time commands were sent first to calibrate the plasma instrument in all gain states (without success in the main mode) and second to "power on reset" (POR) the instruments twice, hoping to recapture the sensitivity (again without success).

In early March further degradation was observed in the ailing main detector, and it appeared that the Jupiter encounter objectives would be affected as well as the cruise measurements. The instrument's side detector continued to operate well.

A series of sensitivity tests were performed in March and April, as was a reset/diagnostic test. There appeared to be a threshold on positive ion measurements, causing the output data to be shifted such that only the peaks of the plasma curve appear. MIT is studying the problem to determine how this could happen and what could be done.

During a calibration of the scan platform on February 23, the azimuth actuator failed to reach its commanded position. This resulted in a scan slew abort, when the Attitude and Articulation Control Subsystem (AACS) detected the slew in progress at the end of 60 minutes. The actuator failed to move appreciably when commanded to the safe position by the scan slew abort routine. The Central Computer and Sequencer (CCS) scan command and scan abort routines were inhibited and the cameras placed in a safe state as a precautionary measure until the problem could be evaluated.

On March 17, a test sequence of slews was commanded and executed which resulted in the platform moving as desired. The slews were performed at the low rate to create maximum torque from the actuator. The first slew appeared to move at an intermittent rate but two additional slews were executed flawlessly.

During the week of March 24-30, 1978, the scan platform was commanded through several slew sequences, which exercised various directions, magnitudes and rates of motion in the region of the science preferred position. During the following week the testing included periods with the scan platform heater *off* and *on*. Further testing is continuing with a plan to define scan platform pointing region limitations, if any.

On 18 May the gyros were turned on by an onboard sequence for calibrations to be performed on May 19. During the GYCAL it was recognized that there was no command in the sequence to turn the gyros *off*. A decision was made to leave the gyros on through the ASCAL to be performed on May 26 and use this opportunity to obtain long-term gyro drift data.

An LECP sun interference test was performed on May 23 by ground-commanding LECP full scan mode. It was found that the sun causes excessive noise in this mode. The LECP was then ground-commanded to the reduced scan (normal) mode.

2. Voyager 2. On February 25, the Photopolarimeter (PPS) principal investigator advised that the PPS filter wheel was stepping erratically. It was requested that the instrument be safed and then turned off until further analysis could be performed. The polarization analyzer wheel had previously indicated that it was stuck. The onboard command sequence resulted in the filter wheel and analyzer wheel being placed in positions other than those which would have resulted from the safing commands. Analysis indicated that not only was the filter wheel stepping erratically prior to instrument turnoff, but that the analyzer wheel seemed to have become unstuck and responded to the safing command. On March 2, a series of commands were sent to see if the erratic stepping continued, but during the testing nominal stepping was observed.

On April 5, 1978, Voyager 2 (spacecraft 32) entered its command loss routine, which switched to the spacecraft secondary receiver (receiver number 2). The receiver switch was the result of the protection algorithm's normal function since the spacecraft did not receive commands within 7 days. The spacecraft remained in this configuration for 12 hours, and during this period many attempts were made to attain two-way lock on receiver number 2. All attempts failed because the voltage-controlled oscillator tracking loop capacitor had failed, but this was not known at the time. Preliminary analysis of the data, about 24 hours after the failure, indicated that the tracking loop capacitor may have failed.

After 12 hours had elapsed and the spacecraft's command loss time had not been reset (no command capability), the spacecraft reentered the command loss routine and switched back to receiver number 1. Receiver number 1 attained two-way lock and several commands were transmitted through the main receiver, thus causing a reset of the 7-day timer. However, about 30 minutes after the switch, an unknown failure in the receiver caused excessive current, which appeared to have blown the receiver fuses. The spacecraft remained on the main receiver and was unable to receive commands from Earth. However, the 7-day timer was set to automatically switch to

the secondary receiver on April 13, at which time attempts would be made to command the spacecraft in spite of the failed capacitor.

The intervening period was a period of intense activity focusing on developing a strategy to permit commanding the spacecraft through the secondary receiver with a failed tracking loop capacitor. The DSN participated in developing the uplink sweep strategies and overall command strategy within the capabilities of the facilities available.

The loss of the radio frequency tracking loop capacitor in receiver 2 (secondary receiver) meant that the receiver could be acquired (i.e., phase coherency established), but the tracking loop could not maintain lock as the receiver frequency shifted due to the doppler effect. It was determined, by testing a test receiver with the capacitor shorted, that the bandpass of the Voyager receiver was approximately 200 Hz (S-band). It was also determined, by testing, that spacecraft command detector lock could be achieved and commands received while on the command subcarrier (512 Hz from the carrier), thus effectively widening the command window.

With this information and following the guideline that at least one command must be received correctly by the spacecraft during a sequence, a sweep profile and test plan was developed. This plan called for one wide sweep of best-lock frequency (XA)±1500 Hz (S-band), equivalent to sweeping through XA and at a rate of 2.4 Hz/s (S-band). During these sweeps, commands would be transmitted from DSS 63 at 15-s centers, the interval computed to give the highest probability of command reception. If these sweeps were unsuccessful, a larger sweep (XA plus or minus 5000 Hz) at a slower tuning rate (1.92 Hz/s) would be performed.

If any of the initial sweeps were successful, the receiver best-lock frequency would be computed using available information on the downlink (lockup time, time of peak AGC, etc.). The station would then transmit this frequency, corrected for doppler, and maintain lock by ramping to compensate for doppler. Commands could be transmitted during this period. This plan was successfully tested with DSS 63 on a training exercise on April 11.

On April 13 this Voyager 2 recovery sequence was initiated by DSS 63. Within 55 minutes it was confirmed that commands had been received through receiver 2. Analysis indicated that the receiver had been acquired during the first sweep with the actual best-lock frequency slightly more than 750 Hz (S-band) from the predicted frequency.

The preplanned command sequence was entered approximately one hour later. The procedure used consisted of updating the best-lock frequency and performing a short sweep every 90 min for the remainder of the pass. Following the sweep, DSS 63 ramped the uplink to compensate for doppler while transmitting blocks of 24 commands. This was done six times, to insure that six different commands were received. By the end of the track, the spacecraft receiver lock had been held for a total of more than 4 hours, proving that the receiver could be acquired and the spacecraft commanded.

Following the initial receiver 2 acquisition, many plans were made to compensate for the loss of tracking capability. The procedure used during 26-meter tracking involved turning on the transmitter at Track Syn Freq (TSF) and allowing the earth rotation induced doppler to sweep the uplink signal through the acquisition bandwidth of the spacecraft receiver.

The characteristics of the spacecraft receiver AGC and the downlink signal during these periods were unlike anything experienced on previous programs. Essentially what occurs is that as the uplink signal approaches the spacecraft receiver acquisition range, the AGC circuit detects the signal and switches the downlink reference to the voltage control oscillator. At this time the receiver is not in lock and the indicated spacecraft AGC is 20 dB below predicts. The downlink reference is now the free-running VCO; as a result the doppler is meaningless (neither one-way nor two-way) and the downlink signal is corrupted by VCO noise. Following the initial AGC acquisition the indicated uplink AGC increases steadily for about 40% of the total two-way period. The AGC then ramps up rapidly to about 8 dB below predicted level, at which time the spacecraft receiver apparently achieves coherent loop lock. At times the indicated spacecraft AGC goes to zero during this ramp. Once the loop is locked, the indicated spacecraft AGC follows a fairly smooth pattern for the remainder of the two-way period. The doppler prior to the first AGC is good one-way Ultra Stable Oscillator (USO) doppler. The doppler between first AGC and loop lock is no good. The doppler from the loop lock to loss of AGC is good two-way doppler. The doppler following loss of AGC is good one-way.

The downlink AGC and SNRs are affected by the VCO phase jitter following the first spacecraft AGC acquisition. At that time the spacecraft selects the VCO as the downlink reference even though phase lock has not been achieved. As a result the downlink is corrupted by the phase noise of the free-running VCO. This is manifested by a decrease in the symbol and bit signal-to-noise ratio. As the uplink signal approaches the loop acquisition range, the phase noise becomes worse since the loop is now attempting to acquire and is slipping cycles. During the steep AGC ramp just prior to acquisition, the loop is in a state of continuous cycle slipping and the resulting phase noise becomes so bad that the indicated downlink AGC is also degraded about 8 dB. Following

loop lock, the downlink AGC and SNRs return to normal levels and stay there throughout the remainder of the two-way period.

Voyager 2 was successfully commanded by a 26-meter station using this procedure on April 18. The receiver was locked as predicted. During the period 24 duplicate commands were sent. Twenty of the commands were received and executed by the CCS. Receiver lock tests were performed daily with the spacecraft to determine the Project's capability to predict and demonstrate receiver and command detector lockup. On April 25 the spacecraft VCO rest frequency unexpectedly increased by 182 Hz over what it had been on the previous 12 station passes. Efforts continued to better model the receiver VCO, so that the rest frequency could be predicted to the accuracy of plus or minus 100 Hz required for commanding.

A trajectory correction maneuver (TCM) was performed on May 3. This was the first Voyager demonstration of a TCM tweak load one day prior to the TCM. Due to the uncertainty in commandability, the enable command was sent about 14 hours earlier than for previous TCMs. Two-way noncoherent (TWNC) mode was entered prior to the TCM to use the USO for downlink frequency. The TCM was executed successfully.

A series of frequency sweeps was started and continued for about 30 hours after the TCM to measure the VCO as a function of temperature change. Telecommunication analysts were able to provide good predicted frequencies so that the receiver maintained lock to allow commanding the TWNC *off* at the end of the sweep period. Planning continues for the continued operation and navigation of the spacecraft through its encounters.

The Voyager 2 CCSL B207 was successfully uplinked to the spacecraft on May 24. The 33 min load was sent twice, since only about 60% of the commands were accepted by the CCS. The lack of a VCO frequency measurement on the tracking pass prior to the load was the primary cause of the command difficulties.

II. Station Operation

A. New Capability

The new MDA software (DMK-5106-OP-C), which provides the TRK 2-14 radio metric data format capability, was distributed to the field on February 27, 1978. This format was basic to the new interface for radio metric data to the Project. The new interface is between the DSN and the Project in the form of an Intermediate Data Record (IDR) and replaces the MCCC Project Tracking Tape (PTT) as the Project interface. The change was necessitated by the MCCC Mark III Data System, in which the IBM 360/75 computers were replaced by Modcomp minicomputers. Under the MCCC Mark III Data System concept, radio metric data is not processed by MCCC.

A series of training/test passes was authorized so that the stations, network data processing terminal and project navigation team personnel could become familiar with the new operation and interface. The normal problems associated with a new operation and software were experienced and appropriate procedures generated to alleviate the problems. On May 1 support of Voyager 1 was converted to the new interface and on May 6 support of Voyager 2 was converted. Simultaneously with the implementation of the MDA software, the associated Planetary Ranging Assembly (PRA) software (DIR-5125 OP) became operational.

DSS 11 was decommitted from Project support and started the Mark III Data System (MDS) implementation on January 15, 1978. The installation and subsystem testing was completed on March 22, 1978. On March 23 the Operational Verification Tests (OVT) were initiated. The minor problems encountered during these tests were corrected and DSN Engineering Interface Verification Tests (DEIVT) were conducted on April 3 and 6, 1978. The Performance Demonstration Test (PDT) was conducted on April 11 and the Ground Data System (GDS) Test on April 17. The GDS test was only partially successful and was rerun on May 12. Interspersed with the tests were demonstration passes during which the Voyager spacecraft were tracked and the data carefully analyzed. The station was put under configuration control on April 26 and assumed its Project support role along with the other 26-meter stations.

B. Operational Support

The support of the Voyager 2 emergency placed an extra burden on the DSN operations in the areas of planning, tracking analysis and real-time operations. Approximately 120 scheduling changes were required in order to meet the station support requirements for real-time and analysis activities. Procedure changes were required which could not be fully tested or refined before being put into the operational support category, placing the DSN in a higher risk situation. An extra requirement was placed on predict generation to meet the increased activity. Most of the activities will continue, especially in the planning and analysis area, to insure that appropriate procedures are developed for station handovers, ranging, doppler and commanding for the immediate real-time support activity as well as for the future Jupiter encounter operation. Although additional burdens are placed on the Deep Space Station Operations, and in some cases the accomplishment is difficult because of manual intervention, it appears as if the DSN can meet its commitment to successfully support the Voyager Project during the encounter of Jupiter.

Acknowledgment

Thanks are due B. Madsen, J. A. Wackley, and R. P. Laeser, all of JPL, for important contributions to this work.

Bibliography

Voyager Mission Status Bulletins 16 through 20 Public Information Office, Jet Propulsion Laboratory, Pasadena, Calif. (internal documents).

D6

N79-19051

Pioneer Venus 1978 Mission Support: DLBI Wind Measurement Experiment End-to-End System Test Phase

R. B. Miller
TDA Mission Support Office

The ten months of end-to-end system checkout for the Differential Long Base Interferometry (DLBI) Wind Measurement Experiment for the Pioneer Venus Mission are described.

I. Introduction

The Pioneer Venus Multiprobe Entry on 9 December 1978 included as a major scientific objective the determination of the wind patterns as a function of altitude in the Venusian atmosphere. This experiment involved a ground-based interferometry experiment in order to measure the components of the wind perpendicular to the line-of-sight of each of the four Probes as they descended through the Venusian atmosphere. The execution of this experiment required coordination between four independent agencies:

(1) The Massachusetts Institute of Technology (MIT), the home of the principal investigator, Dr. Charles C. Counselman III, and the location of the computer systems and software where the station and Probe to Bus differences are taken and the actual science executed.

(2) Ames Research Center, the location of the Project Office.

(3) Jet Propulsion Laboratory, which was assigned tracking and data acquisition management responsibility for the Pioneer Venus Project, responsible for the operation of the Deep Space Network, and assigned responsibility for overall coordination of the four tracking stations which supported the experiment.

(4) Goddard Space Flight Center, responsible for the operation of the Spaceflight Tracking and Data Network and, in particular, for the operation of the Guam and Santiago sites used in the experiment.

Data flow for the experiment involves operation of receivers and recorders at four tracking sites around the Pacific basin (the DSN 64-meter stations located at Goldstone, California (DSS 14) and Tidbinbilla, Australia (DSS 43); and the 9-meter STDN stations located at Guam and Santiago, Chile) (see Fig. 1). The recordings made at the tracking stations are 12-megabit/second wideband digital recordings which have to be shipped to the Jet Propulsion Laboratory for preliminary processing. At the Jet Propulsion Laboratory, the 12-megabit/second recordings are processed to extract each signal of interest (for the mission seven signals: two cal tones, four Probes, and the Bus) individually onto reduced bandwidth computer compatible recordings. These computer compatible recordings are then shipped to MIT where the interferometric differences are taken and analyzed. It was clear from the outset that in order to determine that the total experiment was working properly it would be necessary to operate the entire end-to-end ground system, including equipment and software, at JPL and MIT. Since data from at least two stations were necessary in order to have an interferometer,

each test session would have to involve at least one overseas station. This meant that data tapes would have to be shipped from an overseas site to the Jet Propulsion Laboratory for processing; then the reduced bandwidth tapes would have to be shipped to MIT for further processing before the results can be known for any given test. It was then clear that upwards of a month could be expected between the time of taking test data at the stations and knowing the results of those tests. For this reason, it was planned from the outset to complete the implementation of the equipment necessary to support the experiment at the four tracking stations in February of 1978 to allow ten months to accumulate test data and trouble-shoot all elements of the system.

This report focuses on that ten-month test activity: the activities which took place, and the problems which were uncovered and solved.

II. DLBI Wind Measurement Experiment Prior to February 1978

The list of references at the end of this article gives background information about the experiment and the history of activities in support of the ground system portion of the experiment up to the February 1978 end-to-end system testing. Reference 1, from September 1975, describes the early identification of the DLBI Wind Measurement Experiment requirements and the assignment of the TDA responsibilities to the Jet Propulsion Laboratory when the decision was made that experimenter-provided equipment should not be used at the stations. Reference 2 gives a simplified tutorial as to the fundamental basis of the interferometric experiment and its basic requirements. Reference 3 defines the overall configuration at the four tracking stations and the bandwidth reduction equipment at the Jet Propulsion Laboratory when the basic design had solidified. Reference 4 describes the wideband digital recordings which were used at 12 megabits/second to support this experiment. Reference 5 describes the development of a special-purpose receiver for the support of the experiment. A portion of Ref. 6 describes the completion of the implementation and installation at the four tracking stations.

III. The Ten Months of End-to-End System Checkout

The magnitude of the test activity in retrospect is hard to believe; there were 20 test tracks executed using various combinations of the four tracking stations involved and well over three hundred 12-megabit/second tapes of data which were shipped from the tracking stations to JPL. A mechanism which developed in order to coordinate this rather extensive activity was a teleconference between all supporting agencies on a periodic basis to report results and status and coordinate activity between the agencies. In an attempt to find some logical presentation of all this complex activity, the remainder of this report will give snapshots of the status during the 10-month period as reported at these teleconferences.

A. 26 May 1978

This first phone conference was held only between JPL and the Massachusetts Institute of Technology. This and each subsequent phone conference would always include engineering personnel on both sides of the interface as well as personnel responsible for tracking station operations. Since the technique (see Ref. 2) and the tracking station receiver and recording equipment were designed to accommodate a 2-MHz bandwidth, a complete test of the system was dependent on finding two usable signals that are contained within a 2-MHz bandwidth. From the onset it was planned to use various pairs of the ALSEPs (Apollo Lunar Surface Experiment Packages) on the moon as the signal sources for the test phase. Table 1 lists some of the key characteristics of the ALSEPs.

The first test track took place on 28 February and was to involve ALSEPs 2, 1, and 4, and DSS 14 and Santiago. DSS 14 (the DSN 64-m station at Goldstone, California) experienced considerable difficulties during this track due to a combination of equipment and procedural problems which were compounded by the fact that two of the three ALSEPs were malfunctioning. ALSEP 2 appeared to be blinking off and on and ALSEP 1 was apparently off. The next track was scheduled for 9 March and involved DSS 14, DSS 43 (the DSS 64-m station in Australia), and Guam. Guam tapes for this track were lost before being received at the DSN Network Information Control Center. (During the second week of November the tapes mysteriously turned up in the Network Information Control Center.) Over the course of the next several tracks, tape shipment times were very excessive, and it was decided that for the actual mission day all critical tapes should be handcarried from the four tracking stations. Also, after the first track, the tests switched to using ALSEPs 3 and 5, which were considered less desirable by the experimenter because historically neither ALSEP 3 nor 5 was as stable in frequency as ALSEP 1.

Because of the tape shipment time problems, by the 26 May teleconference MIT had only been able to process the DSS 14 and 43 data from 9 March. With some handwork, MIT was able to compute an interferometric phase but it had a noise level and structure which in no way met the requirements of the experiment. In addition, in processing of a single tone from a single station, there was a great deal of structure, some of it periodic, which should not have been expected if

everything had worked properly. Most of the early tracks had one problem or another generally due to procedural, logistic, or discrete failure. For example, initially the first tapes received from Guam were thought to be degaussed until it was discovered that the Guam tapes merely had not been rewound. Also, there were startup problems in the bandwidth reduction process at JPL where a lot of the initial data was delivered with improperly selected local oscillator functions for doing the bandwidth reduction. In this early phase, very few technical problems with the station equipment were uncovered. There were several errors in the bandwidth reduction software, which were uncovered using the information provided by the experimenter from the March 9 track.

B. 20 July 1978

Between the first and second teleconferences, coordination of problem solving was handled on an individual basis between the supporting agencies. For the 20 July conference, Goddard Space Flight Center was added to aid in coordinating the STDN support activities. At this teleconference, an apparently internal S-band RFI for Santiago track was discussed. MIT also reported further errors apparently made at JPL in selecting the local oscillator function for the bandwidth reduction. In addition, it was reported that the cal tone signal levels from DSS 43 were extremely weak and sometimes not detectable. This problem had been isolated prior to the teleconference to an S-band coupler in the antenna portion of the system, which had been installed backwards.

At this teleconference, the experimenter gave an extensive tutorial on how to use the Fast Fourier Transform output in the bandwidth reduction process to determine if the proper local oscillator function had been chosen. There was considerable discussion as to whether cal tone signal levels had been properly set up at 64-m stations in order to allow for the increases in noise temperature due to the moon. It was determined that mission values for the cal tones should be adequate if the system were operating properly. A new problem realized at this teleconference was that there were also cal tone problems at DSS 14 where the cal tones were significantly weaker than they should be and the upper cal tone was usually missing. By this time, indications were that all systems at the Guam station were fundamentally working properly, although the absolute phase stability of the system was poorer than expected, though tolerable. By now it was recognized that these phone conferences should be scheduled on a routine basis in order to coordinate all activities in the time remaining.

C. 10 August 1978

It was at this phone conference that MIT reported results from some test tracks which indicated for the first time that this experiment might be able to work after all. Dr. Counselman reported the results from two tracks: one at DSS 43 and Guam and the other at DSSs 14 and 43, where the single difference was on the order of 1 to 4 parts in 10^{12} over 15 minutes (probably all attributable to differences in station frequency standards) and a double difference on the order of 0.03 degree (at S-band) per second over a 15-minute interval. Counselman felt at that time that a fair amount of the differential drift may have been attributable to an approximation used in the MIT processing improperly handling lunar librations.

The logistic problems of tape shipments were fairly well resolved by this time, although tape shipment times were still longer than desired. By now it was clear that JPL had learned how to properly handle the local oscillator function in the bandwidth reduction process. Cal tone problems were still evident for DSS 14. The basic signal level problem in the cal tones at DSS 14 had been solved by the discovery that the same coupler was installed backwards at DSS 14 as previously discovered at DSS 43. However, there were still new occurrences of the absence of the upper cal tone.

At about this time, the predict interfaces between the DSN and the STDN seemed to be fairly well worked out; however, a concern had been raised by the STDN about whether they could properly peak their antenna pointing during the actual mission event. Also, subsequent to the last telecon, ALSEP 5 apparently died and the test activity had to switch back to using ALSEPs 1 and 4. This introduced a new constraint that all test tracks be scheduled while the sun was shining on ALSEP 1 because this ALSEP package could not be revived in the dark.

At this teleconference a new problem was identified in that apparently the 12-megabit/second recordings occasionally suffered drop-outs in the servo reference track which caused observed time glitches in the MIT processing. An adjustment of the servo gain settings on all recorders decreased the problem significantly; however, time glitches still existed. It was expected that the time glitches would be minimized on 9 December by the use of more expensive certified tape for the actual mission. Some of the test tracks were now being processed using a linear "ramp" instead of a fixed frequency for the local oscillator function in the bandwidth reduction in order to reduce the bandwidth further and in order to start testing the proper operation and recovery of the data for a dynamic local oscillator function in both the JPL and MIT software.

D. 24 August 1978

One topic for this conference was whether the system noise increase due to the Planet Venus would be detectable at the STDN stations in order to determine that they were on point. It had been determined that the increase was not significant enough to be used for this purpose. The thought developing at that time was that the Orbiter spacecraft might be usable with the STDN spectrum analyzers to determine that the antennas were, indeed, on point. A major topic in this teleconference was the continued cal tone problems at DSS 14.

Also reported by Counselman was a track on 22 June involving all four stations where one of the two ALSEPs was undetectable in the DSS 14 data while that same ALSEP was a good strong signal from the other stations. This single occurrence of an apparent shrinkage in the bandwidth of the MMR (Multi-Mission Receiver, a DSN misnomer for the special 2-MHz bandwidth receiver built to support the experiment). This problem was never observed to recur and was never satisfactorily explained except possibly for the discovery some time after that track of a loose connection in a cable in the MMR.

An extensive test activity to isolate the cal tone problems at DSS 14 as of this teleconference had not been successful. The RFI at Santiago had been isolated to some work which had been taking place on the ranging system at the station. Also, high error rate problems were starting to show up on the DSS 43 12-megabit/second recordings.

At this point, it was decided that the absolute phase drift of 300 and some degrees over 2000 seconds for a single cal tone at the STDN stations observed by MIT was characteristic of the station equipment and not indicative of any problem, particularly since the more critical differential specification of 1 degree over 100 to 1000 seconds was, in general, being met. It was decided to schedule Pioneer 11 tracks for the STDN stations and the DSN stations since Pioneer 11 was currently at a signal level which approximated the expected signal levels during Multiprobe entry. In addition, the STDN had executed special tracks of the Pioneer Venus Orbiter in order to check out the antenna pointing, and this activity was to proceed for several months, resulting in the solving of all remaining antenna-pointing problems.

It was also decided at this teleconference to start sending the tapes from Santiago and Guam directly to JPL to save some of the shipping time. It was at this point in time when JPL was able to find the resources to develop a means of processing special 50-kHz space calibration tone data referred to as rail data. All stations were then requested in the future to take periodic 50-kHz rail data. Problems with the predict interface to the bandwidth reduction were continuing to be pursued. It was decided that a backup form of manual predicts must be available in case the predicts interface problems could not be solved. Although in the months that followed the hardware predict interfaces were demonstrated to be working properly between the predict program and the bandwidth reduction process, the navigation to DSN predict interface in the last two weeks before entry failed to produce any usable post-entry predicts for the small Probes. This problem was never solved, and manually generated predicts were used both for station operations the day of entry and for the bandwidth reduction process that followed.

It was becoming clear that the ALSEP packages were no longer useful since ALSEP 1 had gone completely unstable. It was then discovered that the Voyager spacecraft was able to transmit 320-kHz subcarriers without data modulation and that, therefore, it represented a 3-signal source which might be usable for additional calibration of the experiment. At this teleconference, the experimenter reported that although the results to date were close to meeting the requirement (they missed by about a factor of 5), he still felt that much of the problem might be in the approximate handling of the lunar librations and also in oversensitivity to the short-term instability of the ALSEP signals in the MIT processing. It was anticipated that the switch from ALSEPs 3 and 5 to ALSEPs 1 and 4 should cause a factor of 10 degrees in the lunar libration problem which might confirm that MIT modeling was the major source of the drift in the differential phase. This is because of the shorter distance between ALSEPs 1 and 4 (see table).

E. 13 September 1978

The most recent test tracks were discussed. The first track of six was lost due to ALSEP 1 being off. In the second track, no signals were present in the DSS 14 data, apparently due to a loose cable in the MMR. In the third track, Station 14 suffered a maser failure and could not take any data, and predicts were inadvertently destroyed for DSS 43 prior to the track so that only Guam data could be taken. The Guam data looked good as far as could be told from a single station's data. The next track was the first Pioneer 11 track between DSS 43 and Guam in order to take data at realistic signal levels and a similar track for DSS 14 and Santiago took place. The first attempt at a Voyager track was made; however, data modulation was present on the subcarriers making the data unusable. The problem with DSS 14 cal tones had finally been solved by the discovery of a cracked hardline in an antenna portion of the calibration tone generation equipment.

A major activity underway at MIT in this time period was the debugging of the algorithm for processing the reduced

bandwidth data from JPL. This was a non-trivial debugging process which involved a significant amount of direct engineering interface between MIT and JPL. In order to preserve the phase information, a great deal of attention had to be paid to all buffer structures and update procedures within the bandwidth reduction software. The experimenter reported that the ALSEP 1 and 4 data did verify that lunar libration had been responsible for the majority of the remaining drift in the double difference. The result now was an average slope in the double difference for 1000 seconds of 0.01 degree per second, which corresponds to a velocity measurement error of about 4 centimeters per second. A 4-hour ALSEP track had been desired by MIT in order to get at the lunar libration problem. Due to a variety of problems, a 4-hour track was never successfully achieved, but because of the above results, MIT relaxed the requirement for such a track. It was decided that the remaining tracks should concentrate on realistic mission signal levels and Voyager due to the dying ALSEP packages.

F. 4 October 1978

Santiago and Guam could not detect the Pioneer 11 signal, which was at realistic Probe mission signal level. However, the Bus signal should still be detectable and make possible the use of the spectrum analyzers for end-to-end signal path continuity checking during the actual mission event. A second Voyager track with the spacecraft in the proper mode was successfully executed. Such a tremendous volume of data had been collected that an agreement was reached with MIT as to what data it would be useful to bandwidth-reduce and send on to MIT. Data analysis since the last teleconference confirmed that the cracked hardline was, indeed, the source of the cal tone problems at DSS 14. MIT also reported considerable progress in solving all of the interface problems with the bandwidth-reduced data and in particular the proper handling of dynamic LO functions. Some special test tapes were requested by the experimenter to further check the MIT processing.

A discrepancy in the observed signal level during the Voyager track was observed between Guam and Santiago.

Subsequent to this teleconference, a paramp problem was discovered and isolated at Santiago. Worsening quality of the 12-megabit/second recordings from DSS 43 was reported at this teleconference. At the last teleconference, MIT had reported the development of a software fix to step over the sync track timing glitch problems. It was now reported that this algorithm apparently did not handle all cases and that special processing techniques were requested in the bandwidth reduction in order to enable the software fix at MIT to function. With the limited time remaining, it was agreed by all parties that all future tracks should concentrate on tracking the Bus spacecraft (although this is known to not be a usable source for the double difference interferometry) in order to get data at realistic mission signal levels and to continue to practice operating the equipment.

G. 18 October 1978

By the time of this conference, renewed tape shipment problems had delayed the arrival of the successful Voyager data at JPL. An extensive test activity was still continuing at DSS 14 at this time in order to verify the proper operation of the receiver and the cal tone generation system. It was reported that the DSS 43 noisy recording problems were most likely due to alignment and gain setting problems. A special calibration tape was sent to the station in order to execute a major realignment. It had also been observed that a general slight increase in "noise" level from all stations was occurring and a new head-cleaning procedure was being investigated involving chromium dioxide tapes. MIT reported further refinements in their data processing which had reduced the reported residual drift of the double differenced data from the best ALSEP 1 and 4 tracks from a 0.01 degree per second to 0.003 degree per second for 1000 seconds.

H. 8 November 1978

The strategy was now shaping up for the STDN stations to use the stronger Orbiter spacecraft signal (for peaking antenna pointing) and the Bus signal for validating signal path integrity through the receiver and recorder. The STDN also made known plans to have Goddard engineering personnel on site starting about one week before the Probe entry. The DSS 43 recorders were now believed to be operating satisfactorily except for one minor discrepancy which was not mission critical: DSS 43 could record on Recorder A and play back on A or B, and record on Recorder B and play back on B, but they could not record on Recorder B and play back on A.

A growing concern was raised over phase jumps which had been experienced, particularly in some of the DSS 14 data. These phase jumps seemed to have a characteristic of being a multiple of 120 degrees. DSN engineering personnel spent many test hours at Station 14 but were unable to detect any such phase jumps. However, processing of 50-kHz rail data at JPL did uncover the existence of phase jumps. After this teleconference, it was discovered that the divider in the calibration tone generator (which was selectable from a divide by one to a divide by 99) was marginal and could under certain conditions occasionally divide by n plus one instead of n. This device is used in a divide by three mode in the actual mission and a divide by 99 to generate the 50-kHz rail data. All testing done at Station 14 to try to isolate the phase jumps was executed assuming the problem was in the receiver and calibration signals were generated outside of the calibrator. In addition, rail data from Santiago could only be processed by

assuming divide by 100. This seemed to explain the problem and indicated that it was a potential problem at all four stations.

MIT reported that they had all bugs out of their processing with respect to interfacing with the Bandwidth Reduction Assembly and properly handling dynamic local oscillator functions. In processing the same data with a fixed LO and with ramping, MIT was able to achieve agreement to within 0.01 degree for a thousand seconds. The bad news was that MIT was unable to detect the Pioneer 11 data taken by Santiago, which was supposed to be realistic Probe mission signal level. MIT was able to detect the Voyager data from Santiago. At an STDN station the Pioneer 11 data was approximately −176.5 dBm while the Voyager data was −164 dBm.

I. 22 November 1978

The STDN was having difficulty tracking the Bus because of inaccurate trajectory data. A decision was made to provide daily state vectors from JPL to Goddard so that the long-term integration of the trajectory would be done by the JPL program and concern over compatibility in trajectory modeling between Goddard and JPL could be eliminated. It was also reported at this time that apparently the Goddard predicts did not take account of one-way light time (which, of course, is not necessary for satellite tracking), which accounted for some of the previous biases experienced in antenna pointing. During one test track, Pioneer Project was requested in real-time to change from high to low mod index for the Bus spacecraft telemetry, which gave a 6-dB gain in signal-to-noise ratio for detection of the carrier at STDN stations. It had been the mission plan for some time to use the low mod index on the Bus until the Probe entries were complete so that the STDN stations would have a stronger signal for system validation. From the recent test data, it was now felt that the Bus would be a usable signal instead of the Orbiter for antenna peaking as well as verifying signal path integrity.

An additional concern was brought up when Dr. Counselman reported that from the four-station Voyager track he was able to detect the Voyager signal on every station's data except Santiago. MIT was also having difficulty with the Voyager data due to inaccuracies in handling the Voyager trajectory. A fix had been found for the divide by n plus one problem in adjusting a pot built into the system at all four stations. In the process of adjusting this pot at Santiago, a wiring error was discovered which caused the divider to divide by 100 specifically when the switch was in the 99 position. This explained the previous problems observed in the 50-kHz rail data from Santiago. No further n-plus one problems were seen from Station 14 subsequent to the adjustments made for the mixer. Unfortunately, the independent cause of the divide by 100 at AGO gave less confidence that the n plus one problem was really solved so continued taking of the rail data at DSS 14 would take place until entry to gain confidence that the problem had been solved.

Counselman reported that data from all four stations in recent tracks had many more time glitches than in previous data. From the discussion during the teleconference, it was realized that the DSN in troubleshooting the noise problems with the DSS 43 tapes had changed the settings in the CTA-21 recorder. The CTA-21 recorders were adjusted back to spec subsequent to the teleconference and all future recordings had a more acceptable number of time glitches.

J. 30 November 1978

MIT reported that all was well with Santiago because on re-examining the Voyager data they could now detect the signal and, indeed, detect the even weaker Pioneer 11 signal. MIT had also uncovered some errors in their handling of the Voyager trajectory data, and work was continuing to get the useful content out of the Voyager track. The most urgent problem revealed in this teleconference was that more recent Santiago data had showed a very high noise level with significant phase jumps and an excessively high absolute rate of drift. After an extensive discussion on this issue, several people seemed to focus on the problem probably being in the synthesizer used in the rail generation. Part of the symptoms of the Santiago problem was the presence of 60-Hz spikes on either side of the cal tones. It was also decided that one last teleconference on 6 December would be prudent.

K. 6 December 1978

Once the problem from the last teleconference was identified to Santiago, the station was able to see the 60-Hz noise using their own spectrum analyzer and was quickly able to isolate the problem to a change from a 5-MHz reference to a 1-MHz with a multiple by 5 that somehow slipped by during a major reconfiguration that took place at the station independent of the DLBI support.

The general consensus was that the experiment was as ready as it could be, that readiness had plateaued, and that most recent problems were random equipment failures.

L. The Final Week

In the final week and one-half before the Probe entry, the following discrete failures occurred: DSS 43, coincident with making adjustments to get at the divide by n plus one problem, lost approximately 8-dB gain in the receiver. This problem was traced to a failed mixer for which there was a spare on site. Since it was undesirable to go into the short hours of

9 December without a spare, the failed mixer from DSS 43 was shipped to JPL for repair and the spare mixer from DSS 14 shipped to DSS 43. The spare mixer was repaired at JPL and sent out to DSS 14 before 9 December. Guam experienced a cesium failure, apparently just due to the age of the particular cesium tube, but was able to switch the backup cesium on-line and maintain time due to the availability of a good quality LORAN-C source. Station 14 experienced a complete failure in a commercial part of one of the Spectral Signal Indicators just four days before entry. A JPL engineer removed the device from DSS 14 and flew it to the vendor in San Diego and had a repaired one back, installed and operating at the station two days later.

IV. Summary

At the time of writing, all indications in the post-entry processing to date are that the DLBI Experiment equipment operated near perfectly on 9 December. First results from processing just the calibration signal for the 64-meter stations are a differential phase difference of less than one degree at S-band for 10,000 seconds with the absolute phase of a single cal tone having a variation of less than 20 degrees over 5000 seconds. For the STDN stations, at the time of writing, the preliminary results are less than one degree of differential phase error in 2000 seconds with an absolute phase of a single cal tone variation of about 300 degrees. The latter appears to consist mostly of a linear drift with only about 10 degrees deviation from linear for the 2000 seconds.

The above, of course, does not yet verify that the experiment worked and met the accuracy objectives; however, it is a preliminary indication that the receiving and recording equipment at the stations were operating as well as or better than they operated in any of the ten months of end-to-end system checkout. By the time of the next issue of the DSN Progress Report, more conclusive indications of performance should be available.

References

1. Miller, R. B., "Pioneer Mission Support," in *The Deep Space Network Progress Report 42-30*, pp. 61-64, Jet Propulsion Laboratory, Pasadena, Calif., Dec. 15, 1975.
2. Miller, R. B., "Pioneer Venus 1978 Mission Support," in *The Deep Space Network Progress Report 42-31*, pp. 11-14, Jet Propulsion Laboratory, Pasadena, Calif., Feb. 15, 1976.
3. Miller, R. B., "Pioneer Venus 1978 Mission Support," in *The Deep Space Network Progress Report 42-36*, pp. 22-27, Jet Propulsion Laboratory, Pasadena, Calif., Dec. 15, 1976.
4. Kimball, K. R., "Implementation of Wideband Digital Recording Equipment in the DSN," in *The Deep Space Network Progress Report 42-31*, pp. 96-104, Jet Propulsion Laboratory, Pasadena, Calif., Feb. 15, 1976.
5. Nishimura, H., "Pioneer Venus Wind Experiment Receiver," in *The Deep Space Network Progress Report 42-38*, pp. 141-147, Jet Propulsion Laboratory, Pasadena, Calif., Apr. 15, 1977.
6. Miller, R. B., "Pioneer Venus 1978 Mission Support," in *The Deep Space Network Progress Report 42-45*, pp. 35-38, Jet Propulsion Laboratory, Pasadena, Calif., June 15, 1978.

Table 1. ALSEP characteristics

Frequency (MHz)	2275.5	2276.0	2278.0	2278.5	2279.5
ALSEP number	5	3	2	1	4
Apollo Mission	17	16	15	12	14
ALSEP location	30.8E	15.5E	3.6E	23.4W	17.5W
	20.8N	8.9S	21.1N	3.5S	3.6S

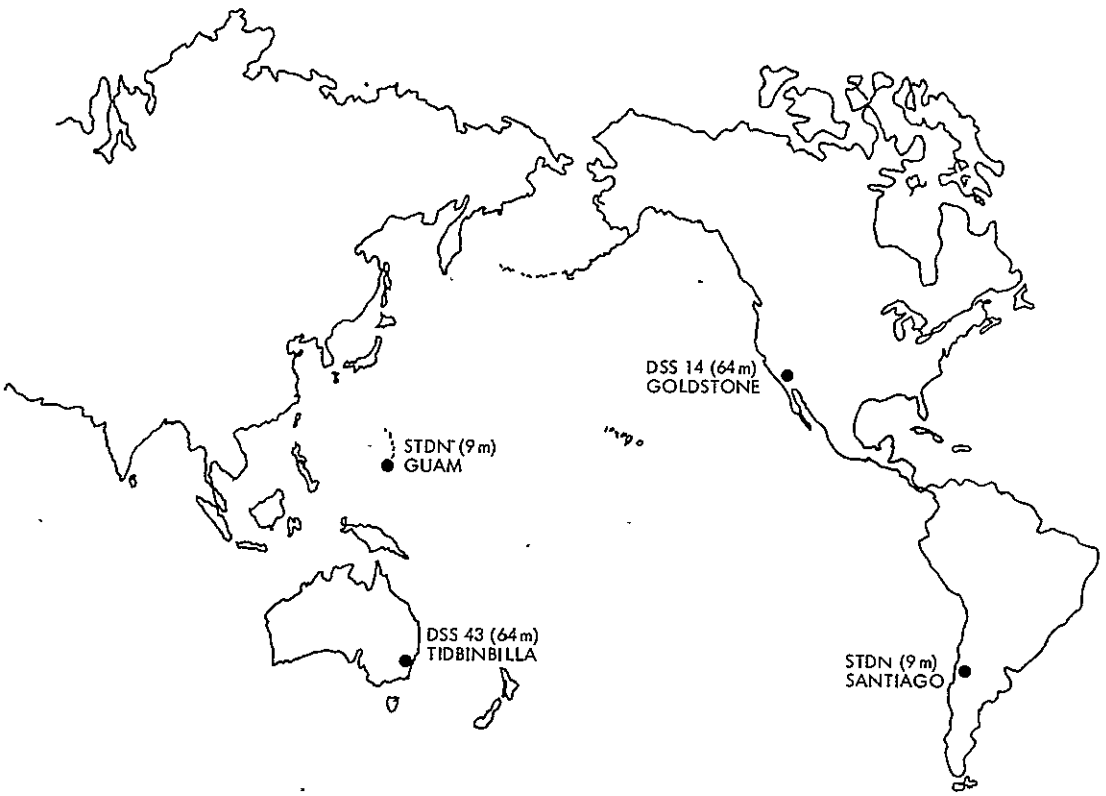

Fig. 1. DSN and STDN station locations, DLBI Wind Measurement Experiment

Helios Mission Support

W. N. Jensen and J. C. Nash
Deep Space Network Operations Section

This article reports on activities of the DSN Network Operations Organization in support of the Helios Project from 15 October through 15 December 1978.

I. Introduction

This article is the twenty-fifth in a continuing series of reports that discuss Deep Space Network support of Helios Mission Operations. Included in this article is information on the 8th perihelion of Helios 1 and the 6th perihelion of Helios 2, science experiments, 22-bit error polynomial code (EPC) testing and other mission-related activities.

II. Mission Operations and Status

The 8th perihelion of Helios 1 occurred on November 5 at 10:11 Universal Time (UTC). The perihelion phase was covered by DSS 68 in Weilheim, West Germany. The data was obtained at a bit rate of 64 bits per second (bps). All spacecraft subsystems and experiments worked excellently, although several temperature hard limit exceedings were encountered, none of which were considered to be critical. A spacecraft emergency was declared on November 11 at 22:40 UTC, when Station 43 in Australia was unable to acquire the downlink at the scheduled 20:30 UTC. Station 44 (Honeysuckle Creek, Australia) was also unsuccessful in attempting to acquire the downlink. After transmission of the appropriate traveling wave tube (TWT) turnon command, DSS 43 acquired the downlink at 23:27.53 UTC. The subsequent data evaluation showed that a regulator switch had occurred (the eleventh). The memory data showed that the switch occurred at 16:48:25 UTC during a noncoverage period. The spacecraft emergency was lifted on November 12 at 09:30 UTC. There still remains a power fluctuation of approximately 21 watts. The experimenters are evaluating their data for any unusual signs.

The Helios 2 spacecraft remains in good condition. All subsystems and experiments worked well during the 6th perihelion on November 2 at 02:00 UTC. Helios 2 also experienced hard limit temperature exceedings, none of which were considered to be critical.

III. Special Activities

A. Support of Onboard and Ground Experiments

During the perihelion and superior conjunction periods, of both Helios 1 and 2, prime data types collected were Faraday rotation, ellipticity (Experiment 12) and solar wind.

B. German Space Operations Center (GSOC) Conversion to the 22-Bit Error Polynominal Code (EPC) and Mark III Data Command System

As reported in the last article (Ref. 1), testing continued until November 3 at 16:00 UTC, at which time the 22-bit EPC system was accepted for operational use.

C. Station 12 34-Meter Conversion

DSS 12 successfully completed its first (post 34-meter conversion) Helios demonstration pass on November 11 and was placed under configuration control for operational support on December 2 00:00 UTC.

Reference

1. Goodwin, P. S., Jensen, W. N., and Rockwell, G. M., "Helios Mission Support," in *The Deep Space Network Progress Report 42-47,* pp. 26-28, Jet Propulsion Laboratory, Pasadena, Calif., Dec. 1978.

Definition of Antenna Microwave Time Delay for VLBI Clock Synchronization

T. Y. Otoshi
Radio Frequency and Microwave Subsystems Section

This article presents derivations and definitions of antenna time delays above the phase calibrator injection points for VLBI time synchronization work. As nearly as possible, the symbols and nomenclature are made to be identical or similar to those used in ranging work. These definitions will be helpful in assessing the accuracy requirements of antenna time delay values to be provided to the VLBI clock sync project by the Microwave Phase Center Calibration work unit.

I. Introduction

Very Long Baseline Interferometry (VLBI) methods are used primarily in the DSN for improving knowledge of station locations, but have other applications as well. A recent publication that gives an overview of the VLBI activity for the DSN is *DSN Progress Report 42-46*, published August 1978. This issue contains tutorial VLBI papers and an extensive VLBI bibliography.

One of the VLBI activities at JPL and an important VLBI application is the clock sync project. This project involves determining how much the master frequency clock at one station is offset from the master clock at another station in the DSN. In order to verify that the VLBI method can be used for clock sync, it is necessary to know the time delays of the antenna feed (and transmission media) above the phase calibrator injection point at each of the two stations involved in the baseline measurement.

The VLBI processing, which includes modeling and a fringe phase stop method (Ref. 1), results in a term that has a time varying component (geometric delay) and a time invariant or constant term. The time varying delay is normally attributed entirely to phase delay changes produced by geometric baseline separation of the two antennas tracking the VLBI source and the changes in antenna pointing angle with time. The constant term is usually attributed to unknown clock errors and unknown delays of the transmission media, antenna, and the microwave subsystem above the phase calibrator injection points. The basic assumption is made that these latter delays are constant with time and antenna pointing angles. The constant term is ignored in VLBI baseline solutions for station location work, but the delays of the individual terms comprising the constant term need to be known for VLBI clock sync work.

The analysis of VLBI clock sync is probably well understood by those involved in this work, but other than an excellent article by Thomas (Ref. 2), these analyses are generally available only in internal JPL documents or unpublished notes.

It is the purpose of this article to present a fundamental VLBI time delay analysis from a microwave engineer's

viewpoint and show the similarity to ranging system analysis. It is also the purpose of this article to present definitions of antenna time delay above the phase calibrator injection point so that responsibilities of the Microwave Phase Center Calibration work unit can be clarified and assessed.

II. Definitions of Symbols

The following is a list of symbols used in this article. As much as possible, the symbols and terminology are like those of ranging (Ref. 3) and those used by Fanselow (Ref. 4). Most of the symbols are indicated on Fig. 1. The i subscript refers to any station (e.g., i = 1, 2). Figure 1 should be regarded primarily as a time delay diagram. An attempt is made to depict both time and space points on the same diagram. It is assumed that both antennas track the VLBI radio source so that the direction of propagation of the plane wave is along a line that is parallel to the antenna axis of dish symmetry at each station.

τ_{Si} = time delay of the VLBI signal measured from the reference plane wave to the phase calibrator injection point via the transmission media, the Cassegrainian antenna path, and the microwave subsystem path at station i.

τ_{FSi} = optical path length delay from the reference plane wave to the station i location. It is assumed here that the antenna is transparent and the plane wave signal propagates at free space velocity to the station location.

$\Delta\tau_{FSi}$ = additional time delay (in excess of free space) due to the effects of solar plasma, ionosphere, and the troposphere.

τ_{Di} = time delay of the plane wave in free space to travel from the aperture of the antenna (edge of dish) to the plane containing the second (moving) axis of antenna rotation. It is assumed here that the antenna is transparent. The same definition is used in ranging work.

τ_{Ci} = time delay from the aperture of the antenna to the receive horn phase center as measured along the convoluted antenna optics path of the Cassegrainian antenna. The same definition is used in ranging work.

$\tau_{4,i}$ = time delay from the receive horn phase center through the horn assembly to the phase calibrator injection point located somewhere in the microwave subsystem. This same definition holds for ranging work if "phase calibrator" in the above is replaced by "translator."

A_i = point defined by the intersection of the axis of dish symmetry with the plane wave front that arrives at the second (moving) axis of rotation.

B_i = point defined by the intersection of the axis of dish symmetry with the plane wave front that arrives at the station i location. This point is shown in Fig. 2 for various types of antennas in the DSN.

R_i = equivalent point or location of the phase calibrator injection point on the antenna axis of symmetry using the *free space propagation distances* to locate this point (see Fig. 1). Point R_i is not the actual physical location of the phase calibrator on the antenna but is a convenient equivalent point useful in a time delay diagram analysis.

b_i = nominal antenna axis offset. It is the perpendicular distance between the primary and secondary antenna axes (see Fig. 2). This is equivalent to the term b used by Moyer (Ref. 5) and h by Fanselow (Ref. 4). The term h is not used here because it is used to denote zero delay device height in ranging work (Ref. 3).

ν_c = speed of light in consistent length and time units.

τ_{Li} = time delay from point A_i to point R_i as measured in free space along the antenna axis of symmetry. This time delay, expressed mathematically in Eq. (17) of this article, shows that if

$$\tau_{Ci} + \tau_{4,i} < \tau_{Di}$$

then τ_{Li} will be a negative number and point R_i would actually be located above point A_i in Fig. 1. This fact will not alter the general case analysis presented in this article.

τ_{Vi} = antenna pointing angle dependent time delay from point A_i to point B_i as measured in free space along the antenna axis of symmetry.

τ_{Ai} = effective antenna-microwave time delay above the phase calibrator injection point.

$\Delta\tau_{CLK}$ = clock sync offset; it is the master clock time at station 2 minus the master clock time at station 1.

τ'_{BWS} = time delay resulting from bandwidth synthesis processing (see Ref. 2) of the data for two stations and two microwave frequencies that

are separated by a frequency interval referred to as the "spanned bandwidth."

τ_{Ui} = cable delay between the actual phase calibrator output and the injection point in the microwave subsystem.

τ_m = modeled geometric delay

III. Derivation of Time Delay Relationships

A. Station Time Delays

From the Fig. 1 time delay diagram, it can be seen that the following absolute time delay relationships hold. All symbols are defined in the previous list of definitions.

$$\tau_{S1} = \tau_{FS1} + \Delta\tau_{FS1} - (\tau_{V1} + \tau_{D1}) + \tau_{C1} + \tau_{4,1} \quad (1)$$

$$\tau_{D1} + \tau_{L1} = \tau_{C1} + \tau_{4,1} \quad (2)$$

so from manipulation of Eq. (2)

$$\tau_{L1} = (\tau_{C1} + \tau_{4,1}) - \tau_{D1} \quad (3)$$

and it should be pointed out that τ_{L1} is the negative of $\tau_{\ell 1}$, which is a similar term used by Fanselow (Ref. 4). Defining the effective antenna-microwave delay as

$$\tau_{A1} = \tau_{L1} - \tau_{V1} \quad (4)$$

then substitution of Eqs. (3) and (4) into Eq. (1) gives

$$\tau_{S1} = \tau_{FS1} + \Delta\tau_{FS1} + \tau_{A1} \quad (5)$$

In a similar manner, it can be seen from Fig. 1 that the following relationship holds for Station 2:

$$\tau_{S2} = \tau_{FS2} + \Delta\tau_{FS2} - (\tau_{V2} + \tau_{D2}) + \tau_{C2} + \tau_{4,2} \quad (6)$$

$$\tau_{D2} + \tau_{L2} = \tau_{C2} + \tau_{4,2} \quad (7)$$

Manipulation of Eq. (7) gives

$$\tau_{L2} = (\tau_{C2} + \tau_{4,2}) - \tau_{D2} \quad (8)$$

Substitution of

$$\tau_{A2} = \tau_{L2} - \tau_{V2} \quad (9)$$

into Eq. (6) gives

$$\tau_{S2} = \tau_{FS2} + \Delta\tau_{FS2} + \tau_{A2} \quad (10)$$

Also, from Fig. 1, it can be seen that the following time delay relationship holds:

$$\tau_{FS2} = \tau_{FS1} + \tau_g \quad (11)$$

It is important to point out that all terms in Eq. (11) are free space or optical path delays and do not require corrections for additional delays occurring in the plasma, ionospheric or tropospheric media. Substitution of Eq. (11) into (10) gives

$$\tau_{S2} = \tau_{FS1} + \tau_g + \Delta\tau_{FS2} + \tau_{A2} \quad (12)$$

B. VLBI Observed Delay

Following the derivation and analysis of Thomas (see Ref. 2, Eq. 65), once the interferometer phase has been corrected with the phase calibrator tone phase, the bandwidth synthesis method will give the result:

$$\tau'_{BWS} = (\tau_{S2} - \tau_{S1}) + \Delta\tau_{CLK} - (\tau_{U2} - \tau_{U1}) - \tau_m \quad (13)$$

where $\Delta\tau_{CLK}$ is the synchronization clock offset of interest in this article and τ_{U1}, τ_{U2} are cable delays from the phase calibrator output to the injection point for Stations 1 and 2, respectively, and τ_m is the modeled geometric delay. Substitution of Eq. (5) and (12) into Eq. (13) gives the desired observed VLBI relationship of

$$\tau'_{BWS} = (\tau_g - \tau_m) + (\Delta\tau_{FS2} - \Delta\tau_{FS1}) + (\tau_{A2} - \tau_{A1}) - (\tau_{U2} - \tau_{U1}) + \Delta\tau_{CLK} \quad (14)$$

In the above equation, τ_m is a quantity that is known exactly. It is the modeled or predicted time varying delay based on assumed station locations. If the modeling is exact and all other terms in Eq. (14) are time invariant, then $\tau_g = \tau_m$ and τ'_{BWS} is also time invariant and one can assume that the modeling is correct as far as station location (geodetic) solutions are concerned. Clock sync-work involves the determination of the term $\Delta\tau_{CLK}$. As can be seen from Eq. (14) for the special case of $\tau_g \simeq \tau_m$ then manipulation of (14) gives

$$\Delta\tau_{CLK} \approx \tau'_{BWS} - (\Delta\tau_{FS2} - \Delta\tau_{FS1}) - (\tau_{A2} - \tau_{A1}) + (\tau_{U2} - \tau_{U1}) \quad (15)$$

The parameters needed for clock sync work then are $\Delta\tau_{FS2}$, $\Delta\tau_{FS1}$, of which major portions will be calibrated by techniques developed by the Water Vapor Radiometer work unit; τ_{A2}, τ_{A1}, whose techniques for measurement are to be furnished jointly by the Antenna Mechanical work unit and the Microwave Phase Center Calibration work unit and finally τ_{U2}, τ_{U1}, whose technique for measurement is the responsibility of the Phase Calibrator work unit. These are divisions of responsibilities that were unofficially agreed upon in Ref. 6. Since there is no obvious way to make direct differential measurements of the above required quantities, it is necessary to make absolute measurements of the individual delays and then difference them.

IV. Discussion of Antenna and Microwave Delays

In the preceding section, the terms required for VLBI clock sync project have been defined. In summary, the portion of time delays concerned with the antenna structure and microwave subsystem for any station i is the delay τ_{Ai}, which has been expressed mathematically in the preceding section as:

$$\tau_{Ai} = \tau_{Li} - \tau_{Vi} \tag{16}$$

where in more familiar ranging system terminology (Ref. 3)

$$\tau_{Li} = (\tau_{Ci} + \tau_{4,i}) - \tau_{Di} \tag{17}$$

and from Fanselow (Ref. 4)

$$\tau_{Vi} = \frac{b_i}{v_c}\left[f_{1i} \times (\text{geodetic elevation}) + f_{2i} \times (\text{declination}) + f_{3i} \times (\text{geodetic latitude})\right] \tag{18}$$

and values of b_i, f_{1i}, f_{2i}, and f_{3i} are given in Table 1 for various stations in the DSN. The parameter v_c is the speed of light in consistent time and length units. It should be remembered that even though the symbols of τ are similar for ranging, they are not exactly the same because τ in VLBI is defined for a measurement using a spanned bandwidth of about 40 MHz, while for ranging the equivalent spanned bandwidth is about 1 MHz. It should also be pointed out that it has been assumed that the antenna delay terms in Eq. (17) are constants with time during the period of observation of a VLBI radio source. This is an erroneous assumption for DSN antennas because subreflector defocussing and antenna structural deformation due to gravity loading and multipath cause the quantity $(\tau_{Ci} - \tau_{Di})$ to change as a function of elevation angle and therefore also as a function of time. In a recent publication (Ref. 7), it was shown that computer methods can be used to compute the quantity $(\tau_{Ci} - \tau_{Di})$ for defocussed subreflector cases. It is the objective of the Microwave Phase Center Calibration work unit and Antenna Mechanical Calibration work unit to provide some data on the effects of multipath and structural deformations on the variations of $(\tau_{Ci} - \tau_{Di})$ as a function of elevation angle.

The equations presented in this article are applicable for the general case. Some interesting special case derivations, such as for dish-mounted phase calibrators, Z-corrections for VLBI, and changes of reference plane for antenna optic delays, are presented in Appendices A and B.

V. Summary and Conclusion

The time delay terms for microwave subsystem and antenna delays above the phase calibrator injection point have been defined. These definitions are helpful in forming a basis for assessing the quantities and accuracies that can be achieved for VLBI clock sync project.

Nominal time delay values for τ_{Ai} have been obtained for the current S-band configurations for DSS 14 and DSS 13. These quantities and measurement techniques will be reported in a subsequent DSN article.

References

1. Thomas, J. B., "An Analysis of Long Baseline Interferometry, Part III," Technical Report 32-1526, Vol. XVI, pp. 47-64, Jet Propulsion Laboratory, Pasadena, Calif., Aug. 15, 1973.

2. Thomas, J. B., "The Tone Generator and Phase Calibration in VLBI Measurements," in *The DSN Progress Report 42-44*, pp. 63-74, Jet Propulsion Laboratory, Pasadena, Calif., Apr. 15, 1978.

3. Komarek, T., and Otoshi, T., "Terminology of Ranging Measurements and DSS Calibrations," in *The DSN Progress Report 42-36*, pp. 35-40, Jet Propulsion Laboratory, Pasadena, Calif., Dec. 15, 1976.

4. Fanselow, J. L., "The Definition and Measurement of Antenna Location in Very Long Baseline Interferometry," JPL IOM 315.2.014, Oct. 15, 1976 (an internal document).

5. Moyer, T. D., *Mathematical Formulation of the Double-Precision Orbit Determination Program (DPODP)*, Technical Report 32-1527, p. 82, Jet Propulsion Laboratory, Pasadena, Calif., May 15, 1971.

6. Ham, N., and Layland, J. W., "Station Delay Measurement and Calibration for VLBI," JPL IOM 331-76-88, Sept. 27, 1976 (an internal document).

7. Cha, A. G., Rusch, W. V. T., and Otoshi, T. Y., "Microwave Delay Characteristics of Cassegrainian Antennas," *IEEE Trans. on Antennas and Propagation*, Vol. AP-26, No. 6, pp. 860-865, Nov., 1978.

Table 1. Algorithm for computation of τ_{Vi} (from Ref. 4)

$$\tau_{Vi} = \frac{b_i}{v_c} \cos \left[f_{1i} \times (\text{geodetic elevation}) + f_{2i} \times \text{declination} + f_{3i} \times (\text{geodetic latitude}) \right]$$

i	DSS	Nominal b, m	f_1	f_2	f_3
1	11	6.706	0.0	1.0	0.0
2	12	6.706[a]	0.0	1.0	0.0
3	13	0.9144	1.0	0.0	0.0
4	14	0.000	0.0	0.0	0.0
5	41	6.706	0.0	1.0	0.0
6	42	6.706	0.0	1.0	0.0
7	43	0.000	0.0	0.0	0.0
8	44	1.2192	(To be determined)		
9	51	6.706	0.0	1.0	0.0
10	61	6.706	0.0	1.0	0.0
11	62	6.706	0.0	1.0	0.0
12	63	0.000	0.0	0.0	0.0

[a] Still valid after recent 34-m-diameter update.

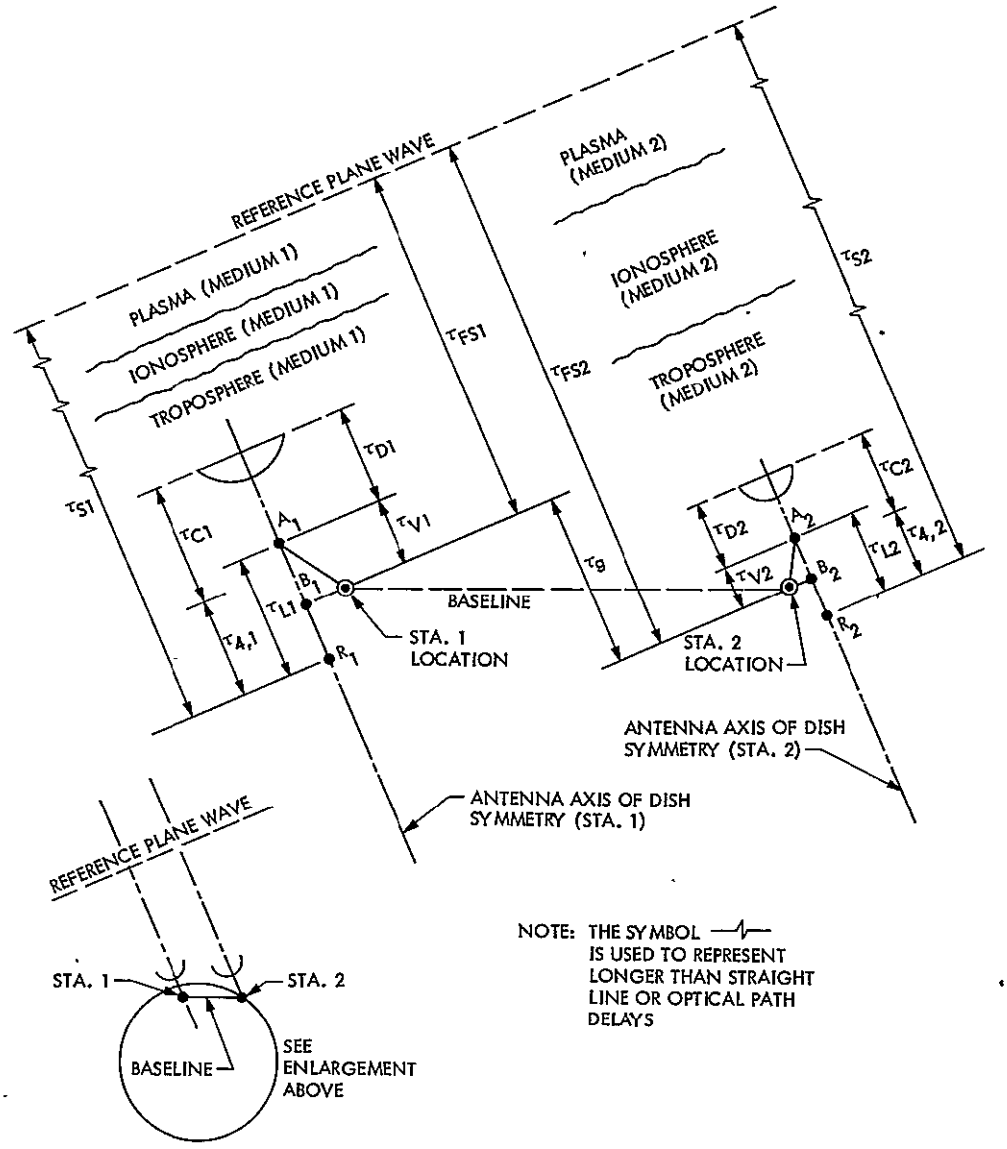

Fig. 1. Time delay diagram for two station VLBI measurement

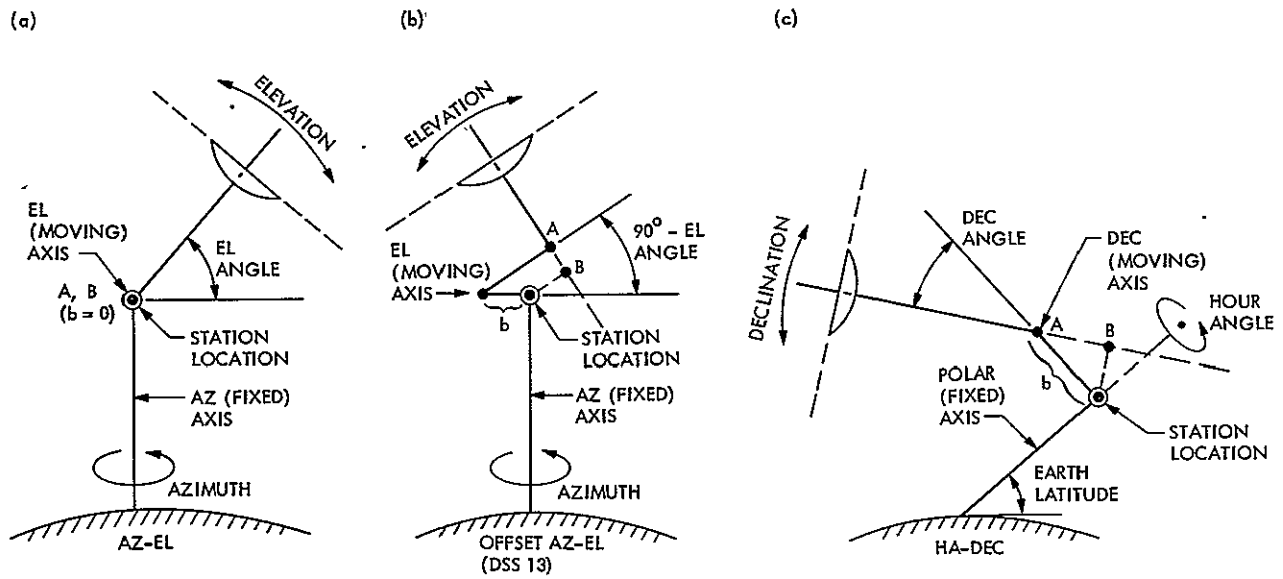

Fig. 2. Station locations and points A and B for various types of DSN antennas (a) AZ-EL, (b) offset AZ-EL, and (c) HA-DEC

Appendix A

Equivalent Z-Correction for VLBI

I. Dish-Mounted Phase Calibrator

Figure A-1 shows a dish-mounted phase calibrator similar to a dish-mounted Zero Delay Device (ZDD) described in Ref. 3. From the time delay diagram in Fig. A-1, it can be seen that

$$\tau_{Si} = \tau_{FSi} + \Delta\tau_{FSi} - (\tau_{Vi} + \tau_{hi}) \qquad \text{(A-1)}$$

and τ_{hi} here is the free space delay from the point R_i (projection of point where the phase calibrator is mounted on the dish surface) to point A_i on the antenna. Manipulation of Eq. (A-1) gives

$$\tau_{FSi} + \Delta\tau_{FSi} = \tau_{Si} + (\tau_{Vi} + \tau_{hi}) \qquad \text{(A-2)}$$

Comparison to the Round Trip Delay Time Equations in Ref. 3 shows that the equivalent Z-correction for VLBI for this dish-mounted case is

$$Z_{VLBI} = \tau_{Vi} + \tau_{hi} \qquad \text{(A-3)}$$

which is very similar to the ranging Z-correction for dish-mounted ZDD except it is only one-half the value. This is because VLBI is a downlink measurement only, while ranging is a round trip time delay measurement.

II. General Case

For the general case configuration shown in Fig. 1, where the phase calibrator is located internal to the antenna system, the time delay from the VLBI source to the phase calibrator injection point was derived as

$$\tau_{Si} = \tau_{FSi} + \Delta\tau_{FSi} + (\tau_{Li} - \tau_{Vi}) \qquad \text{(A-4)}$$

where in this general case

$$\tau_{Li} = (\tau_{Ci} + \tau_{4,i}) - \tau_{Di} \qquad \text{(A-5)}$$

Manipulation of Eq. (A-5) gives

$$\tau_{FSi} + \Delta\tau_{FSi} = \tau_{Si} + Z_{VLBI} \qquad \text{(A-6)}$$

where

$$Z_{VLBI} = \tau_{Vi} - \tau_{Li} = -\tau_{Ai}$$

$$= \tau_{Vi} + \tau_{Di} - (\tau_{Ci} + \tau_{4,i}) \qquad \text{(A-7)}$$

and for 64-m antennas

$$\tau_{Vi} = 0$$

So we have exact agreement with the ranging Z-corrections if all uplink terms in the ranging Z-corrections were eliminated.

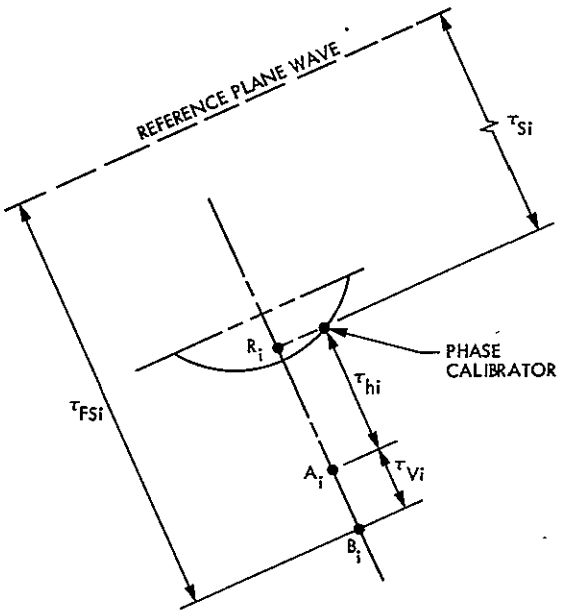

NOTE: POINT R_i IS THE PROJECTION OF THE PHASE CALIBRATOR ONTO THE ANTENNA AXIS OF SYMMETRY

Fig. A-1. Dish-mounted phase calibrator

Appendix B

Change of Reference for Antenna Optics Delay to an Arbitrary Plane in Front of the Dish Aperture Plane

For the derivations presented in the main part of this article, the common reference plane for the definitions of τ_C and τ_D was arbitrarily chosen to be the dish aperture plane (i.e., the plane that touches the edge of the dish). This reference plane could have been defined to be any plane in front of the antenna as shown in Fig. B-1 so that

$$\tau'_{Di} = \tau_{Di} + \tau_{Ki} \tag{B-1}$$

$$\tau'_{Ci} = \tau_{Ci} + \tau_{Ki} \tag{B-2}$$

where τ_{Ki} is the delay from the new reference plane to the dish aperture plane. The value of τ_{Ki} may or may not necessarily be the equivalent free space delay because of the effects of quadripod scattering, subreflector edge diffraction, and multipath effects. This is a problem area that is currently being investigated by this author under the Microwave Phase Center Calibration work unit. The term τ_{Ki} can be made large to correspond to the far field criteria $2D^2/\lambda$ or can be made much smaller to correspond to the distance to the paraboloid focal plane (a plane perpendicular to the antenna axis of symmetry passing through the paraboloid focus). The latter reference plane was used by Cha et al. (Ref. 7) in his definition of antenna delay. To derive the first component of antenna delay for the geometry of Fig. B-1, it is necessary only to use Eq. (B-1) and (B-2) in Eq. (17) to obtain

$$\tau_{Li} = (\tau'_{Ci} + \tau_{4,1}) - \tau'_{Di} \tag{B-3}$$

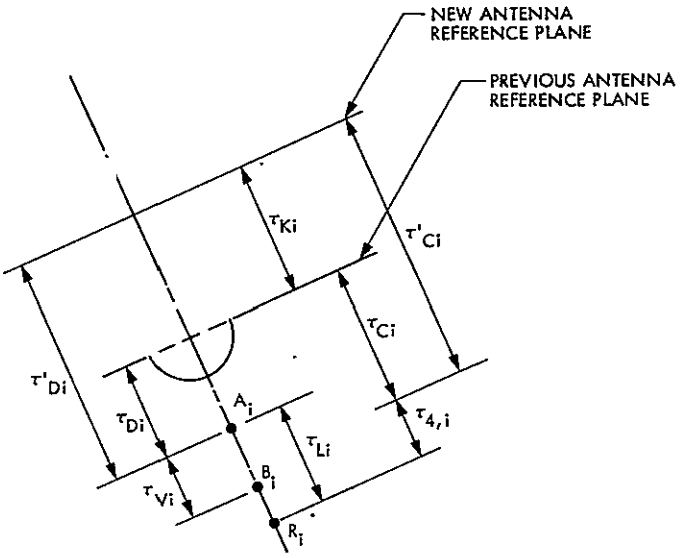

Fig. B-1. Geometry for change of reference plane for τ_{Ci} and τ_{Di}

Comparison of Phase Modulation Systems

J. L. Massey
Consultant to JPL

Comparison of the energy-to-noise ratio necessary to obtain a given modulation bit error probability has indicated that three-phase modulation is about 0.75 dB superior to four-phase. It is shown that this apparent superiority results entirely from the greater bandwidth required by the three-phase system for the same bit transmission rate. Two further comparison criteria are proposed, which are based on the cut-off rate R_0 of the discrete channel created by the modulation system. For the criterion which constrains both the bandwidth and transmitted power, it is shown that four-phase modulation is always superior to three-phase modulation. The conclusion is that three-phase modulation offers no practical advantage over four-phase modulation.

I. Introduction

In a recent memorandum (Ref. 1), Pierce has shown a substantial superiority for three-phase modulation, compared to two-phase and four-phase, for signaling in the presence of additive white Gaussian noise (AWGN). In this memorandum, we will show that Pierce's criterion of goodness is only one among three criteria that can reasonably be chosen, and is in fact the least "fair" of the three in that it both gives a larger bandwidth to three-phase modulation and also presumes that coding will not be used. We will show that if the criterion is changed to permit coding, then the superiority of three-phase modulation is negligible in spite of its requirement for greater bandwidth. We will show further that if coding is permitted and bandwidth is specified, then four-phase modulation is always superior to three-phase.

We shall in fact consider the general case of M-ary phase modulation in AWGN where a sinusoid with phase $2\pi\, m/M$ radians is transmitted in each signaling interval, or *baud*, where $m \in \{0, 1, 2, \ldots, M-1\}$. The following notation will be used:

E = transmitted energy per baud

E_0 = transmitted energy per modulation bit

P_0 = bit error probability at output of a "hard decision" demodulator

P_e = baud error probability for a "hard decision" demodulator

N_0 = one-sided noise power spectral density

R_0 = (also denoted by R_{comp}) cut-off rate per baud of the discrete memoryless channel created by the modulator, waveform channel, and an "infinitely-soft decision" demodulator

S = transmitted power

B = transmitter bandwidth measured in bauds per second

There are three useful relations among the above quantities, namely

$$E_0 = \frac{E}{\log_2 M} \tag{1}$$

$$S = EB \tag{2}$$

which are always true, and

$$P_0 \simeq \frac{P_e}{\log_2 M} \tag{3}$$

which is a good approximation when P_e is small. Equation (3) presumes, when $M = 2^i$, that the i modulation bits in each baud are gray-coded into the M phases so that baud errors by the demodulator, which with high probability are errors between adjacent phases, result in single bit errors with high probability. When $M \neq 2^i$, we presume that the modulation bits are appropriately mapped over several bauds so that Eq. (3) is still approximately valid when P_e is small (or, equivalently, when E_0/N_0 is large).

We shall consider only $M \geqslant 3$ for the following reason. Four-phase modulation can be thought of as two independent two-phase modulations in each baud. Thus, it is superfluous to consider two-phase modulation. Moreover, we thus avoid the question of whether B is the appropriate measure of bandwidth for two-phase modulation. We note, however, that B is certainly the appropriate measure of bandwidth when $M \geqslant 3$, since then both the "sine" and "cosine" quadrature components must be available in each baud.

II. The Comparison Criteria

Criterion 1: Fix P_0, the demodulator bit error probability, at some small value and compare the necessary E_0/N_0, the modulation bit energy-to-noise ratio.

Criterion 1 makes sense only if coding is prohibited so that P_0 is the error probability in the transmitted information bits, which is the only "error probability" of real interest to the user of the communication system. Note, however, that Eqs. (1) and (2) imply

$$B = \frac{S}{E_0 \log_2 M} \tag{4}$$

so that, for a specified S and E_0, the bandwidth decreases as M increases. In particular

$$\frac{(B)_3}{(B)_4} = \frac{\log_2 4}{\log_2 3} = 1.262 \tag{5}$$

(where the subscripts on the parentheses here and hereafter denote the value of M) which shows that three-phase modulation will use 1.01 dB more bandwidth than four-phase modulation when the transmitted power, S, and modulation bit energy, E_0, are fixed. Criterion 1 is indifferent to this increased bandwidth requirement for three-phase modulation, so it is perhaps not surprising that three-phase modulation will emerge as optimum for this criterion.

We remark that Criterion 1 is equivalent to that used by Pierce (Ref. 1), who argued that $P_e/\log_2 M$ should be fixed (at some small value) so that all systems would deliver the same "symbol error probability" for "symbols" consisting of a fixed number of binary digits. The equivalence to our Criterion 1 follows from Eq. (3).

Criterion 2: Fix E_0/N_0, the modulation bit energy-to-noise ratio, and compare the resulting cut-off rate per modulation bit, $R_0/\log_2 M$.

There are strong arguments supporting the claim that R_0 is the best measure of quality for a modulation system that may be used together with coding (Refs. 2, 3). In a very real sense, R_0 is the "practical upper limit" of information bits per baud for reliable transmission, just as channel capacity is the theoretical upper limit. Criterion 2 thus shows how many reliable information bits per modulation bit one is buying per unit of modulation bit energy.

Because the modulation bit energy rather than the baud energy is fixed in Criterion 1, it follows that the bandwidth of the different M-ary phase modulation systems for the same transmitted power will again be inversely proportional to $\log_2 M$. Thus, because the three-phase system is given more bandwidth, it is again not surprising that it appears superior to four-phase modulation under Criterion 2.

Criterion 3: Fix E/N_0, the baud energy-to-noise ratio, and compare the resulting cut-off rate per baud, R_0.

In our opinion, Criterion 3 is the most appropriate one for comparing M-ary phase modulation systems with different values of M. By fixing the energy per baud, one assures that the systems compared will have the same bandwidth when they use the same transmitted power. Moreover, the use of R_0, rather than P_e, in the criterion has the other advantages discussed above under Criterion 2. Criterion 3 thus directly measures the quality of M-ary modulation systems when both the transmitted power and bandwidth are specified – and this seems to be the fairest comparison possible.

The fact that three-phase modulation is always inferior to four-phase modulation under Criterion 4 strongly suggests that three-phase modulation is devoid of practical interest.

III. Analysis

A. Criterion 1

We use the signal space approach given in Ref. 4. The error probability p for the maximum-likelihood decision between two signal vectors at euclidean distance d from one another in the presence of AWGN with variance $N_0/2$ in each dimension is very closely approximated (and always over-bounded) by

$$P \approx \frac{1}{\sqrt{\frac{\pi d^2}{N_0}}} e^{-d^2/(4N_0)} \tag{6}$$

when $p \ll 1$ (Ref. 4). In M-ary phase modulation, the distance between signal vectors for adjacent phases is just

$$d = 2\sqrt{E}\sin\left(\frac{\pi}{M}\right) \tag{7}$$

Moreover, when p is small, almost all errors occur between the transmitted phase and its two adjacent phases so that $2p$ is a very close approximation to the baud error probability for $M \geqslant 3$. Thus, using Eqs. (1), (6), and (7), we obtain, for $M \geqslant 3$,

$$P_e \approx \frac{1}{\sqrt{\pi \log_2 (M) \sin^2\left(\frac{\pi}{M}\right)\frac{E_0}{N_0}}} e^{-\log_2 (M) \sin^2 (\pi/M) E_0/N_0} \tag{8}$$

where the approximation is extremely tight when P_e is small.

Let

$$\gamma_1 = \frac{(E_0)_4}{(E_0)_M} \tag{9}$$

be the *efficiency factor under Criterion 1* for M-ary phase modulation relative to four-phase modulation when $(P_0)_M = (P_0)_4$ or, equivalently by Eq. (3), when

$$\frac{(P_e)_M}{\log_2 M} = \frac{(P_e)_4}{2} \tag{10}$$

In the high signal-to-noise-ratio (SNR) limit where E_0/N_0 is extremely large, we see that Eq. (10) will hold only if the corresponding two exponents in Eq. (8) are (approximately) equal. Thus, in the high SNR limit, the efficient factor in Eq. (9) becomes simply

$$\gamma_1 = \log_2 (M) \sin^2\left(\frac{\pi}{M}\right) \tag{11}$$

which is tabulated in Table 1. Three-phase modulation, in the high SNR limit, is thus seen to be 0.75 dB better than four-phase modulation, *according to Criterion 1.* (Pierce's memo in Ref. 1 states the advantage as 0.5 dB, but 0.75 is, in fact, consistent with the curves given in Ref. 1.)

To find γ_1 elsewhere than for the high SNR limit, we can proceed as follows: first, choose a value γ_1 smaller than the high SNR limit, then substitute Eq. (8) into Eq. (10) and solve for $(E_0)_4/N_0$; finally, compute $P_0 = (P_e)_4/2$ from Eq. (8). Defining

$$A \doteq \sqrt{\log_2 \frac{(M)}{\gamma_1}} \sin\left(\frac{\pi}{M}\right) \tag{12}$$

we can write the solution for $(E_0)_4/N_0$ as

$$\frac{(E_0)_4}{N_0} = \frac{\log_e\left(\frac{A \log_2 M}{2}\right)}{1 - A^2} \tag{13}$$

In Table 2, we show the bit energy-to-noise ratio $(E_0)_4/N_0$ and corresponding bit error rate P_0 at which three-phase modulation achieves the indicated efficiency factor. (The numbers in Table 2 agree with the curves in Pierce's memo, Ref. 1.)

B. Criterion 2

For any M-ary signal set (such as the M-ary phase modulation signal set) for which the uniform probability distribution maximizes the defining expression for R_0, R_0 for the AWGN case is given (Ref. 3) by

$$R_0 = \log_2 M - \log_2 \left[1 + \frac{1}{M}\sum_{i=1}^{M}\sum_{\substack{j=1 \\ j\neq i}}^{M} e^{-|s_i - s_j|^2/(4N_0)}\right] \tag{14}$$

where $s_1, s_2, \cdots, s_M$ are the signal vectors. Using the symmetry of the M-ary phase modulation signal set, we can rewrite Eq. (14) as

$$R_0 = \log_2 M - \log_2 \left[1 + \sum_{j=1}^{M-1} e^{-E \sin^2 (j\pi/M)/N_0} \right] \quad (15)$$

where we have also used the fact that

$$|s_i - s_j|^2 = 4E \sin^2 \left[(j - i) \frac{\pi}{M} \right] \quad (16)$$

We define the efficiency factor under Criterion 2 for M-ary phase modulation relative to four-phase modulation to be

$$\gamma_2 = \frac{\left(\frac{R_0}{\log M} \right)_M}{\left(\frac{R_0}{2} \right)_4} \quad (17)$$

when the modulation bit energy-to-noise ratio is fixed, i.e., when $(E_0)_M/N_0 = (E_0)_4/N_0$.

In Table 3, we show this efficiency factor for three-phase modulation relative to four-phase modulation, over an interesting range of modulation bit energy-to-noise ratios, as found from Eqs. (15) and (17). From Table 3, we see that three-phase modulation offers only a slight advantage over four-phase modulation — the maximum advantage being only 0.16 dB — even though, under Criterion 2, three-phase modulation uses 1.26 times as much bandwidth compared to four-phase modulation. We see that this additional bandwidth is not being exploited very efficiently by three-phase modulation.

C. Criterion 3

We define the efficiency factor under Criterion 3 for M-ary phase modulation relative to four-phase modulation to be

$$\gamma_3 = \frac{(R_0)_M}{(R_0)_4} \quad (18)$$

when the baud energy-to-noise ratio is fixed, i.e., when $(E)_M/N_0 = (E)_4/N_0$. In Table 4, we show this efficiency factor, for three-phase modulation relative to four-phase modulation, over an interesting range of baud energy-to-noise ratios. We see that three-phase modulation, under Criterion 3 which constrains both the bandwidth and transmitted power of the compared systems to be the same, is *always inferior* to four-phase modulation, although by a small amount. We have also included the cut-off rate for eight-phase modulation in Table 4 to illustrate the fact that eight-phase modulation is always superior to four-phase. Does this suggest that one should always choose eight-phase modulation over four-phase? The answer to this question is an emphatic no! For baud energy-to-noise ratios, E/N_0, of 3.0 (5 dB) or less, the loss in R_0 suffered by four-phase modulation relative to eight-phase is negligible; thus, the greater simplicity of four-phase modulation makes it the practical choice. For large E/N_0, however, one should seriously ask whether the increased R_0 offered by eight-phase (or even higher order phase modulation) is sufficient to justify choosing the more complex modulation rather than four-phase modulation. However, we do argue that the Criterion 3 comparison does dictate that *four-phase modulation should always be chosen over three-phase modulation.* Our reasoning is that three-phase modulation is actually more difficult to implement than four-phase so that the former offers no compensating advantage for its loss in cut-off rate, R_0.

IV. Reconciling Criteria 1 and 2

It may appear puzzling that Criteria 1 and 2 lead to such different measures of the improvement that three-phase modulation offers over four-phase modulation, since both criteria give three-phase the same bandwidth advantage. One might conclude that this discrepancy is due to the use of P_0 (the demodulation bit error probability) in Criterion 1 versus the use of $R_0/\log_2 M$ (the cut-off rate per modulation bit) in Criterion 2. But we shall now show that this difference is not the cause of the discrepancy, after which we shall indicate the true cause.

Consider the following criterion:

Criterion 2′: Fix $R_0/\log_2 M$, the cut-off rate per modulation bit, and compare the necessary E_0/N_0, the modulation bit energy-to-noise ratio.

Notice that Criterion 2′ differs from Criterion 2 only as to which of the parameters, $R_0/\log_2 M$ and E_0/N_0, is held fixed. We find the *efficiency factor under Criterion 2′* for M-ary phase modulation relative to four-phase modulation to be

$$\sigma_{2'} = \frac{(E_0)_4}{(E_0)_M} \quad (19)$$

when $(R_0)_M/\log_2 M = (R_0)_4/2$.

Using Eq. (1) in Eq. (15) and solving for E_0/N_0, we find

$$\frac{(E_0)_4}{N_0} = -\log_e \left[2^{1-(R_0)_4/2} - 1 \right] \quad (20)$$

and

$$\frac{(E_0)_3}{N_0} = -\frac{4}{3\log_2 3}\log_e\left\{\frac{1}{2}\left[3^{1-(R_0)_3/\log_2 3} - 1\right]\right\}. \quad (21)$$

In Table 5, we show the efficiency factor σ_2' for three-phase modulation relative to four-phase modulation, over an interesting range of modulation bit energy-to-noise ratios. In particular, the values of $(E_0)_4/N_0$ in the upper half of Table 5 are the same as those in Table 3 – we see from these that three-phase modulation has a much greater advantage over four-phase when measured under Criterion 2′ rather than Criterion 2. In fact, *the advantage measured under Criterion 2′ coincides almost exactly with that measured under the error probability Criterion 1* – as can be seen from the lower half of Table 5 where the values of $(E_0)_4/N_0$ are the same as those in Table 2.

We are now in position to see why Criteria 1 and 2′ give, in our opinion, a misleadingly large advantage to three-phase modulation over four-phase. As can be seen from Table 5, the apparent advantage (under Criterion 2′) of three-phase increases markedly as $R_0/\log_2 M$ approaches its asymptotic value of 1 for large energy-to-noise ratios. Criterion 2′ thus shows three-phase to be most favorable when modulation energy is being "wasted" to drive R_0 extremely close to 1. In our view, the purpose of the modulation system is to maximize the number of information bits that can be transmitted reliably per unit of modulation energy, i.e., to maximize $R_0/\log_2 M$ per unit of E_0. This dictates operation at a fairly low E_0/N_0 so that operation is in the range where R_0 is linear with E_0. The burden of actually achieving the desired reliability should be placed on the coding system, not the modulation system! This is the reason we argue that, even if three-phase is given a bandwidth advantage over four-phase as with Criteria 1, 2, and 2′, one should fix E_0/N_0 and compare $R_0/\log_2 M$ instead of vice versa. That is, for the same modulation energy one should see how good a channel is created for coding, rather than starting from some arbitrary channel and measuring how much energy is needed to create it. We note that the former kind of comparison is impossible with a modulation bit error probability criterion – there is no natural way to compare different error probabilities in "dBs" – and this dooms, in our opinion, most modulation comparisons based on error probability to be misleading.

We have argued that the apparent 0.75 dB superiority of three-phase modulation over four-phase at high energy-to-noise ratios is an advantage that results only when the modulation system is misused to deliver reliable bits to the user, rather than to pave the way for the coding system to do this. In the next and final section, we give an example of how a very simple coding system can make four-phase modulation appear superior to uncoded three-phase modulation when both systems use the same bandwidth. This example illustrates very clearly, we believe, why Criteria 1, 2, and 2′ are all misleading, although Criterion 2 is the least so.

V. Remarks and Conclusions

We have argued that Criterion 1 is an inappropriate criterion for comparing phase-modulation systems since it ignores bandwidth requirements and prohibits the use of coding. We now give an example to buttress our case against Criterion 1.

Suppose that four-phase modulation is encoded by adding one parity bit to each four information bits to be transmitted, the parity bit being the modulo-two sum of the 4 information bits. This expands the bandwidth by a factor of $5/4 = 1.25$ so that, for the same energy per information bit, the coded four-phase modulation system has the same bandwidth as uncoded three-phase modulation (which requires 1.26 times the bandwidth of uncoded four-phase modulation). For the same information bit error probability, a calculation similar to that in Section III A above shows that the coded four-phase system is 1.29 dB superior to the uncoded three-phase system with the same bandwidth, for large values of the modulation bit energy-to-noise ratio. Moreover, the necessary encoder and decoder for the four-phase system are probably no more complex than the additional equipment needed to implement three-phase rather than four-phase modulation. Thus, when attention is given to bandwidth, the alleged superiority of three-phase modulation vanishes entirely.

We argue that, because it is the only one of the three criteria above which constrains both bandwidth and power, Criterion 3 is the most useful for comparing phase modulation systems. We have shown that Criterion 3 indicates that four-phase modulation should always be preferred over three-phase.

For some channels, notably the deep-space channel, bandwidth is of secondary importance so that there is a strong case for comparing modulation systems under a power constraint only. We argue that, in this instance, the appropriate choice is Criterion 2, rather than Criterion 1 (bit error probability) or Criterion 2′, for the following reason. Criterion 2 compares the quality of two modulation systems when both have the *same* transmitter power; whereas Criteria 1 and 2′ fix the quality and *then* compare the necessary power – this leads to misleading comparisons in the "inefficient" (or "saturated") modula-

tion region where small improvements in quality require large increases of power. Thus, the latter two criteria actually constrain channel quality, *not* transmitted power. We have seen that, under Criterion 2, three-phase modulation is superior to four-phase, but the maximum advantage (about 0.16 dB) is so slight that it generally would not be worth the extra complexity required to implement three-phase rather than four-phase modulation.

References

1. Pierce, J. R., "Three-Phase vs Two-Phase and Four-Phase Modulation, California Institute of Technology Internal Memorandum, Electrical Engineering Department, October 10, 1977.
2. Wozencraft, J. M. and Kennedy, R. S., "Modulation and Demodulation for Probabilistic Coding," *IEEE Trans. Info. Th.*, Vol. IT-12, pp. 291-297, July, 1966.
3. Massey, J. L., "Coding and Modulation in Digital Communications," in *Proc. 1974 Int. Zurich Seminar on Digital Comm.*, pp. E2(1)-E2(4), March 12-15, 1974.
4. Wozencraft, J. M. and Jacobs, I. M., *Principles of Communication Engineering*, New York, Wiley, 1967.

Table 1. Efficiency factor γ_1 by Criterion 1 for M-ary phase modulation in the high SNR limit

M	γ_1	γ_1 in dB
3	1.189	+0.752
4	1	0
5	0.802	−0.957
6	0.6462	−1.896
7	0.5285	−2.770
8	0.4393	−3.572
16	0.1522	−8.175

Table 2. Demodulator bit error probability P_0 at which the efficiency factor γ_1 is obtained for three-phase modulation (relative to four-phase modulation)

γ_1	γ_1 in dB	$(E_0)_4/N_0$	$(E_0)_4/N_0$ in dB	P_0
1.10	0.414	2.403	0.381	1.65×10^{-2}
1.13	0.531	3.988	6.01	2.62×10^{-3}
1.15	0.607	6.416	8.07	1.82×10^{-4}
1.16	0.645	8.900	9.49	1.29×10^{-5}
1.17	0.682	14.04	11.47	6.01×10^{-8}
1.18	0.719	30.97	14.91	1.80×10^{-15}
1.189	0.752	995.0	30.0	$<10^{-99}$

Table 3. Efficiency factor γ_2 for three-phase modulation (compared to four-phase modulation under Criterion 2) vs the modulation bit energy-to-noise ratio

E_0/N_0	$R_0/\log_2 M$		γ_2	γ_2 in dB
	$M = 4$	$M = 3$		
0.01	0.0072	0.0072	1.000	0
0.10	0.0703	0.0707	1.001	0.02
0.30	0.2002	0.2031	1.014	0.06
1.00	0.5481	0.5670	1.035	0.147
1.30	0.6523	0.6767	1.037	0.159
1.50	0.7094	0.7362	1.038	0.161
1.70	0.7579	0.7860	1.037	0.159
3.00	0.9299	0.9499	1.022	0.093
10.0	0.9999	1.0000	1.000	0

Table 4. Efficiency factor γ_3 for three-phase modulation (compared to four-phase modulation under Criterion 3) vs the band energy-to-noise ratio

E/N_0	R_0		γ_3	γ_3 in dB	R_0
	$M = 4$	$M = 3$			$M = 8$
0.01	0.0072	0.0072	1.000	0	0.0072
0.10	0.0712	0.0712	1.000	0	0.0712
0.30	0.2083	0.2081	0.999	0	0.2083
1.0	0.6321	0.6254	0.989	−0.05	0.6326
3.0	1.4188	1.3090	0.923	−0.35	1.444
10.0	1.9806	1.5834	0.799	−0.97	2.4380
30.0	2.0000	1.5850	0.7925	−1.01	2.9648

Table 5. Cut-off rate per modulation bit and modulation bit energy-to-noise ratios at which the efficiency factor σ_2' is obtained for three-phase modulation [a]

R_0 per modulation bit	$(E_0)_4/N_0$	$(E_0)_3/N_0$	σ_2'	σ_2' in dB
0.0072	0.0100	0.0100	1.000	0
0.0703	0.1000	0.0994	1.005	0.02
0.2002	0.3000	0.2955	1.015	0.07
0.5481	1.000	0.9547	1.048	0.20
0.6523	1.300	1.227	1.060	0.25
0.7094	1.500	1.406	1.067	0.28
0.7579	1.700	1.583	1.074	0.31
0.9299	3.000	2.707	1.108	0.45
0.9999	9.577	8.252	1.161	0.65
0.8751	2.403	2.196	1.095	0.39 (0.41)
0.9735	3.988	3.546	1.125	0.51 (0.53)
0.9976	6.416	5.593	1.147	0.60 (0.61)
0.99980	8.900	7.683	1.158	0.64 (0.65)
0.99999885	14.04	12.007	1.169	0.68 (0.68)
→1	→∞	→∞	1.189	0.75 (0.75)

[a] Numbers in parentheses are the values of σ_2 at the same $(E_0)_4/N_0$.

Submicrosecond Comparison of Intercontinental Clock Synchronization by VLBI and the NTS Satellite

W. J. Hurd
Communications Systems Research Section

S. C. Wardrip
NASA Goddard Space Flight Center

J. Bussion, J. Oaks, and T. McCaskill
Naval Research Laboratory

H. Warren
Bendix Field Engineering Corp.

G. Whitworth
Applied Physics Laboratory

The intercontinental clock synchronization capabilities of Very Long Baseline Interferometry (VLBI) and the Navigation Technology Satellite (NTS) were compared in May 1978 by using both methods to synchronize the cesium clocks at the NASA Deep Space Net complexes at Madrid, Spain, and Goldstone, California. The VLBI experiments used the Wideband VLBI Data Acquisition System developed at the NASA Jet Propulsion Laboratory. The Navigation Technology Satellites, which were designed and built by the Naval Research Laboratory, were used with NTS Timing Receivers developed by the Goddard Space Flight Center. The two methods agreed at about the one-half microsecond level. The VLBI system also obtained long-term stability information on the HP5061A-004 cesium standards by measuring $\Delta T/T$ over four 3- to 4-day intervals, obtaining stability estimates of $(1 \pm 1) \times 10^{-13}$ for the combined timing systems.

I. Introduction

A series of experiments were conducted in May 1978 to compare the intercontinental clock synchronization capabilities of the Navigation Technology Satellite (NTS) time transfer system and a Very Long Baseline Interferometry (VLBI) system which is in use in the NASA Deep Space Net. The purpose of the experiments was to provide independent verification of the accuracy of both systems. This verification was accomplished at the 0.5-μs level.

The experiments were conducted between the 64-m Deep Space Stations at Goldstone, California (DSS 14) and Madrid,

Spain (DSS 63). The VLBI experiments used the Wideband Digital VLBI Data Acquisition System (WBDAS), developed at NASA's Jet Propulsion Laboratory, which has been in routine use in its present configuration since January 1978. The satellite time transfer experiments used the NTS 1 satellite, designed and built by the Naval Research Laboratory, and the NTS Timing Receivers developed by Goddard Space Flight Center. The NTS receivers were brought to the DSS's especially for these experiments. Unfortunately the NTS 2 satellite was not available for the experiments; use of this satellite might have improved the accuracy of the intercomparison by an order of magnitude.

II. Experiment Configuration

The configuration of the VLBI data acquisition system and the NTS time transfer receiver at each DSS is shown in Fig. 1. Of particular interest is the clock system. The primary frequency standard at each station was a HP5061A-004 cesium oscillator. Various frequencies are derived from the reference in a coherent reference generator, including 50 MHz, which is used in the VLBI system, and various coherent timing signals are made available at the output of the Time Format Assembly. For the purpose of this experiment, the station reference clock is the 1-pps signal at the output of the TFA, since both the VLBI and the NTS systems connect to the station timing system at this point. In comparing the results for the two systems we accounted for the cable delays according to the specified or measured physical lengths of the cables, and we measured the delay from the 1-pps input to the 1-pps output of the NTS receivers, which is the reference for these receivers. The delay within the WBDAS units is less than 20 ns and is not significant.

III. NTS Time Transfer Results

Time transfer using a NTS satellite is accomplished by using the stable oscillator onboard the satellite as a portable clock, and reading this clock over a microwave link as the satellite passes near the various ground stations. The two major fundamental sources of error in the time transfer are the instability of the oscillator on the satellite and propagation delays in the ionosphere. These error sources affect the time transfer measurement both directly and through errors in the satellite orbit. Raymond et al. (Ref. 1) describe the timing receiver used here, and present the results of some time transfer experiments between Rosman, N.C. and the Naval Research Laboratory, using the NTS 1 satellite which was also used here. These experiments demonstrated rms errors of 8.6 ns with respect to a portable clock. Errors over intercontinental distances are somewhat more due to time separation, orbit errors, and larger ionospheric effects. The ionospheric effect and its uncertainty is often on the order of 1 μs at the radio frequency of 335 MHz, but this error source tends to cancel when the time and space separation are small.

The NTS time transfer measurements reported on here were more or less adjunct to the six-nation cooperative experiment described by Buisson et al. (Ref. 2). The receiver used at the Madrid station was the same as the one used at Bureau International de l'Heure, France, and a spare receiver was used at Goldstone, California. As indicated in Fig. 1, the receivers were installed in the DSS control rooms, with the NTS antennas on the roofs. The positions of the antennas were measured to within a few feet with respect to benchmarks at the stations, and errors in the antenna coordinates are not expected to contribute significantly to errors in the results. The data were processed in the same manner as in the six-nation experiment, thereby estimating the offsets in the DSS clocks with respect to the USNO master clock C8D, at the Naval Observatory.

Figure 2 shows the results of 13 measurements made at Goldstone from day 145 (May 25) through day 151 (May 31), 1978. The results are corrected for a delay of 0.232 μs from the Goldstone clock reference point to the NTS receiver clock. A least squares linear fit to the data results in an offset USNO minus Goldstone of -0.688 μs at 0 hours on day 147, with a rate offset of -0.9×10^{-12} and an rms residual of 0.341 μs.

Ten measurements were conducted at Madrid during the same time frame, with results shown in Fig. 3. These results are corrected for a delay of 0.279 μs from the DSS clock reference point to the NTS receiver output. The least squares fit indicates an offset USNO minus Madrid of 8.593 μs at 0 h on day 147, with a rate offset of -0.28×10^{-12} and rms residuals of 0.226 μs.

IV. VLBI System Description

Station clock offset is one of the many parameters which can be estimated by Very Long Baseline Interferometry. The random radio signal from an extragalactic radio star is observed at two antenna stations. Because the antennas are widely separated and the Earth is rotating, there is a time varying time delay between the arrival of the signal at the two stations. This time delay and its derivative can be estimated from the geometry, and can be measured by cross-correlating the signals received at the two stations. Because the arrival of the signal is time-tagged by the clocks at the stations, the difference between the measured and the predicted time delays forms an estimate of the offset between the station clocks.

The Wideband VLBI Data Acquisition System (WBDAS) has been described elsewhere (Ref. 3), together with results of experiments held in 1976, so we present only a brief description here. A simplified block diagram of the WBDAS is given in Fig. 4. As shown in Fig. 1, the system interfaces to the standard DSN receiving system at the 55 ±18 MHz output of the Block IV receiver. The receiver output is digitally demodulated to baseband by sampling at 50 MHz in each of two phase-quadrature 3-bit analog-to-digital converters. The A/D converter outputs are then low-pass-filtered, if desired, by summing N consecutive samples in a digital integrate-and-dump filter. These experiments used both unfiltered sampling, and filtering with $N = 3$, for a filter bandwidth of 16 2/3 MHz, which was a reasonably good match to the receiver system bandwidths.

The digital filter outputs are quantized to 1 bit and stored in a high-speed buffer of 4096 bits. When the buffer is full, which takes about 120 μs for $N = 3$, sampling is inhibited and the buffer is emptied through the control computer onto digital magnetic tape. The total data rate onto magnetic tape is 57 kb/s, consisting of 14 bursts of 4096 bits. The control computer utilizes knowledge of the radio source position to predict the geometric signal delay from the source and controls the hardware buffer so that the same segments of the signal wavefront are sampled and recorded at both stations.

The utilized receiver bandwidth of 16 2/3 MHz is sufficient to achieve measurement resolutions of under 10 ns for any radio source which is strong enough to be detected. Resolution of about 1 ns is achieved with strong sources, using 1 minute of data (3×10^6 bits).

The accuracy of the system is limited primarily by propagation uncertainty in the ionosphere, which is often 20 ns at the S-band receiving frequency of 2290 MHz; by uncertainty in the Earth's orientation (UT1), which causes errors of about 5 ns; by errors in the positions of the radio sources; and by receiving system delays. We currently estimate the total day to day consistency in results to be about 30 ns, and the constant bias due to unknown but constant receiving system delays to be another 40 ns, for an estimated total error of 50 ns. (It is possible that the error in the receiving system delays is greater than 40 ns, because the delays have not been measured, but were estimated from cable length specifications).

V. VLBI Results and Comparison to NTS Results

Four VLBI clock sync experiments were conducted on May 15, 20, 24, and 27, 1978. The last three experiments consisted of from 8 to 13 total observations of 7-11 radio sources over total time spans of 1.5 to 3 hours. On May 15, due to operational problems, only two sources were observed, about 10 minutes apart. Despite the discrepancy in the amount of data, the expected clock sync errors are about the same on all days, except that the expected error on May 15 is slightly larger. As shown in Fig. 4, the computer associated with the WBDAS is interfaced to data transmission lines. We used this capability to transmit some of the data from Madrid to JPL, and processed this data between experiments to provide confirmation that the stations were properly configured.

Figure 5 shows the final clock offset estimates for the four days. The results are compensated for all known clock and signal delays, and are expressed as Goldstone clock minus Madrid clock. A linear least squares fit to the data yields an estimated clock offset of 8.775 μs at 0 h on day 147, with a rate offset of 0.33×10^{-12}. The rms of the residuals is 20.7 ns, and the sample standard deviation is 29.3 ns, with the difference due to estimating two parameters with only four data points. This is compatible with our a priori estimate of day-to-day consistency of 30 ns.

Also shown in Fig. 5 is the NTS time transfer experiment estimate of the clock and clock rate offset between the two stations. This estimate is 9.281 μs at 0 h on day 147, with a rate offset of 0.62×10^{-12}, which is just the USNO-Madrid result of Fig. 3, minus the USNO-Goldstone result of Fig. 4. The difference between the VLBI and the NTS estimates is 0.506 μs at 0 h on day 147, with a rate offset of 0.29×10^{-12}. Day 147 was chosen as the reference epoch because both experiments were in progress at that time.

The difference of 0.5 μs between the two experiments is probably mainly due to the ionospheric effects on the NTS measurements, both directly and through errors in orbit determination. There may also be a larger constant error in the estimated station delays for the VLBI experiment than the anticipated ±40 ns. The difference between the rate estimate is within the error bounds of the NTS experiment.

VI. Oscillator Stability Estimate from the VLBI Data

The instabilities of the HP5061A-004 cesium oscillators at the two stations can be bounded by using the VLBI results. The four experiments form three time intervals of 3 to 4.5

days. Differencing the clock offset estimates for successive experiments leads to frequency offset estimates of 1.85×10^{-13}, 4.26×10^{-13}, and 3.63×10^{-13}. Successive absolute differences between the offsets, divided by root 2, yield Allan variance σ's of 1.70×10^{-13} and 0.44×10^{-13}. The average of the two Allan variance pairs yields an average σ of 1.07×10^{-13} with a sample sigma of 0.9×10^{-13}.

We have estimated the combined instability of the two cesium oscillators, the station time distribution systems, and the VLBI measurements, over 3- to 4-day intervals, to be approximately one part in 10^{13}, with an uncertainty of one part in 10^{13}. By increasing the time interval to about 10 days and reducing the ionospheric effect on the VLBI measurements by use of X-band, long-term frequency stability measurements at the 10^{-14} level seem feasible.

VII. Conclusion

By intercomparison of results, we have demonstrated the absolute accuracy of the NTS time transfer system and the WBDAS VLBI system to be 0.5 μs or better between Goldstone, California, and Madrid, Spain. For the VLBI system, we have produced clock sync residuals which demonstrate day-to-day consistency at the 20- to 30-ns level and the ability to use this system to measure long-term frequency stability at the 10^{-13} level. Frequency stability measurements at the 10^{-14} level are indicated to be feasible.

References

1. Raymond, L., et al., "Navigation Technology Satellite (NTS) Low Cost Timing Receiver," Technical Report X-814-77-205, Goddard Space Flight Center, Greenbelt, Md. Aug. 1977.
2. Buisson, J., et al., "Submicrosecond Comparisons of Time Standards Via the Navigation Technology Satellites (NTS)," Proceedings of the Tenth Annual Precise Time and Time Interval (PTTI) Applications and Planning Meeting, U.S. Naval Research Laboratory, Washington, D.C., Nov. 28–30, 1978.
3. Hurd, W. J., "Preliminary Demonstration of Precision DSN Clock Synchronization by Radio Interferometry," in *The Deep Space Network Progress Report 42–37,* Jet Propulsion Laboratory, Pasadena, Calif., Feb. 15, 1977, pp. 57–68.

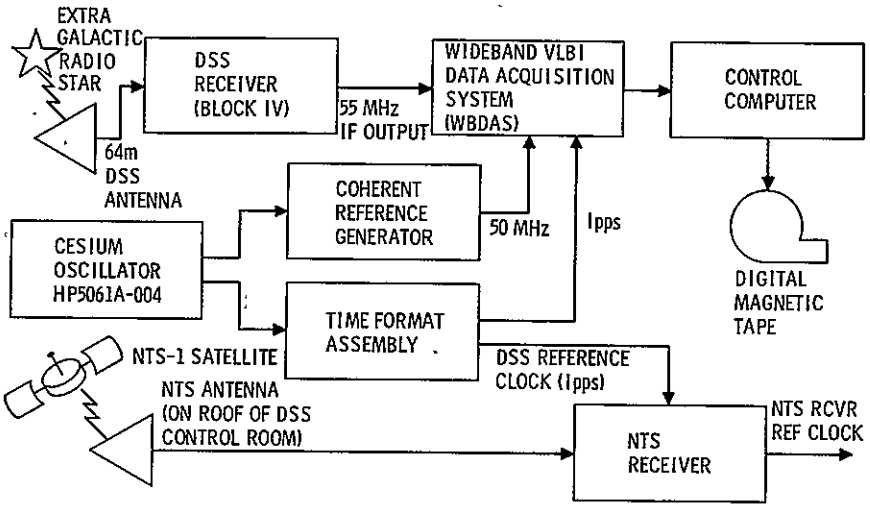

Fig. 1. Configuration of the NTS receiver and the VLBI system in a Deep Space Station

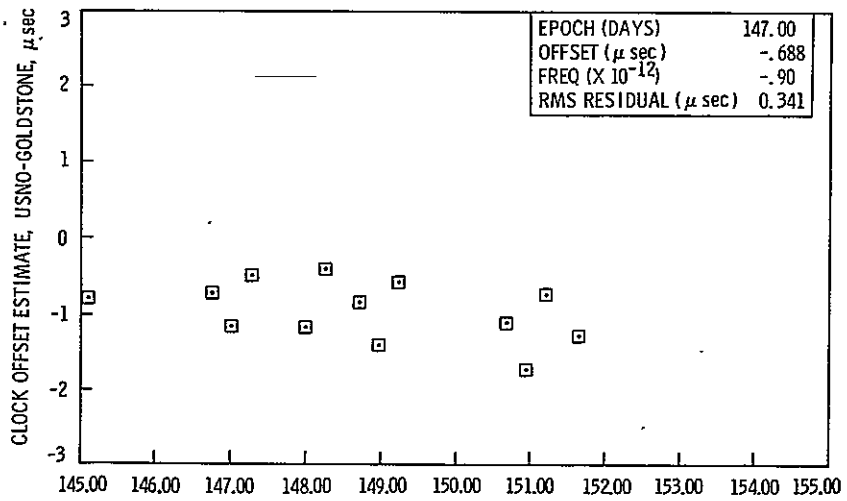

Fig. 2. NTS 1 time transfer results for Goldstone: USNOMC (C8D) – Goldstone (DSS 14)

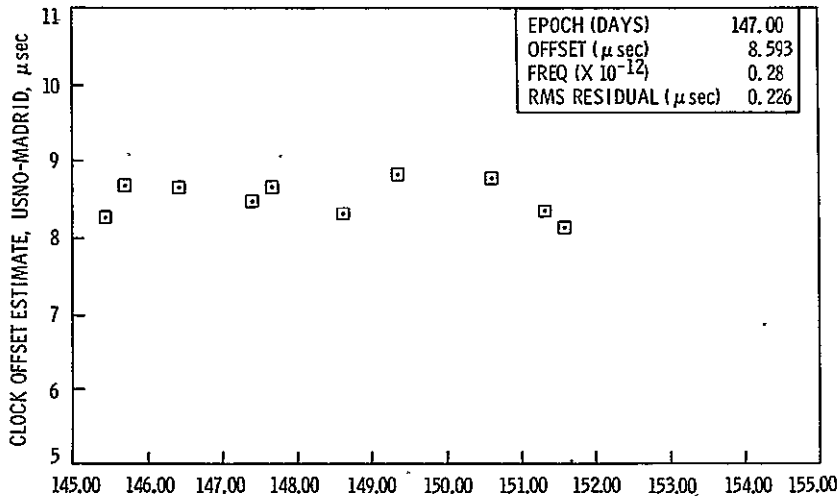

Fig. 3. NTS 1 time transfer results for Madrid: USNOMC (C8D) – Madrid (DSS 63)

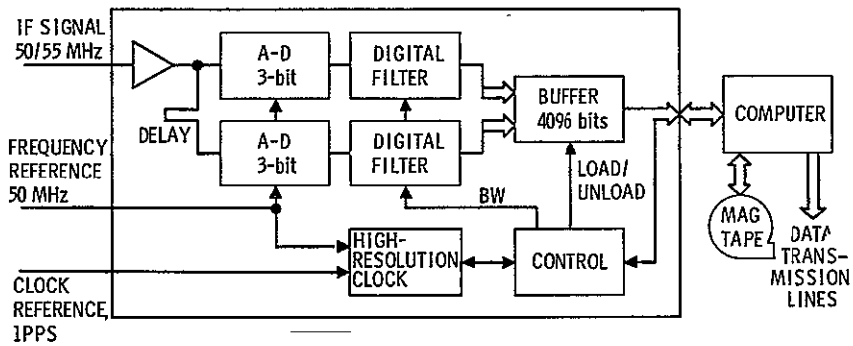

Fig. 4. Wideband digital data acquisition system block diagram

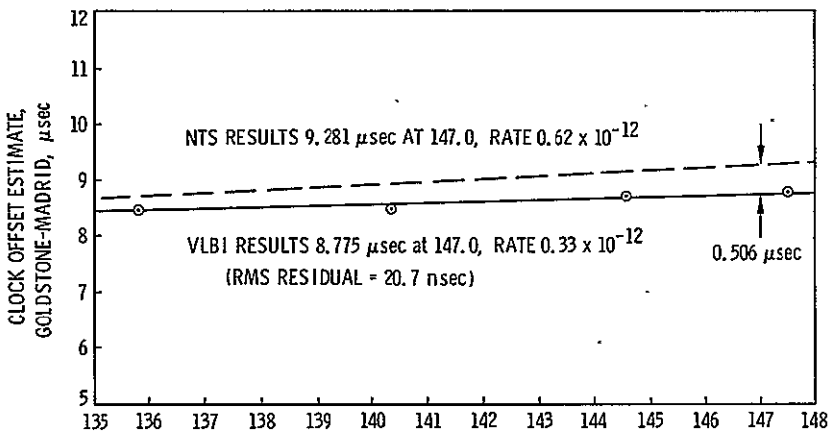

Fig. 5. VLBI clock offset measurements and comparison to NTS results: Goldstone (DSS 14) – Madrid (DSS 63)

D10

N79-19055

Coding for Optical Channels

L. D. Baumert
Arizona State University

R. J. McEliece
University of Illinois

H. Rumsey, Jr.
Communications Systems Research Section

In a recent paper Pierce considered the problem of optical communication from a novel viewpoint, and concluded that performance will likely be limited by issues of coding complexity rather than by thermal noise. This paper reviews the model proposed by Pierce and presents some results on the analysis and design of codes for this application.

I. Introduction

In a recent paper Pierce (Ref. 1) considered the problem of optical communication from a novel point of view. He showed that for optical frequencies and low temperatures, the maximum signaling rate will be determined by coding complexity issues rather than by thermal noise. He exhibited one simple coding scheme (referred to below as a type 1 code), and challenged future workers to go further. This paper is a response to that challenge.

In Section II, we will describe the model Pierce arrived at as an appropriate description of the optical communication problem. It will be seen that Pierce's model is the familiar Z-channel. A complication arises because in Pierce's model the transmission of a "1" (which corresponds physically to the transmission of photons) is more costly than the transmission of a "0" (no photons). After some fairly simple analysis, we conclude that an appropriate figure of merit for a binary code $\{\mathbf{x}_1, \ldots, \mathbf{x}_M\}$ which is to be used on Pierce's channel is

$$Q = \left[\frac{M \log M}{\sum_{i=1}^{M} w(\mathbf{x}_i)} \right] d_a \qquad (1)$$

where $w(\mathbf{x}_i)$ is the Hamming weight of the codeword $\mathbf{x}_i$, and d_a is the minimum *asymmetric distance* of the code. (The term is defined precisely in Section II).

Calling the first term on the right side of Eq. (1) R_0, in Section III we show that R_0 is largest for Pierce's type 1 code. In fact, we show that $R_0 \leq [(n+1)/n] \log (n+1)$, with equality only for type 1 codes. On the other hand, Pierce's codes all have $d_a = 1$, and in Section IV, we exhibit several codes with larger d_a which are in a certain sense superior to Pierce's codes.

Finally, in Section V, we prove the existence of a sequence of codes for which Q grows *linearly* with the block length n. (For Pierce's codes Q grows only logarithmically.)

II. The Channel Model

The channel model arrived at by Pierce (Ref. 1) can be described as follows. At the transmitting end there is a light source and a shutter, and at the receiving end there is a photon counter. To transmit a binary sequence $\mathbf{x} = (x_1, \ldots, x_n)$ over this channel in T seconds, we divide the time interval into n equal segments of duration T/n; we close the shutter during the i-th time interval if $x_i = 0$, and open it if $x_i = 1$. The receiver's estimate of x_i is 0 if no photons strike the photon counter during the appropriate interval, and 1 if one or more do. Assuming that the expected number of photons emitted by the light source during an interval of length T/n is λ, the probability that a transmitted 1 will be detected as a 0 is $e^{-\lambda}$, because of the Poisson nature of photon emissions. Of course if no photons are transmitted, none will be detected, and so this channel is the Z-channel depicted in Fig. 1. Furthermore it is assumed that there is a unit energy "cost" associated with the transmission of each photon. The basic coding problem here is to study the trade-off between the transmission rate measured in nats per photon) and the decoded bit error probability.

Suppose we wish to communicate over this channel using a binary code $\{\mathbf{x}_1, \ldots, \mathbf{x}_M\}$ of length n with M code words. The rate of the code is $\log M$ nats[1] per code word. On the other hand the expected number of photons required by the i-th code word is $\lambda w(\mathbf{x}_i)$, where $w(\mathbf{x}_i)$ denotes the Hamming weight of $\mathbf{x}_i$. Hence (provided each code word is transmitted with probability M^{-1}) the average number of photons required per code word is

$$\frac{\lambda \sum_{i=1}^{M} w(\mathbf{x}_i)}{M}$$

Hence the transmission rate, measured in *nats per photon* is

$$R = \frac{1}{\lambda}\left[\frac{M \log M}{\sum_{i=1}^{M} w(\mathbf{x}_i)}\right] \tag{2}$$

The quantity in brackets in Eq. (2) depends only on the code, and we call it the *asymmetric rate* of the code:

$$R_0 = \frac{M \log M}{\sum_{i=1}^{M} w(\mathbf{x}_i)} \tag{3}$$

[1]Throughout, all logarithms will be natural.

We have now defined the transmission rate of a code for our channel model. We now need a measure of the code's error correcting ability. To this end we are led to define the *asymmetric distance* between two binary n-tuples $\mathbf{x} = (x_1, \ldots, x_n)$ and $\mathbf{y} = (y_1, \ldots, y_n)$. Let r denote the number of coordinates where $x_i = 1$ and $y_i = 0$, and s = number where $x_i = 0$ and $y_i = 1$. Then we define

$$d_a(\mathbf{x}, \mathbf{y}) = \max(r, s) \tag{4}$$

This distance plays a role for asymmetric errors analogous to that played by the Hamming distance $d_H(\mathbf{x}, \mathbf{y}) = r + s$ for symmetric errors. The main result is the following.

Theorem 1: If the minimum asymmetric distance between distinct code words is d_a, then the code is capable of correcting any pattern of $d_a - 1$ or fewer asymmetric errors. (N. B. An asymmetric error is an error of the type $1 \to 0$. The symmetry of the definition in Eq. (4) implies immediately the curious fact that any code capable of correcting $d_a - 1$ "$1 \to 0$" errors will also correct $d_a - 1$ "$0 \to 1$" errors.)

Proof: We begin by considering an example:

$$\mathbf{x} = 1\,1\,1\,1\,1\,1\,0\,0\,0\,0\,0\,0$$

$$\mathbf{y} = \underbrace{0\,0\,0\,0\,0\,0}_{r}\,\underbrace{1\,1\,1\,1\,1\,1}_{s}$$

If x is transmitted over the Z-channel of Fig. 1, can it be mistaken at the receiver as y? Clearly not, unless *each* of the 1's in x is received as 0, since the presence of a 1 in the first r received components would immediately rule y out. (The transition $0 \to 1$ is impossible.) Hence, the smallest number of errors that could possibly cause confusion is r. If then x is received with these r errors as $\mathbf{x}' = 0\,0\,0\,0\,0\,0\,0\,0\,0\,0\,0\,0$, $\mathbf{x}'$ differs from x in r positions and from y in s positions. If the decoder picks the vector for which the number of disagreements is smallest, an error is possible only if $r \geq s$ (and certain only if $r > s$). The conclusion is that if x is transmitted, an error is possible only if at least r errors occur, and $r \geq s$. Similarly if y is transmitted, an error is possible only if at least s errors occur, and $s \geq r$. This shows that the code consisting of only the two code words $\{\mathbf{x}, \mathbf{y}\}$ can correct any pattern of up to $\max(r, s) - 1 = d_a(\mathbf{x}, \mathbf{y}) - 1$ asymmetric errors. Finally if the code has M code words $\{\mathbf{x}_1, \ldots, \mathbf{x}_M\}$, and $d_a = \min\{d_a(\mathbf{x}_i, \mathbf{x}_j): i \neq j\}$, the above argument shows that no pattern of $d_a - 1$ or fewer asymmetric errors can possibly cause one transmitted code word to be mistaken for another.

Now consider the decoded error probability P_E of the code $\{x_1, \ldots, x_M\}$, when it is used on the channel of Fig. 1. P_E is given by a complicated expression of the form

$$P_E = \frac{1}{M} \sum_{i=1}^{M} \sum_{z \in B_i} e^{-\lambda w(z)} (1 - e^{-\lambda})^{n-w(z)} \quad (5)$$

where B_i is the set of error patterns which causes decoder error, when x_i is transmitted. Theorem 1 implies that $w(z) \geq d_a$ for all

$$z \in \bigcup_{i=1}^{M} B_i$$

and so in the limit as $\lambda \to \infty$, the sum on the right side of Eq. (5) is dominated by the terms of the form $e^{-\lambda d_a}$, i.e.,

$$\lim_{\lambda \to \infty} \frac{1}{\lambda} \log P_E = -d_a \quad (6)$$

where d_a is the code's asymmetric minimum distance. If now we define the parameter γ to be the number of photons per nat required by the code (this is a sort of normalized energy budget, analogous to the bit signal-to-noise ratio on the more familiar Gaussian channel), we get from Eq. (2) that $\lambda = R_0 \gamma$, and Eq. (6) becomes

$$\lim_{\gamma \to \infty} \frac{1}{\gamma} \log P_E = -R_0 d_a \quad (7)$$

Hence we are led to define the following quantity Q for any binary code, which is a measure of its asymptotic effectiveness when used on our photon counting channel:

$$Q = R_0 d_a \quad (8)$$

In summary: the bigger the code's "Q," the better we expect it to be.[2] In the next section we will show that $R_0 \leq [(n+1)/n] \log (n+1)$ for any code of length $n+1$. In Section IV, we give some examples of binary codes with fairly large "Q." Finally in Section V we demonstrate that as a function of n, the code length, the best possible Q grows linearly with n.

[2]For the Gaussian channel, the corresponding number is $R \cdot d_H$, where R is the ordinary dimensionless rate of the code, and d_H is its minimum Hamming distance.

III. An Upper Bound on R_0

In view of the definition in Eq. (8), it is clearly important to know how large the asymmetric rate R_0 (see Eq. 3) can be. Theorem 2, below, shows that R_0 can be no larger than $(1 + n^{-1}) \log (n+1)$.

Thus let $C = \{x_1, x_2, \ldots, x_M\}$ be any binary code of length n. Define

$$R_0(C) = \frac{M \log M}{\sum_{i=1}^{M} w(x_i)}$$

Theorem 2: $R_0(C) \leq [(n+1)/n] \log (n+1)$, with equality if and only if C consists of the $n+1$ words of weight ≤ 1.

Proof: Let $y_1, y_2, \ldots$ be an ordering of the 2^n binary vectors according to increasing weight: $0 = w(y_1) \leq w(y_2) \leq \ldots \leq w(y_{2^n}) = n$. If $C = \{y_i : i \in I\}$ is any code with $|I| = M$ code words, then clearly the code $C' = \{y_i : i \leq M\}$ must satisfy $R_0(C') \geq R_0(C)$. Thus, for the remainder of the proof we focus our attention on the codes $C_M = \{y_1, y_2, \ldots, y_M\}$ for $M = 1, 2, \ldots, 2^n$. If we let $\rho_M = R_0(C_M)$, the assertion of the theorem is that ρ_M, as a function of M, is maximized for $M = n+1$.

Let $\overline{M}$ be a value of M that maximizes ρ_M. Our first result is that if we define, for each $k = 0, 1, \ldots, n$,

$$M_k = \sum_{j=0}^{k} \binom{n}{j} \quad (9)$$

we must have $\overline{M} \in \{M_0, M_1, \ldots, M_n\}$. To see this suppose that $M_k < M < M_{k+1}$, let $x = M - M_k$, and observe that ρ_M is given by

$$\rho_M = f(x) = \frac{(M_k + x) \log (M_k + x)}{w_k + (k+1)x} \quad (10)$$

where

$$w_k = \sum_{j=0}^{k} j \binom{n}{j}$$

Suppose $\rho_M \geq \max(\rho_{M_k}, \rho_{M_{k+1}})$. Then the function $f(x)$, viewed as a continuous function of the real number x, would have a maximum somewhere in the interval $[0, \binom{n}{k+1}]$, i.e., $f'(x) = 0$ and $f''(x) \leq 0$. But from Eq. (10) one easily sees that

$$f'(x) = \frac{1}{w_k + (k+1)x}$$

$$\left\{1 + [w_k - (k+1)M_k] \frac{\log (M_k + x)}{w_k + (k+1)x}\right\} \quad (11)$$

From Eq. (11) it follows that $f'(x) = 0$ can only occur if the equation

$$[(k+1)M_k - w_k] \frac{\log (M_k + x)}{w_k + (k+1)x} = 1 \quad (12)$$

is satisfied. One easily verifies, however, that if Eq. (12) is satisfied, then $f''(x) = (M_k + x)^{-1} [w_k + (k+1)x]^{-1} > 0$; hence, $f(x)$ has no maximum for $x > 0$. Thus $\rho_M < \max(\rho_{M_k}, \rho_{M_{k+1}})$, and we have shown that the largest value of ρ_M occurs for $M \in \{M_0, M_1, \ldots, M_n\}$.

It remains to show that the maximum of $\rho(C_{M_k})$ occurs at $k = 1$. To do this, define

$$T_k = M_k \log M_k \quad (13)$$

and let $k \geqslant 1$ be an index that maximizes the function $\rho(C_{M_K}) = T_K/w_k$. Then in particular $T_k/w_k \geqslant T_{k-1}/w_{k-1}$; substituting $w_{k-1} = w_k - k\binom{n}{k}$ into this inequality we obtain

$$w_k(T_k - T_{k-1}) \geqslant k\binom{n}{k} T_k \quad (14)$$

But $T_k - T_{k-1} = M_k \log M_k - M_{k-1} \log M_{k-1} = [\binom{n}{k} + M_{k-1}] \log M_k - M_k \log M_{k-1} = \binom{n}{k} \log M_k + M_{k-1} \log (M_k/M_{k-1})$. Using the elementary inequality $\log x \leqslant x - 1$, we thus obtain $T_k - T_{k-1} \leqslant \binom{n}{k} (1 + \log M_k)$. Substituting this into Eq. (14) we obtain $1 + \log M_k \geqslant kT_k/w_k$. But since k is presumed to maximize the ratio T_k/w_k, it follows that $T_k/w_k \geqslant T_1/w_1 = [(n+1)/n] \log (n+1) > \log n$. Hence, from Eq. (14) follows

$$1 + \log M_k < k \log n \quad (15)$$

Equation (15) is a strong necessary condition on the optimizing parameter k; it cannot be satisfied unless $k = 1$ or 2, or $k = 3$ and $n \leqslant 2$, as we shall now see.

By a well-known inequality (Ref. 2), we have

$$\log M_k \leqslant k \log \frac{n}{k} + (n-k) \log \frac{n}{n-k}$$

$$= k \log n - k \log k + (n-k) \log \left(1 + \frac{k}{n-k}\right) \quad (16)$$

Again using the inequality $\log x \leqslant x - 1$, we get from Eq. (16)

$$\log M_k < k \log n - k \log k + k \quad (17)$$

It follows from Eq. (17) that $1 + \log M_k < k \log n$, provided $k < k \log k - 1$. This is true for all $k \geqslant 4$, and hence Eq. (15) is *not* true if $k \geqslant 4$.

If $k = 3$ we compute directly that $M_k = (n^3 + 5n + 6)/6$, and hence Eq. (15) is false for $k = 3$ and all $n \geqslant 3$.

Thus we have shown that for $n \geqslant 3$, the optimizing value for k must be $k = 1$ or $k = 2$. (The verification that Theorem 1 is true for $n = 1$ or 2 is trivial). We now conclude our proof of Theorem 1 by showing that $R_0(C_{M_2}) < R_0(C_{M_1})$. Since $M_2 = (n^2 + n + 2)/2$, $w_2 = n^2$, $M_1 = n + 1$, $w_1 = n$, this is equivalent to

$$\frac{n^2+n+2}{2} \log \frac{n^2+n+2}{2} < n(n+1) \log (n+1) \quad (18)$$

For $n \geqslant 1$, $n^2 + n + 2 \leqslant (n+1)^2$, and so the left side of Eq. (18) is upper bounded by

$$\frac{n^2+n+2}{2} \log \frac{(n+1)^2}{2} = (n^2+n+2) \log (n+1) - \frac{\log 2}{2} (n^2+n+2)$$

This is less than the right side of Eq. (15) since

$$\frac{n^2+n+2}{2} \log (n+1) - \frac{\log 2}{2} (n^2+n+2) - n(n+1) \log (n+1)$$

$$= 2 \log (n+1) - \frac{\log 2}{2} (n^2+n+2)$$

and $\log (n+1)/(n^2+n+2) \leqslant (\log 2)/4$ for all $n \geqslant 2$. This completes the proof of Theorem 1.

IV. Examples

Example 1: In the previous section we saw that the code of length n with 1 word of weight zero and n of weight 1 (hereafter called a *type 1* code) has the largest possible R_0 among codes of length n. Clearly $d_a = 1$ for these codes, and so from Eq. (8), the coding gain Q is given by

$$Q = \frac{n+1}{n} \log (n+1) \tag{19}$$

Surprisingly, it is quite difficult to find codes of length n for which Q is larger than this, for small values of n.

Example 2: Consider the extended (24, 12) Golay code. The average weight of its code words is 12 (this follows from the general theorem that any linear code of length n whose generator matrix has no zero columns has average weight $n/2$). Hence from Eq. (3) $R_0 = \log 2^{12}/12 = \log 2$. It is well-known that the minimum Hamming distance of this code is 8, i.e., if r and s are as in Eq. (4), $r + s \geqslant 8$; and hence $d_a \geqslant 4$ for this code. In fact one can also show that $d_a = 4$ for the Golay code, and so

$$Q = 4 \log 2 = 2.7726$$

Note that a type 1 code with $n = 12$ has $Q = (13/12) \log (13) = 2.7787$, which exceeds that of the Golay code. The type 1 code with $n = 24$ has $Q = 3.3105$, so that whatever desirable properties the Golay code may have in ordinary circumstances are certainly lost in the present application.

Example 3: Let C be the (128, 64) extended BCH code, with $d_H = 22$, hence $d_a \geqslant 11$ (actually $d_a = 11$). Then as above the average weight is 64 and so

$$Q = 11 \log 2 = 7.6246$$

This is better than the type 1 code with $n = 128$, which has only $Q = 4.8978$. Indeed, one needs $n \geqslant 2041$ in order to exceed $Q = 11 \log 2$ with a type 1 code.

V. The Existence of Codes With Large Q

In the last example of Section IV, we saw that it is possible for the best code of length n to have a value of Q which is larger than $(1 + 1/n) \log (n+1)$. In fact, if we denote the largest possible Q for a code of length n by Q_n, we can show that Q_n grows *linearly* with n. Specifically, we shall show in this section that

$$0.052 \leqslant \liminf_{n\to\infty} \frac{Q_n}{n} \leqslant \limsup_{n\to\infty} \frac{Q_n}{n} \leqslant 1.39 \tag{20}$$

(Note: The implied logarithms in Eq. (20) are natural logarithms.)

First we derive the upper bound in Eq. (20). From Eq. (4) we know that the asymmetric distance d_a of a given code is less than or equal to the Hamming distance, d_H, and so by Eqs. (3) and (8) we have

$$Q \leqslant \frac{\log M}{\frac{1}{M}\sum_{i=1}^{M} w(\mathrm{x}_i)} \cdot d_H \tag{21}$$

for any code $\{\mathrm{x}_1, \mathrm{x}_2, \ldots, \mathrm{x}_M\}$ of length n. Let us view this code as an $M \times n$ binary array, and let s_k denote the number of ones in the k-th column of this array. We now compute the sum $\Sigma d(\mathrm{x}_i, \mathrm{x}_j)$ over all distinct pairs $i < j$ in two ways. On one hand it is $\geqslant \binom{M}{2} d_H$, since $d(\mathrm{x}_i, \mathrm{x}_j) \geqslant d_H$ for all $i \neq j$. On the other hand, a pair of entries (x_{ik}, x_{jk}) in column k contribute 1 to the sum if and only if $x_{ik} \neq x_{ij}$. Thus

$$\binom{M}{2} d_M \leqslant \sum_{i<j} d(\mathrm{x}_i, \mathrm{x}_j) = \sum_{k=1}^{n} s_k(\mathrm{M} - s_k)$$

$$= M \sum_{k=1}^{n} s_k - \sum_{k=1}^{n} s_k^2 \tag{22}$$

Now

$$\sum_{k=1}^{n} s_k = \sum_{i=1}^{M} w(\mathrm{x}_i)$$

and by Schwarz's inequality

$$\sum_{k=1}^{n} s_k^2 \geqslant \frac{1}{n}(\Sigma s_k)^2$$

Hence, if we denote

$$\frac{1}{nM}\sum_{i=1}^{M} w(\mathrm{x}_i)$$

by ω, Eq. (22) yields

$$\omega(1-\omega) \geqslant \frac{M-1}{2M} \cdot \frac{d_H}{n} \tag{23}$$

Denoting the ratio d_H/n in Eq. (23) by δ, and using the fact that $(M-1)/M \leqslant 1$, Eq. (23) gives

$$\omega \geqslant \frac{1-\sqrt{1-2\delta}}{2} \tag{24}$$

Using Eq. (24) in Eq. (21), we obtain

$$Q \leqslant \frac{\log M}{n} \cdot \frac{2}{1-\sqrt{1-2\delta}} \cdot \delta n \tag{25}$$

In Eq. (25) the term $(\log M)/n$ is the rate of the code. If we denote by $R(n, d)$ the rate of the largest code of length n and minimum Hamming distance d, and for $0 \leqslant \delta \leqslant 1$

$$R(\delta) = \sup_{n\to\infty} \lim r(n, d_n)$$

where the "sup" is over all sequences (d_n) such that $d_n/n \to \delta$, it follows from Eq. (25) that

$$\limsup_{n\to\infty} \frac{Q_n}{n} \leqslant \sup_{\delta} \frac{2R(\delta)}{1-\sqrt{1-2\delta}} \cdot \delta \tag{26}$$

Now the function $R(\delta)$ is not precisely known, but using the well-known Plotkin bound

$$R(\delta) \leqslant 1-2\delta \qquad 0 \leqslant \delta \leqslant \frac{1}{2}$$

$$= 0 \qquad \delta \geqslant \frac{1}{2}$$

we find that (let $x = \sqrt{1-2\delta}$)

$$\limsup_{n\to\infty} \frac{Q_n}{n} \leqslant \sup_{0\leqslant x\leqslant 1} (x^2 + x^3) = 2 \tag{27}$$

Finally we make a small correction in Eq. (27). The rate of a code, $R = (1/n)\log M$, is usually defined for base 2 logarithms, and so our bound in Eq. (27) is a bound using base 2. Recalling that our assertions in Eq. (20) are base e, we must replace $2 = \log_2 (4)$ with $\log_e (4) = 1.386$. Hence we have, finally, one-half of Eq. (20), viz,

$$\limsup_{n\to\infty} \frac{Q_n}{n} \leqslant 1.386$$

It remains to prove the lower bound of Eq. (20). To do this we consider the class of *constant weight* codes. A code $C = \{x_1, x_2, \ldots, x_M\}$ is said to be a constant weight code of weight w if all code words have weight w. For such a code the formula for Q simplifies:

$$Q = \frac{\log M}{w} \cdot d_a \tag{28}$$

Or since we know that $d_a \geqslant d_H/2$,

$$Q \geqslant \frac{\log M}{2w} d_H \tag{29}$$

Now according to the Gilbert bound for constant weight codes for any δ and α satisfying

$$0 \leqslant \delta \leqslant \frac{1}{2}$$

$$\frac{1-\sqrt{1-2\delta}}{2} \leqslant \alpha \leqslant \frac{1}{2}$$

there exists a sequence of constant weight codes with (length, minimum Hamming distance, weight) $= (n, d_n, w_n)$ such that $d_n/n \to \delta$, $w_n/n \to \alpha$ and with rates at least $R(\delta, \alpha) = H(\alpha) - 2H(\delta/2\alpha) - (1-\alpha)H[\delta/2(1-\alpha)]$, where $H_2(x) = -x \log x - (1-x) \log (1-x)$ is the entropy function. Using this result, we see from Eq. (29) that

$$\liminf_{n\to\infty} \frac{Q_n}{n} \geqslant \frac{R(\delta, \alpha)}{\alpha} \cdot \frac{\delta}{2} \tag{30}$$

for all choices of α and δ. The maximum of the function on the right side of Eq. (30) can be found numerically. It is 0.052, and occurs at $\delta = 0.06$, $\alpha = 0.264$. Hence

$$\liminf_{n\to\infty} \frac{Q_n}{n} \geqslant 0.052$$

as asserted in Eq. (20).

Of course the bounds in Eq. (20) are very far apart and it would be desirable to improve them. One obvious weakness in our technique is that we nowhere deal directly with the asymmetric distance d_a, but use instead the weak bounds $d_H/2 \leqslant d_a \leqslant d_H$. It would be highly desirable to develop techniques for constructing and analyzing codes with good asymmetric distance properties, for both theoretical and practical reasons.

References

1. Pierce, J. R., "Optical Channels: Practical Limits With Photon Counting," *IEEE Trans. Comm.*, COM-26 (1978), in press.
2. Peterson, W. W., *Error-Correcting Codes*, MIT Press, 1961, Appendix A.

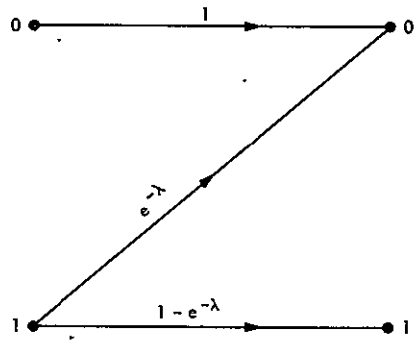

Fig. 1. The Z-channel

Initial Economic and Operations Data Base for DSS 13 Automation Test

D. S. Remer
Communications Systems Research Section
and Harvey Mudd College

G. Lorden
California Institute of Technology

This article summarizes the data base collected for nine weeks of recent operation at DSS 11. Life cycle cost (LCC) parameters on efficiency and productivity ratios, costs, and telemetry were calculated from this data base. The data base and LCC parameters will be used as part of the economic and performance evaluation of the operations demonstration of running DSS 13 unattended and remotely controlled from JPL. The results will enable a comparison to be made between the remote operation of telemetry at DSS 13 with the cost and performance of a comparable manned operation at DSS 11.

I. Introduction

Over the last decade, there has been a gradual increase in automation of the DSN to reduce manpower and to improve network productivity. For example, the crew size at DSS 12 has been reduced by 80 percent since 1967. The next major step is to completely automate a station so that no operators are required. Such an experiment is now underway at DSS 13. This automated station is being run unattended and remotely controlled from JPL in Pasadena. This automation demonstration has three objectives:

(1) To see if an unattended operation can be accomplished.

(2) To collect operations data so an evaluation of unattended operation can be performed.

(3) To provide a single point, remote, unattended control of DSS 13 to accomplish Voyager spacecraft telemetry reception and transmission to the Network Operations Control Center (NOCC) via DSS 12 during DSS 12 downtime for S/X upgrade from a 26-meter to a 34-meter antenna.

A previous article (Ref. 1) was concerned with the second objective, namely, what data do we collect, how do we analyze the data, and what can and cannot be learned from this automation demonstration test? In that article, the goals of the test were outlined and LCC parameters were developed for comparing the unattended remote operation of telemetry at DSS 13 with the operation of a typical DSN manned station, namely DSS 11. It is hoped that this comparison will give valuable insight into the advantages and disadvantages of automated remote operation compared to our present method of manned operation throughout the network.

In this article we will present preliminary data collected at DSS 11 over a nine-week period. Also, we will describe the life cycle cost parameters computed from this data base.

II. DSS 11 Data Base

During the nine-week period of May 14, 1978, to July 9, 1978, a preliminary data base was collected on the operation of DSS 11. This data base serves two purposes. First, it allows

us to check the data base requirements outlined in a previous paper (Ref. 1) and make necessary adjustments. Second, it serves as a bench mark to compare future data from both DSS 11 and DSS 13 during the actual automation demonstration. Data base requirements for this test period were scaled down because no additional station data could be collected at DSS 11 over and above what is normally collected at the station as a result of the contractor turnover and the resulting shortage of operations manpower.

A summary of the data collected is shown in Tables 1 through 3. The life cycle cost parameters calculated from this data base are summarized in Table 4. The definitions of these LCC parameters are also given in Table 4. For a more detailed development of these LCC factors, see Ref. 1.

III. Discussion of Results

A. Efficiency and Productivity Ratios

The first two LCC parameters are efficiency and productivity ratios. These ratios are concerned with comparing end user hours to station operating hours and M&O manhours as shown below:-

$$\text{Efficiency ratio} = \frac{\text{EUH/unit time}}{\text{SOH/unit time}}$$

where

SOH = station operating hours: those hours when a station is required to be available to conduct DSN activities. (SOH are usually 40, 80, 120, 160, or 168 hours per week).

EUH = end user hours: those station operating hours where data, test, or training information is obtained for the end user.

$$\text{Productivity ratio} = \frac{\text{EUH/unit time}}{\text{M\&O MH/unit time}}$$

where

M&O MH = the manhours spent on operations, corrective and preventive maintenance, and training.

Most of the data were collected in weekly increments so the "unit time" is a week for this data base.

The station operating hours (SOH) were usually 160 hours per week, while the end user hours (EUH) varied from a low of 96.7 to a high of 109.4 hours per week. The allocation of EUH and SOH for the entire period is summarized in Tables 2 and 3. Note that personnel training accounted for 8 percent of SOH. This will probably be greatly reduced with automation. The total M&O manhours varied a lot more from week to week than the SOH and EUH. For example, the EUH and weekly manhours for operations, training, corrective maintenance, and preventive maintenance are shown below.

	Mean	Standard deviation	Coefficient of variation
End user hours	102.8	4.6	4.5%
Operation manhours	326.8	36.9	11.3%
Training manhours	130.7	52.1	39.9%
Corrective maintenance manhours	153.5	65.6	42.7%
Preventive maintenance manhours	56.4	35.1	62.2%

From the above table, we see that the coefficient of variation, which is the standard deviation as a percent of the mean, increases from 4.5 percent for end user hours to 62.2 percent for preventive maintenance. Also note that preventive maintenance is a lot more variable than corrective maintenance manhours, and maintenance manhours are a lot more variable than operations. A summary of the productivity and efficiency ratios is shown in Table 4.

Another interesting observation is that there are about twice as many manhours for operations (including training) as for maintenance. Though automation has a dramatic effect on reducing operations manhours, its effect upon maintenance manhours is not clear. There is the potential for designing automated systems to improve isolation and diagnosis of failures. On the other hand, there is the need to maintain the additional equipment required for automation. We hope to gain some insight into maintenance requirements of automation equipment from the DSS-13 demonstration.

B. Cost Parameters

Now that we have looked at manhours, let's consider costs. We will examine two costs: end user hourly M&O cost and station hourly M&O cost. In our calculations, we used current hourly labor costs that include contractor and JPL burden.

The following LCC parameters were calculated in order to compare the maintenance and operations costs at a station per end user hour. There is a separate parameter for operations and another for maintenance, because we expect that unattended operation will reduce operating manpower costs but

may increase maintenance costs as a result of the additional equipment required. We also divided maintenance costs into preventive and corrective. The following definition was used to calculate end user hourly M&O cost.

$$\text{End user hourly M\&O cost} = \frac{\text{M\&O cost \$/unit time}}{\text{EUH/unit time}}$$

The M&O cost is made up of four components:

(1) Corrective maintenance

(2) Preventive maintenance

(3) Operations

(4) Training

For each of these components an hourly cost was calculated by using the following four equations. Only manpower costs are included in this M&O analysis.

$$\text{End user hourly corrective maintenance cost} = \frac{\text{Corrective maintenance cost \$/unit time}}{\text{EUH/unit time}}$$

$$\text{End user hourly preventive maintenance cost} = \frac{\text{Preventive maintenance cost \$/unit time}}{\text{EUH/unit time}}$$

$$\text{End user hourly operations cost} = \frac{\text{Operations cost \$/unit time}}{\text{EUH/unit time}}$$

$$\text{End user hourly training cost} = \frac{\text{Training cost \$/unit time}}{\text{EUH/unit time}}$$

In addition to end user hourly costs, another key index is station hourly costs. The following equation was used to calculate station hourly M&O costs:

$$\text{Station hourly M\&O cost} = \frac{\text{M\&O cost \$/unit time}}{\text{SOH/unit time}}$$

Similar to end user M&O costs, station hourly M&O costs are made up of the same four components: (1) corrective maintenance, (2) preventive maintenance, (3) operations, and (4) training. These components were calculated by simply using the previous four equations for end user hourly costs and replacing EUH with SOH. The average values obtained for the end user hourly cost and the station hourly cost are summarized below for DSS 11 during the nine-week test.

	Average end user hourly cost, \$/EUH	Average station hourly cost, \$/SOH
Corrective maintenance	20.07	12.86
Preventive maintenance	7.38	4.73
Operations manpower	41.81	26.77
Training	16.86	10.68
Total	86.12	55.04

C. Tracking

The number of tracks per week at DSS 11 during this nine-week test varied between 11 and 14. The data lost per week varied from a low of 61 to a high of 185 min, with an average loss of 86 min per week or 7 min per track.

Telemetry data averaged about 85 hours per week, and the lost data of 1.4 hours per week represents about 1.7 percent of the data. This is a conservative number for data lost because it only accounts for lost data when the TPA is out of lock. Additional losses such as between Goldstone and NOCC via the high-speed data line are not included in the above data.

IV. Summary

The data in this article is a preliminary data base collected at DSS 11 during the nine-week period from May 14, 1978, to July 9, 1978. The purpose of this preliminary data base was twofold. First, to initiate a data collection system that will be required to analyze the upcoming DSS 13 unattended operations demonstration, and second, to provide a data base that will serve as a bench mark for comparing the future data collected at DSS 11 and DSS 13 during the automation demonstration.

The results from this preliminary data show that end user hours per week were relatively constant at 102.8, with a coefficient of variation of only 4.5 percent. However, corrective and maintenance manhours varied considerably, with a coefficient of variation of 42.7 and 62.2 percent respectively. Also, there were about two operations manhours for each maintenance manhour. We would expect that for the automated station, the operator manhours would approach zero.

The average operations and maintenance manpower in dollars per end user hour was 88.12 and per station operating hour was 55.04 during the nine-week test at DSS 11.

NASA-CR-158154

The telemetry data lost averaged 7 min per track or about 1.7 percent of the data.

V. Future Work

A. DSS 13 Data Base

Data will be collected at DSS 13 and NOCC during the unattended operations demonstration. This data will be similar to the data collected during this initial test period at DSS 11. In addition, more detailed data by subsystem will be collected at DSS 13 for preventive and corrective maintenance. The subsystems at DSS 13 that may require maintenance were summarized by E. Jackson and are shown in Table 5. The DSS 13 subsystems required for automation that would not be found at a typical DSN station are shown with an asterisk in Table 5. The data from this table will allow us to compare maintenance required for items at a regular station to the additional items needed for an automated station.

B. DSS 11 and DSS 13 Data Bases

Data will continue to be collected at DSS 11. Throughout the DSS 13 unattended operations demonstrations, comparable data will also be collected at DSS 13. This will probably mean continuing data collection throughout the rest of calendar year 1978.

C. Comparison of DSS 13 to DSS 11

We will compare the life cycle cost parameters for a conventional DSN station, DSS 11, to an automated DSN station, DSS 13. We will analyze the efficiency and productivity, the end user hourly costs and station hourly costs, and the amount of tracking and data lost for the conventional and automated stations. In addition to these quantitative goals, we will also document qualitative advantages or disadvantages for operating in remote, unattended mode. We also plan to list any trouble areas that may require design or operating changes or that may provide inputs to a future automated station design.

Acknowledgement

We wish to thank Earl Jackson for supplying the DSS 11 data and providing insight into station operation.

Reference

1. Remer, D. S., Eisenberger, I., and Lorden, G., "Economic Evaluation of DSS 13 Unattended Operations Demonstration," PR 42-45, Jet Propulsion Laboratory, Pasadena, Calif., pp. 165-171.

Table 1. DSS 11 data base

Parameter	Week ending dates, 1978								
	05/14	05/21	05/28	06/04	06/11	06/18	06/25	07/02	07/09
Station operating hours	160	168	160	160	160	160	160	160	160
End user hours	109.4	97.6	96.7	105.7	103.6	102.1	101.7	99.1	109
Tracking hours	78.8	89.8	75.9	96.3	85.6	81.1	79.4	89.4	85.4
Operation manhours	386.8	283.6	294.2	344	354.3	295.7	330.7	292	360.1
Data lost hours	2.47	2.81	0.39	0.93	1.42	1.02	1:20	1.40	1.03
Number of tracks	12	13	14	14	11	12	11	10	12
Preventive maintenance manhours	18.7	55.1	93.05	34.5	112.1	64.4	86.4	14.1	29.4
Corrective maintenance manhours	70.5	55.25	82.33	202.45	219.1	211.5	183.75	159.7	196.5
Training manhours	54.5	171.3	79.9	106.7	74.5	156.7	179.5	194.8	158

Table 2. DSS 11 end user hour allocation

Week ending May 14, 1978, through week ending July 9, 1978	
Spacecraft tracking	91.8%
Project related support	4.0
Radio science	2.2
DSN project preparation	1.6
DSN engineering	0.4
	100.0

Table 3. DSS 11 station operating hour allocation

Week ending May 14, 1978, through week ending July 9, 1978	
Spacecraft tracking	69.3%
Preventive maintenance	14.4
Personnel training	8.4
DSN engineering	3.8
Radio science	1.5
DSN project preparation	1.1
Corrective maintenance	0.9
Project related support	0.6
	100.0

Table 4. DSS 11 life cycle cost parameters

Parameter	05/14	05/21	05/28	06/04	06/11	06/18	06/25	07/02	07/09
Efficiency ratio = $\frac{\text{EUH}}{\text{SOH}}$	0.684	0.581	0.604	0.661	0.648	0.638	0.636	0.619	0.681
M&O EUH productivity = $\frac{\text{M\&O MH}}{\text{EUH}}$	4.85	5.79	5.68	6.51	7.34	7.13	7.67	6.67	6.83
M&O SOH productivity = $\frac{\text{M\&O MH}}{\text{SOH}}$	3.32	3.36	3.43	4.30	4.75	4.55	4.88	4.13	4.65
End user hourly M&O cost = $\frac{\text{M\&O cost}}{\text{EUH}}$	64.08	76.57	75.55	86.28	97.48	94.68	101.76	88.27	90.45
End user hourly OC = $\frac{\text{OC}}{\text{EUH}}$	46.56	38.27	40.30	42.86	45.04	38.14	42.82	38.81	43.51
End user hourly MC = $\frac{\text{MC}}{\text{EUH}}$	10.96	15.19	24.37	30.13	42.97	36.32	35.70	23.57	27.85
End user hourly TC = $\frac{\text{TC}}{\text{EUH}}$	6.56	23.11	10.88	13.29	9.47	20.22	23.24	25.89	19.09
Station hourly M&O cost = $\frac{\text{M\&O cost}}{\text{SOH}}$	43.78	44.48	45.53	57.0	63.11	60.42	64.69	54.68	61.63
Station hourly OC = $\frac{\text{OC}}{\text{SOH/week}}$	31.80	22.23	24.22	28.31	29.16	24.34	27.22	24.04	29.64
Station hourly MC = $\frac{\text{MC\$/week}}{\text{SOH/week}}$	7.49	8.83	14.73	19.91	27.82	23.18	22.69	14.60	18.98
Station hourly TC = $\frac{\text{TC\$/week}}{\text{SOH/week}}$	4.49	13.42	6.58	8.78	6.13	12.90	14.78	16.04	13.01
Manpower ratio 1 = $\frac{\text{Operations MH}}{\text{Maintenance MH}}$	4.95	4.12	2.13	1.90	1.29	1.64	1.89	2.80	2.29
Manpower ratio 2 = $\frac{\text{Operations MH}}{\text{Operations MH and Maintenance MH}}$	0.832	0.805	0.681	0.655	0.564	0.621	0.654	0.737	0.696
Lost data ratio = $\frac{\text{Lost data}}{\text{Good telemetry data}}$	0.031	0.031	0.005	0.010	0.017	0.013	0.015	0.016	0.012
Tracking productivity = $\frac{\text{Operations MH}}{\text{Tracking hours}}$	5.60	5.07	4.93	4.68	5.01	5.55	6.43	5.45	6.07
Operations SOH productivity = $\frac{\text{Operations MH}}{\text{SOH}}$	2.76	2.71	2.34	2.82	2.68	2.81	3.19	3.04	3.24
Operations EUH productivity = $\frac{\text{Operations MH}}{\text{EUH}}$	4.03	4.66	3.87	4.26	4.14	4.41	5.02	4.91	4.75

Abbreviations

EUH = end user hour
SOH = station operating hour
MH = manhour
M&O = maintenance and operations
OC = operating cost
MC = maintenance cost
TC = training cost

Table 5. DSS 13 Maintenance activities data sheet

Week Ending_____

PREVENTIVE MANHOURS:

26-m Antenna

Hydraulic Systems _____

Electronic Systems _____

*Control Computer (MODCOMP II/25) _____

*Clock _____

*Terminetr _____

*Microprocessor _____

Waveguide Configuration Assembly _____

Low Noise Amplifier (Maser)

Maser Compressor _____

Refrigerator _____

Block III Receiver _____

Block III SDA _____

*108 KHz Subcarrier Oscillator (Microwave Link Transmission) _____

*Station Controller (8080 based microcomputer) _____

Star Switch & Controller _____

*SDA Controller _____ *Block III Receiver Controller _____

*Waveguide Configuration Assembly Controller _____

High Speed Data Line

Data Set _____ Microwave Line Channel _____

CORRECTIVE MANHOURS:

26-m Antenna

Hydraulic Systems _____

Electronic Systems _____

*Control Computer (MODCOMP II/25) _____

*Clock _____

*Terminetr _____

*Microprocessor _____

Waveguide Configuration Assembly _____

Low Noise Amplifier (Maser)

Maser Compressor _____

Refrigerator _____

Block III Receiver _____

Block III SDA _____

*108 KHz Subcarrier Oscillator (Microwave Link Transmission) _____

*Station Controller (8080 based microcomputer) _____

Star Switch & Controller _____

*SDA Controller _____ *Block III Receiver Controller _____

*Waveguide Configuration Assembly Controller _____

High Speed Data Line

Data Set _____ Microwave Link Channel _____

*Automation Equipment

D/2

N79-19057

LS47: A DSN Station Location Set Compatible With JPL Development Ephemeris DE108

J. Ellis
Navigation Systems Section

An updated DSN station location set, LS47, is presented which is compatible with JPL Development Ephemeris DE108. Analytic procedures for linearly correcting station spin axis and longitude estimates for an ephemeris update based on Brouwer-Clemence Set III parameters are briefly discussed. The validity of this technique is demonstrated by a comparison of a linearly corrected solution with one explicitly determined by reprocessing the data. A mission data base, including Viking 1 and 2 encounter data, is first used to obtain an updated DE96 compatible station location solution, LS46, which in turn is adjusted to form the DE 108 solution, LS47. Improved station Z-heights are estimated by using available very long baseline interferometry (VLBI) data. Spin axis differences between LS46 and LS47 are relatively insignificant; however, the ephemeris change introduces a -0.8×10^{-5} *degree rotation in the DE96 longitude ephemeris.*

I. Introduction

This article presents a set of station location estimates for navigation support for Voyager Jupiter encounter and Pioneer-Venus operations. The new solution, Location Set (LS)47, is compatible with JPL Development Ephemeris DE108 (Ref. 1), which will be used for navigation by these projects. LS47 replaces the DE96 compatible station solution set LS45 (Refs. 2 and 3) which supported Voyager and Pioneer-Venus launch and cruise operations.

Several significant changes have been made in the procedures for updating station spin axis and longitude estimates for an ephemeris change and in the mission set data base and auxiliary source data used to determine station locations. These changes include the following:

(1) Development of analytic techniques for correcting station spin radius and longitude estimates for an ephemeris change.

(2) Addition of Viking 1 and Viking 2 encounter data to the mission set data base.

(3) Treatment of geodetic survey data directly as additional observations.

(4) Use of very long baseline interferometry (VLBI) data to determine Z-heights.

A comprehensive software system and supporting data base have been designed and implemented for generating station location estimates and analytically correcting station spin radii and longitudes for an ephemeris update. The major advantage of this approach is that it eliminates the need to repeat the orbit determination process when an ephemeris is replaced. This system combined with the data base is expected to form the foundation for future station location efforts. As such, LS47 is the first set to be generated based on this new system. A brief discussion of the computational techniques is presented in this article. Details of the procedure and software implementation will be discussed in a future article.

Considerable effort has been expended in developing and validating these procedures. As a preliminary step, a DE96 compatible station location set LS46 was computed to evaluate the effect of changes in the mission set data base and the software. Solution sets for LS45 and LS46 were compared to determine the effect of the above changes. Finally, station solutions LS47 and LS46 were compared to determine the effect of the ephemeris change.

II. Computational Procedures for Station Location Determination

A. Correcting for an Ephemeris Update

DSN station locations are computed in a geocentric reference frame defined by the Earth's mean pole (axis of rotation), equator and prime meridian of 1903.0. The location of the station with respect to this frame is expressed in cylindrical coordinates r_s, λ and Z_s, where

r_s = "distance from" the axis of rotation (spin axis)

λ = longitude as measured east from the prime meridian

Z_s = height above equator plane (Z-height)

The conventional procedure for estimating the coordinates of the tracking station is based on using a data base consisting of radio metric tracking data from a set of planetary encounter missions to provide an accurate determination of the planet-relative spacecraft state. This knowledge combined with the planetary direction information inherent in the planetary ephemeris is used to determine a least squares solution for the station spin axis and longitude. Historically, updating a DSN station location set to account for an ephemeris change has required reprocessing the radio metric data for all missions in the data base. A complete refit of the radio metric data for each mission is repeated using the Double Precision Orbit Determination Program (DPODP). This requires iterating to convergence for a new trajectory which best fits the data using the new planetary ephemeris.

The useful results of each such data fit can be compactly represented in terms of a triangularized information array, referred to as the data equation; i.e.,

$$Z = Rx + \eta \tag{1}$$

where

x = the parameters to be estimated

R = the "packed" information matrix

η = the measurement error

Z = the "packed" data residuals

The conventional procedure is to statistically combine the information arrays for all missions in the data base and to estimate the spin axis and longitude from the combined information matrix.

The basic disadvantage of this approach is that it requires lengthy and costly DPODP runs to obtain each information array compatible with an updated ephemeris. A way of avoiding this is to recognize that a small ephemeris change can be expressed as a linear perturbation to the nominal data residuals. The perturbation due to the ephemeris change can in turn be *approximated* in terms of the partials of the observations with respect to the appropriate Brouwer and Clemence Set III parameters (Ref. 4) and the planetary mass, and the actual Set III and mass correction, from the "nominal" ephemeris; i.e.,

$$Z_{new} = Z + \frac{\delta Z}{\delta E}\Delta E + \frac{\delta Z}{\delta m}\Delta m \tag{2}$$

where E are the Brouwer and Clemence Set III parameters for the target body and the Earth, m is the planetary mass of the target body, and Z_{new}, Z are the data residuals.

Corrections ΔE, in turn, are approximated by transforming the differences of the cartesian positions and velocities of the target body and the Earth-Moon barycenter at the mission encounter time to Set III corrections defined at the osculating epoch of the ephemeris. Mass differences are simply determined by reading the new and nominal ephemerides files.

This technique had been suggested in a memo by H. Koble (Ref. 5); however, its accuracy had never been verified. For purposes of testing the procedure, DE96 station location estimates obtained from DPODP runs were compared with an equivalent DE84 data base which had been linearly corrected to DE96. Solutions were determined for each individual mission as well as for the combined data set. The maximum differences observed in the station spin radius and longitude estimates were 0.02 meters and 0.03×10^{-5} degrees respectively, which are significantly below our estimation accuracies of 0.6m and 2.0×10^{-5} deg.

In practice a "nominal" mission data base has been established which is based on the DE96 ephemeris and the LS43 station set. Information arrays for all missions have been standardized to DE96. This data base will form the data set for the current and future station location efforts and will be expanded to include new data when available.

B. Geodetic Survey Information

A second major difference in the computational procedures is the manner in which geodetic survey information is treated.

The final station location estimates are determined by adjoining the geodetic survey information (Ref. 6) to the combined information array for the individual missions. For the LS45 determination the relative survey information was treated as an a priori covariance constraint (Ref. 5). For stations related by survey information, the correlation coefficient of the spin radius and longitude a priori covariance were computed to reflect the survey accuracy of 0.3m and 0.3×10^{-5} deg.

The above procedure suffers from the deficiency that it assumes the a priori values of the station location estimates satisfy the relative coordinate difference specified by the geodetic survey measurements. For LS46 and LS47, geodetic survey measurements were included directly as additional observations, with accuracies of a 0.3 m for spin radius and 0.3×10^{-5} deg for longitude. This approach has the further advantage that it can be expanded to include other relative data types, such as VLBI data.

C. Station Z-height Determination

Since station Z-heights cannot be determined from conventional radio metric data, it is necessary to rely on other data sources to compute Z-heights. The LS45 Z-heights were computed by combining the results of geodetic surveys (Ref. 6) made at the various sites with the geocentric-geodetic differences obtained from optical and laser data (Ref. 7). The availability of preliminary VLBI results (Ref. 8) provides us with an additional source for determining intercontinental relative Z-heights. The strategy adopted for computing Z-heights for LS47 consisted of the following:

(1) The absolute Z-height for DSS 14 was computed by correcting the geodetic survey value for the datum correction.

(2) The Z-heights of DSS 43 and DSS 63 were then determined from the VLBI intercontinental baseline observations for the polar component (i.e., relative 14-63, 14-43 Z-height differences).

(3) The relative geodetic survey data was then used to compute Z-heights for the remaining stations (DSS 11, 12, 13, 42, 44, 61, 62) within each complex.

(4) Since no VLBI data was available for DSS 41 and DSS 51, the LS45 Z-height values were retained for these stations.

Tables 1 and 2 summarize the geodetic and VLBI data that were used. This procedure is equivalent to replacing the laser and optically determined Z-heights offsets, which have a one-sigma accuracy of 5 meters, with equivalent VLBI information which has a reported accuracy of 1.2 meters. The maximum difference between the LS47 and LS45 Z-heights is 4.7 m, which is consistent with the quoted accuracy of the LS45 set of 15m.

III. Location Set 47

A. Mission Data Base

LS47 spin radius and longitude estimates are based on a mission data set which includes the original LS45 data base supplemented with the Viking 1 and Viking 2 encounter data (Ref. 9). The complete data set is summarized in Table 3. The LS45 data base includes the planetary encounter data arcs for Mariners 4, 5, 6, 9, 10-Venus and 10-Mercury (first encounter) as well as zero declination data arcs for Mariner 5 pre- and post-encounter. Each mission data set uses the best BIH timing and polar motion data and calibrations for troposphere, ionosphere and space plasma. Only radio metric data calibrated for charged particle effects are included in the final Viking data set.

For consistency, the parameter solution sets for the Mariner 10 encounters were modified relative to those used for LS45 analysis. The planet mass and oblateness were eliminated from the estimated parameter set. For the Venus encounter arc a 9-parameter solar pressure model was added, so that the complete set of estimated parameters included the spacecraft state, solar pressure and the station locations. The final solution set for the Mariner 10 Mercury encounter includes the spacecraft state, solar pressure, range bias and station locations. Parameter sets for the remaining missions were identical to the sets which produced the LS45 results (Refs. 2 and 3).

B. DE96 Compatible Solution, LS46

As a preliminary step in deriving LS47, a DE96 compatible solution set, designated LS46, was initially generated to evaluate the effects of the various data base changes on the station solutions. LS46 represents an "updated" LS45 solution which includes the additional Viking encounter data, the effect of parameter set modifications, changes in the computational procedure and the application of VLBI data. Both solutions are documented in Tables 4 and 5, with differences and the effect of the Viking data summarized in Table 6. The maximum spin radius and longitude differences between LS45 and LS46 are 0.1 m and 0.33×10^{-5} deg, respectively. Use of the VLBI data introduces a Z-height change of -4.7 m for DSS 42, 43 and 44, and a change of +4.1 m for DSS 61, 62 and 63. In summarizing, it appears that the addition of the Viking data as well as the other changes has a small effect on the combined spin axis and longitude solution. The new results are within the 0.6 m spin axis and 2.0×10^{-5} deg longitude accuracies quoted for LS45 (Refs. 2 and 5).

C. DE108 Compatible Solution, LS47

The LS47 solution, presented in Table 7, is the result of linearly correcting the LS46 spin axis and longitudes to account for differences in the DE108 and 96 ephemerides. The resulting differences between the LS47 and LS46 solutions are listed in Table 8. While spin axis differences are statistically insignificant, DE108 longitudes are rotated approximately 0.8×10^{-5} deg west relative to the DE96 values.

The change in station location due to an ephemeris update can be approximated from the differences in the geocentric right ascensions and declinations of the target body at encounter time. The relationship is given by

$$\Delta r_s = r_s \Delta\delta \tan\delta$$

$$\Delta\lambda = \Delta\alpha$$

where

r_s = the station spin radius

λ = the station longitude

δ = the target body declination

α = the target body right ascension

Figure 1 plots the differences in DE108 and DE96 right ascensions at the encounter times. There is a clear secular trend of -0.15×10^{-5} deg/year for the right ascension differences between DE108 and DE96, which translates into longitude corrections that range from 0.27×10^{-5} deg for Mariner 4 to -1.08×10^{-5} deg for Viking B. The -0.8×10^{-5} change for the combined set represents a weighted average of the DE108-DE96 right ascension changes. The maximum predicted spin axis change is approximately 0.12 m.

The effect of the secular trend in right ascension on the LS47 solution can be observed by plotting the difference between the individual data arc solutions for each mission and the combined solutions. These differences are plotted for LS46 and LS47 in Figs. 2 through 5. Each difference is plotted along with its formal standard deviation as a vertical bar, with the length of the bar determined by the formal standard deviation of each solution and the expected difference represented by a horizontal line. A comparison of these plots for LS46 and LS47 reveals that the spin radius differences are approximately the same, whereas the longitude differences appear to be rotated. The LS47 longitude scatter is the result of a rotation of the abscissa of the LS46 scatter about a center approximated by the Mariner 10 encounter time, with the resulting slope of 0.15×10^{-5} deg. This result is predictable from a weighted least squares analysis of the effect of a rotation of the longitudes from DE96 to DE108.

An examination of the individual mission error plots for LS46 and LS47, as well as similar figures for LS44 (Refs. 2 and 9), reveals several disturbing anomalies which have not been satisfactorily explained. Basically, the plots for LS46 and LS44 are similar, as expected. The inconsistencies in the individual solutions for the "earlier" missions, Mariners 4, 5, and 6, may largely be due to the procedures for reconstructing ad hoc calibrations. For the more recent missions, Mariner 10 Mercury solutions for DSS 12 and 42 appear to be inconsistent, while the Viking solutions exhibit a disturbing inconsistency in the spin axis solution for DSS 11.

D. DSS 12 Conversion to 34-Meter Antenna

DSS 12 has recently been converted from a 26- to a 34-m antenna. This conversion entailed a 10-ft vertical displacement of the antenna with respect to the local gravity vector. The tolerance of this vertical displacement is 1/10,000 of a foot. Since an updated survey was not available, spin axis and Z-height coordinates for DSS 12 were computed by transforming the 10-ft vertical displacement to geodetic spin axis and Z-height components. Table 7 lists the coordinates for DSS 12 before and after the conversion.

E. Station Location Estimates for DSS 13 and 14

Radio metric data was not available in the current mission set data base for DSS 13 and 44. As a result, the coordinates for the nonparticipating stations were based strictly on relative geodetic survey information. DSS 13 coordinates were computed from relative survey differences between DSS 12 and 13. Relative survey differences between DSS 42 and 44 were used to compute the DSS 44 locations.

IV. Summary and Future Directions

An analytic procedure has been developed for linearly correcting station location estimates for an ephemeris update. The validity of the procedure has been demonstrated and the technique has been applied to computing a station location set LS47 compatible with ephemeris DE108. Spin axis differences between LS45, LS46, and LS47 are relatively insignificant. However, the ephemeris change introduces a -0.8×10^{-5} deg rotation in the DE96 longitude estimates.

Based on a series of parametric studies (Refs. 2 and 5) it was concluded that the maximum 1-sigma errors for LS45 spin axis and longitudes were bounded by 0.6 m and 2.0×10^{-5} deg, respectively, relative to DE96. These error bounds were applicable to stations for which radio metric data was available. The same level of confidence can be established for the LS46 solution, which agrees with LS45 to within 0.1 m in spin radius and 0.33×10^{-5} deg in longitude. Since the same data base, calibrations and basic procedures were used for LS46 and

LS47, the accuracy of the LS47 set can be expected to be comparable *relative to DE108*.

Several areas are currently being explored in an attempt to improve the LS47 station estimates and to confirm the quoted accuracies. These include the following:

(1) Evaluation of the feasibility of incorporating Viking orbiter and lander data.

(2) Utilization of VLBI data for improving relative spin, radius and longitude estimates.

(3) Evaluation of precession effects on longitude solutions.

(4) Evaluation of updated survey information.

(5) Application of filtering strategies which weight results from recent missions more heavily than results from the earlier missions.

Any adjustments to the LS47 station set based on the above efforts are expected to be available for the final Voyager encounter lockfile.

Acknowledgment

The author wishes to acknowledge the assistance of R. Henderson, G. Pease and J. Gliniak for their contributions in developing and implementing the computer software and performing the computer runs. C. Thornton, H. Koble and N. Mottinger were responsible for the basic computer software, for updating and combining information arrays, and for assistance in analyzing the results.

References

1. Standish, E. M., "DE108 Announcement," IOM 315.5-132, Jet Propulsion Laboratory, Pasadena, Calif., Oct. 6, 1978 (an internal document).

2. Koble, H. M., "LS45 A Station Location Set Compatible with DE96," IOM 314.5-87, Jet Propulsion Laboratory, Pasadena, Calif., May 20, 1977 (an internal document).

3. Koble, H. M., "Recommended Update to DSS 44 Location Estimates," IOM 314.5-100, Jet Propulsion Laboratory, Pasadena, Calif., Oct. 27, 1977 (an internal document).

4. Brouwer, D. and Clemence, G. M., *Methods of Celestial Mechanics*, Academic Press, 1961.

5. Koble, H. M., "LS44 - An Improved Deep Space Network Station Location Set for Viking Navigation," EM 314-60, Jet Propuslion Laboratory, Pasadena, Calif., Aug. 24 1976 (an internal document).

6. *NASA Directory of Observation Station Locations, 3rd Edition*, Goddard Space Flight Center, Vol. 1, Nov. 1973.

7. Marsh, J. G., Douglas, B. C., and Losko, S. M., "A Global Station Coordinate Solution Based Upon Camera and Laser Data – Goddard Space Flight Center 1973," Report X-592-73-177, Goddard Space Flight Center, May 1973.

8. Fanselow, J. L., et al., "Determination of UTI and Polar Motion by the Deep Space Network Using Very Long Baseline Interferometry," IAU Symposium 82, May 1978.

9. Campbell, J. K., and Rinker, G. C., "An Evaluation of Deep Space Network Station Locations from the Viking Encounters," EM 314-107, Jet Propulsion Laboratory, Pasadena, Calif., Jan. 11, 1977 (an internal document).

Table 1. Relative coordinate differences based on geodetic survey information

Station pair	Longitude, deg	Spin axis, km	Z-height, km
11-12[a]	−0.0439311	−5.71166	8.136
13-12[a]	0.0105998	3.43285	−4.672
14-12[a]	−0.084045	−8.05467	11.424
43-42	0.0	−0.10110	0.167
44-42	0.00347689	−11.37076	−16.765
62-61	−0.1188072	−1.79030	2.023
63-61	0.0010142	−0.15712	−0.226

[a]Survey based on DSS 12 before modification to 34-m antenna.

Table 2. VLBI results for intercontinental baseline

Station pair	Polar component, km
63-14	438.0561
32-14	−7351.8023
63-43	7789.8584

Table 3. Summary of radiometric data used in LS46 and LS47

	Tracking arc	Stations	Data types and number of measurements
Mariner IV encounter	7/6/65→7/28/65 (Enc: 7/15/65)	11, 42, 51	Doppler – 899
Mariner V pre-encounter zero declination arc	7/22/67→9/16/67	11, 12, 14 42, 61, 62	Doppler – 986
Mariner V encounter	10/14/67→10/25/67 (Enc: 10/19/67)	12, 14, 41, 62	Doppler – 759
Mariner V post-encounter zero declination arc	10/29/67→11/21/67	12, 14, 41, 62	Doppler – 704
Mariner VI encounter	7/25/69→7/31/69 (Enc: 7/31/69)	12, 14, 41 51, 62	Doppler – 642 Tau range – 322
Mariner IX encounter	11/9/71→11/13/71 (Enc: 11/14/71)	12, 14, 41, 62	Doppler – 798 Mu range – 6
Mariner X Venus encounter	1/28/74→2/14/74 (Enc: 2/5/74)	12, 14, 42 43, 62, 63	Doppler – 4162
Mariner X Mercury I encounter	3/21/74→4/10/74 (Enc: 3/29/74)	12, 14, 42 43, 62, 63	Doppler – 1871 Mu 2 range – 43 Plop range – 68
Viking I encounter	6/10/76→6/19/76 (Enc: 6/19/76)	11, 14, 43, 61, 63	Doppler – 641 Plop range – 43
Viking II encounter	7/28/76→8/7/76 (Enc: 8/7/76)	11, 14, 42, 43, 61	Doppler – 586 Plop range – 43

Table 4. Location set 45

Station	Spin axis, km	Longitude, deg	Z-height, km
11	5206.340046	243.1506103	3673.764
12	5212.051731	243.1945377	3665.628
13	5215.484580	243.2051375	3660.956
14	5203.996994	243.1104930	3677.052
41	5450.203099	136.8875110	−3302.189
42	5205.351556	148.9812947	−3674.588
43	5205.251036	148.9812975	−3674.755
44	5193.980796	148.9778178	−3691.353
51	5742.939395	27.6854493	−2768.744
61	4862.608228	355.7509964	4114.878
62	4860.818049	355.6321890	4116.901
63	4862.451240	355.7520093	4115.104

Table 5. Location set LS46

Station	Spin axis, km	Longitude, deg	Z-height, km
11	5206.339972	243.15061282	3673.764
12	5212.051635	243.19453947	3665.628
13	5212.484485	243.20513927	3660.956
14	5203.996942	243.11049354	3677.052
41	5450.203117	136.88751270	−3302.189
42	5205.351635	148.98129334	−3674.5833
43	5205.251074	148.98129542	−3674.7503
44	5193.980875	148.97781645	−3691.3483
51	5742.939341	27.68544919	−2768.744
61	4862.608297	355.75099792	4114.8821
62	4860.817979	355.63219164	4116.9051
63	4862.451306	355.75200886	4115.1081

Table 6. Analysis of LS46 spin axis and longitude update

Station	LS46/LS45	Effect of Viking data
	Spin radius, m	
11	−0.074	−0.006
12	−0.096	−0.015
14	−0.052	−0.040
41	0.018	0.010
42	0.079	0.060
43	0.038	0.063
51	−0.054	−0.007
61	0.068	0.046
62	−0.070	−0.024
63	0.066	0.019
	Longitude, 10^{-5} deg	
11	0.25	0.100
12	0.18	0.072
14	0.05	0.072
41	0.17	0.069
42	−0.14	−0.041
43	−0.33	−0.133
51	−0.01	−0.029
61	0.15	0.17
62	0.26	0.098
63	−0.04	−0.12

Table 7. Location set LS47

Station	Spin axis, km	Longitude, deg	Z-height, km
11	5206.339943	243.15060463	3673.764
12(34M)	5212.054081	243.19453139	3665.6298
12(26M)	5212.051599	243.19453139	3665.628
13	5215.484840	243.20513119	3660.956
14	5203.996900	243.11048519	3677.052
41	5450.203047	136.88750535	-3302.189
42	5205.351564	148.98128494	-3674.5833
43	5205.250988	148.98128679	-3674.7503
44	5193.980804	148.97780805	-3691.3483
51	5742.939219	27.68544265	-2768.744
61	4862.608263	355.75098948	4114.8821
62	4860.817963	355.63218340	4116.9051
63	4862.451243	355.75200027	4115.1081

Table 8. LS47/LS46 difference

Station	Spin axis, m	Longitude $\times 10^{-5}$ deg
11	-0.029	-0.819
12	-0.036	-0.808
14	-0.043	-0.835
41	-0.070	-0.735
42	-0.071	-0.840
43	-0.086	-0.863
44	-0.071	-0.840
51	-0.121	-0.654
61	-0.033	-0.844
62	-0.017	-0.825
63	-0.063	-0.856

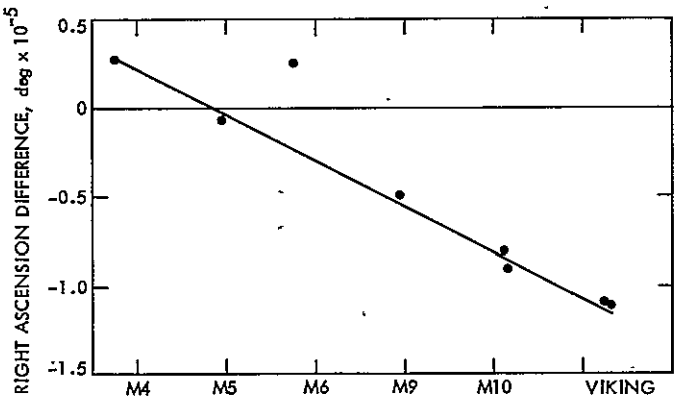

Fig. 1. DE108 and DE96 right ascension differences at planetary encounter

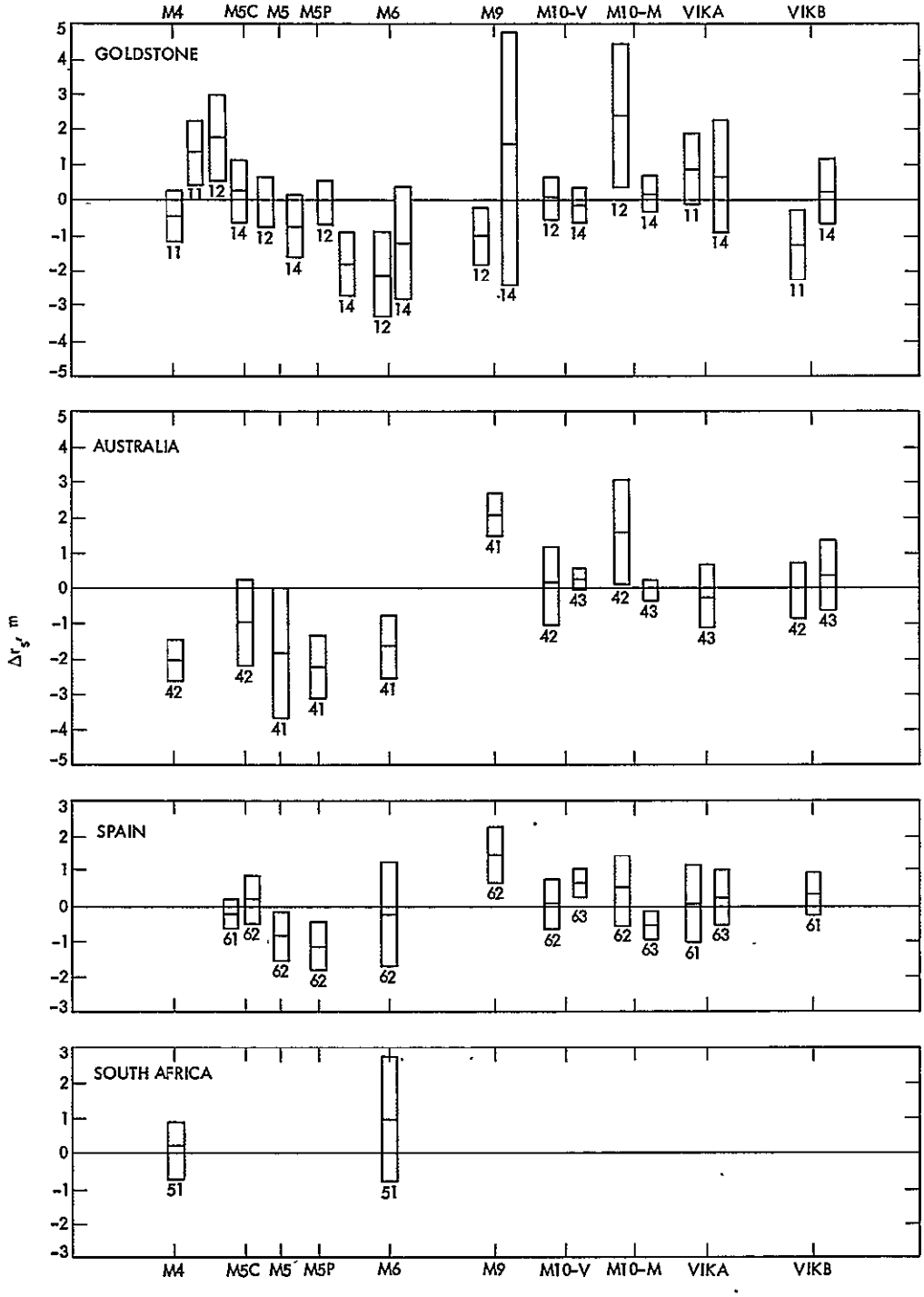

Fig. 2. Difference between individual data arc spin radius estimates and the DE96 solution, LS46

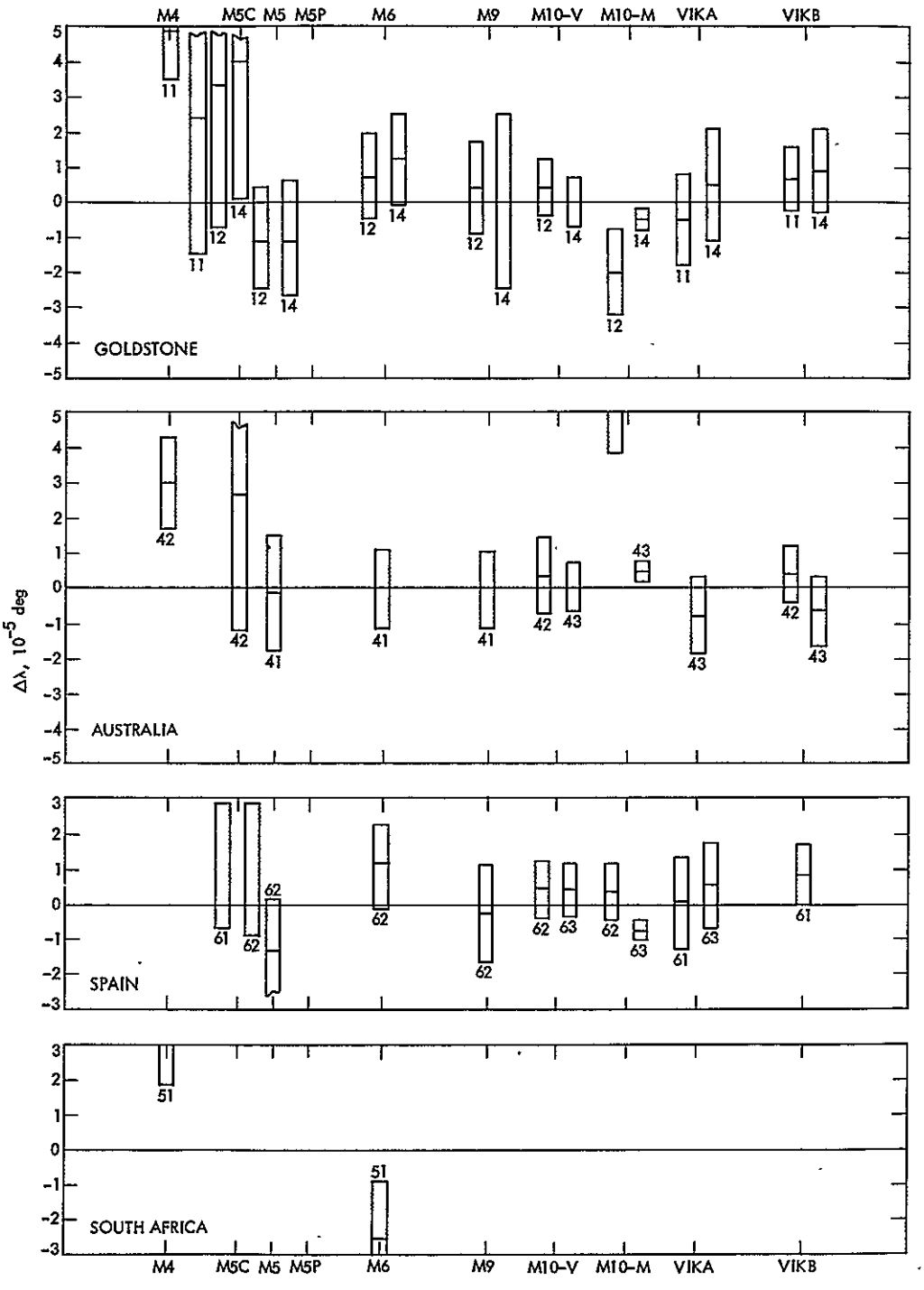

Fig. 3. Difference between individual data longitude estimates and the DE96 solution, LS46

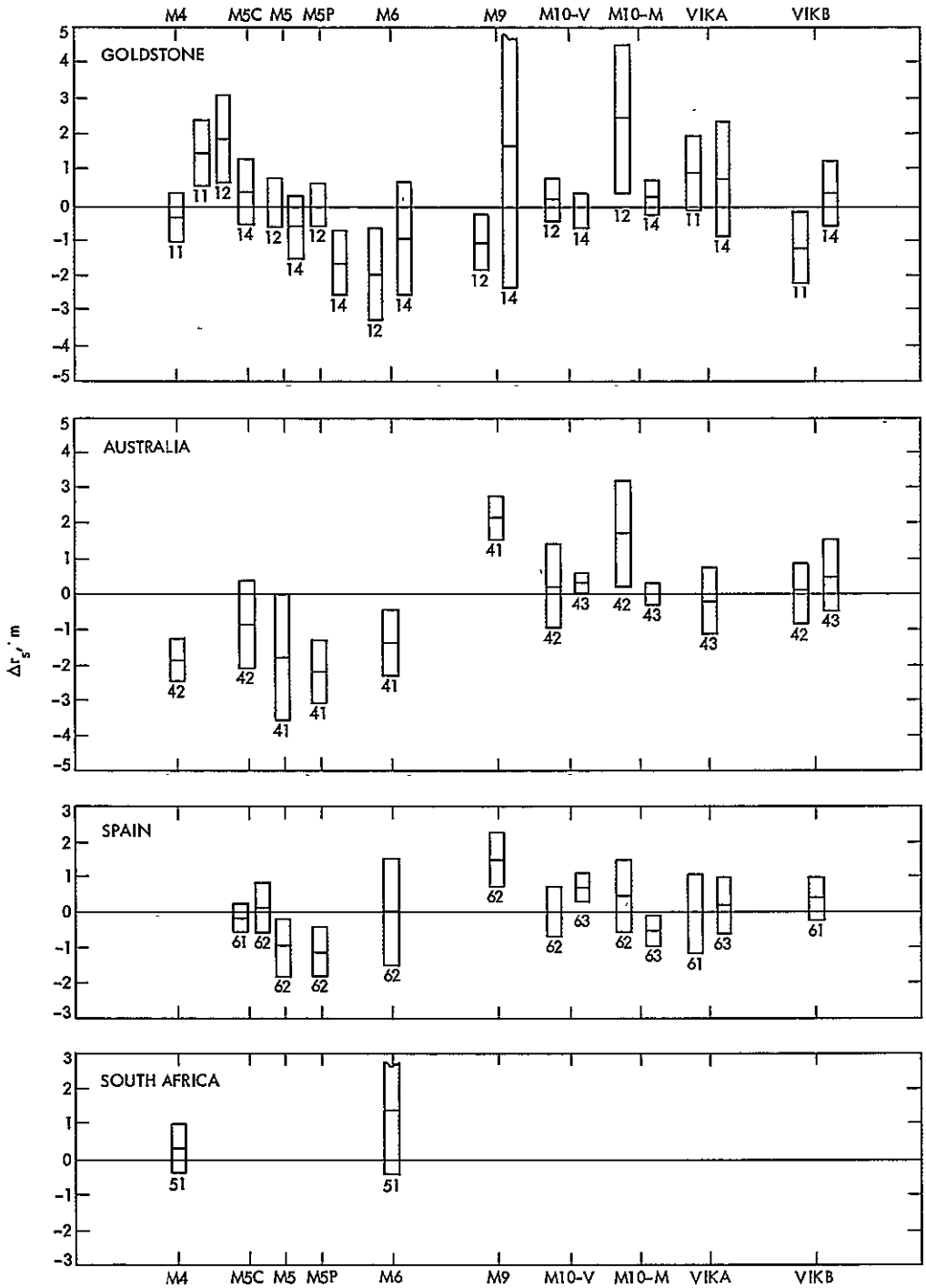

Fig. 4. Difference between individual data arc spin radius estimates and the DE108 solution, LS47

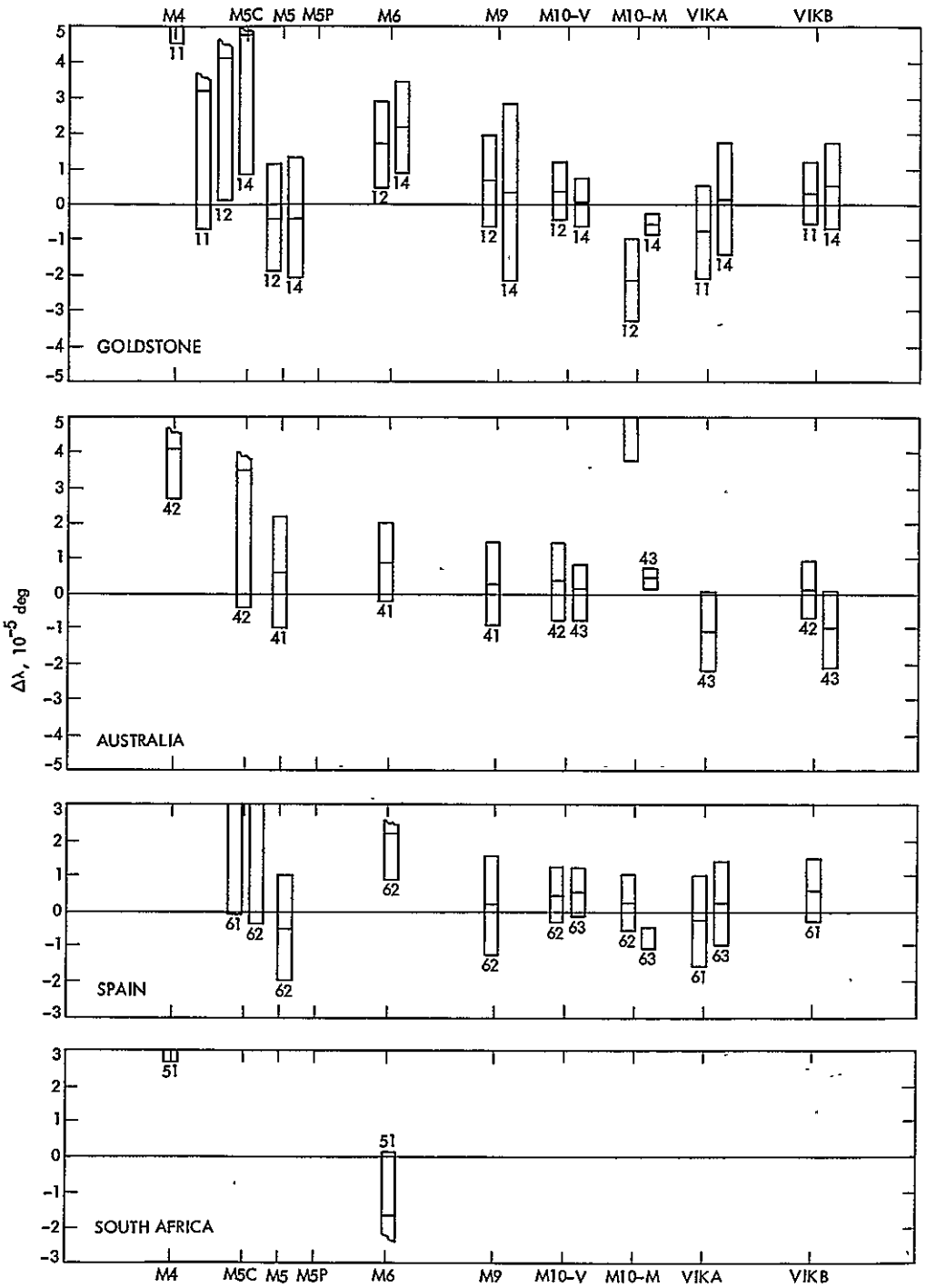

Fig. 5. Difference between individual data arc longitude estimates and the DE108 solution, LS47

D13

N79-19058

Radio Frequency Carrier Arraying for Near Maximum Carrier Signal-to-Noise Ratio Improvement

M. H. Brockman
Telecommunications Science and Engineering Division

Radio frequency arraying of several receiving systems provides signal-to-noise ratio improvement relative to a single receiving system. This report considers radio frequency carrier arraying which provides near maximum signal-to-noise ratio improvement for carrier reception and demodulation.

I. Introduction

An earlier report ("Radio Frequency Carrier Arraying for High Rate Telemetry Reception," Ref. 1) presented a method for obtaining adequate radio frequency carrier signal-to-noise ratio improvement for high-rate telemetry reception by arraying receiving systems or stations. This report considers RF carrier arraying of receiving systems or stations to provide near maximum improvement in carrier signal-to-noise ratio for coherent RF carrier reception and RF carrier demodulation which is applicable to low-rate telemetry with its attendant smaller RF carrier margin. This RF carrier signal-to-noise ratio improvement (achieved by arraying) provides a corresponding improvement in minimum RF carrier level for radio metric tracking (e.g., doppler and ranging) relative to a single receiving system or station.

II. Receiver Configuration

Figure 1 illustrates the method for achieving RF carrier arraying for near maximum carrier signal-to-noise ratio improvement. Two receiving systems are shown to illustrate the concept. However, additional receiving systems can be added to expand the signal-to-noise improvement capability for RF carrier arraying. In addition, each receiving system can be fed from its own antenna. The concept shown in Fig. 1 is similar to that presented for high-rate telemetry reception (Ref. 1), with some additions to the block diagram which will be discussed later in this report. The following discussion of the input signal(s), which was presented in Ref. 1, is included here for clarification. The input signal to N receiving systems or stations is a radio frequency signal ($\cos \omega_{RF}t$) phase-modulated with telemetry and/or a ranging waveform. Consider, as an example, the case for telemetry where the RF carrier is phase-modulated with a square-wave subcarrier ($\mathrm{Los}\ \omega_{sc}t$) at a peak modulation index m_{pD} that is in turn, biphase-modulated with data $D(t)$. Refer to Fig. 1 during the following development. The signal at the input to the low noise amplifier in receiving system 1 is

$$2^{1/2}A_1(t)\cos$$

$$[\omega_{RF}t + \theta_{i1} + D(t+\tau_{i1}) \cdot m_{pD} \cdot \mathrm{Los}\,(\omega_{sc}t + \theta_{sc_{i1}})]$$

$$+ n_{i1}(t) \qquad (1a)$$

For a binary modulation waveform, the carrier component becomes

$$2^{1/2}A_1(t) \cdot \cos m_{pD} \cos(\omega_{RF}t + \theta_{i1})$$

The sideband component becomes

$$+2^{1/2}A_1(t) \sin m_{pD} \cdot D(t+\tau_{i1}) \text{Cos}(\omega_{sc}t + \theta_{sc_{i1}})$$

$$\cdot \sin(\omega_{RF}t + \theta_{i1}) \qquad (1b)$$

and the noise component is $n_{i1}(t)$.

For receiving system 2, the corresponding input signal is

$$2^{1/2}A_2(t) \cdot \cos m_{pD} \cos(\omega_{RF}t + \theta_{i2} + 2^{1/2}A_2(t)$$

$$\cdot \sin m_{pD} \cdot D(t+\tau_{i2}) \cdot \text{Cos}(\omega_{sc}t + \theta_{sc_{i2}})$$

$$\cdot \sin(\omega_{RF}t + \theta_{i2}) + n_{i2}(t)\,. \qquad (2)$$

The other N-2 receiving systems will have corresponding input signals. Since antenna 1 and antenna 2 are separate antennas, physically separated, the phase shift on the RF carrier (θ_{i2}) and square wave subcarrier ($\theta_{sc_{i2}}$) and the group delay on the data (τ_{i2}) in receiving system 2 are different from the corresponding phase shifts and modulation group delay in receiving system 1. In general, the differences in RF carrier phase shift ($\theta_{i2} - \theta_{i1}$), subcarrier phase shift ($\theta_{sc_{i2}} - \theta_{sc_{i1}}$) and modulation group delay ($\tau_{i2} - \tau_{i1}$) will vary with time during a station pass. The above applies in general to all N receiving systems. The terms $n_{i1}(t)$, $n_{i2}(t)$, etc. represent a combination of galactic noise, atmospheric noise, noise in the antenna sidelobes due to the Earth, noise due to losses in microwave reflectors, and noise due to losses in microwave components all lumped with noise due to input amplifier(s). This combined noise is measured relative to reference temperature load(s) connected to the amplifier input (during the measurement) and designated as the operating equivalent system temperature T_{op_1}, T_{op_2}, etc. The noise term $n_{i1}(t)$ has a double-sided noise spectral density $N_{0_1}/2 = (k \cdot T_{op_1} \cdot 1)/2$ watts/Hz, where k is Boltzmann's constant, $1.38 \cdot 10^{-23}$ joule/K. The noise terms $n_{i2}(t)$, etc. have noise spectral densities related to T_{op_2}, etc. as above.

As described in Ref. 1, the first local oscillator signal, which is derived from a voltage-controlled oscillator (VCO) through a frequency multiplier (XM), is:

$$2^{1/2}\cos(\omega_{LO}t + \hat{\theta}_{RF}) \qquad (3)$$

at the first mixer in receiving system 1. The term $\hat{\theta}_{RF}$ represents a noisy estimate of the input signal phase to the first mixer. Note that this first local oscillator signal (expression 3) is also applied to the first mixers of the other receiving systems. In particular, this local oscillator signal will experience an additional phase shift of $Y_2 \cdot 2\pi + \theta_2$ to the first mixer of receiving system 2 where Y_2 is an integer (a large integer for separate antennas). As a consequence, the first local oscillator signal (receiving system 2) becomes:

$$2^{1/2}\cos(\omega_{LO}t + \hat{\theta}_{RF} + \theta_2) \qquad (4)$$

For receiving system N, the additional first local oscillator phase shift is $Y_N \cdot 2\pi + \theta_N$, which provides a local oscillator signal $2^{1/2}\cos(\omega_{LO}t + \hat{\theta}_{RF} + \theta_N)$ to its first mixer.

Description of the received signal as it passes through receiving system 1 was presented in Ref. 1. At the output of second IF filter F_{A1} (which is narrow band relative to the sidebands) the signal becomes:

$$K_{A_1} \cdot K_{DIST_1} \cdot 2^{1/2} A_1 \cos m_{pD} \cdot \cos\left[\omega_{REF_2}t + (\theta_{FA_{10}} - \hat{\theta}_{RF})\right] + n_{FA_{10}}(t) \qquad (5)$$

where $\theta_{FA_{10}}$ represents the RF phase shift up to this point in system 1 and $n_{FA_{10}}(t)$ represents the amplified receiver noise related to T_{op_1} in the noise bandwidth of F_{A_1}. Note that since the gain from (5) in Fig. 1 to the AGC detector is constant at $K_{2nd_{IF1}}$ (minus the summing junction loss), the attenuator ($Atten_1$) at the input to the second IF amplifier in receiving system 1 provides a means for setting the signal level to provide the required output level for the telemetry subcarrier spectrum in receiving system 1 when RF carrier arraying with receiving system 2, etc. This attenuator setting ($Atten_1$) also establishes the proper level for the ranging spectrum at the output of the second IF distribution amplifier in receiving system 1 for ranging demodulation (not shown).

Description of the received signal as it passes through receiving system 2 was also presented in Ref. 1. Note that the receiving systems considered here are similar so that the signal-to-noise ratio at the output of the first IF amplifier (with gain K_{IFV_2}) in receiving system 2 is nearly equal to that at the corresponding point in receiving system 1. (The concept developed herein however, can be applied to arraying receiving systems where the signal-to-noise ratios are not equal.) The second local oscillator signal in receiving system 2 is derived

from a voltage-controlled crystal oscillator (VCO_2) through a frequency multiplier (XQ). From inspection of Fig. 1, the frequency VCO_2 XQ is equal to $(\omega_{REF_1} t)$ although its phase is modified by differences in carrier phase as pointed out in the discussion relative to expression (2) plus any differences in carrier phase relative to receiving system 1 up to this point in system 2. The second local oscillator signal can be expressed as

$$2^{1/2} \cos\left(\omega_{REF_1} t - \hat{\theta}_{LO_2}\right) \tag{6}$$

where $\hat{\theta}_{LO_2}$ represents the estimate of the RF carrier input phase to the lower second mixer (receiving system 2). The phase estimate $\hat{\theta}_{LO_2}$ is derived from a phase locked loop whose closed loop noise bandwidth is a small fraction of the closed loop noise bandwidth of the RF carrier phase tracking loop in receiving system 1 which provides the first local oscillator signal. Hence the noise on phase estimate $\hat{\theta}_{LO_2}$ is much less than that on $\hat{\theta}_{RF}$ (first local oscillator signal). Note that if the carrier signal-to-noise ratio in receiving system 2 were significantly less than that in receiving system 1, this effect could be offset by making the closed loop noise bandwidth in receiving system 2 a still smaller fraction of that in receiving system 1.

Although the noise on phase estimate $\hat{\theta}_{LO_2}$ is much less than that on $\hat{\theta}_{RF}$, the effect of the noise on phase estimates $\hat{\theta}_{LO_2}, \hat{\theta}_{LO_3}, \ldots, \hat{\theta}_{LO_N}$ is cumulative (in an rms sense) in the summing junction when arraying many receiving systems. This cumulative phase noise effect is kept small relative to the phase noise on $\hat{\theta}_{RF}$ (the first local oscillator) by including an additional second mixer (upper mixer) shown in receiving system 2 with the second local oscillator fed to this additional second mixer through a narrow-band phase locked local oscillator tracking loop. The phase noise on the output of the local oscillator tracking loop $\hat{\theta}'_{LO_2}$ is small compared to the phase noise at its input. Consequently, the second local oscillator signal fed to the additional (upper) second mixer becomes

$$2^{1/2} \cos\left(\omega_{REF_1} t - \hat{\theta}'_{LO_2}\right) \tag{7}$$

Receiving system 2 shows two second IF distribution amplifiers (see Fig. 1). The upper IF distribution amplifier accepts the output of the upper second mixer (described above) and in turn provides its output signal to the upper IF filter F_{A_2} (and to the telemetry IF channel) in receiving system 2.

Note that the additional filtering of phase estimate $\hat{\theta}_{LO_2}$ and the additional (upper) second mixer, IF distribution amplifier and IF filter F_{A_2} described in the preceding paragraph represent additions to Fig. 1 relative to Ref. 1. These additions to receiving systems 2 through N provide the near maximum signal-to-noise ratio improvement for RF carrier arraying presented in this report.

The upper and lower second IF filter F_{A_2} in receiving system 2 have the same noise bandwidth as IF filter F_{A_1} in receiving system 1 (by design). The signal at the output of the upper IF filter F_{A_2} (with gain K_{A_2}) can be expressed as

$$K_{A_2} \cdot K_{DIST_2} \cdot 2^{1/2} A_2 \cos m_{pD} \cdot \cos\left[\omega_{REF_2} t + \left(\theta_{FA_{20}} - \left(\hat{\theta}_{RF} - \hat{\theta}'_{LO_2}\right)\right)\right] + n_{FA_{20}}(t) \tag{8}$$

where $\theta_{FA_{20}}$ represents the RF phase shift up to this point in system 2 and $n_{FA_{20}}(t)$ represents the amplified receiver noise in the noise bandwidth of F_{A_2} at the operating equivalent system noise temperature T_{op_2}. This signal is provided as an input to the summing junction (see Fig. 1). The signal at the output of the lower IF filter F_{A_2} is the same as expression (8), with $\hat{\theta}'_{LO_2}$ replaced by $\hat{\theta}_{LO_2}$, which has higher phase noise as discussed in the preceding paragraph. Note that the phase shift from the output of the upper IF filter F_{A_2} (expression 8) in Fig. 1 to the phase detector which provides the error signal to the tracking filter (receiving system 2) is a constant by design. Consequently the phase shifter marked A, which is in series with the input (ω_{REF_2}) in receiving system 2 provides a means for setting the RF phase of expression (8) equal to the RF phase of expression (5) in receiving system 1 at the summing junction. The second IF amplifier gain $K_{2nd_{IF2}}$ is designed so that the signal level $(K_{A_2} K_{DIST_2} 2^{1/2} A_2)$ can be set as required relative to the signal level $(K_{A_1} \cdot K_{DIST_1} \cdot 2^{1/2} A_1)$ in receiving system 1 at the input to the summing junction.

III. Predetection Signal-to-Noise Ratio and Resultant Phase Noise

As developed in Ref. 1, with the other receiving system(s) (2 through N) switched out of the summing junction, the predetection carrier signal-to-noise power ratio in receiving system 1 represented by expression (5) is

$$P_{c_1}/P_{n_1} = \frac{A_1^2 \cos^2 m_{pD}}{NBW_{F_{A1}} \cdot N_{0_1}} \text{ or } \frac{P_{c_1}}{NBW_{F_{A1}} \cdot N_{0_1}} \tag{9}$$

where $NBW_{F_{A1}}$ represents the noise bandwidth of F_{A_1} and N_{0_1} is the one-sided noise spectral density for receiving system 1 which was defined in the discussion relative to expression (1). The receiving system contains a second-order RF carrier phase tracking loop which utilizes a bandpass limiter and a

sinusoidal phase detector. Utilizing the information in Refs. 2 and 3 and limiting $\sigma_n \leq 1$ radian, the rms phase noise σ_{ϕ_n} at the output of the RF carrier tracking loop (i.e., on the first local oscillator signal) can be expressed as:

$$\sigma_{\phi_{n1}} = \frac{\frac{N_{01}}{2} \cdot 2B_{L_1}}{P_{c_1}} \left[\frac{1 + \frac{P_{c_1}}{NBW_{F_{A1}} \cdot N_{0_1}}}{0.862 + \frac{P_{c_1}}{NBW_{F_{A1}} \cdot N_{01}}} \cdot \frac{\exp\left(\frac{N_{01} B_{L_1}}{P_{c_1}}\right)}{\sinh\left(\frac{N_{01} B_{L_1}}{P_{c_1}}\right)} \right]^{1/2} \text{radians, rms} \quad (10)$$

where $2B_{L_1}$ is the two-sided closed loop noise bandwidth of the RF carrier phase tracking loop. As described in Ref. 1,

$$2B_{L_1} = \frac{2B_{LO_1}}{r_0 + 1} 1 + \left(r_0 \frac{\alpha}{\alpha_{0_1}}\right)$$

where $r_0 = 2$ by design (0.707 damping) and $2B_{LO_1}$ is the design point (threshold) two-sided closed loop noise bandwidth in receiving system 1. The term α_1 is the limiter suppression factor resulting from the noise power to carrier power ratio in $NBW_{F_{A1}}$, α_1 has a value of α_{01} at design point (threshold). At threshold, the predetection carrier signal-to-noise ratio in a noise bandwidth equal to the threshold closed loop noise bandwidth ($2B_{LO}$) is unity (i.e., $P_c/2B_{LO} \cdot N_0 = 1$).

With receiving system 2 connected to the summing junction, the summed predetection carrier signal-to-noise ratio in receiving system 1 (as developed in Ref. 1) becomes:

$$\frac{P_{c_{1\Sigma 1,2}}}{P_{n_{1\Sigma 1,2}}} = \frac{P_{c_1}}{NBW_{F_{A1}} \cdot N_{0_1}} \cdot \frac{(1 + \beta_2\gamma_2)^2}{1 + \beta_2^2} \quad (11)$$

where β_2 is the voltage coupling of receiving system 2 relative to receiving system 1 into the summing junction and γ_2^2 is the carrier power-to-noise spectral density of the receiving system 2 relative to the receiving system 1. The resultant phase noise on the first local oscillator due to this summed predetection carrier signal-to-noise ratio is (Ref. 1)

$$\sigma_{\phi_{n1\Sigma 1,2}} = \frac{\frac{N_{0_1}}{2} \cdot 2B_{L_1}}{P_{c_1}} \cdot \frac{1}{\eta_2} \left[\frac{1 + \frac{P_{c_1}\eta_2}{NBW_{F_{A1}} \cdot N_{0_1}}}{0.862 + \frac{P_{c_1} \cdot \eta_2}{NBW_{F_{A1}} \cdot N_{0_1}}} \cdot \frac{\exp\left(\frac{N_{0_1} B_{L_1}}{P_{c_1} \cdot \eta_2}\right)}{\sinh\left(\frac{N_{0_1} B_{L_1}}{P_{c_1} \eta_2}\right)} \right]^{1/2} \quad (12)$$

where $\eta_2 = (1 + \beta_2\gamma_2)^2/(1 + \beta_2^2)$ for two receiving systems arrayed. The corresponding $\alpha_{\phi_{1n\Sigma 1, \ldots, N}}$ for N similar receiving systems arrayed become

$$\sigma_{\phi_{n1\Sigma 1, \ldots, N}} = \frac{\frac{N_{0_1}}{2} \cdot 2B_{L_1}}{P_{c_1}} \cdot \frac{1}{\eta_N} \left[\frac{1 + \frac{P_{c_1} \cdot \eta_N}{NBW_{F_{A1}} \cdot N_{0_1}}}{0.862 + \frac{P_{c_1} \cdot \eta_N}{NBW_{F_{A1}} \cdot N_{0_1}}} \cdot \frac{\exp\left(\frac{N_{0_1} \cdot B_{L_1}}{P_{c_1} \cdot \eta_N}\right)}{\sinh\left(\frac{N_{0_1} \cdot B_{L_1}}{P_{c_1} \cdot \eta_N}\right)} \right]^{1/2} \quad (13)$$

where $\eta_N = (1 + \beta_2\gamma_2 + \cdots + \beta_N\gamma_N)^2/(1 + \beta_2^2 + \cdots + \beta_N^2)$ for N receiving systems arrayed.

Up to this point, first local oscillator phase noise due to predetection carrier signal-to-noise ratio in receiving system 1 has been examined. However, phase noise on the first local oscillator is due not only to the predetection carrier signal-to-noise ratio as described above; it also includes the local oscillator (VCO_2 XQ) phase noise from receiving system 2 which is coupled through the summing junction into the phase locked loop in receiving system 1 (Ref. 1). The rms phase noise $\sigma_{\phi_{n2}}$ on phase estimate $\hat{\theta}_{LO_2}$ is derived with a two-sided closed loop noise bandwidth $2B_{L_2}$ in receiving system 2 (see expression 17 below). The additional filtering provided by the local oscillator tracking loop in receiving system 2, described relative to expression (7) above, reduces the rms phase noise $\sigma_{\phi_{n2}}$

to a value $\sigma'_{\phi_{n2}}$. This output rms phase noise $\sigma'_{\phi_{n2}}$ is less than $\sigma_{\phi_{n2}}$ by the square root of the ratio of the local oscillator tracking loop noise bandwidth to $2B_{L2}$. Consequently the total rms phase noise on the first local oscillator (Ref. 1)

$$\left[\sigma^2_{\phi_{n1\Sigma,2}} + \left(\frac{\beta_2 \sigma'_{\phi_{n2}}}{1+\beta_2}\right)^2\right]^{1/2} \tag{14}$$

is essentially equal to $\sigma^2_{\phi_{n1\Sigma 1,2}}$. From inspection of expressions (11) and (12), the improvement in carrier signal-to-noise ratio for two receiving systems arrayed approaches $(1+\beta_2\gamma_2)^2/(1+\beta_2^2)$. Note that for N receiving systems arrayed, the total rms phase noise on the first local oscillator is

$$\left[\sigma^2_{\phi_{n1\Sigma 1,\cdots,N}} + \left(\frac{\beta_2 \sigma'_{\phi_{n2}}}{1+\beta_2}\right)^2 + \cdots + \left(\frac{\beta_N \sigma'_{\phi_{nN}}}{1+\beta_N}\right)^2\right]^{1/2} \tag{15}$$

The total rms phase noise represented by expression (15) can be considered as due to an equivalent predetection carrier signal-to-noise ratio for N receiving systems arrayed. To the extent that expression (15) is essentially equal to $\sigma_{\phi_{n1\Sigma 1,\cdots,N}}$, the improvement in carrier signal-to-noise ratio approaches $(1+\beta_2\gamma_2+\cdots+\beta_N\gamma_N)^2/(1+\beta_2^2+\cdots+\beta_N^2)$. In any case, comparison of this equivalent predetection carrier signal-to-noise ratio with the initial predetection carrier signal-to-noise ratio in a single receiving system (i.e., system 1) provides the improvement due to radio frequency carrier arraying for N receiving systems.

As developed in Ref. 1, the predetection carrier signal-to-noise power ratio in receiving system 2 represented by expression (8) is:

$$\frac{P_{c_{2\Sigma 1,2}}}{P_{n_2}} = \frac{A_2 \cos^2 m_{pD}\left(1 - \frac{\sigma^2_{\phi_{n1\Sigma 1,2}}}{2}\right)^2}{NBW_{F_{A2}} \cdot N_{0_2}}$$

or

$$\frac{P_{c_2}\left(1 - \frac{\sigma^2_{\phi_{n1\Sigma 1,2}}}{2}\right)^2}{NBW_{F_{A2}} \cdot N_{0_2}} \tag{16}$$

The carrier tracking loop in receiving system 2 is a second-order loop ($r_0 = 2$) which also utilizes a bandpass limiter and a sinusoidal phase detector. The rms phase noise $\sigma_{\phi_{n2}}$ in receiving system 2 carrier tracking loop becomes

$$\sigma_{\phi_{n2\Sigma 1,2}} = \frac{\frac{N_{0_2}}{2} 2B_{L_2}}{P_{c_{2\Sigma 1,2}}} \left[\frac{1 + \frac{P_{c_{2\Sigma 1,2}}}{NBW_{F_{A2}} \cdot N_{0_2}}}{0.862 + \frac{P_{c_{2\Sigma 1,2}}}{NBW_{F_{A2}} N_{0_2}}} \cdot \frac{\exp\left(\frac{N_{0_2} \cdot B_{L_2}}{P_{c_{2\Sigma 1,2}}}\right)}{\sinh\left(\frac{N_{0_2} B_{L_2}}{P_{c_{2\Sigma 1,2}}}\right)}\right]^{1/2}$$

radians, rms (17)

where

$$P_{c_{2\Sigma 1,2}} = P_{c_2}\left(1 - \frac{\sigma^2_{\phi_{n1\Sigma 1,2}}}{2}\right)^2$$

for two receiving systems arrayed.

For N receiving systems arrayed, the predetection carrier signal-to-noise power ratio in receiving system 2 becomes

$$\frac{P_{c_{2\Sigma 1,\cdots,N}}}{P_{n_2}} = \frac{P_{c_2}\left(1 - \frac{\sigma^2_{\phi_{n1\Sigma 1,\cdots,N}}}{2}\right)^2}{NBW_{F_{A2}} N_{0_2}} \tag{18}$$

and the corresponding $\sigma_{\phi_{n2\Sigma 1,\cdots,N}}$ can be determined by substitution of $P_{c_{2\Sigma 1,\cdots,N}}$ in the place of $P_{c_{2\Sigma 1,2}}$ in expression (17). The predetection carrier signal-to-noise power ratio in receiving system N becomes

$$\frac{P_{c_{N\Sigma 1,\cdots,N}}}{P_{n_N}} = \frac{P_{c_N}\left(1 - \frac{\sigma^2_{\phi_{n1\Sigma 1,\cdots,N}}}{2}\right)^2}{NBW_{F_{AN}} N_{0_N}} \tag{19}$$

The resultant rms phase noise $\sigma_{\phi_{nN}}$ in receiving system N carrier tracking loop is

$$\sigma_{\phi_{nN\Sigma 1,\cdots,N}} = \frac{\frac{N_{0_N}}{2} \cdot 2B_{LN}}{P_{c_{N\Sigma 1,\cdots,N}}} \left[\frac{1 + \frac{P_{c_{N\Sigma 1,\cdots,N}}}{NBW_{F_{AN}} \cdot N_{0_N}}}{0.862 + \frac{P_{c_{N\Sigma 1,\cdots,N}}}{NBW_{F_{AN}} \cdot N_{0_N}}} \cdot \frac{\exp\left(\frac{N_{0_N} \cdot B_{L_N}}{P_{c_{N\Sigma 1,\cdots,N}}}\right)}{\sinh\left(\frac{N_{0_N} \cdot B_{L_N}}{P_{c_{N\Sigma 1,\cdots,N}}}\right)} \right]^{1/2} \text{radians, rms} \quad (20)$$

IV. Performance

The improvement in carrier signal-to-noise ratio resulting from arraying receiving systems as shown in Fig. 1 can be determined using the preceding development. In order to illustrate performance improvement, a representative set of design parameters are used to provide the performance shown in Figs. 2 and 3. The following parameters are used for receiving system 1:

Threshold two-sided noise bandwidth $(2B_{LO_1}) = 12$ Hz.

Predetection IF filter noise bandwidth $(NBW_{F_{A1}}) =$ 2200 Hz.

The parameters used for receiving system 2 through N are:

Threshold two-sided noise bandwidth $(2B_{LO_{2,\cdots,N}}) =$ 1 Hz.

Predetection IF filter noise bandwidth $(NBW_{F_{A2,\cdots,N}}) =$ 2200 Hz.

Local oscillator tracking loop two-sided noise bandwidth = 0.1 Hz.

It is interesting to note that essentially the same performance as shown in Figs. 2 and 3 is obtained with $2B_{LO_{2,\cdots,N}}$ equal to 0.1 Hz (and local oscillator tracking loop bandwidth equal to 0.1 Hz).

Figure 2 shows the near maximum RF carrier signal-to-noise ratio improvement which results from arraying up to 12 similar receiving systems. Performance is shown for $\gamma_N = \beta_N$ for values of 1.0, 0.95, 0.90, and 0.84, where γ_N and β_N are defined in the preceding development and on Fig. 2. Note that for 10 receiving systems arrayed, the improvement in carrier signal-to-noise ratio for $\gamma_N = \beta_N = 1$ is 9.6 dB compared to maximum improvement which is

$$\frac{(1 + \beta_2\gamma_2 + \cdots + \beta_{10}\gamma_{10})^2}{1 + \beta_2^2 + \cdots + \beta_{10}^2} \; (= 10) \text{ or } 10 \text{ dB},$$

Figure 3 shows the effect of varying β_N, the voltage coupling of receiving system N into the summing junction relative to receiving system 1, on carrier signal-to-noise ratio improvement for 2, 3, 4, and 10 systems arrayed. Note that voltage coupling can vary considerably with a small resultant change in performance.

References

1. Brockman, M. H., "Radio Frequency Carrier Arraying for High Rate Telemetry," in *The Deep Space Network Progress Report 42-45,* pp. 209-223, Jet Propulsion Laboratory, Pasadena, Calif., June 15, 1978.
2. Tausworthe, R. C., *Theory and Practical Design of Phase-Locked Receivers,* Vol. I., Technical Report 32-819, Jet Propulsion Laboratory, Pasadena, Calif., Feb. 15, 1966.
3. Tausworthe, R. C., "Limiters in Phase-Locked Loops: A Correction to Previous Theory," in *Space Program Summary No. 37-54, Vol. III,* pp. 201-203, Jet Propulsion Laboratory, Pasadena, Calif., 1968.

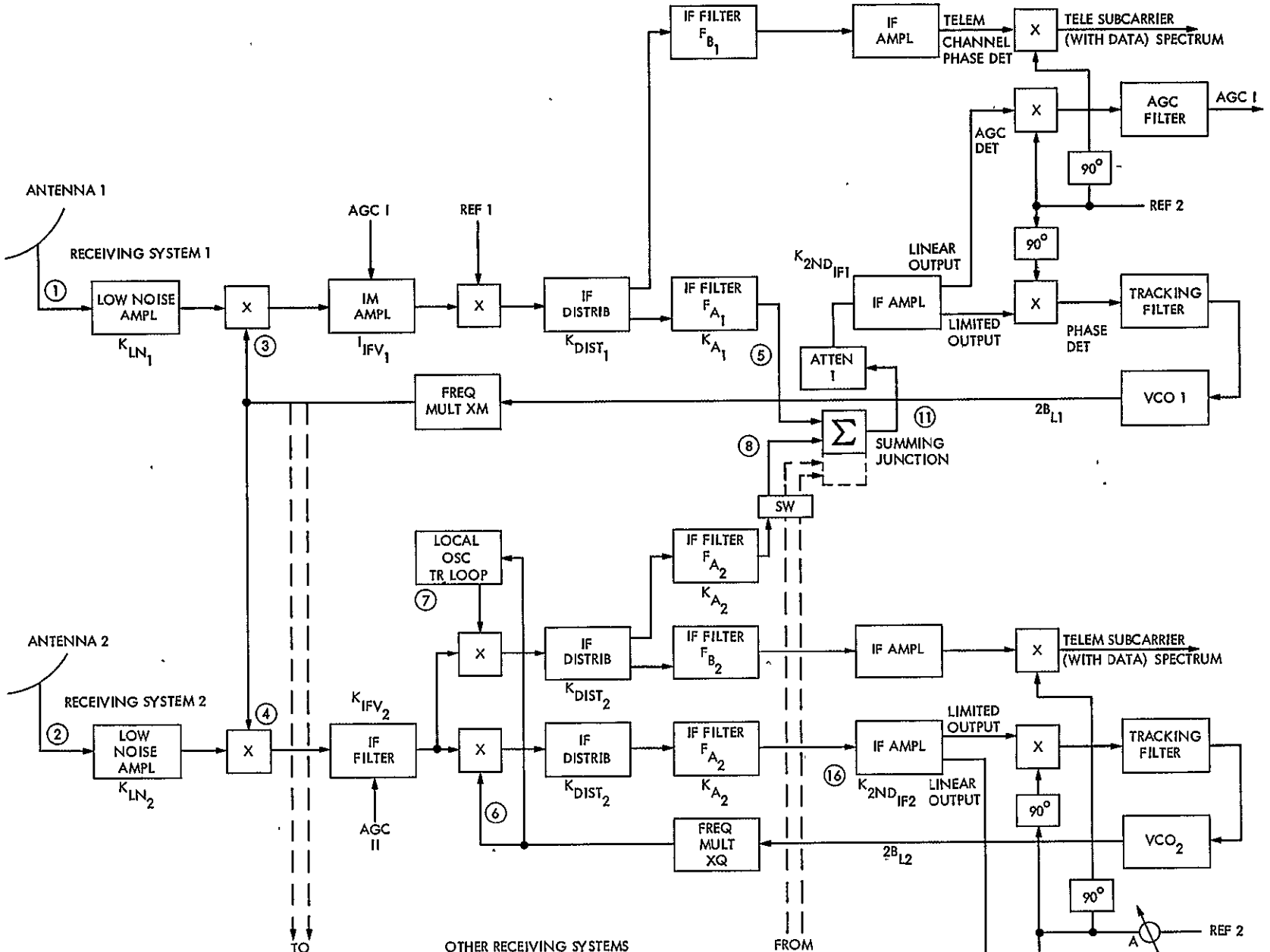

FREQ. REF. 1 AND 2 SYNTHESIZED FROM COMMON FREQ. STD.
$NBW_{F_{A1}} = NBW_{F_{A2}}$

Fig. 1. Radio frequency carrier arraying for near maximum carrier signal-to-noise ratio improvement

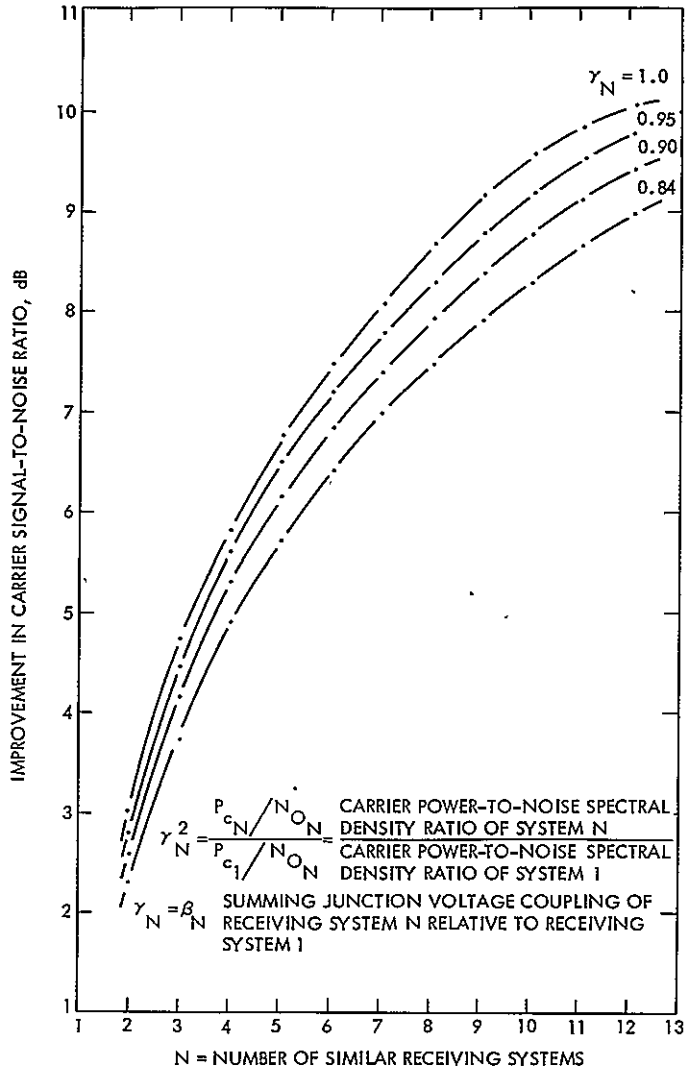

Fig. 2. Near maximum carrier signal-to-noise ratio improvement for radio frequency carrier arraying for reception vs number of receiving systems

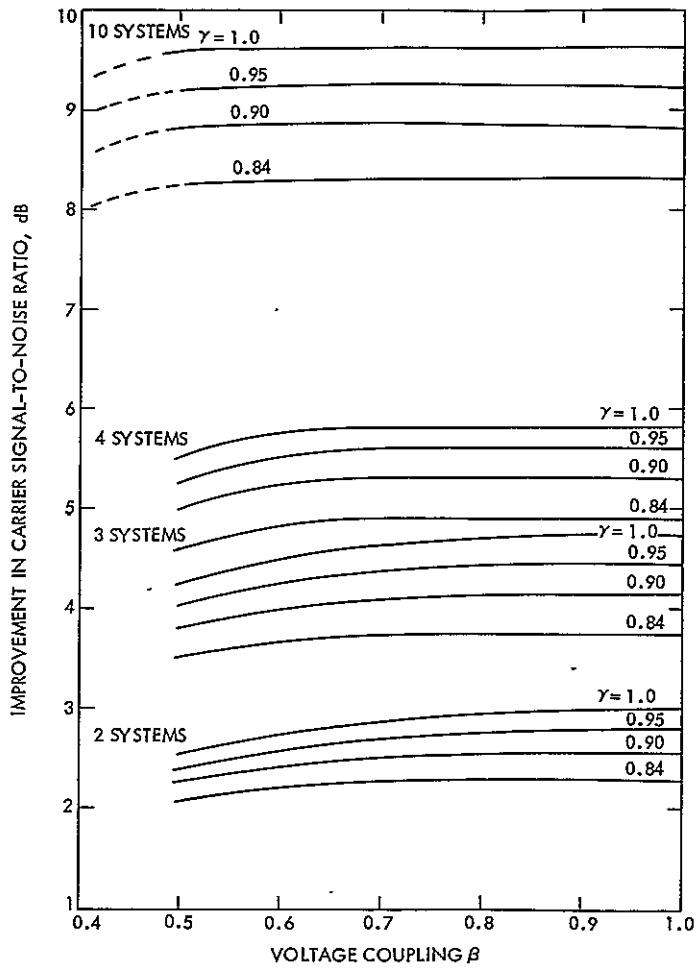

Fig. 3. Effect of summing junction voltage coupling on near maximum carrier signal-to-noise ratio improvement

D14

N79-19059

The Updated Algorithm of the Energy Consumption Program (ECP) – A Computer Model Simulating Heating and Cooling Energy Loads in Buildings

F. L. Lansing, D. M. Strain, V. W. Chai, and S. Higgins
DSN Engineering Section

The Energy Consumption Computer Program (ECP) was developed to simulate building heating and cooling loads and compute thermal and electric energy consumption and cost. This article reports on the new additional algorithms and modifications made in an effort to widen the areas of application. The program structure has been rewritten accordingly to refine and advance the building model and to further reduce the processing time and cost. The program is noted for its very low cost and ease of use compared to other available codes. The accuracy of computations is not sacrificed however, since the results are expected to lie within ±10% of actual energy meter readings.

I. Introduction

The Energy Consumption Program (ECP), reported earlier in Refs. 1, and 2, was originally developed to satisfy the Deep Space Network needs in conducting complete energy surveys (audits) and to support the ongoing energy conservation project studies. The computer program proved to be a useful tool in evaluating many energy-saving suggestions and proposals presented by DSN personnel. Because of low running cost, ease of use, and accuracy of computations, the program has been accepted recently by NASA as a new technology item. The program applicability has also been increased since it was first put together in September 1977. Since its conception, experience with the program has been instructive as to both new ways to model and new fields of application. Accordingly, it has become essential, for many reasons, to enlarge the program structure, improve the coding techniques and make the necessary component additions or deletions that not only benefit the growing needs of the DSN but attract other NASA government or non-government users also.

The updated algorithm of the energy consumption program has a structure which can be divided into five parts:

(1) Calculation of space (zone) loads for the net heat gain or loss.

(2) Simulation of fan-coil (air handler) systems to meet above space loads.

(3) Simulation of primary equipment such as chillers (vapor compression or absorption types), heaters, boilers, and heat pumps.

(4) Design of proper air discharge, ventilation to each space, and capacity of primary equipment.

(5) A short economic analysis to evaluate the payback period of money spent on a specific modification.

The following sections describe the main additions, deletions or modifications made to the internal algorithms to widen

the applicability areas and, as a side benefit, shorten the already small processing time and running cost.

II. Program Structure

A. Dimensions

The dimensioning of the various parameters has been changed to be open-ended subject to the maximum limit of the local computer system memory. This means that there is no fixed limit on the number of zones, air handlers, or primary equipment to be handled in any problem. This open-ended dimension changes the size of program storage, which has the advantage of not only increasing the upper limit when handling high rise buildings or groups of buildings with a very large number of zones, but also reducing the problem size for buildings with a single zone or a small number of zones.

B. Namelist of Input Data

Program input data are presently contained in one namelist for user convenience. Many built-in default values are assigned to fill in for some input data unknown to the user.

Architectural and physical characteristics of the building (or zones) include latitude, elevation, wall areas and orientation, glass areas and orientation, shade factors, space volume, outside wall solar absorptivity and the physical properties of layers forming walls, roofs and floors.

Input data for the fan-coil (air handler) include the outside ventilation air, the zone-air handler circulating air rate, the heating and cooling set point temperatures, and whether or not these set points are automatically varying as a function of load (floating set points) or fixed. The use of outside air economizer cycles and time clocks can be identified. Also, the air-handlers field arrangement in feeding the various zones and the interconnection with the primary equipment (chillers or heaters) are needed. Besides the external weather data, the internal sources of heat gain, such as people, lighting, and mechanical, electrical and heat generating equipment are required. The rest of the input data in the namelist provides information regarding the cost of energy, interest rates and installation cost. More details are given in the new program documentation.

C. Sequence of Computations

The program starts by converting all input data units to one standard, which is arbitrarily selected to be the English system. Zone sensible heat gain is computed hourly and summed with the internal heat gain, solar and transmission heat gain through glass and walls, infiltration and exfiltration. The net zone heat gain (or loss) is used next to determine the desired temperature of the supply air necessary to maintain the zone design conditions. Two-level zones are handled in a special manner throughout the program. The effects of outside air economizer cycles, automatic (or floating) set points, and zone "dead bands" are placed in the proper control sequence. The heating and cooling loads on the various air handlers are then computed and summed to the appropriate primary equipment (cooler, heater or reheater). The association of zones, air handlers and primary equipment is in a free form, whereby more than one air handler can feed a zone and vice versa. However, more than one air handler can be connected to a primary equipment, but not vice versa.

Once the primary equipment load is determined, the input energy necessary to operate the unit is computed according to the coefficient of performance (COP) subroutine. Moreover, the program includes special routines for designing new equipment to determine ventilation air, zone air flow rates, and capacity of primary equipment. The economics section is added at the end of the program together with all the necessary printing and plotting procedure. The results are then converted to either the English or SI (metric) unit system as the user desires.

D. Output Forms

The program output forms are tabulated and grouped mainly according to zone, air handler, and primary equipment. The output includes:

(1) Input data echo for the user to check all the entered data.

(2) Diagnostic messages.

(3) Hourly, daily, and monthly itemization of zone sources of heat gain/loss and zone-air handler heating and cooling loads, for two-day types each month.

(4) Hourly, daily, and monthly mixed air temperature, air handler heating/cooling loads and maximum and minimum supply air temperature of all zones fed by a given air handler.

(5) Hourly, daily, and monthly supply air temperature to each zone.

(6) Equilibrium zone inside temperature.

(7) Peak hourly heating and cooling loads for each piece of primary equipment.

(8) Hourly, daily, and monthly heating/cooling loads and the necessary thermal or electrical input energy for primary equipment.

(9) Design values of zone ventilation, conditioned air flow, and capacity of primary equipment.

(10) Hourly, daily, and monthly electric, thermal, heating and cooling load profiles for the building under study.

(11) Monthly itemization or energy consumed in lighting, mechanical, electrical and HVAC equipment and the corresponding cost.

(12) Money payback period for a given modification.

(13) Yearly thermal and electrical energy index for the building.

The program output is coded to be selective according to the user's needs. This means that the user will be able to print out only specific information to save printing costs.

E. Units

Input data can be entered either in English units or in SI (metric) units. Likewise, the program output can be printed in either unit system as the user specifies. The above feature is a new addition made to match the current worldwide trend of conversion to the SI units.

F. Data Plotting

This new feature is added to present the results graphically in 2-dimensional and 3-dimensional plots. Local plotting subroutines available at JPL-1108 computer system are used for this purpose. However, these subroutines are considered external to the program's main function.

G. Two-level Zones

The unique feature of ECP compared to other codes in this field is the ability to simulate two-level air-conditioned zones with two air streams. These two-level zones are commonly encountered in air conditioning electronic control rooms. The first air stream is cold air, which is provided through a common plenum floor underneath the electronic racks. The second air stream (comfort air) is provided to the second level to mix with the first air stream. A special zone index is defined in ECP for differentiation of two-level zones with simple zones. Each of the two-level zones is treated independently and special attention is given to their temperature equilibrium.

III. Description of Updated Program

The following subsections supersede those presented in Refs. 1 and 2 and describe the updated methodology used in each of the program steps, with special attention to the new points made. The program is written in FORTRAN V using the EXEC-8 codes of the 1108 machines at JPL. It requires approximately 32K of computer memory of 36-bit words.

A. Weather

Required weather information includes outside air dry bulb temperature, cloud cover factors and wind speed. For the outside air dry bulb temperature, 24-h values for each of the 12 typical days (one for each month) per year are needed. Twelve cloud cover factors are also needed: one for each month. A monthly cloud cover factor is determined by the ratio of accumulated daily, direct solar energy incident on site to that accumulated theoretically by ASHRAE model (Ref. 3). If no solar insolation data were available, the cloud-cover factors would be estimated from past site experience by the percentage of clear sky area. Hourly wind speeds for a representative day of the year are needed. The above weather data are considered the least information needed to obtain reliable results.

B. Transmission Loads

The Total Equivalent Temperature Difference method (TETD), as described in Ref. 4, is used for its good accuracy and small computer memory requirement. Walls, roofs, and floors are assumed homogeneous, with average material properties that are determined internally using the data provided about their multilayers. Several additions are made in the computations of the steady-state heat transfer coefficients and the transient heat transfer coefficient amplitude and phase angle to make them zone-dependent. Since these heat transfer coefficients need to be determined only once for each zone, the program is coded to print the above coefficients and use them as input data for later runs of the same zone (or building) in order to save repetition time and cost.

C. Solar Heat Gain

Direct, diffuse and ground-reflected solar radiation values are generated internally using the known ASHRAE model described in Ref. 3. Cloud cover factors are applied to attenuate the theoretical ASHRAE values to yield the site-specific radiation values.

D. Infiltration/Exfiltration Loads

The effect of repetitive opening and closing of doors or windows and the leakage of outside air or conditioned air to or from the space through cracks, clearances or by buoyancy is calculated using the air change method. The corresponding sensible heat loss or gain is computed assuming quasi-steady-state.

E. Internal Heat Loads

Since the latent loads are often less than 10% of the total heat gain, only sensible heat gain is considered in ECP. The number of persons occupying the space and the wattage rating

of electrical, mechanical, lighting (incandescent and fluorescent) and heat generating equipment are entered hourly for two-day types representing repetitive events for the whole year. Day type (1) is a typical week day (approximately 251 week days per year); day type (2) is a typical weekend/holiday (approximately 114 days to include 10 official holidays). Heat gain due to the above internal heat loads is computed hourly based on quasi-steady state and no storage effects. Monthly variations of the magnitude of these sources of heat gain but not of their schedule are considered by zone multiplication factors.

F. Shading Effects

A zone shading factor due to overhangs, side projections, or adjacent buildings is considered as a fraction between 0 and 1, given by the user based on annual observations. Shading factors are used in the heat transmission computations to reduce the solar radiation falling on walls, windows, and roofs.

G. Loads Due to Neighboring Areas

When a neighboring zone is kept at a temperature different from that of the zone under study, the corresponding heat gain or loss is taken into consideration. The new program algorithm accounts for heat exchange through floors and ground floors not considered in the old version.

H. Fan-Coil (Air Handler) Types

Seven major classes of zone-air handler arrangements have been incorporated into ECP, which can be further divided into 18 different combinations as illustrated in Figs. 1 through 7. The seven classes are:

(1) Air handlers that provide cold air modulated by subsequent heating. Heating coils are located either in the air handler or at each zone supply air outlet as shown in Fig. 1.

(2) Air handlers that provide simultaneously two streams of hot and cold air (as shown in Fig. 2). Modulation is made by mixing different proportions of each stream to satisfy the zone needs. Mixing is done either in the air handler or in mixing boxes located at each zone supply air outlet.

(3) Air handlers that provide cold air mixed with bypassed mixed air as a first modulation, followed by heating as a second modulation. Heating coils are located either in the air handler or at each zone outlet, as shown in Fig. 3.

(4) Air handlers that operate either in heating or cooling modes at any one time with bypassed mixed air modulation. This is also the case of a heat pump/refrigerator unit with mixed air bypass control, as shown in Fig. 4.

(5) Air handlers that provide cold air mixed with a fixed ratio of bypassed return air as a first modulation and followed by heating as a second modulation. Heating coils are located either in the air handler or at each zone outlet, as shown in Fig. 5.

(6) Variable air volume air handlers that control, through restrictions, the air discharge to each zone while keeping the hot or cold supply air temperature fixed, as shown in Fig. 6.

(7) Air handlers that provide unmodulated cold air only year-round, as shown in Fig. 7.

These classifications are made differently compared to the old ECP version. For special two-level zones, each level is handled as a separate entity where a combination of the above air handler types is used. The new code provides greater flexibility in the analysis especially when a zone (single or two-level) is fed by more than one air handler, each of a different type. The program structure allows any future inclusion or modification of air handler configuration that the user desires, to include either special cases or new designs.

I. Outside Air Economizer Cycles

To take full advantage of relatively cold outside air at times when cooling is needed, for example, the concept of outside air economizer cycle is introduced and included in ECP as an energy-conservation mode of operation. The logic of the controlling mechanism is embedded into ECP, whereby an hourly survey is made of the temperatures of outside air, return air, cooling and heating set points, and minimum and maximum supply air temperatures.

J. Temperature Bands and Automatic Set Points

As another energy saving feature, zone thermostat controls are set to vary between some lower and some higher limits, i.e., to a have a "dead band." The "dead band" limits are specified by the user. The controls logic is made such that the zone will not need active heating or cooling if its inside temperature lies between the "dead band" limits. Similarly, the set points for cooling and heating coils can be specified by the user to be fixed year-round or automatically adjusted. The recent advances in automatic temperature control allow the set points to vary within a practical range to match the zones requiring the most cooling and/or heating.

K. Time Clocks

The time clock on/off controls are only applied to air handlers and are not applicable to lighting, electronic or mechanical equipment since their effects appear under the internal heat sources schedule. Zone inside temperatures will

be assumed at ambient if air handlers are off under a time clock control.

L. Primary Equipment Performance

The primary equipment included in the new algorithm are:

(1) Electric-driven vapor compression refrigeration.

(2) Absorption chillers powered by fuel combustion, solar or other heat source.

(3) Electric-driven heat pumps.

(4) Heaters, reheaters or boilers powered by electricity or fuel combustion.

Default values built in for component efficiency and coefficient-of-performance can be superseded by user's input data. The capacity of primary equipment can either be entered as input data, if known, or given to the user as one of the design parameters. Vapor-compression chillers are assumed to have a maximum of four stages, and all other items of primary equipment are assumed to have only a single stage. Heaters, reheaters, boilers and absorption refrigeration equipment are assumed to have a constant efficiency at all loads. The coefficient of performance for heat pumps and vapor compression chillers is taken as a fraction (~50%) of the ideal Carnot's cycle working between the evaporator and condenser temperature. Partial-load performance takes into consideration the variation of outside air temperature and is assumed proportional from 100% full load till 40% of full load, below which the input energy is constant. The above approximation accounts for the inefficiency at very small partial loading caused by hot-gas bypass and electric motor.

M. Energy Consumed by Auxiliary Equipment

Auxiliary equipment is defined as equipment outside the air conditioning zone (or space) which is necessary to operate the building but does not affect the internal heating or cooling loads. For equipment located inside the air-conditioned zone, the data are entered into internal heat sources tables.

Electric auxiliary equipment includes external building lights and other outdoor equipment. Air-handler fans, condenser fans (air-cooled), condenser pumps (water-cooled) and boiler pumps are internally tied to the operation of primary equipment. Thermal auxiliary equipment includes fuel-consuming devices that are not located within any air-conditioned zone such as domestic hot water boilers. Auxiliary equipment energy consumption directly affects thermal or electric energy meters. Consumption is modeled for simplicity by using name plate capacities only. No allowance is made at this stage to partial load performance or flow pressure and discharge variations. However, monthly variations and schedules are considered.

N. Energy Cost and Payback Period

The economic part in ECP is designed to provide few parameters such as the monthly and yearly cost of electric and thermal energy consumed and the money payback period of a selected hardware modification. However, the program can be enlarged to include any detailed economic analysis as desired by the user.

A new documentation package is underway to include the updated guidelines for entering data, algorithm description, input and output formats and the program flow charts. The new documentation will supersede Ref. 2. The cost of running the program is still very low compared to commercial codes. The simulation accuracy, on the other hand, is under verification and is expected to be within. ±10% range of actual watt-hour meters values.

References

1. Stoller, F. W., Lansing, F. L., Chai, V. W., and Higgins, S., "Energy Consumption Program – A Computer Model Simulating Energy Loads in Buildings," in *The Deep Space Network Progress Report 42-45*, pp. 288-293, Jet Propulsion Laboratory, Pasadena, Calif., June 1978.

2. Lansing, F. L. et al., *JPL Energy Consumption Program (ECP) Documentation*, Publication 78-76, Jet Propulsion Laboratory, Pasadena, Calif., Sept. 1978.

3. *Handbook of Fundamentals*, American Society for Heating, Refrigeration and Air Conditioning Engineers (ASHRAE) 1972.

4. Threlkeld, J. L., *Thermal Environmental Engineering*, Prentice-Hall Inc., New Jersey, 1962.

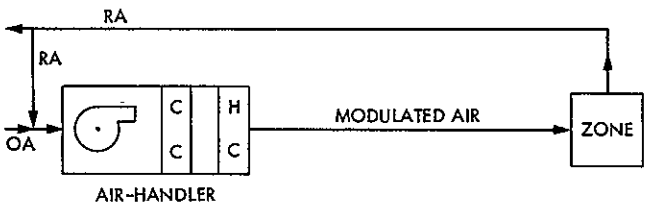

(a) A SINGLE ZONE AIR-HANDLER. COLD AIR IS MODULATED BY A HEATING COIL LOCATED AT THE AIR-HANDLER

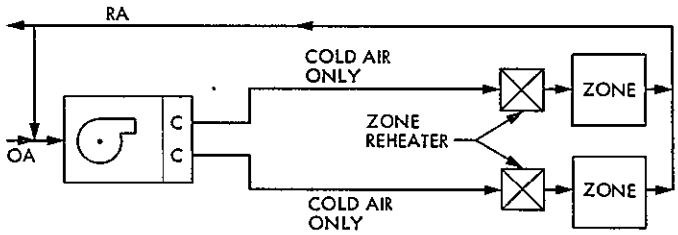

(b) A MULTIZONE AIR-HANDLER, PROVIDING COLD AIR DUCT(S). MODULATION IS BY TERMINAL ZONE REHEATERS

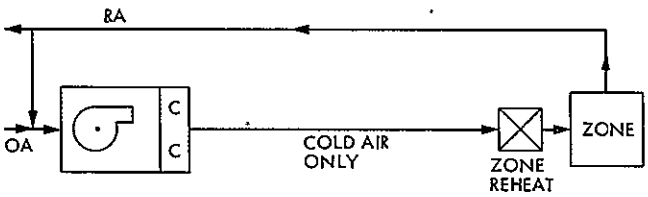

(c) A SINGLE ZONE AIR-HANDLER, PROVIDING A COLD AIR DUCT WITH TERMINAL ZONE REHEAT

Fig. 1. Type 1 air handlers: cooling followed by heating

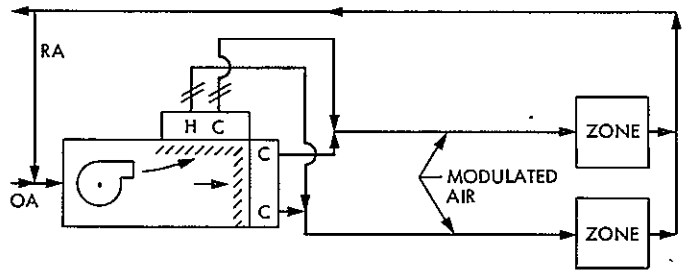

(a) A MULTIZONE AIR-HANDLER PROVIDING MULTI-FEED DUCTS. MODULATION IS CONTROLLED BY MIXING DAMPERS AT THE AIR-HANDLER

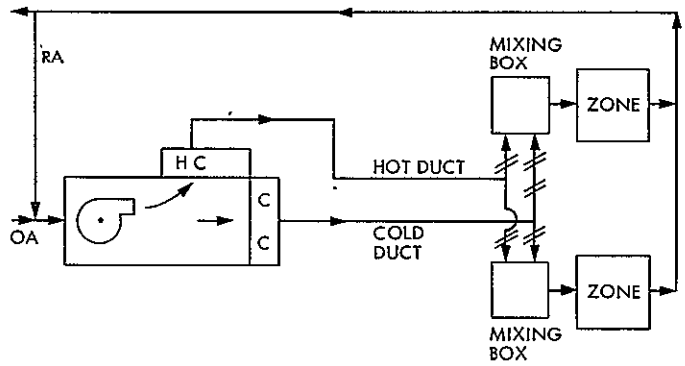

(b) MULTIZONE AIR-HANDLER WITH DOUBLE FEED DUCT (ONLY TWO COLD AND HOT DUCTS). MODULATION IS CONTROLLED BY ZONE MIXING BOXES

Fig. 2. Type 2 air handlers: mixing cold and hot air streams

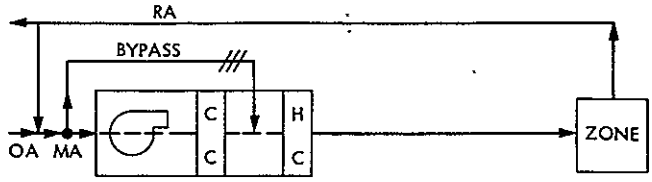

(a) A SINGLE ZONE AIR-HANDLER WITH COOLING COIL, BYPASS MIXED AIR CONTROL AND HEATING COIL

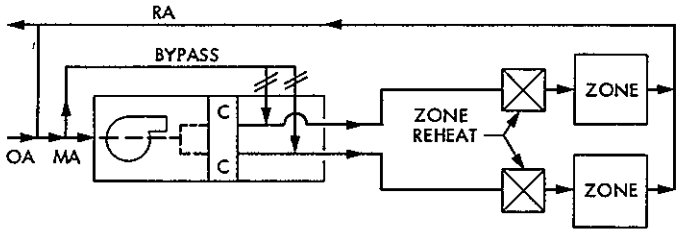

(b) MULTIZONE AIR-HANDLER WITH COOLING COIL, MIXED AIR BYPASS DAMPERS AND ZONE LOCATED REHEATERS. BYPASSED AIR IS ZONE-DEPENDENT

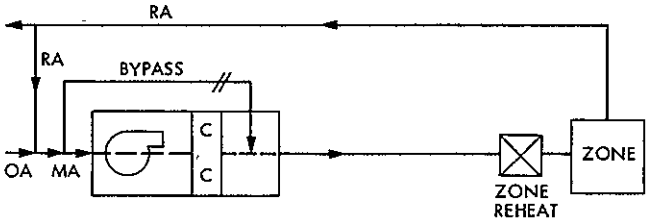

(c) A SINGLE ZONE AIR-HANDLER WITH COOLING COIL, BYPASS MIXED AIR CONTROL AND A HEATER LOCATED AT THE ZONE

Fig. 3. Type 3 air handlers: cold air modulated by bypass mixed air followed by heating

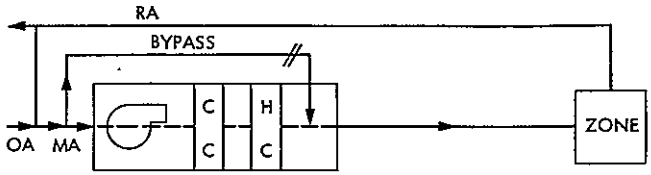

(a) SINGLE ZONE AIR-HANDLER WITH HEATING AND COOLING COILS USING BYPASS CONTROL. EITHER HEATING OR COOLING IS ON AT ONE TIME

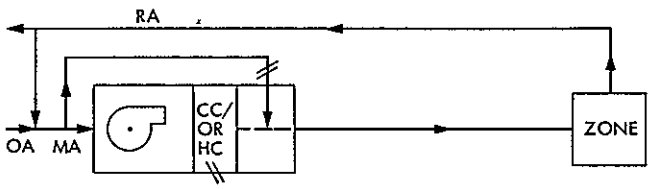

ONE COIL ACTING EITHER AS HEATER OR COOLER AS NEEDED

(b) SINGLE ZONE HEAT PUMP WITH BYPASS CONTROL

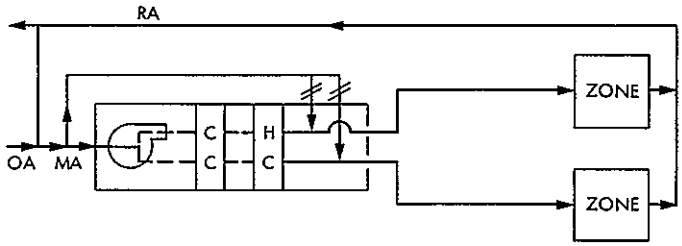

(c) MULTIZONE AIR-HANDLER WITH HEATING AND COOLING COILS USING BYPASS CONTROL FOR EACH ZONE. EITHER HEATING OR COOLING IS ON AT ONE TIME

Fig. 4. Type 4 air handlers: alternate heating and cooling with mixed air bypass control for each mode

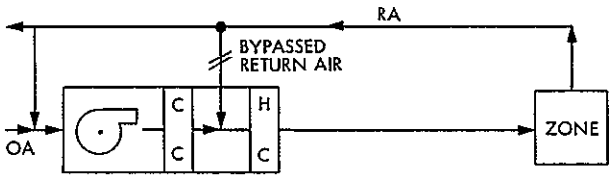

(a) SINGLE ZONE AIR-HANDLER WITH FIXED BYPASS RETURN AIR, COOLING AND HEATING COILS

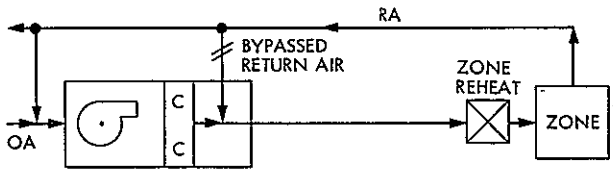

(b) SINGLE ZONE AIR-HANDLER WITH FIXED BYPASS RETURN AIR AND COOLING COIL. HEATING IS LOCATED AT THE ZONE

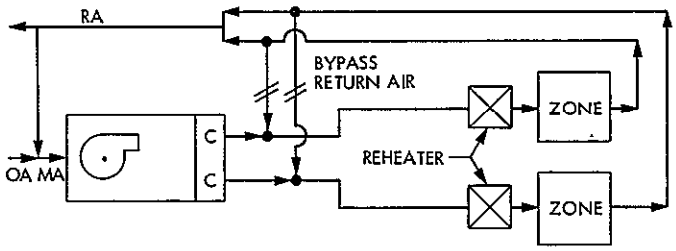

(c) MULTIZONE AIR-HANDLER

Fig. 5. Type 5 air handlers: cold air modulation by fixed position bypassed return air followed by heating

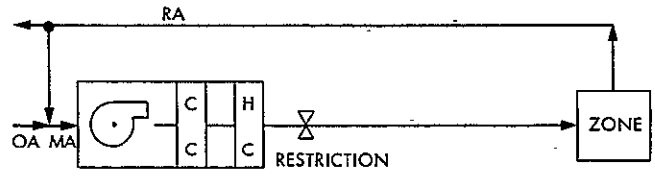

(a) SINGLE ZONE AIR-HANDLER WITH EITHER HEATING OR COOLING ON AT ONE TIME

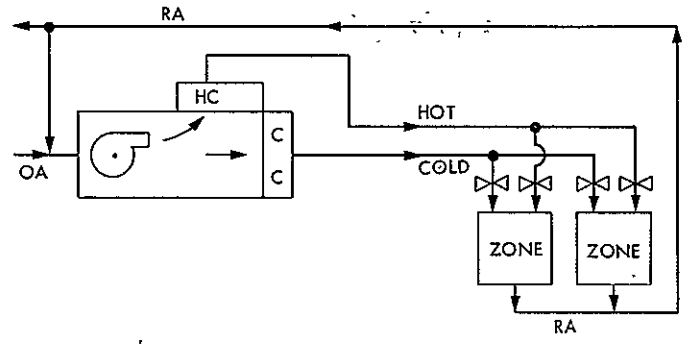

(b) MULTIZONE AIR-HANDLER WITH BOTH HEATING AND COOLING COILS ON. MODULATION IS BY VOLUME RATE CONTROL

Fig. 6. Type 6 air handlers with both heating and cooling coils on: modulation is by volume-rated control

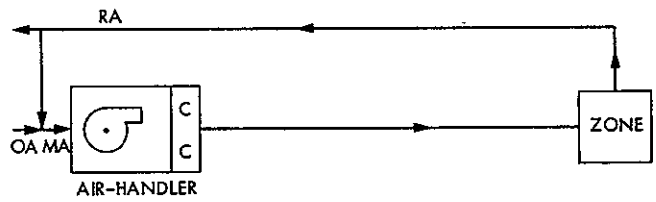

(a) SINGLE ZONE AIR-HANDLER PROVIDING UNMODULATED COLD AIR ONLY

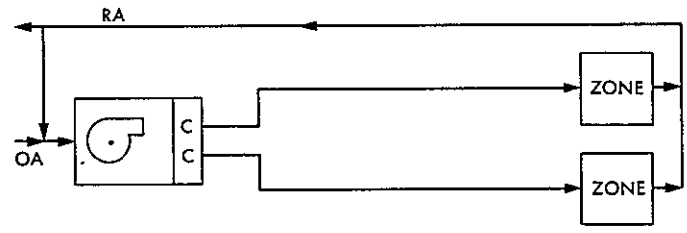

(b) MULTIZONE AIR-HANDLER PROVIDING UNMODULATED COLD AIR ONLY

Fig. 7. Type 7 air handlers: cold air all year-round; no modulation by any heaters or air mixing

D15

N79-19060

A Two-Dimensional Thermal Analysis of a New High-Performance Tubular Solar Collector

F. L. Lansing and C. S. Yung
DSN Engineering Section

This article is the first of two which describe and analyze the thermal performance of the new General Electric vacuum tube solar collector. The assumptions and mathematical modeling are presented. The problem is reduced to the formulation of two simultaneous linear differential equations characterizing the collector thermal behavior. After applying the boundary conditions, a general solution is obtained which is found similar to the general Hottel, Whillier and Bliss form but with a complex flow factor.

I. Introduction

Several solar-powered heating and cooling facility modifications in the Deep Space Network ground stations are planned for future implementation as part of the DSN Energy Conservation Project. In order to support the relevant feasibility and advanced engineering studies, special attention is given to new technologies in low-concentration, nontracking solar collectors. These nonimaging low-concentration types (with intensity concentration between 1 and 5) possess several advantages compared to the high-temperature, high-concentration ones. Examples are:

(1) The ability to harness, diffuse and direct portions of sunlight.

(2) Low cost due to less precision requirements in manufacturing, no sun-tracking mechanisms and no sophisticated optics controls.

(3) Good collection efficiency in the range of heating/cooling interest from 80 to 140°C.

One of the new designs that emerged in this field is the tubular and evacuated collector manufactured by General Electric (Ref. 1). The collector resembles, but is not identical to, a hybrid system combining (1) the serpentine tube on a flat absorber enclosed in an evacuated glass cylinder manufactured by Corning Glass Works, and (2) the all-glass concentric tubes manufactured by Owens-Illinois (Refs. 2-4). The semiproprietary GE collector performance data given by the manufacturer claim that the collector is able to provide about double the energy collection capability of flat plate collectors employing double glazing and selective coating. Although the GE collector does possess the best of each of the Owens-Illinois and the Corning types, it is felt that its performance superiority is in need of an in-depth investigation at a wide range of operating conditions. This article, the first of two, is intended to provide the collector thermal analysis and the relevant equations needed for a full parameterization study.

II. Collector Description

Figure 1 illustrates the design details of one module of the tubular collector with 10 heat collection units. The units are mounted in parallel and each unit contains, as shown in Fig. 2, a U-shaped copper tube. The copper tubes of the units are connected in series to form a serpentine of 10 loops.

Each collector unit consists of two coaxial glass tubes. The annular space between the glass tubes is evacuated and sealed to form a "thermos-bottle" effect. A thin cylindrical shell made of copper conforms to the inside diameter of the inner glass tube and is attached to the copper U-tube. The vacuum tubes are mounted in a polished aluminum V-shaped back reflector tray. The back reflector enhances the solar concentration and allows both direct and diffuse portions of the sunlight to be collected.

The solar collector manufactured by General Electric has a selective coating on the outer surface of the inner glass tube, thus making the inner glass tube serve as the absorber that transmits heat to the copper shell by conduction. Since glass is a poor conductor compared to copper, the present collector under study is made differently and more efficient by selectively coating the outer surface of the copper shell instead, while keeping the inner glass tube transparent. Accordingly, the double-walled glass bottle serves as the window and the thin copper shell with its selective outer surface acts as the absorber.

Besides employing (1) a vacuum technique to reduce convection losses, (2) a selective coating to reduce outward infrared radiation losses, and (3) a back augmenting reflector, the collector has unique features compared to other commercial tubular collectors. Examples are (1) a glass tube which, if damaged, will not discontinue the collector service, and (2) the collector is lightweight with a low thermal inertia which can be translated to ease in installation, connection and structural requirement plus a fast temperature response that increases a full-day performance.

III. Thermal Analysis

Before we proceed with the analytical energy expression for each collector tube in a collector unit, the following assumptions were made to simplify the simulation process.

(1) The collector is assumed at steady state, located in an environment with uniform ambient temperature and solar irradiation.

(2) The problem is treated as a two-dimensional heat transfer in the axial and radial directions. Collector tubes are assumed to be of uniform temperature in the tangential direction, even though the solar flux distribution on the outer glass tube may not be uniform due to the space allowed between the collector units and the effect of the back V-reflector. In the radial direction, the temperature distribution is assumed to be in steps with negligible conduction thermal resistance for all thin tubes.

(3) Axial conduction heat transfer from one end to another is neglected.

(4) Material optical properties are assumed uniform and independent of temperature and direction. Physical properties for solids and liquids are also assumed uniform and independent of working temperature and pressure.

(5) Sky and ambient temperatures are assumed approximately the same to simplify computations. Also, the ambient air temperature to the air core and external to the collector unit is assumed the same.

(6) The metallic absorber shell, the hot water tube wall and the cold water tube wall are all assumed at a single temperature, which is the average of these three surfaces. The absorber temperature varies only axially. The metallic absorber actually acts as a fin stretched from both sides of the fluid tubes in a circular shape. This assumption is supported by the observation that the difference in temperature between inlet and outlet fluids is small at each collector unit.

(7) The convective heat transfer coefficient between the serpentine tube and either the hot or cold fluid sides is assumed the same since its variation with temperature is insignificant. The convective coefficient is a dominant function of tube diameter length and fluid mass flow in the laminar range.

A segment of the collector unit whose thickness is dx and located at a distance x from the open end of the fluid tubes is analyzed. Appendix A gives the effective optical properties of the double concentric glass cylinders. In Appendix B, the details of the heat balance equations are given for reference. The collector and thermal behavior is characterized by the following two linear simultaneous differential equations for the hot fluid temperature $T_h(x)$ and the cold fluid temperature $T_c(x)$:

$$\frac{dT_h}{dx} = -\delta - C_0 T_c + C_1 T_h \tag{1}$$

$$\frac{dT_c}{dx} = \delta + C_0 T_h - C_1 T_c \tag{2}$$

where δ, C_0 and C_1 are collector characteristic constants given in Appendix B. If Eqs. (1) and (2) are solved for either T_c or T_h alone, then

$$\left.\begin{aligned}\frac{d^2T_c}{dx^2} - (C_1^2 - C_0^2)\,T_c + \delta\,(C_1 + C_0) = 0\\ \frac{d^2T_h}{dx^2} - (C_1^2 - C_0^2)\,T_h + \delta\,(C_1 + C_0) = 0\end{aligned}\right\} \quad (3)$$

The general solution for Eq. (3) can be written after substitution in Eqs. (1) and (2) to be in the form

$$T_c(x) = Y_1 \exp(nx) + Y_2 \exp(-nx) + \frac{\delta}{(C_1 - C_0)} \quad (4)$$

$$T_h(x) = \left(\frac{C_1 + n}{C_0}\right) Y_1 \exp(nx) + \left(\frac{C_1 - n}{C_0}\right) Y_2 \exp(-nx) + \frac{\delta}{(C_1 - C_0)} \quad (5)$$

where Y_1 and Y_2 are arbitrary constants to be determined from the boundary conditions, and n is determined from

$$n = \sqrt{C_1^2 - C_0^2} \quad (6)$$

IV. Boundary Conditions

Equations (4) and (5) are subject to the following two boundary conditions:

(1) At the inlet fluid section (X=0), the cold fluid temperature $T_c(0)$ is given. .

(2) At the closed end section (X=L), the cold fluid temperature is equal to the hot fluid temperature.

Substituting in Eqs. (4) and (5), the temperature distribution $T_c(x)$ and $T_h(x)$ is given by

$$T_c(x) = \frac{\delta}{(C_1 - C_0)} - \left[\frac{\delta}{(C_1 - C_0)} - T_c(0)\right] \left[\frac{n\cosh n(L - x) + (C_1 - C_0)\sinh n(L - x)}{n\cosh nL + (C_1 - C_0)\sinh nL}\right] \quad (7)$$

$$T_h(x) = \frac{\delta}{(C_1 - C_0)} - \left[\frac{\delta}{(C_1 - C_0)} - T_c(0)\right] \left[\frac{n\cosh n(L - x) - (C_1 - C_0)\sinh (L - x)}{n\cosh nL + (C_1 - C_0)\sinh nL}\right] \quad (8)$$

V. General Findings

A. The Flow Factor (*F*)

The temperature difference between cold and hot fluids at any location (x) is given from Eqs. (7) and (8) by

$$[T_h(x) - T_c(x)] = \left[\frac{\delta}{(C_1 - C_0)} - T_c(0)\right] \left[\frac{2(C_1 - C_0)\sinh n(L - x)}{n\cosh nL + (C_1 - C_0)\sinh nL}\right] \quad (9)$$

Particularly, at the open end (x=0), both the temperature difference and the net heat collected per unit collector area are determined using Eq. (9) as

$$[T_h(0) - T_c(0)] = \left[\frac{\delta}{(C_1 - C_0)} - T_c(0)\right] \left[\frac{2(C_1 - C_0)\sinh nL}{n\cosh nL + (C_1 - C_0)\sinh nL}\right] \quad (10)$$

and

$$Q''_{coll} = \frac{\dot{m}c_p}{SL}\,[T_h(0) - T_c(0)] \quad (11)$$

where S is the spacing between any two collector units.

Using the conductance coefficients (B's) defined in Appendix B, the extracted energy by the fluid is rewritten as

$$Q''_{coll} = \left[\underbrace{\left(E_1 + E_2\frac{B_4}{B_7} + E_3\frac{B_6}{B_7}\right)}_{\text{Energy absorbed}} - \underbrace{B_0\,(T_c(0) - T_A)}_{\text{Energy lost to ambient air}}\right] \cdot F \quad (12)$$

where F is a dimensionless "flow-factor" defined by

$$F = \frac{GD_{f,0}}{SL\,B_0}\left[\frac{2\sinh nL}{\left(\frac{B_3}{nG}\right)\cosh nL + \sinh nL}\right] \qquad (13)$$

where B_0 is the overall heat transfer coefficient given by Eq. B-25. If the collector glass tubes were made such that the glass absorptivity $\alpha_{f,e}$ and $\alpha_{s,e}$ are negligible, Eq. (12) will become similar to the general Hottel, Whillier and Bliss form

$$Q''_{coll} \cong \left\{E_1 - B_0\,[T_c(0) - T_A]\right\} \cdot F$$

B. Collector Efficiency

The collector efficiency based on the solar radiancy on the projected area is defined by

$$\eta = \frac{Q''_{coll}}{I}$$

or, using Eq. (12),

$$\eta = F\left\{\lambda\left[\alpha_{a,e} + \alpha_{f,e}\frac{B_4}{B_7} + \alpha_{s,e}\frac{B_6}{B_7}\right] - B_0\frac{[T_c(0) - T_A]}{I}\right\} \qquad (14)$$

Equation (14) suggests that if the collector efficiency is plotted vs $(T_c(0) - T_A)/I$, the results would fit approximately a straight line whose slope (B_0F) is an indication of the heat losses to the ambient and the intercept is an indication of the optical characteristics.

C. Highest Temperature at "No-Flow"

The temperature of the collector with "no-flow" or stagnant condition is an important value needed for coating stability and temperature control. Setting the temperature difference $[T_h(0) - T_c(0)]$ from Eq. (10) to the limit as G approaches zero (or n approaches ∞) one can prove that

$$\lim_{\text{as } n \to \infty}\,[T_h(0) - T_c(0)] = \frac{2\left[\left(E_1 + E_2\frac{B_4}{B_7} + E_3\frac{B_6}{B_7}\right) - (T_c(0) - T_A)\right]}{B_0\left[1 + \sqrt{1 + (2\overline{B}_3/B_0)}\right]} \qquad (15)$$

where $\overline{B}_3$ is the free-convection heat transfer coefficient between absorber tubes and fluid. If the collector was left with a very small flow rate under the sun with an inlet temperature equal to ambient temperature T_A, the simulated maximum temperature of the leaving fluid will be

$$T_{h_{max}}(0) \cong T_A + \frac{E_1}{B_0} \cdot \frac{2}{1 + \sqrt{(2\overline{B}_3/B_0) + 1}} \qquad (16)$$

To support the parameterization study and the numerical evaluation of the above findings, a short computer program is written using the optical properties of Appendix A, the heat balance equations of Appendix B, and the temperature distribution given by Eqs. (7) and (8). The results of the second phase of this study will be the subject of the second report.

References

1. General Electric Solartron Model TC100 Vacuum Tube Solar Collector Publication, General Electric, Space Div., Phil., Pa.

2. Lansing, F. L., "Heat Transfer Criteria of a Tubular Solar Collector – The Effect of Reversing the Flow Pattern on Collector Performance," in *The Deep Space Network Progress Report 42-31*, pp. 108-114, Jet Propulsion Laboratory, Pasadena, Calif., Feb. 1976.

3. Lansing, F. L., *The Transient Thermal Response of a Tubular Solar Collector,* Technical Memorandum 33-781, NASA, July 1976.

4. Lansing, F. L., "A Two-Dimensional Finite Difference Solution for the Transient Thermal Behaviour of a Tubular Solar Collector," in *The Deep Space Network Progress Report 42-35*, pp. 110-127, Jet Propulsion Laboratory, Pasadena, Calif., Oct. 1976.

5. Kreith, F., *Principles of Heat Transfer*, Second Edition, Intext Educational Publishers, New York, 1968.

6. Duffie, J. A., and Beckman, W. A., *Solar Energy Thermal Process*, Wiley Interscience Publication, New York, 1974.

Definitions of Terms

a	glass absorption coefficient
b	absorber reflection coefficient
$B_0 \rightarrow B_8$	thermal conductance, kW/m^2°C
C_P	fluid specific heat, kWh/kg°C
C_0, C_1	constants
D	diameter
$E_1 \rightarrow E_6$	energy flux, kW/m^2
F	flow factor
G	heat capacity = $\dot{m}C_p/D_{f,o}$
H	convective heat transfer coefficient, kW/m^2°C
I	solar flux kW/m^2
K	thermal conductivity, kW/m°C
L	collector-unit length, m
$\dot{m}$	fluid mass flow rate, kg/h
n	characteristic constant, m^{-1}
Q	heat rate, kW
r	glass reflection coefficient
R	equivalent radiation heat transfer coefficient, kW/m^2°C
S	spacing between two consecutive collector units, m
T	temperature, K
X	distance
Y	constants, K
α	absorptivity
ρ	reflectivity
τ	transmissivity
λ	augmented radiation factor
η	collector efficiency
δ	parameter, °C/m
ϵ	emissivity

Subscripts

A	air in collector core
Am	ambient air
a	absorber shell
c	cold fluid
e	effective
f	first (outer) glass tube
h	hot fluid
i	inside
o	outside
s	second (inner) glass tube
t	serpentine tube
v	V-shaped reflector

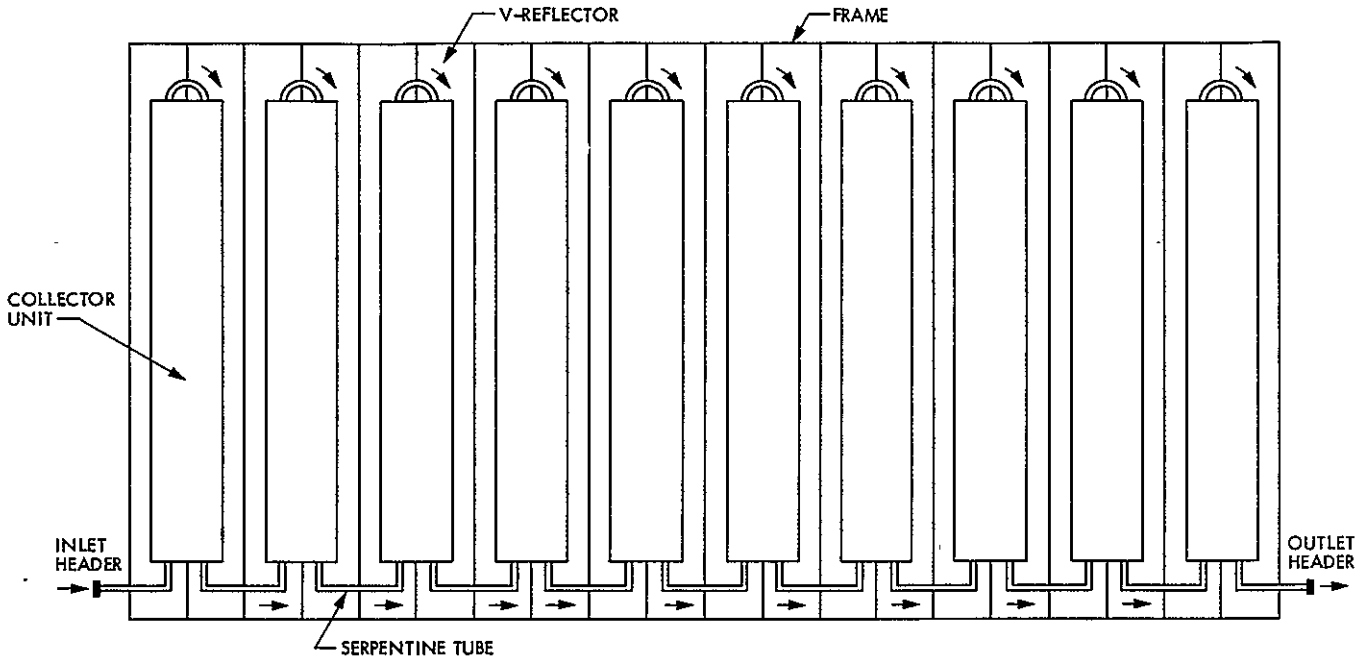

Fig. 1. A single collector module composed of 10 units

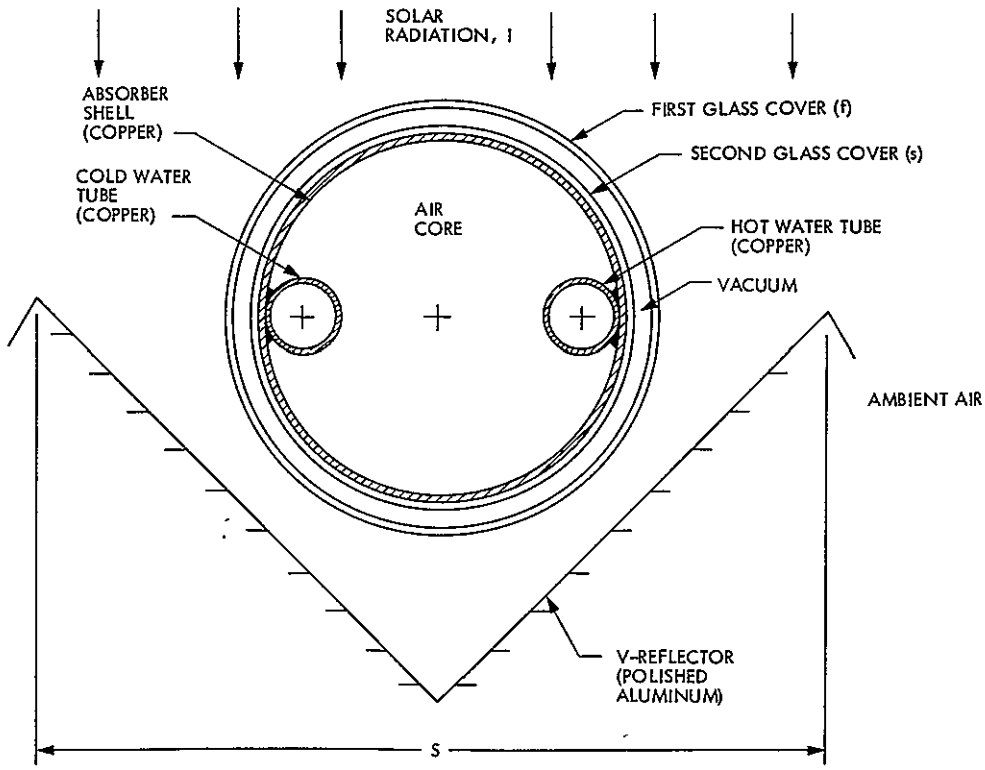

Fig. 2. Collector unit

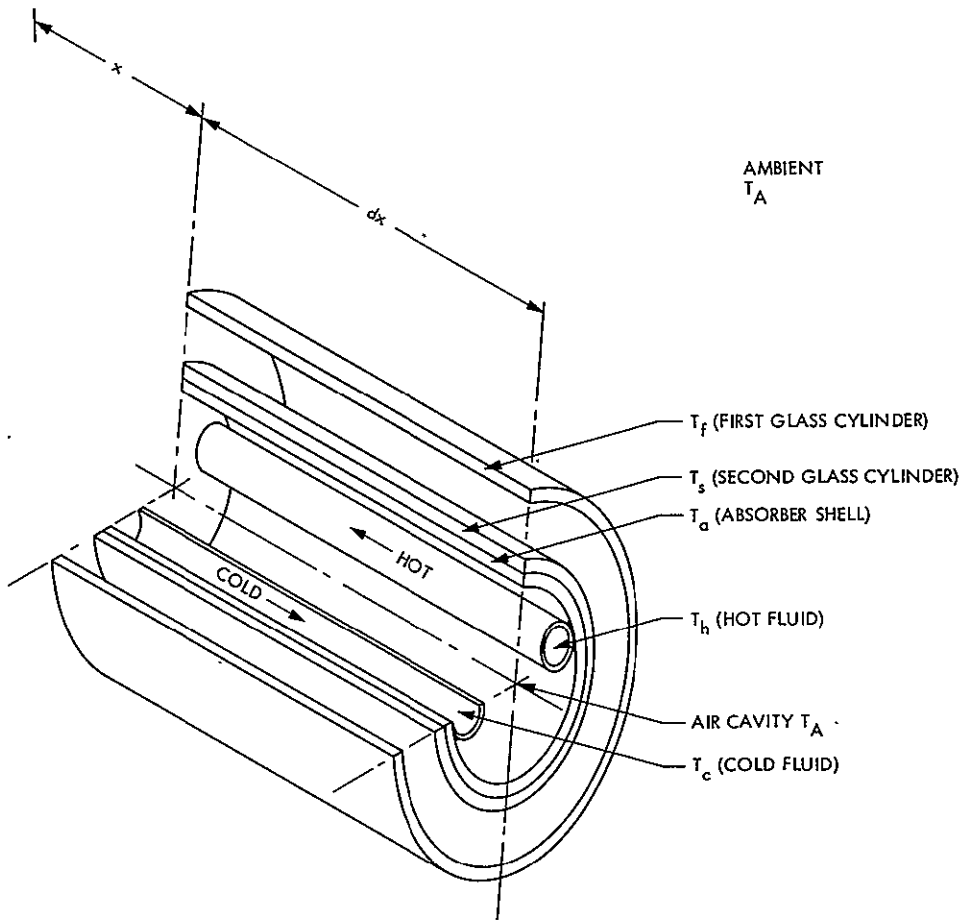

Fig. 3. Segment of a collector unit with thickness *dx*

Appendix A

Derivation of Optical Properties

In this appendix the effect of multiple reflections, absorption, and refraction of direct solar rays incident upon the collector tubes is discussed. The derivation of the effective absorptivity, reflectivity, and transmissivity will be made for each of the exterior glass tubes, the interior glass tube and the metallic absorber shell.

Since the radial spacing between the two coaxial glass tubes is small compared to their diameter, the optical properties derivation will be carried out assuming two parallel glass plates instead.

A-1. Optical Properties of a Single See-Through Sheet of Glazing

Figure A-1 shows the paths of a single beam of light when it falls on a single see-through sheet of glass. The intensity is assumed unity since the optical properties are dimensionless. The coefficients of absorption a and reflection r are applied both to the top and the bottom surfaces of the single glazing. The net transmissivity of a single glazing will be given by

$$\tau_f = a(1-r)^2 + a^3 r^2 (1-r)^2 + a^5 r^4 (1-r)^2 + \cdots$$

Using the infinite geometric series sum, τ_f is written as

$$\tau_f = \frac{a(1-r)^2}{1-a^2 r^2} \qquad \text{(A-1)}$$

Similarly, the absorptivity α_f is written as

$$\alpha_f = (1-a)(1-r) + ar(1-a)(1-r) + a^2 r^2 (1-a)(1-r) + \cdots$$

or

$$\alpha_f = \frac{(1-r)(1-a)}{1-ra} \qquad \text{(A-2)}$$

Since the first law of thermodynamics states that

$$\alpha_f + \tau_f + \rho_f = 1$$

then, the reflectivity ρ_f can be expressed as

$$\rho_f = r + \frac{ra^2 (1-r)^2}{1-r^2 a^2} \qquad \text{(A-3)}$$

The above optical properties are given the subscript f since they represent the properties of the first (outer) glass tube of the collector unit.

A-2. Optical Properties of a Single Sheet of Glazing with Opaque Bottom Surface

Figure A-2 illustrates the paths of a single light beam on a single sheet of glass whose bottom surface is opaque. The optical properties for this glazing type will be given a subscript S since it represents the second (inner) glass tube that surrounds the metallic absorber shell. In this case, the reflection coefficient r at the top surface and that at the bottom opaque surface b will be different. The absorption coefficient a will be the same as in case A-1, if all glazings have the same thickness and material. The optical properties can be obtained by summing the infinite geometric series of intensity taken from Fig. A-2. Accordingly, for the bottom surface

$$\alpha_B = a(1-r)(1-b) + a^3 br(1-r)(1-b)$$

$$+ a^5 b^2 r^2 (1-r)(1-b) + \cdots$$

or

$$\alpha_B = \frac{a(1-b)(1-r)}{1-a^2 br} \qquad \text{(A-4)}$$

Also,

$$\alpha_S = (1-r)(1-a) + ab(1-a)(1-r) + a^2 br(1-r)(1-a) + \cdots$$

$$\alpha_S = \frac{(1-r)(1-a)(1+ab)}{1-a^2 br} \qquad \text{(A-5)}$$

Since the energy conservation law can be written as

$$\alpha_B + \alpha_S + \rho_S = 1$$

then one can prove that

$$\rho_S = r + \frac{a^2 b\,(1-r)^2}{1 - a^2 br} \qquad \text{(A-6)}$$

A-3. Combining Two Sheets of Glazing With an Opaque Bottom Surface for the Second Sheet

Combining the above two separate cases in Sections A-1 and A-2, the effective optical properties of each glazing will be derived using the light paths as illustrated in Fig. A-3. The properties of the first glazing will be τ_f, α_f, and ρ_f as expressed by Eqs. (A-1), (A-2), and (A-3), respectively. For the second glazing, the properties α_B, α_S, and ρ_S are given by Eqs. (A-4), (A-5), and (A-6), respectively. The effective absorptivity $\alpha_{a,e}$ of the metallic absorber shell surface next to the second glazing will be found by summing the infinite series.

$$\alpha_{a,e} = \alpha_B \tau_f + \alpha_B \tau_f \rho_f \rho_S + \alpha_B \tau_f \rho_f^2 \rho_S^2 + \cdots$$

or

$$\alpha_{a,e} = \frac{\alpha_B \tau_f}{1 - \rho_f \rho_S} \qquad \text{(A-7)}$$

Also, the effective absorptivity of the first glazing $\alpha_{f,e}$ when it is placed next to the second glazing is determined by summing the infinite series

$$\alpha_{f,e} = \alpha_f + \alpha_f \tau_f \rho_S + \alpha_f \tau_f \rho_f \rho_S^2 + \alpha_f \tau_f \rho_f^2 \rho_S^3 + \cdots$$

or

$$\alpha_{f,e} = \alpha_f + \frac{\alpha_f \tau_f \rho_S}{1 - \rho_f \rho_S} \qquad \text{(A-8)}$$

Similarly, for the second glazing, the effective absorptivity $\alpha_{S,e}$ is expressed as:

$$\alpha_{S,e} = \alpha_S \tau_f + \alpha_S \tau_f \rho_f \rho_S + \alpha_S \tau_f \rho_f^2 \rho_S^2 + \cdots$$

or

$$\alpha_{S,e} = \frac{\alpha_S \tau_f}{1 - \rho_f \rho_S} \qquad \text{(A-9)}$$

On the other hand, the sum of reflections from the first glazing will be written as:

$$\rho_{f,e} = \rho_f + \rho_S \tau_f^2 + \rho_f \rho_S^2 \tau_f^2 + \rho_f^2 \rho_S^3 \tau_f^2 + \cdots$$

or

$$\rho_{f,e} = \rho_f + \frac{\rho_S \tau_f^2}{1 - \rho_f \rho_S} \qquad \text{(A-10)}$$

Equations (A-7) through (A-10) are the effective properties to be used for the thermal analysis. As a cross-checking, the properties also satisfy the energy conservation law where

$$\alpha_{f,e} + \alpha_{s,e} + \alpha_{a,e} + \rho_{f,e} = 1 \qquad \text{(A-11)}$$

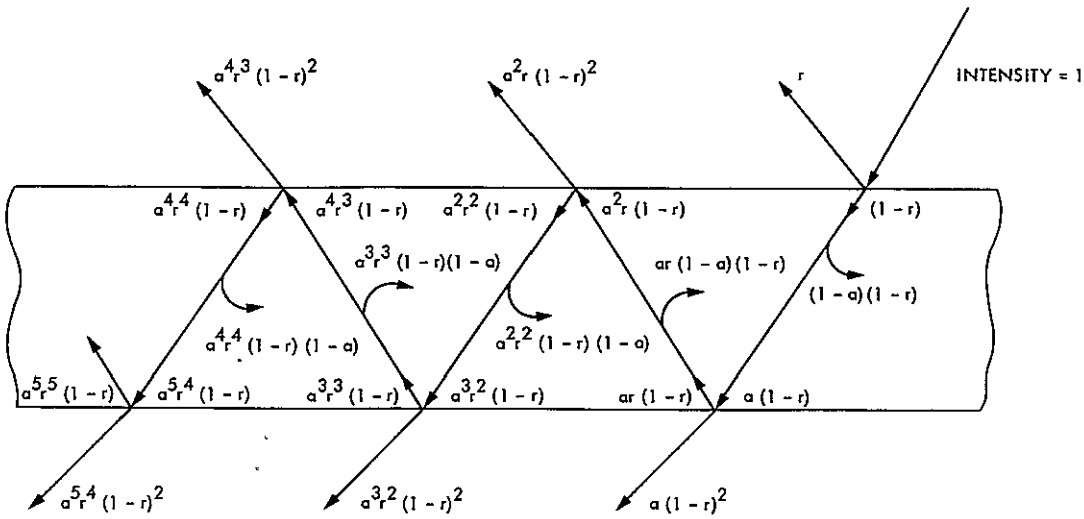

Fig. A-1. Paths and intensities of a light beam on a single glazing

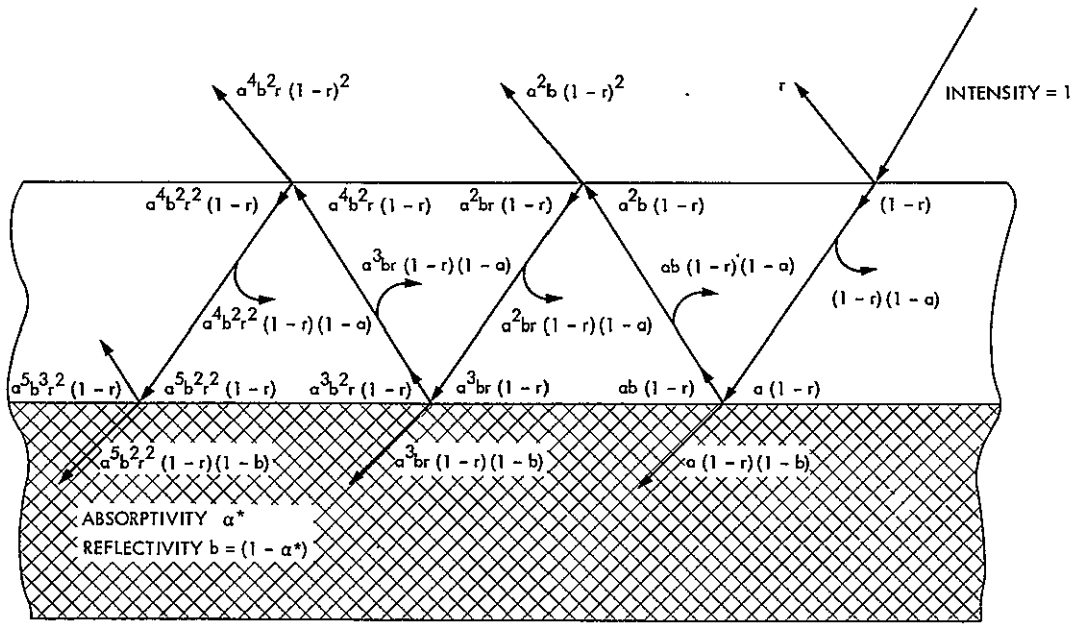

Fig. A-2. Paths and intensities of a light beam on a single glazing with opaque bottom surface

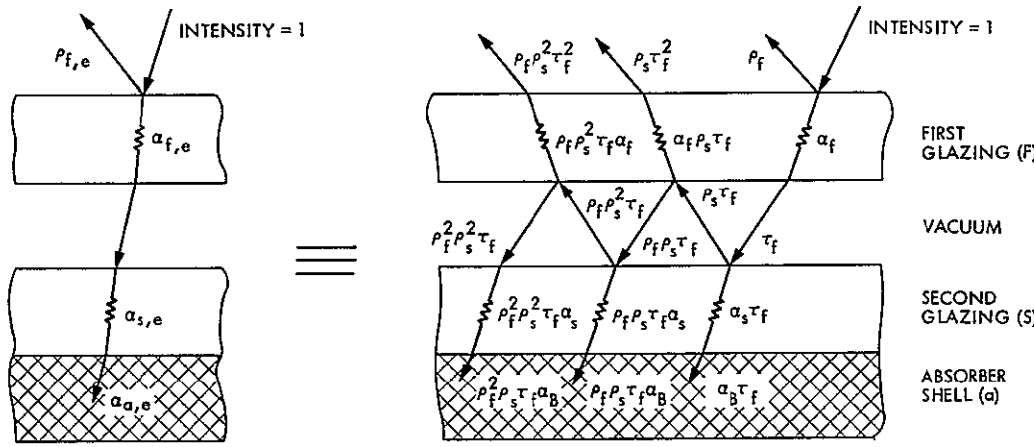

Fig. A-3. Combination of two sheets of glazing with an opaque bottom surface for the second

Appendix B

Derivation of Heat Transfer Rate Equations

Following the assumptions made in the Section III, a segment of the collector unit whose thickness is dx and located at a distance x from the inlet fluid section is as shown in Fig. 3. The differential rates of heat flux are divided as shown by Sankey diagram in Fig. B-1, whereby

dQ_1 = total solar irradiation (direct and diffuse) on the outer glass tube from all sides including the irradiation from the back V-reflector.

$$dQ_1 = \lambda I D_{f,o} dx \tag{B-1}$$

where λ is given by

$$\lambda = 1 + \rho_v \left(\frac{S}{D_{f,o}} - 1 \right) \tag{B-2}$$

dQ_2 = outward reflection loss from the collector unit

$$dQ_2 = \rho_{f,e} \, dQ_1 \tag{B-3}$$

where $\rho_{f,e}$ is given by Eq. (A-10)

dQ_3 = effective absorbed energy by the outer glass tube

$$dQ_3 = \alpha_{f,e} dQ_1 \tag{B-4}$$

where $\alpha_{f,e}$ is given by Eq. (A-8)

dQ_4 = effective absorbed energy by the second (inner) glass tube

$$dQ_4 = \alpha_{s,e} \, dQ_1 \tag{B-5}$$

where $\alpha_{s,e}$ is given by Eq. (A-9)

dQ_5 = effective absorbed energy by the metallic absorber shell

$$dQ_5 = \alpha_{a,e} \, dQ_1 \tag{B-6}$$

where $\alpha_{a,e}$ is given by Eq. (A-7)

dQ_6 = conduction heat transfer between the second (inner) glass tube and the absorber shell

$$dQ_6 = \frac{2\pi (T_a - T_s) \, dx}{\left[\frac{\ell n \, (D_{S,o}/D_{S,i})}{K_s} + \frac{\ell n \, (D_{a,o}/D_{a,i})}{K_a} \right]} \tag{B-7}$$

dQ_7 = convection heat transfer between the absorber shell and the air trapped in the absorber core

$$dQ_7 = H_{aA} \, (T_a - T_A) \pi (D_{a,i} + 2D_{t,o}) \, dx \tag{B-8}$$

dQ_8 = convection heat transfer between the absorber tubes and the hot fluid

$$dQ_8 = H_{ah} \, (T_a - T_h) \pi D_{t,i} \, dx \tag{B-9}$$

dQ_9 = convection heat transfer between the absorber tubes and the cold fluid

$$dQ_9 = H_{ac} \, (T_a - T_c) \, \pi D_{t,i} \, dx \tag{B-10}$$

dQ_{10} = sensible heat gain by the hot fluid

$$dQ_{10} = -\dot{m} c_p \left(\frac{dT_h}{dx} \right) dx \tag{B-11}$$

where the (-) sign was introduced since the hot fluid flow is in the opposite direction to the positive x direction.

dQ_{11} = sensible heat gain by the cold fluid

$$dQ_{11} = + \dot{m} c_p \left(\frac{dT_c}{dx} \right) dx \tag{B-12}$$

dQ_{12} = radiation heat transfer between the second (inner) glass tube and the first (outer) glass tube

$$dQ_{12} = \frac{\sigma (T_S^4 - T_f^4) \, \pi D_{S,o} \, dx}{\frac{1}{\epsilon_S} + \left(\frac{1}{\epsilon_f} - 1 \right) \left(\frac{D_{S,o}}{D_{f,i}} \right)} \tag{B-13}$$

dQ_{13} = radiation heat losses from the outer surface of the first (outer) glass tube to the ambient air

$$dQ_{13} = \sigma \epsilon_f (T_f^4 - T_A^4) \pi D_{f,o}\, dx \qquad \text{(B-14)}$$

dQ_{14} = convection heat transfer from the outer surface of the first (outer) glass tube to the ambient air

$$dQ_{14} = H_{fAm} (T_f - T_A) \pi D_{f,o}\, dx \qquad \text{(B-15)}$$

Applying the first law of thermodynamics at steady state to the collector components will yield the following heat balance equations (see Refs., 5 and 6):

For the absorber tube:

$$dQ_5 - (dQ_6 + dQ_7 + dQ_8 + dQ_9) = 0 \qquad \text{(B-16)}$$

For the hot fluid:

$$dQ_8 - dQ_{10} = 0 \qquad \text{(B-17)}$$

For the cold fluid:

$$dQ_9 - dQ_{11} = 0 \qquad \text{(B-18)}$$

For the first (outer) glass cover:

$$dQ_3 + dQ_{12} - dQ_{13} - dQ_{14} = 0 \qquad \text{(B-19)}$$

For the second (inner) glass cover:

$$dQ_4 + dQ_6 - dQ_{12} = 0 \qquad \text{(B-20)}$$

For the incident solar energy:

$$dQ_1 - dQ_2 - dQ_3 - dQ_4 - dQ_5 = 0 \qquad \text{(B-21)}$$

Summing Eqs. (B-16) through (B-21) yields

$$dQ_1 - (dQ_2 + dQ_7 + dQ_{13} + dQ_{14}) = 0 \qquad \text{(B-22)}$$

Equation (B-22) shows that the thermal losses from the collector will be only the summation of (1) the outward light reflection from the first (outer) glass tube, (2) the convection and radiation heat transfer to the ambient air and sky from the first (outer) glass, and (3) the convection heat transfer from the inner absorber walls to the air core and ambient air.

The elementary radiation heat transfer dQ_{12} and dQ_{13} are further linearized by defining the radiation heat transfer coefficients R_{sf} and R_{fAm} such that

$$\left.\begin{aligned} R_{sf} &= \frac{\sigma (T_s^4 - T_f^4)}{(T_s - T_f)\left[\frac{1}{\epsilon_s} + \left(\frac{1}{\epsilon_f} - 1\right)\left(\frac{D_{s,o}}{D_{f,i}}\right)\right]} \\ R_{fAm} &= \epsilon_f \frac{\sigma (T_f^4 - T_A^4)}{(T_f - T_A)} \end{aligned}\right\} \qquad \text{(B-23)}$$

Equations (B-13) and (B-14) are reduced to

$$dQ_{12} = R_{sf} \pi D_{s,o} (T_S - T_f)\, dx \qquad \text{(B-13)}$$

$$dQ_{13} = R_{fAm} \pi D_{f,o} (T_f - T_A)\, dx \qquad \text{(B-14)}$$

The five linearized heat balance equations, Eqs. (B-16) through (B-20), will be grouped after division by $(D_{f,o}\, dx)$ as follows:

For the absorber shell:

$$E_1 - B_1 (T_a - T_s) - B_2 (T_a - T_A) - B_3 (T_a - T_c) - B_3 (T_a - T_h) = 0 \qquad \text{(B-24)}$$

For the hot fluid:

$$G \frac{dT_h}{dx} = -B_3 (T_a - T_h) \qquad \text{(B-25)}$$

For the cold fluid:

$$G \frac{dT_c}{dx} = B_3 (T_a - T_c) \qquad \text{(B-26)}$$

For the first (outer) glass tube:

$$E_2 + B_4 (T_s - T_f) - B_5 (T_f - T_A) = 0 \qquad \text{(B-27)}$$

For the second (inner) glass tube:

$$E_3 + B_1 (T_a - T_s) - B_4 (T_s - T_f) = 0 \qquad \text{(B-28)}$$

where

$$
\left.
\begin{aligned}
B_1 &= \frac{2\pi/D_{f,o}}{\left[\frac{\ell n\,(D_{s,o}/D_{s,i})}{K_s} + \frac{\ell n\,(D_{a,o}/D_{a,i})}{K_a}\right]} \\
B_2 &= \pi\,(D_{a,i} + 2\,D_{t,o})\,H_{aA}/D_{f,o} \\
B_3 &= \pi\,(D_{t,i}/D_{f,o})\,H_{ah} \\
B_4 &= \pi\,R_{sf}\,(D_{s,o}/D_{f,o}) \\
B_5 &= \pi\,(H_{fAm} + R_{fAm})
\end{aligned}
\right\} \quad \text{(B-29)}
$$

$$
\left.
\begin{aligned}
E_1 &= \alpha_{a,e}\,\lambda I \\
E_2 &= \alpha_{f,e}\,\lambda I \\
E_3 &= \alpha_{s,e}\,\lambda I \\
G &= \dot{m}c_p/D_{f,o}
\end{aligned}
\right\} \quad \text{(B-30)}
$$

Expressing the temperatures T_f and T_s in terms of T_a using Eqs. (B-24), (B-27), and (B-28) yields

$$
\left.
\begin{aligned}
T_f &= (E_4 + B_4\,T_s)/B_6 \\
T_s &= (E_5 + B_6\,T_a)/B_7 \\
T_a &= [E_6 + B_3\,(T_h + T_c)]\,/B_8
\end{aligned}
\right\} \quad \text{(B-31)}
$$

where

$$
\left.
\begin{aligned}
E_4 &= E_2 + B_5 T_A \quad , \quad B_6 = (B_4 + B_5) \\
E_5 &= E_3\frac{B_6}{B_1} + E_4\frac{B_4}{B_1} \quad , \quad B_7 = B_6 + \frac{B_4 B_5}{B_1} \\
E_6 &= E_1 + B_2 T_A + \frac{B_1 E_5}{B_7}, \quad B_8 = B_2 + 2B_3 + \frac{B_4 B_5}{B_7}
\end{aligned}
\right\} \quad \text{(B-32)}
$$

Substituting in Eqs. (B-25) and (B-26), the two differential equations for the hot and cold fluid streams at any position X will be

$$
\frac{dT_h}{dx} = -\delta - C_0\,T_c + C_1\,T_h \qquad \text{(B-33)}
$$

and

$$
\frac{dT_c}{dx} = \delta + C_0\,T_h - C_1\,T_c \qquad \text{(B-34)}
$$

where

$$
\left.
\begin{aligned}
\delta &= \frac{B_3}{B_8}\,,\frac{E_6}{G} \\
C_0 &= \frac{B_3^2}{GB_8} \\
C_1 &= \frac{B_3}{GB_8}\,(B_8 - B_3)
\end{aligned}
\right\} \quad \text{(B-35)}
$$

The term $\delta/(C_1 - C_0)$ appears in solving Eqs. (B-33) and (B-34) and can be expressed as:

$$
\frac{\delta}{(C_1 - C_0)} = T_A + \frac{\left(E_1 + E_2\frac{B_4}{B_7} + E_3\frac{B_6}{B_7}\right)}{\left(B_2 + \frac{B_4 B_5}{B_7}\right)} \qquad \text{(B-36)}
$$

The overall heat loss coefficient B_0 follows from Eq. (B-36), to be

$$
B_0 = \left(B_2 + \frac{B_4 B_5}{B_7}\right) \qquad \text{(B-37)}
$$

Eqs. (B-36) and (B-37) are useful in giving the physical meaning needed to the collector efficiency expression as shown in the text.

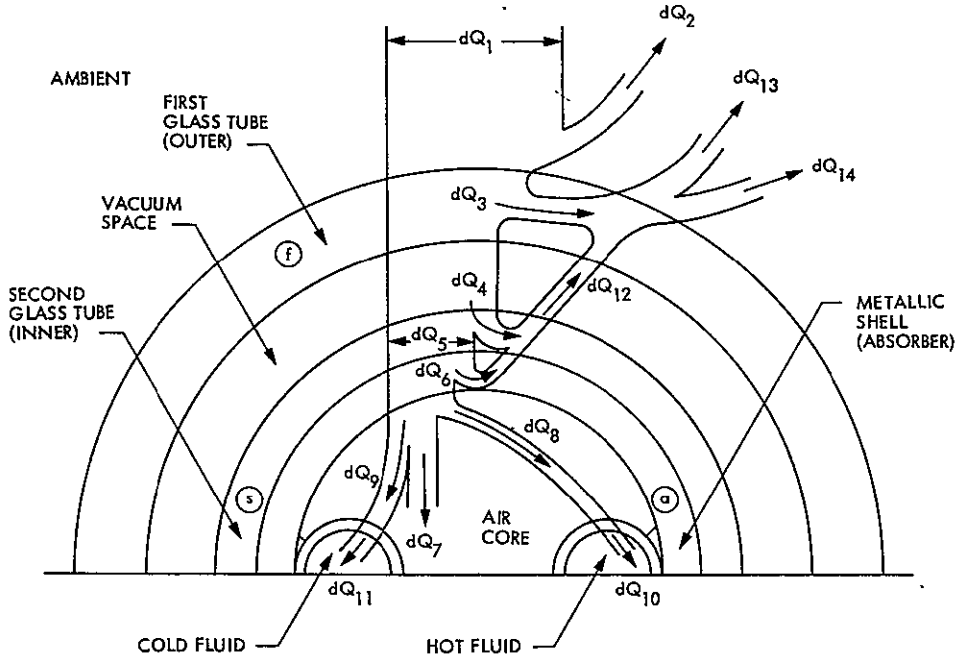

Fig. B-1. Sankey diagram for tubular collector

D/6

N79-19061

Automatic Filament Warm-Up Controller

J. McCluskey and J. Daeges
Radio Frequency and Microwave Subsystems Section

As part of the unattended operations objective of the DSN deep space stations, this filament controller serves as a step between manual operation of the station and complete computer control. Formerly, the operator was required to devote five to fifteen minutes of his time just to properly warm up the filaments on the klystrons of the high power transmitters. The filament controller reduces the operator's duty to a one-step command and is future-compatible with various forms of computer control.

I. Motivation

As part of the unattended operations objective of the DSN deep space stations, this filament controller serves as a step between manual operations of the station and complete computer control. Formerly, the operator was required to devote five to fifteen minutes of his time just to properly warm up the filaments on the klystrons of the high power transmitters. The filament controller reduces the operator's duty to a one-step command and is future-compatible with various forms of computer control.

II. Design Requirements

The controller was designed to incorporate the following characteristics:

(1) Automatic warm-up of filament upon command

(2) Noise immunity to crowbar firings on beam supply

(3) Fail-safe power failure design

(4) Protection from operator induced errors

(5) Beam interlocks to prevent maltreatment of tube

(6) Filament current and voltage monitoring outputs

(7) Compatibility with computer control

(8) Digital switches for setting klystron operating filament voltage and current

III. System Configuration

Klystron application circuitry is such that the filament floats at full beam potential. This can be up to 70 kV, so an isolation transformer with filament voltage and current sense windings is used to supply filament power. These sense voltages are rectified with peak detectors using operational amplifier and appropriately filtered to remove transients. The power to the isolation transformer is supplied by a motor-controlled Variac, which is controlled, in turn, by the circuit board (Figs. 1 and 2).

When the user issues a warm-up command (raise) at the Local Control Console (LCC), the circuit applies power to the Variac via a solid state relay, and turns the motor on in the "up" direction. The motor continues to run until the maximum programmed current or the operating voltage limit is

reached. When the filament is cold and the resistance low, it will always current limit first, and will pulse the motor every few seconds, maintaining the current at the limit as the filament warms up. When the filament reaches 70 percent of its operating voltage, a 20-minute timer is started. This timer, with other conditions, generates the filament ready signal, which enables the beam voltage interlock (Fig. 3).

When the filament is hot and current limiting no longer occurs, the filament voltage is regulated to within ±0.1 volt. A filament shutdown can now be initiated by three events: (1) a down command from the operator, (2) a failure of the cooling (filament flow), or (3) a power failure for more than a few seconds.

An operator shutdown command would consist of pressing "lower" switch (Fig. 1), which changes the circuit mode from "up" to "halt" to "down." A cooling failure forces a "down" mode, but only after a one-minute time delay. A power failure longer than five seconds causes the circuit to be reset, removing filament power and mechanically lowering the Variac when power returns. The Variac must be lowered to its limit before it can again be raised.

Another feature allowing either manual or external computer control is the override function (Fig. 3). When enabled, it suppresses the voltage regulating action of the circuit, but not the safety features. When override is enabled, the raise and lower buttons at the LCC control the motor connected to the Variac, still subject to the current and voltage limit set by switches in the filament supply chassis. This allows an operator or computer to directly control the filament power.

A complete filament chassis has now been built and will be tested in an operational transmitter at DSS 13.

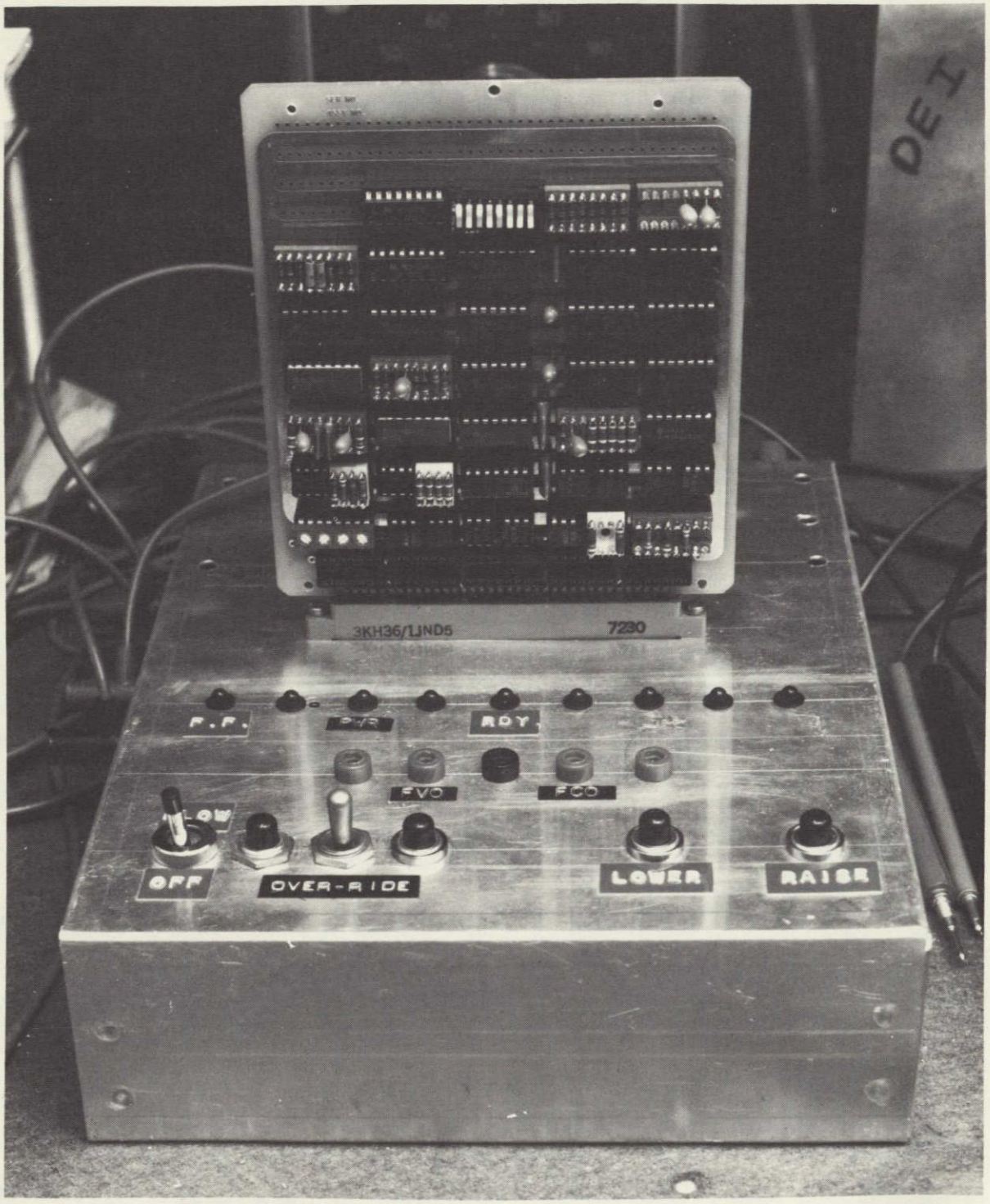

Fig. 1. Prototype circuit board to bench test the automatic circuit

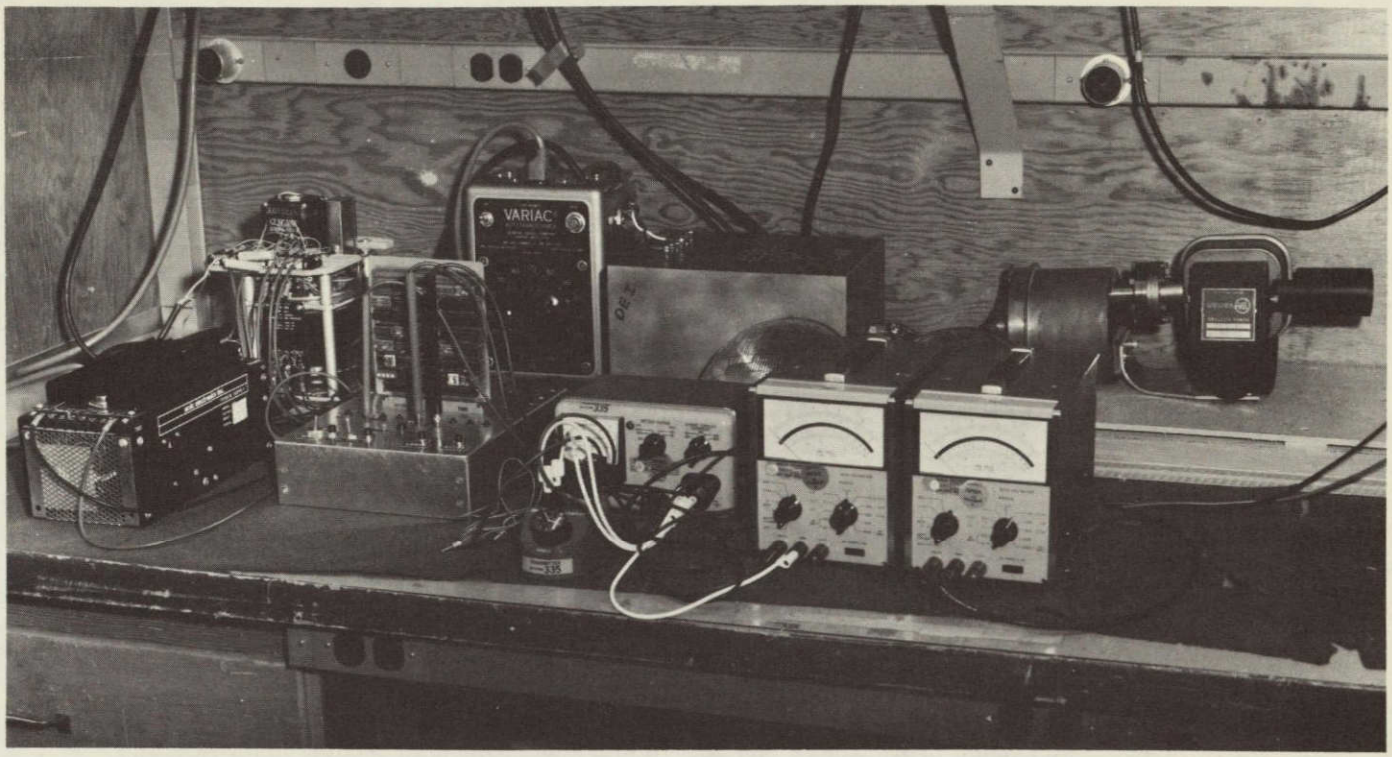

Fig. 2. Complete bench test setup using an actual klystron filament

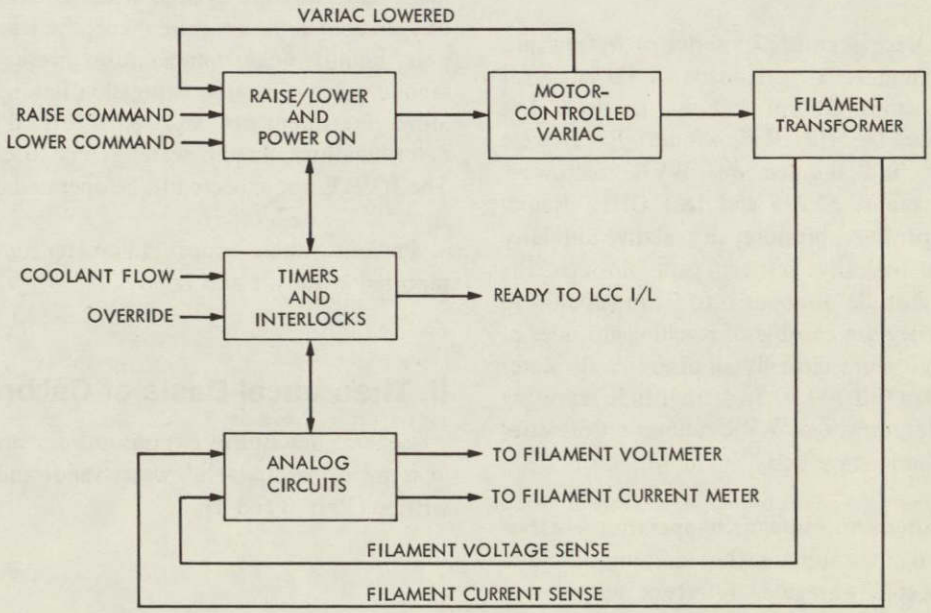

Fig. 3. Block diagram of the controller

D17

N79-19062

DSN Water Vapor Radiometer—Tropospheric Range Delay Calibration

S. D. Slobin and P. D. Batelaan
Radio Frequency and Microwave Subsystems Section

This report discusses the calibration of the DSN water vapor radiometer by means of simultaneous antenna temperature and radiosonde measurements at Edwards Air Force Base. The calibration of radiometer gain and hot load radiometric noise temperature is also described. Calibration equations are given. It is found that with a selected data set, the RMS error is less than 1 cm over a total delay range of 9 to 38 cm. Limitations on the use of the water vapor radiometer are also given.

I. Introduction

During August and December 1977 a series of water vapor radiometer (WVR) system tests were made at Edwards Air Force Base (EAFB), about 80 km (50 mi) north of Los Angeles, in the Mojave Desert. Radiosondes (RWS) were launched there daily, and simultaneous WVR microwave measurements were made at 22.235 and 18.5 GHz. Radiosondes report the temperature, pressure, and relative humidity in flight along some basically vertical path through the atmosphere up to an altitude of about 6 to 9 km (20,000 to 30,000 ft) at EAFB. They are capable of reaching altitudes of 30 km (100,000 ft), but since virtually all atmospheric water vapor resides below 6 km (20,000 ft), higher altitude reporting is not necessary for the purpose of WVR calibration of water vapor-induced tropospheric range delay.

Tipping curve measurements (antenna temperature vs elevation angle) were used to calibrate the radiometric noise temperature of the heated waveguide reference termination (hot load).

With a calibrated hot load, absolute determinations of antenna temperature were made using the ambient and hot loads as calibration points. When corrections for cosmic and oxygen contributions were made, the resulting "water" (vapor plus liquid) noise temperatures were used to develop a second-order regression expression linking WVR noise temperature measurements and RWS-derived tropospheric delay determinations. Liquid water refers to clouds only, not rain. The WVR is not expected to be operated during rain.

Previous water vapor radiometer development has been reported in Refs. 1 and 2.

II. Theoretical Basis of Calibration

General descriptive expressions for brightness temperature in terms of precipitable[1] water vapor and liquid water can be written (Refs. 3 and 4):

[1] Precipitable water is the amount or depth of water along a particular path that would lie on the ground in liquid form if it were removed from moist air or clouds. It has the units g/cm² or cm.

$$T_{22.235} = \overbrace{2.7}^{\text{cosmic}} + \overbrace{3.8m}^{\text{oxygen}} + \overbrace{16M_V}^{\text{vapor}} + \overbrace{237M_L}^{\text{liquid}} \quad (1)$$

$$T_{18.5} = 2.7 + 3.0m + 4.416M_V + 164M_L \quad (2)$$

where

T = antenna temperature at the given frequency

m = number of air masses through which the antenna looks; e.g., $m = 2$ at 30-deg elevation angle

M_V = precipitable water vapor along antenna beam, cm

M_L = precipitable liquid water along antenna beam, cm

Typical values used in this expression are:

M_V = 1.2 g/cm^2 (cm) along a vertical path for a surface density of 7.5 g/m^3 and a scale height[2] of 1.6 km above the ground

M_L = 0.1 g/cm^2 (cm) along a vertical path for a dense cloud (1 g/m^3) 1 km thick

16 = water vapor emission coefficient as determined in Ref. 4 by integrating radiosonde runs at Tuscon, Arizona (K/g/cm^2)

16/4.416 = ratio of water vapor attenuation (emission) at 22.235 and 18.5 GHz, respectively

237 = K/g/cm^2 from emission calculations using a particular cloud model (Refs. 5 and 6)

237/164 = (frequency)^2 attenuation relationship in liquid water clouds (Refs. 5 and 6).

Whereas the vapor coefficients can be determined with fair accuracy (10 percent) from radiosonde measurements and integration of the equation of radiative transfer, the liquid coefficients may be in error by an order of magnitude, as they are based on assumptions of the values of "unmeasurables," such as the index of refraction of an inhomogeneous distribution of liquid water particles with unknown size distribution (1 to 50 microns radius).

Tropospheric range delay can be determined theoretically and experimentally as a function of precipitable vapor and liquid (Refs. 3 and 4):

$$\Delta L = 6.1 M_V + 1.6 M_L$$

$$= 7.32 + 0.16 = 7.48 \text{ cm for the typical values given above} \quad (3)$$

[2]Scale height is that height above the ground where the water vapor density has decreased to $1/e$ of its surface value, assuming an exponential distribution of density.

It is seen that even a dense cloud has a small effect on range delay when compared to the effect of a normal water vapor distribution. The principal confusing aspect of liquid water is its large contribution to antenna temperature without a corresponding effect on range delay. The two-frequency atmospheric probing technique allows the separation of vapor and liquid effects.

Manipulation of the previous equations allows one to solve for range delay and precipitable water in terms of "water" noise temperature, where the "water" noise temperature is inferred from measurements of antenna temperature:

$$\Delta L = 0.624T_{W22} - 0.899T_{W18} \quad (4)$$

where T_{W22} and T_{W18} are water noise temperatures at 22.235 and 18.5 GHz, with typical values of 42.9 K and 21.7 K, respectively, for the vapor and liquid (cloud) combination described above.

$$M_V = 0.103\,T_{W22} - 0.150\,T_{W18}$$

$$= 1.2 \text{ g/cm}^2 \text{ (cm) typically for vapor} \quad (5)$$

$$M_L = -0.00273T_{W22} + 0.0101T_{W18}$$

$$= 0.1 \text{ g/cm}^2 \text{ typically for liquid} \quad (6)$$

The solution for zenith range delay in terms of zenith *antenna* temperatures is:

$$\Delta L = 1.034 + 0.624T_{22} - 0.899T_{18} \quad (7)$$

where the T's are antenna temperatures measured at zenith only. Note that the coefficients of the temperature terms remain the same.

Figure 1 shows a plot of Eq. (4) in the region of validity (the tilted triangular region):

$$\Delta L > 0.0$$

$$T_{W18} < 0.687T_{W22} \text{ (liquid only, } M_V = 0.0)$$

$$T_{W18} > 0.270T_{W22} \text{ (vapor only, } M_L = 0.0)$$

In the vapor-only condition, all data points would lie along the edge of the plane defined by the line:

$$\Delta L = 0.624T_{W22} - 0.899T_{W18} \quad (8)$$

where $T_{W18} \cong 0.270T_{W22}$.

The liquid-only condition results in data points lying along the line:

$$\Delta L = 0.624T_{W22} - 0.899T_{W18} \tag{9}$$

where $T_{W18} = 0.687T_{W22}$. Delay values for this condition are small, approximately 0.6 cm for water noise temperatures of 100 K and 68.7 K at 22.235 and 18.5 GHz, respectively.

The real world operates with antenna temperatures which show a condition known as "saturation." In this case, the antenna temperatures do not rise as rapidly as increasing amounts of vapor and liquid. Indeed, infinite amounts of atmospheric water would result in antenna temperatures at both frequencies "saturated" at approximately 290 K. Graphically, the saturation effects may be shown as in Fig. 2, where the calibration plane shows an upward curvature—the delay rising faster than the temperature. Alternatively, the plane may be allowed to remain flat and the temperature axes stretched to accommodate the saturation effects.

Clearly, the calibration of the WVR must entail defining the bounded curved plane. Data should be taken under a variety of weather conditions to accurately define the surface. It should be remembered at this point that the examples given previously are for illustrative purposes and only approximately and occasionally represent values obtained by experiment.

III. Airmass Correction for Antenna Beamwidth

The WVR horn antenna has a moderately wide 3-dB beamwidth, 7 deg (±3.5 deg) at 22.235 GHz and 9 deg (±4.5 deg) at 18.5 GHz. Because of this, the net airmass through which the antenna looks is not given by the classic cosecant (elevation angle), even though the flat-earth assumption is made in this analysis. The lower half of the beam weights the pointing more than the upper half, so that electrically the antenna points lower than the geometric axis of the horn. For tipping curve analysis, the net airmass through which the antenna looks must be calculated.

This is done by integrating over the antenna beam:

$$\langle CSC(EL) \rangle = \frac{\int\int CSC(EL)\, G(\theta,\phi)\, dA}{\int\int G(\theta,\phi)\, dA} \tag{10}$$

where

EL = elevation angle

$G(\theta,\phi)$ = horn pattern gain

The results for particular angles are shown in Table 1.

For ease of calculation, the following expressions approximate the airmass values (m) in Table 1 for elevation angles greater than 30 deg:

$$m = (1/\sin EL)^{1.025} \text{ for } 22.235 \text{ GHz}$$

$$m = (1/\sin EL)^{1.035} \text{ for } 18.5 \text{ GHz} \tag{11}$$

EL = elevation angle of horn axis

Alternate expressions may be used for elevation angles less than 30 deg.

IV. Hot Load Calibration

The start of the WVR calibration sequence is to do a series of tipping curves, where noise temperature measurements (data counts) are made looking at the sky at elevation angles from zenith (one air mass) down to about 15 deg (4 airmasses). When these data are extrapolated to 0 airmasses (a purely imaginary condition, or one which results if the atmosphere is removed), the radiometer sees only the cosmic background and the horn, waveguide, and ground (spillover) thermal noise temperature contributions. We can write, in this case, for the zero airmass intercept value:

$$V_0 = k(T_A + T_C + T_E) \tag{12}$$

where

V_0 = data counts at zero airmass intercept

k = receiver gain, counts/K

T_A = sum of assumed or measured values for horn, waveguide switch, and ground contribution

T_C = cosmic background noise temperature, 2.7 K

T_E = receiver noise temperature, K

Switching to the ambient ("room" temperature) waveguide load results in:

$$V_1 = k(T_P + T_E) \tag{13}$$

where

V_1 = data counts on ambient load

k = receiver gain, counts/K

T_P = physical temperature of ambient load (the waveguide system is assumed to have the same temperature)

T_E = receiver noise temperature, K

A typical value of $T_A + T_C$ (cosmic + horn + ground) is 14 K ± 1 K based on waveguide measurements and estimates of horn spillover.

From these equations, one can solve for k and T_E. Typical values for some of the above values are:

k = 0.004135 counts/K at 22.235 GHz

k = 0.002467 counts/K at 18.5 GHz

$T_E \approx$ 700 K at 22.235 GHz

$T_E \approx$ 900 K at 18.5 GHz

Switching the receiver to the heated waveguide termination (hot load) allows one to solve for the radiometric noise temperature of the hot load:

$$T_{H,RAD} = \frac{1}{k}(V_2 - V_1) + T_P \qquad (14)$$

where

k = gain, counts/K

V_2 = data counts on hot load

V_1 = data counts on ambient load

T_P = physical temperature of ambient load (which equals the radiometric temperature of the ambient load)

Previous measurements of waveguide switch insertion loss and hot load parameters enable one to make preliminary adjustments to the measured physical temperature of the hot load as a first cut at determining its equivalent radiometric noise temperature. A multiplicative factor may be applied to the insertion-loss adjusted value to get the radiometric value as determined by Eq. (14). This method is valid because the physical temperature of the hot load is well regulated, and the correction should remain constant under this condition. Thus, operationally, the hot load radiometric noise temperature may be strictly related to its physical temperature without the necessity of doing tipping curves to continually re-determine receiver gain. Also, a radiometer temperature scale is set up, using the ambient and hot waveguide loads.

Table 2 shows the progressive correction of hot load temperatures from raw to calibrated for a typical hot load physical temperature.

V. Radiosonde Range Delay Measurements

A radiosonde measures pressure, temperature, and relative humidity during its ascent along a nearly vertical path through the atmosphere.

The "wet" range delay may be expressed as:

$$\Delta L = 10^{-6} \int_0^\infty N(h)\, dh \qquad (15)$$

where

N = refractivity = $373256.0 \cdot e/T_K^2$

h = height above surface, meters

e = water vapor pressure, millibars (1 mb = 100 N/m^2)

= $6.1 \cdot 10^B \cdot RH/100$

T_K = temperature, K

$B = \dfrac{7.4475 T_C}{234.7 + T_C}$

T_C = temperature, °C

RH = relative humidity, 0 to 100

For each radiosonde launch at Edwards AFB, the range delay was calculated. Typical values for zenith range delay range from 3 cm on a cold, dry winter night to 20 cm on a summer day when the warm air might contain a large amount of water vapor.

A uniform layer of water vapor 3 km thick, relative humidity 50 percent, temperature 7°C, would result in a range delay of 7.13 cm. Typical measurement accuracies of radiosondes are about 10 percent. The radiosonde does not measure liquid water parameters; but since the liquid effect on delay is usually very small, this is not a calibration problem.

VI. WVR Calibration Using EAFB Radiosondes

It was found that only 17 of the many radiosonde measurements made at Edwards AFB could be used in the calibration of the water vapor radiometer. In many cases either the scheduled radiosonde-launch was cancelled or the radiometer was not operating properly during a launch.

As stated in Section II, noise temperature saturation effects cause a curved "calibration surface" to result. It is postulated, then, that this surface may be described by:

$$\Delta L = a_0 + a_1 T_{W22} + a_2 T_{W22}^2 + a_3 T_{W18} + a_4 T_{W18}^2 \quad (16)$$

where

ΔL = range delay, cm

T_W = "water" noise temperatures at 22.235 and 18.5 GHz

It is expected that $a_0 = 0.0$ (see Eq. 4).

A plot of the data (T_{W22} vs T_{W18}) shows that the points lie nearly along the theoretical "vapor only" line in Fig. 1. The range of T_{W22} is 24 K to 108 K, and corresponding ΔL's of 9 cm to 38 cm at a 30-deg elevation angle. This indicates that the measurements did not encompass weather conditions in which liquid water (clouds) was present. Also, it can be seen that it is not possible to accurately describe a surface by a line of experimental points.

In the second-order surface-fit program, various combinations of experimental points and theoretical liquid-only points were used as input data so as to give the surface a 3-dimensional nature. The regression technique uses radiosonde determination of ΔL along with WVR noise temperature values.

Table 3 shows the results of using various combinations of real and theoretical data points. Cases 2 to 6 do not use four data points which appear to be inconsistent with the remaining data.

Referring to Eq. (4), it is seen that, for the case where the noise temperatures are due to vapor and liquid only, there will be no constant term in the calibration equation for ΔL. This is sensible because with no vapor or liquid, there will be no "wet" range delay. For this reason it is probably wise to eliminate Cases 4, 5, and 6 as having an a_0 term which is too large. These three cases show the insensitivity of the first-order terms to different liquid-only points. Of the remaining three cases, Case 1 has a large RMS curve-fit error and a moderately large constant term a_0. Case 2 has four non-experimental liquid-only points derived from imprecise theory. Case 3 has only two of these points.

Considering the limited amount and scope of the data used, either of the following two expressions could be used as the WVR calibration equation (Cases 2 and 3) (RMS surface-fit errors are below 1 cm in both cases):

$$\Delta L = -0.419 + 0.478 T_{W22} - 0.000155 T_{W22}^2 - 0.665 T_{W18} - 0.0000696 T_{W18}^2 \quad (17)$$

$$\Delta L = -0.442 + 0.479 T_{W22} - 0.000158 T_{W22}^2 - 0.663 T_{W18} - 0.0000444 T_{W18}^2 \quad (18)$$

where

ΔL = tropospheric range delay, cm

T_{W22}, T_{W18} = "water" noise temperatures at 22.235 and 18.5 GHz, calculated using the JPL Section 333 data reduction program and the parameters and methods described in this report

The calibration equations above result after the long process of radiometer gain determination and hot load calibration using the tipping curve technique. These calibrations use measurements of waveguide insertion loss, horn beamwidth adjustments, and assumptions of ground spillover contribution. Any change in WVR hardware would make recalibration necessary. The JPL Section 333 WVR data reduction program should be used in conjunction with the given calibration equations. Operators of the same instrument, using a different data reduction method to measure antenna temperature, should use the given calibration equations only with the greatest care.

VII. Remarks

(1) The WVR calibration Eqs. (17) and (18) result from a limited set of data. The RMS surface-fit errors are below 1 cm, but this may be valid only for vapor-only atmospheric conditions.

(2) The calibration equations given are not universal. They should be regarded as applicable only to the DSN Water Vapor Radiometer when data is reduced by means of the JPL Section 333 data reduction program.

(3) Users of the DSN WVR should verify by independent means (radiosondes, VLBI base-line closure, etc.) the accuracy and usefulness of the instrument.

(4) Further field calibration of the WVR should be done in conjunction with radiosonde measurements. Cloudy weather conditions should be included in these tests.

(5) Investigation of alternative frequency selection (Ref. 2) should continue in an attempt to improve the inherent accuracy of the two-frequency water vapor radiometry technique to determine tropospheric range delay.

(6) Further calibration of the WVR should be carried out using refractometers and laser-microwave ranging instrumentation to achieve higher accuracy measurements of ΔL.

Acknowledgment

The authors wish to thank Manuel Franco, Daniel Giles, and Bruce Lyon for their tireless efforts in both operating and maintaining the DSN Water Vapor Radiometer during the numerous field tests at Pt. Mugu, El Monte, Goldstone, and Edwards Air Force Base. Charles Stelzried guided the development of the WVR for the major portion of its early life. His insightful suggestions and assistance regarding operational methods and data reduction techniques are greatly appreciated. Bruce Crow guided WVR development during this last year and brought the WVR to its final configuration.

References

1. Slobin, S. D., and Batelaan, P. D., "DSN Water Vapor Radiometer Development – A Summary of Recent Work, 1976-1977," in *The Deep Space Network Progress Report 42-40*, pp. 71-75, Jet Propulsion Laboratory, Pasadena, Calif., Aug. 15, 1977.

2. Batelaan, P. D., and Slobin, S. D., "DSN Water Vapor Radiometer Development – Recent Work, 1978," in *The Deep Space Network Progress Report 42-48*, pp. 129-135, Jet Propulsion Laboratory, Pasadena, Calif., Dec. 15, 1978.

3. Waters, J. W., *Atmospheric Effects on Radio Wave Phase . . . Water Vapor Emission*, VLA Scientific Memorandum No. 8, National Radio Astronomy Observatory, Sept. 14, 1967.

4. Waters, J. W., *Analysis of Water Vapor Data from the Green Bank Interferometer*, Progress Report No. 1, National Radio Astronomy Observatory, Aug. 31, 1970.

5. Staelin, D. H., "Measurements and Interpretation of the Microwave Spectrum of the Terrestrial Atmosphere near 1-Centimeter Wavelength," *Journal of Geophysical Research*, Vol. 71, No. 12, pp. 2875-2881, June 15, 1966.

6. Goldstein, H., *Propagation of Short Radio Waves*, edited by D. E. Kerr, McGraw-Hill Book Co., New York, 1951.

Table 1. Airmass correction for antenna beamwidth

	22.235 GHz		18.5 GHz	
Horn elevation, deg	Apparent beam elevation, deg	Number of airmasses	Apparent beam elevation, deg	Number of airmasses
90.0	90.0	1.00	90.0	1.01
80.0	78.7	1.02	78.0	1.02
70.0	69.3	1.07	69.0	1.07
60.0	59.5	1.16	59.3	1.16
50.0	49.6	1.31	49.3	1.32
40.0	39.6	1.57	39.3	1.58
30.89	–	–	30.0	2.00
30.59	30.0	2.00	–	–
30.0	29.5	2.03	29.2	2.05
20.0	19.2	3.04	18.8	3.11
15.0	13.9	4.16	13.3	4.36

Table 2. Progressive hot load radiometric noise temperature correction

Frequency, GHz	Typical raw physical temperature, K	Temperature after waveguide loss correction, K	Adjustment factor	Net radiometric hot load noise temperature, K	Total difference, K
22.235	420.83	413.34	0.9729	402.14	18.69
18.5	420.83	410.59	0.9821	403.24	17.59

Table 3. Results of second-order surface fit to EAFB calibration data

Case	Number of points	Number of liquid only	a_0	a_1	a_2	a_3	a_4	RMS error
1	17	7	1.006	0.410	0.000536	-0.639	-0.000538	1.77
2	13	4	-0.419	0.478	-0.000155	-0.665	-0.0000696	0.80
3	13	2	-0.442	0.479	-0.000158	-0.663	-0.0000444	0.85
4	13	1	-4.337	0.675	-0.00128	-1.086	0.00964	0.80
5	13	1	-4.220	0.670	-0.00135	-1.064	0.0110	0.79
6	13	1	-3.952	0.642	-0.000700	-1.026	-0.000768	0.86

Notes.

Case 1: All radiosonde values and many theoretical points.
Large RMS error of surface fit to data
Liquid-only points have T_{W22} = 0, 12.5, 25, 37.5, 50, 75, 100
with $T_{W18} = 0.687\ T_{W22}$

Case 2: Four worst data points of Case 1 eliminated.
Liquid-only points reduced to 0, 25, 50, 100

Case 3: Liquid-only points 0 and 50

Case 4: Liquid-only point T_{W22} = 50, T_{W18} = 34.6

Case 5: Liquid-only point T_{W22} = 50, T_{W18} = 50

Case 6: Liquid-only point T_{W22} = 50, T_{W18} = 25

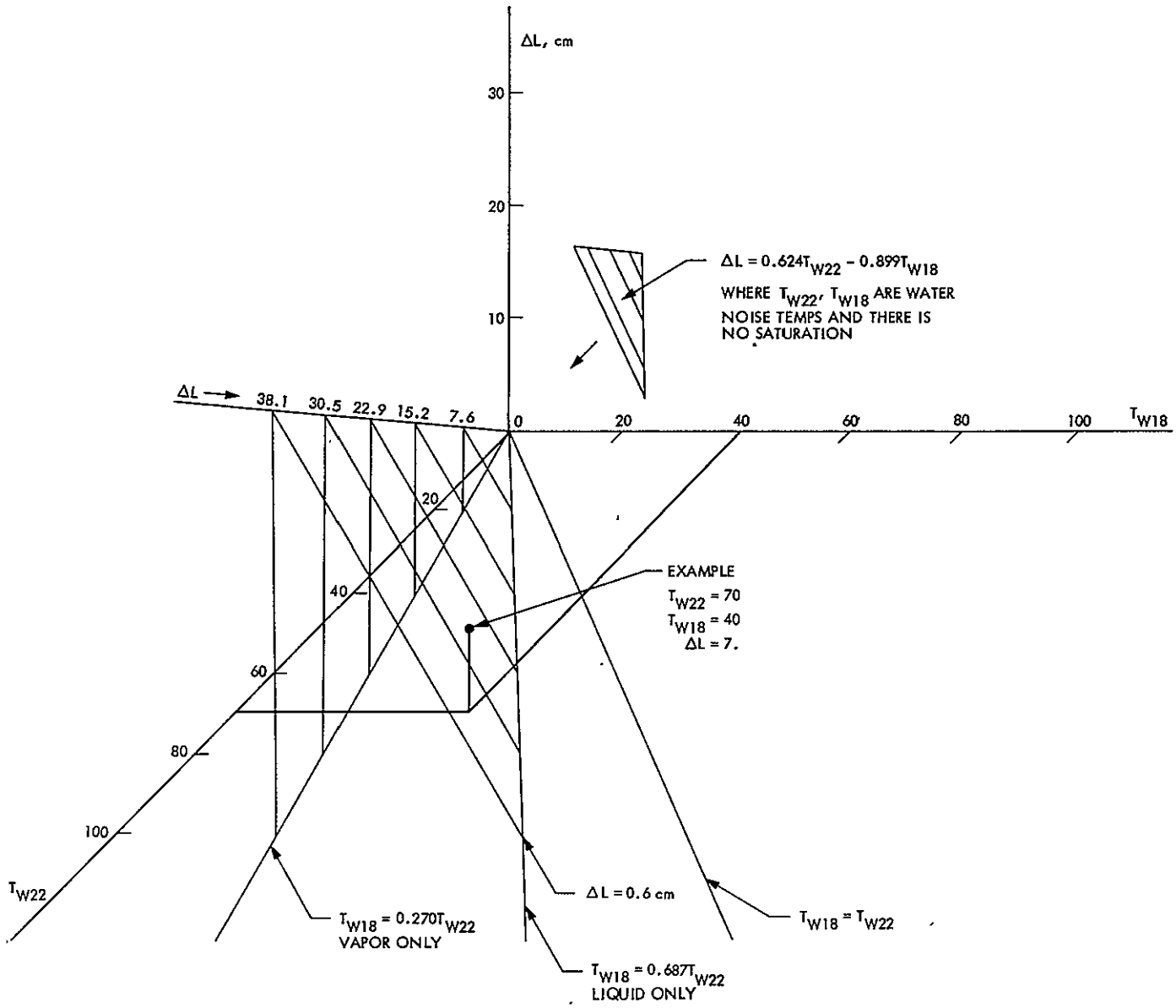

Fig. 1. Tropospheric delay vs brightness tem

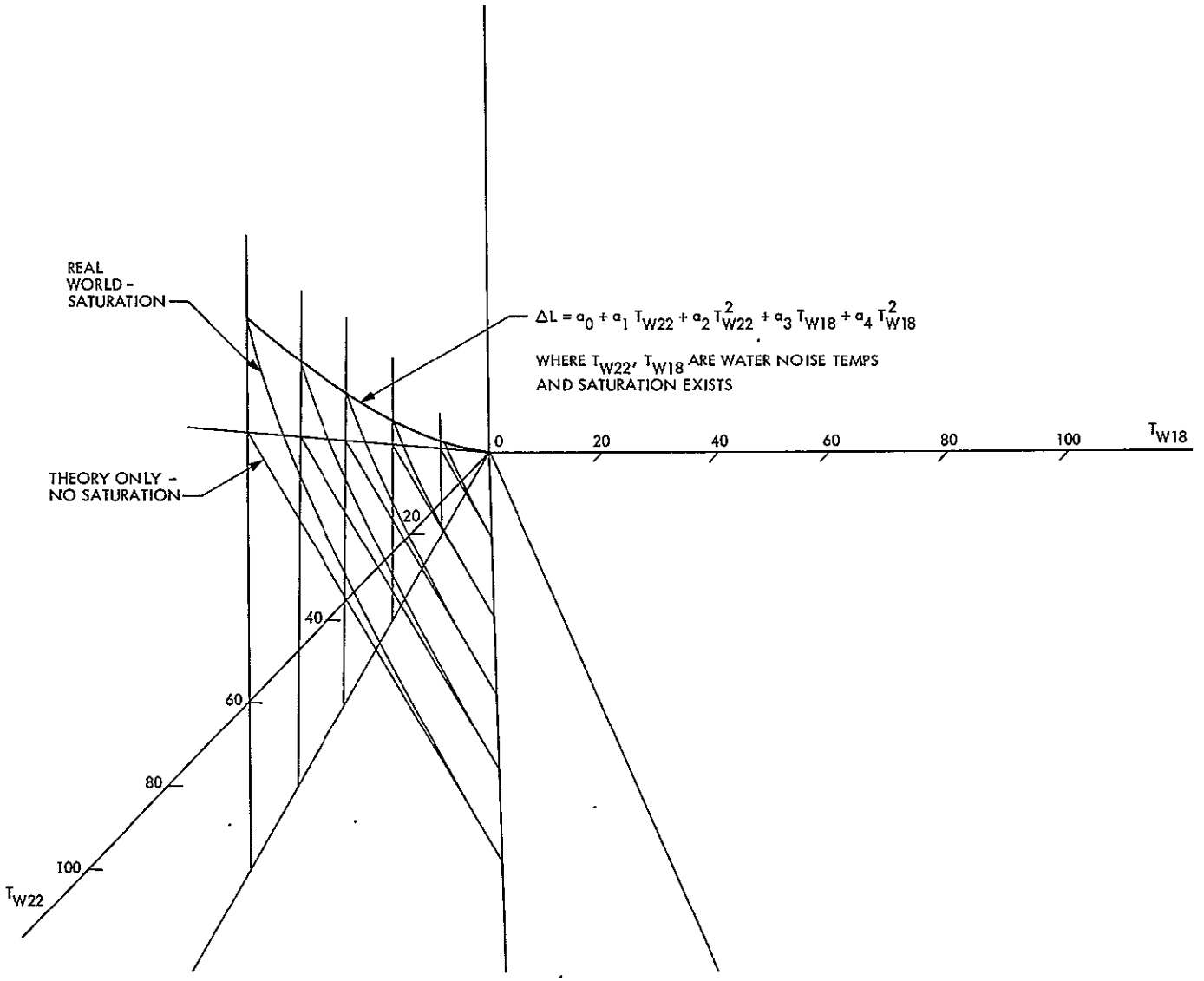

Fig. 2. Tropospheric delay-saturation effect

FTS Maintenance and Calibration at DSS 42/43

P. R. Dachel
Communications Systems Research Section

J. Wells
Deep Space Station 43, Tidbinbilla

An FTS maintenance and calibration task was conducted at DSS 42/43 during August 1978. The objectives of this effort were (1) the routine maintenance and calibration of hydrogen masers, (2) installation and calibration of cesium standards, (3) installation of test equipment for frequency measurement, (4) CRG testing, (5) cabling inspection and repair, (6) check thermal and magnetic environment of H-maser/cesium room, and (7) calibration of frequency and timing subsystem.

I. Introduction

During August 1978, an FTS maintenance and calibration effort was organized by the station director at DSS 42/43. The objectives of this effort were (1) the routine maintenance and calibration of hydrogen masers, (2) installation and calibration of cesium standards, (3) installation of test equipment for frequency measurement, (4) CRG testing, (5) cabling inspection and repair, (6) check thermal and magnetic environment of H-maser/cesium room, and (7) calibration of frequency and timing subsystem. This report describes the work accomplished in these areas.

II. Routine Maintenance and Calibration of Hydrogen Maser System

Work on the H-maser was given top priority because of the frequency settling period required after the physics package is serviced. With the exception of an uninterruptable power supply (UPS) failure, the DSS 42/43 H-maser had run uninterrupted for two and one-half years. This particular maintenance interval was chosen over the standard three-year interval because of Voyager commitments.

All H-maser system operating parameters were tested before the physics package maintenance was started. These tests included:

(1) Checkout of all electronic monitoring, control and synthesis circuits.

(2) Checkout of optical alignment of atomic beam.

(3) Observation of cavity Q, loaded and unloaded.

(4) Measurement of atomic line Q.

(5) Measurement of magnetic shield gaussing effects.

(6) Checkout of long- and short-term system frequency stability against cesium and rubidium standards.

The only adjustment necessary was to realign the 100-MHz voltage-controlled oscillator, which had drifted slightly in frequency. This misalignment affected the period necessary for the post receiver phase lock loop to reacquire lock after a major frequency change was set into the system by the master synthesizer. All other maser system parameters were within the DSN specified limits.

The physics package was then vented to atmospheric pressure with dry nitrogen and the ion vacuum pump elements were changed. The physics unit was reevacuated and the atomic beam optics realigned. Maser frequency settling was monitored over a four-day period. This frequency transient occurs because of the disturbance to the physics package thermal equilibrium.

III. Installation and Calibration of Cesium Standards

A Hewlett Packard cesium standard (Model 5061A) with the high-performance tube (option 004) was installed in the H-maser room. The Cs standard was degaussed as per H.P. specification and the output levels were checked. After degaussing, the Zeeman frequency was checked and compared to the original calibration number supplied by the timing standards laboratory of the Goldstone Deep Space Complex. The Zeeman frequency agreed with the original calibration and all system parameters were within H.P. specifications.

IV. Installation of Test Equipment for Measurement of Long- and Short-Term Frequency Stabilities

A Tracor 895-A linear phase and time comparator was installed to monitor long-term frequency stability. This equipment was used to intercompare the two stations' rubidium standards vs the cesium standard vs the hydrogen maser. The Tracor allowed any two standards to be compared; therefore, switching and time sharing were necessary for an overall comparison.

The autotuner was installed as an integral subsystem of the H-maser monitoring and control system. The autotuner's primary function is to tune the microwave cavity resonant frequency to the atomic hydrogen transition frequency. This tuning function is performed at regular intervals to remove long-term drift caused by thermal and mechanical changes of the microwave cavity.

The theory and operation of the automatic cavity tuner are discussed in Section VIII.

V. Coherent Reference Generator (CRG) Testing

Work was carried out on the CRG equipment concurrently with checkout of the new cesium standard and refurbishing of the H-maser. The CRG switching and status functions were first isolated by supplying the distribution amplifiers and the FTS clocks directly from rubidium standard No. 1. The CRG was reconfigured in this manner to provide the station with its regular FTS inputs while the CRG switching functions were being tested.

The following work was carried out:

(1) The coax switches which select the 0.1-, 1.0-, 5.0-, and 10-MHz sources were exercised from the H_1 and H_2 switches. No problems were observed.

(2) A failed LED status light in the control and status panel was replaced.

(3) Reasons for other status light indications of failure from various distribution amplifiers were investigated.

(4) Switching transients on the 1-MHz switch module output were checked and recorded. A Tektronix 466 storage oscilloscope was used as the monitoring device. The wave form and trigger source test points were listed on JPL drawings No. 9455669 and 9459378 respectively. The aim of this exercise was to look for transients in the output of the 1-MHz clock reference switch assembly when switching between two sources (hydrogen maser and cesium frequency standards). Past experience has shown that there is a significant chance of loss of FTS clock synchronization when manually switching between time reference standards. These sources were connected to input ports such that by switching between HM_1 and HM_2 source select buttons on the CRG status and control panel, the desired transition between these two standards could be observed at the clock reference assembly primary output. The phase difference indicated on the Fig. 1 diagrams was measured at the primary and secondary outputs of the 1-MHz clock reference switch assembly and is an approximate value. The diagrams are free-hand sketches of the single scan transient waveforms. The observed frequency is 1 MHz; the time-base setting was 1 μs/cm and the vertical gain was 0.5 v/cm. A delayed trigger mode was necessary to observe the transitions which occurred randomly around two fixed delay times. The delay time for switching from HM_1 to HM_2 was approximately 185 μs. The delay time for switching from HM_2 to HM_1 was approximately 70 μs. The observed waveform also depends largely on the phase of the two sources with respect to the time of switching. Note that 0° phase difference resulted in a nonobservable switching transient.

(5) Efforts were made to check switching transients in the 1-MHz output due to failure of the prime standard. These attempts were unsuccessful in the time available.

VI. Repair and Recabling of Portions of FTS

The type N cable connectors were replaced on all of the H-maser pressurized hardlines. These connectors had been a constant source of leaks in the dry nitrogen pressurized cable runs. The cable run between the H-maser/cesium distribution to the CRG was shortened and rerouted. All cables in this system were mechanically inspected and electrically checked for proper characteristic impedance with a time domain reflectometer. The cable connections are in agreement with DSN specifications.

VII. Check Thermal and Magnetic Environment of H-Maser/Cesium Room

Temperature variations in the room were measured and recorded with the Hewlett Packard 2801A crystal thermometer, D to A converter and a strip chart recorder.

With the door to the room left open, temperature variations of 3°C peak to peak were observed. Turning the overhead lights on in the room caused the temperature to rise approximately 1°C. With the lights off and the door closed, a diurnal drift of 1.3°C peak to peak was observed. The magnetic changes in the room were measured with an RFI fluxgate magnetometer. The magnetometer probe was stationed in three positions as shown (Fig. 2); B and C are perpendicular to axis A and to each other. The axial position A was the most sensitive to magnetic changes. The diurnal magnetic change in the room varied approximately 1.5 milligauss P to P.

The movement of magnetic equipment in the surrounding area had a much greater effect on field measurements. An 8 milligauss peak was observed by shifting magnetic tape racks in the overhead adjacent tape storage room. A peak of 2 milligauss was noticeable by swinging out the carpool status board in the office directly overhead.

VIII. Calibration of FTS for Frequency Stability and Accuracy

Temperature drifts and mechanical changes cause H-maser cavity frequency displacements which must be periodically corrected (Ref. 1). To maintain long-term maser frequency stabilities of one Q part in 10^{-14}, the resonant frequency of the 1420-MHz maser RF cavity must be maintained within 0.5 Hz. If a periodic cavity retuning scheme were not employed, a 10^{-14} maser stability requirement would dictate that cavity dimensions must be maintained within 10^{-10} and cavity temperature must be controlled within 0.003°C. In the long term (days/months), these tolerances on dimensional and thermal stability are not practical.

Another possible source of long-term frequency drift could be the physical change of the Teflon coating in the atomic storage bulb. This coating is constantly bombarded by highly reactive atomic hydrogen and ultraviolet from the atomic hydrogen source.

There is physical evidence of this wear phenomenon in storage bulbs out of masers that have been operated over a long term, i.e., greater than 4 years. This erosion of the storage bulb coating could cause a long-term frequency drift by changing the atomic and wall shift.

The automatic cavity tuner (autotuner) was developed to periodically retune the maser RF cavity to the atomic transition frequency. The quantitative effect of cavity pulling of the maser output frequency is given by (Ref. 2):

$$f_n - f_0 \approx (f_n - f_c)\frac{Q_c}{Q_L}$$

where

f_n = the atomic hydrogen transition frequency ($\approx$1.420 $\times 10^9$ Hz)

f_0 = the maser oscillation frequency caused by f_c

f_c = the cavity resonance frequency

Q_c = the cavity frequency divided by its bandwidth ($\approx$45,000)

Q_L = the atomic hydrogen transition frequency divided by its linewidth ($\approx 1.4 \times 10^9$)

Therefore, the maser output frequency is pulled by the cavity resonance frequency by the ratio of Q_c/Q_L (10^{-4} to 10^{-5} dependent on atomic storage time). The most acceptable maser cavity tuning method (Ref. 2) is to increment the transition linewidth and adjust the cavity frequency f_c such that this increment in linewidth does not change the output frequency. The cavity frequency is then centered upon the atomic transition frequency in such a manner that the least amount of cavity pulling occurs.

A block diagram of the autotuner servo system is shown in Fig. 3. The autotuner modulates the hydrogen transition linewidth by limiting the supply of hydrogen atoms to the cavity oscillator assembly. This feat is accomplished by moving a mechanical vane into the atomic beam, thereby limiting usable atoms to the storage bulb. The decrease of atoms from the atomic source increases the lifetime of excited atoms in the storage bulb by reducing the collision factor. The atomic transition Q_L increases as the linewidth decreases.

The cavity is tuned by a varactor connected through a directional coupler to the cavity coupling loop. The period of the beat frequency between the H-maser and a frequency reference (R_{B_1} at DSS 43) is measured to determine incremental frequency change produced by changing the atomic transition linewidth. This frequency change is registered in count time by the autotuner, which then sends a proportionate voltage to the varactor to cancel this frequency offset. The autotuner continues to integrate this frequency/varactor voltage function to 0. The oscillator cavity is then tuned to the atomic transition.

The DSS 43 H-maser was autotuned using rubidium No. 1 as a reference clock. A 100-second "0" cross-averaging period was set in by shifting the H-maser master synthesizer. This 100-second count was chosen because it is the best averaging period for a rubidium standard, i.e., at least 5×10^{-13}/100 seconds as per Hewlett-Packard specification.

There were two major problems encountered with the autotuning subsystem.

(1) The autotuner was false triggering on the start of the count period. Upon investigation of the problem a 1-kHz pulse was detected riding on the 0 crossing input. This 1-kHz pulse appeared randomly and was being fed back by the autotuner's internal 1-kHz generator. A 200 P.F. bypass capacitor was installed in the 0 crossing input circuit to shunt this transient pulse. This modification eliminated the false triggering.

(2) The autotuner's servo loop gain control switches in decade steps. The 3-position switch in its lowest gain position would take a month to integrate the H-maser to a tuned point using a rubidium as a clock reference. The medium gain position which is used for maser vs maser tuning has too much gain for rubidium vs maser tuning.

The 100-second average for a H-maser is approximately two orders of magnitude more stable (5×10^{-15}) than that of a rubidium. The rubidium's added noise for these short-term counts causes the servo loop to overshoot and hunt.

The maser tuning was accomplished by comparing autotuner data to manual tuning numbers and averaging. This decade stepping loop gain control switch should be replaced with a Vernier control. Then each tuning situation may be optimized to the upper noise limits of the standard with the poorest short-term stability.

A. Stability

The data in Table 1 were taken with the Tracor comparator and the H-maser autotuner. The 5-MHz output from the cesium and rubidium standards were multiplied to 100 MHz while being compared to H-maser for short term tests. Both rubidium standards maintained mid-range parts in 10^{-12} for 4 hour runs.

The best long term data was taken at 5 MHz between the H-maser/cesium over a thermally and magnetically quiet weekend. The total frequency drift between both standards was 3.4×10^{-13} for a 48-hour period, which is a time shift of 60×10^{-9} seconds. The H-maser master synthesizer was set to the calibrated cesium frequency. The station rubidiums will be set to the cesium frequency when tracking schedules permit.

B. Conclusion

The most cost effective methods for improving the stability of the FTS are:

(1) Provide a thermally and magnetically stable central environment for all frequency standards.

(2) Modify electronic switching functions of the CRG.

(3) Control all cabling and distribution functions from the central standards room to the user.

(4) Place all frequency and timing functions on the U.P.S.

Acknowledgment

The authors wish to express their gratitude to G. Baines, P. Churchill, J. Hoyland and J. Mann of Tidbinbilla. Without their help this effort would not have been possible.

References

1. Finnie, C., "Frequency Generation and Control: Atomic Hydrogen Maser Frequency Standard," in *The Deep Space Network Progress Report*, Technical Report 32-1526, Vol. I, pp. 73-75, Jet Propulsion Laboratory, Pasadena, Calif., Feb 15, 1971.

2. Gordon J. P., Zeiger, H. J., and Townes, C. H., "The Maser – New Type of Microwave Amplifier, Frequency Standard, and Spectrometer," *Phys. Rev.*, Vol. 99, pp. 1264-1274, 1955.

Table 1. Short-term 100 MHz/vs hydrogen maser averaging time: 100 seconds

HP5061 Option 004 Cesium	HP5065A No. 1 Rubidium	HP5065A No. 2 Rubidium
6×10^{-13}	2.3×10^{-13}	3.4×10^{-13}

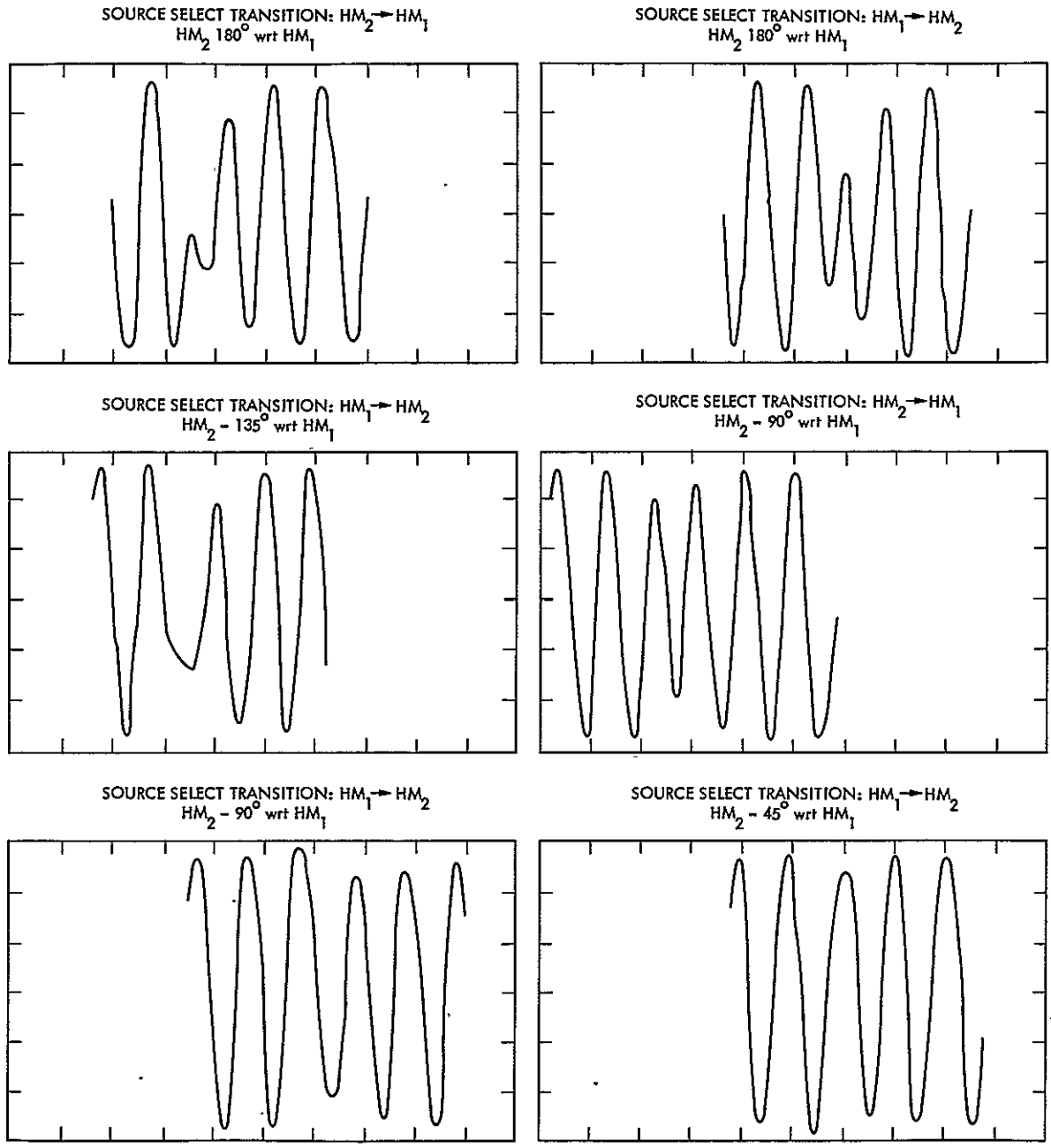

Fig. 1. Phase difference diagrams

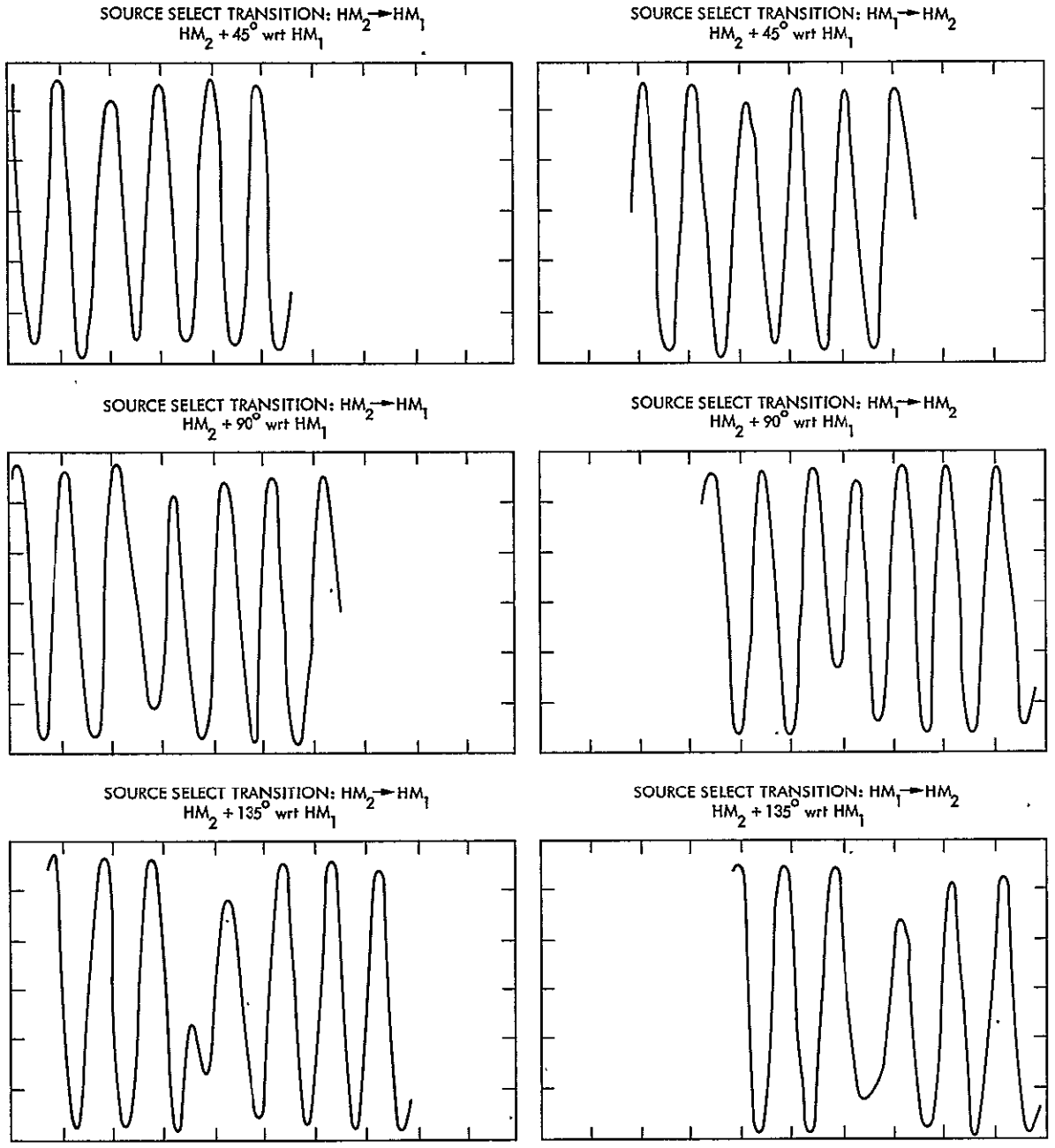
SOURCE SELECT TRANSITION: $HM_2 \rightarrow HM_1$
HM_2 + 45° wrt HM_1
SOURCE SELECT TRANSITION: $HM_1 \rightarrow HM_2$
HM_2 + 45° wrt HM_1
SOURCE SELECT TRANSITION: $HM_2 \rightarrow HM_1$
HM_2 + 90° wrt HM_1
SOURCE SELECT TRANSITION: $HM_1 \rightarrow HM_2$
HM_2 + 90° wrt HM_1
SOURCE SELECT TRANSITION: $HM_2 \rightarrow HM_1$
HM_2 + 135° wrt HM_1
SOURCE SELECT TRANSITION: $HM_1 \rightarrow HM_2$
HM_2 + 135° wrt HM_1

Fig. 1 (contd)

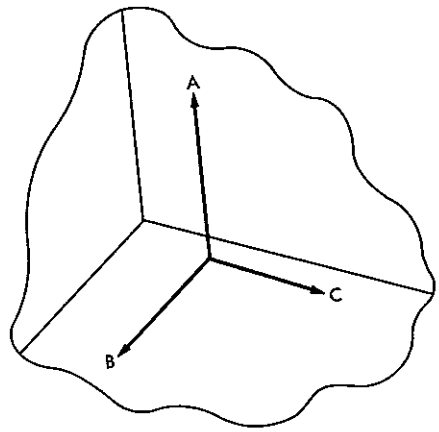

Fig. 2. Magnetometer probe axial orientation

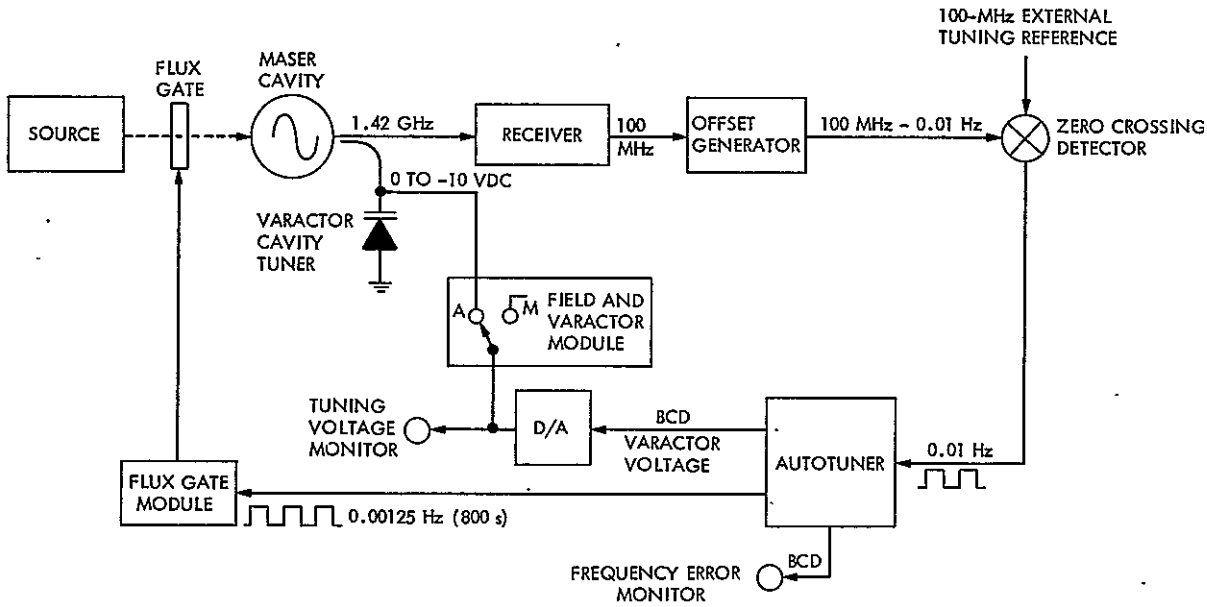

Fig. 3. Autotuning block diagram

A Maximum Likelihood Convolutional Decoder Model vs Experimental Data Comparison

R. Y. Chen
DSN Operations Section

This article describes the comparison of a maximum likelihood convolutional decoder (MCD) prediction model and the actual performance of the MCD at the Madrid Deep Space Station. The MCD prediction model is used to develop a subroutine that has been utilized by the Telemetry Analysis Program (TAP) to compute the MCD bit error rate for a given signal-to-noise ratio. The results indicate that the TAP can predict quite well compared to the experimental measurements. An optimal modulation index also can be found through TAP.

I. Introduction

A model has been developed (Ref. 1) that will be utilized by the Telemetry Analysis Program (TAP) to compute the maximum likelihood convolutional decoder (MCD) bit error rate (BER).

This report shows the comparison of an MCD Prediction Model and the actual performance of the MCD at the Madrid Deep Space Station (Ref. 2) and Merritt Island Goddard Space Flight Center Station (Ref. 3). The results show that the model can predict quite well when compared to the experimental measurements.

The MCD Performance Prediction Model was developed by L. Webster (Ref. 1), and a subroutine has been integrated into the TAP. With a specified energy per bit to noise spectral density ratio (*Eb/No*) as the MCD input, the model can predict the bit error rate as the output of the model. In order to use TAP efficiently, energy per symbol to noise spectral density ratio (*STs/No*) as measured at the input to the receiver is expected to be specified as the TAP input.

The telemetry system performance testing data that are used for comparison are from two sources (Refs. 2 and 3).

II. Comparison Objectives

The objectives of the comparison were:

(1) Given a bit error rate (obtained from measurement) compute the corresponding bit error rate and determine the required *Eb/No* (MCD model) measured at the MCD input and compare to the *Eb/No* (measurement).

(2) Given an *Eb/No* (obtained from measurement) compute the corresponding bit error rate (MCD model) and compare to the bit error rate (measurements).

(3) Determine the optimal modulation index as noted in Fig. 1 (Ref. 2).

To achieve the above objectives, we use the system setup conditions (Refs. 2 and 3) as the setup conditions for TAP.

Based on the test results (pp. 52-57, Ref. 2), we pick up a bit error rate as a reference, and by trying different *Sts/No* as TAP input, it is found that a typical *STs/No* MCD model input can generate a very close bit error rate with respect to our reference. With this typical *STs/No*, we can find an *Eb/No* measured at the input to MCD model that yields this required BER and compare it to the *Eb/No* measured at the input to the MCD at the station.

By the same procedure, we can pick an *Eb/No* (measured) converted to *Sts/No* as TAP input and compute the corresponding bit error rate from the MCD model. The bit error rate computed by the MCD model should be close to the measured BER. Since the output of the MCD model is a theoretical value, the deviation of *Eb/No* and bit error rate should indicate which modulation index is the optimal one (minimum system degradation).

III. Analysis

With the Telemetry Analysis Program, it is not difficult to find a specified *Eb/No* (or bit error rate) and its corresponding bit error rate (or *Eb/No*); comparison results are stated in Tables 1-3. Table1 shows that at an optimal modulation index of 69 deg the $\Delta Eb/No$ (dB) comparison between the Performance Prediction Model and the actual data taken from DSS 62/63 (Spain) is approximately 0.165 dB average. Taking an average of the $\Delta Eb/No$ column shows that the Prediction Model predicts an average of 0.28 dB of $\Delta Eb/No$ over the optimal modulation index range at approximately 70 ± 1 deg (Fig. 1).

Table 2, which shows the deviation of bit error rate, again shows that at a modulation index of 69 deg, the deviation is smaller than any other measured modulation index; thus 69 deg was taken as the optimal modulation index (Fig. 1). Table 2 also shows that the theoretical value of bit error rate is always less than the actual bit error rate. Table 3 shows the comparison of the MCD model and the data from MIL 77 (Ref. 3).

Based on the data from Spain (Ref. 2), the MCD model predicts the bit error rate just as shown in Fig. 1. Moreover, examining the TAP printout carefully shows that the optimal modulation index should fall between 65 and 70 deg.

IV. Summary

Most of the comparison objectives were achieved. The MCD works quite well in predicting the performance of the on-station MCD. It also should be noted that the maximum likelihood convolutional decoder at the station can perform well, with a modulation index range from 67 to 70 deg and an MCD *Eb/No* input range from 4 to 6 dB. The bit error rate should be between 10^{-4} and 10^{-6}.

References

1. Webster L., "Maximum Likelihood Convolutional Decoding (MCD) Performance Due to System Losses," in *The Deep Space Network Progress Report 42-34*, pp. 108-118, Jet Propulsion Laboratory, Pasadena, Calif., Aug. 15, 1976.
2. Urech, J. M., and Delgado L., "Final Report on the DSN Performance for Convolutional Codes with a Viterbi Decoder," JPL System Engineering Section DSS 62/63, Madrid, Spain, Jan. 1976 (an internal document).
3. Kemp, R. P., "Telemetry System Performance Testing at MIL 71 Utilizing Convolutionally Encoded RN Data at Rate 7, 1/2 and 1/3 and the Maximum Likelihood Convolution Decoder," JPL Interoffice Memo 430B-77-044 May 18, 1977 (an internal document).

Table 1. Comparison of the MCD performance data from DSS 62/63 and the MCD Performance Prediction Model for optimum mod index, selected from Fig. 1

Mod index	*Pt/No*, dB	Bit error rate	Energy per bit to noise spectral density ratio (Spain), dB	Energy per bit to noise spectral density ratio (MCD model), dB	Δ *Eb/No*, dB
69	39.67	1.19×10^{-5}	4.42	4.36	0.06
69	39.77	8.0×10^{-6}	4.43	4.47	0.06
69	39.82	3.45×10^{-5}	4.33	4.06	0.27
69	40.26	3.55×10^{-6}	4.97	4.68	0.29
70	39.67	2.04×10^{-5}	4.56	4.16	0.40
70	39.77	2.5×10^{-5}	4.30	4.12	0.18
70.8	39.82	4.56×10^{-5}	4.24	3.9	0.34
70	40.26	4.48×10^{-6}	4.94	4.58	0.36
71	39.67	5.36×10^{-5}	4.6	4.49	0.11
71	39.77	3.88×10^{-5}	4.42	3.93	0.49
71	39.82	3.4×10^{-5}	4.34	4.0	0.34
71	40.26	5.47×10^{-6}	5.06	4.5	0.56

Condition setup for TAP: refer to pp. 52-57, Ref. 2; system temperature, 20K.

Table 2. Comparison of the MCD performance data from DSS 62/63 and the MCD Performance Prediction Model for measured *Eb/No*

Mod index	*Pt/No*, dB	*Eb/No* (SSA), dB	Bit error rate (Spain)	Bit error rate (MCD model)	Bit error rate MCD less than Spain
69	39.67	4.42	1.19×10^{-5}	0.922×10^{-5}	Yes
69	39.77	4.53	8.0×10^{-6}	6.293×10^{-6}	Yes
69	39.82	4.33	3.45×10^{-5}	1.329×10^{-5}	Yes
69	40.26	4.97	3.55×10^{-6}	1.112×10^{-6}	Yes
70	39.67	4.56	2.04×10^{-5}	0.506×10^{-5}	Yes
70	39.77	4.30	2.5×10^{-5}	1.387×10^{-5}	Yes
70.8	39.82	4.24	4.56×10^{-5}	1.397×10^{-5}	Yes
70	40.26	4.94	4.48×10^{-6}	1.072×10^{-6}	Yes
71	39.67	4.6	5.36×10^{-5}	0.35×10^{-5}	Yes
71	39.77	4.42	3.88×10^{-5}	0.7088×10^{-5}	Yes
71	39.82	4.34	3.4×10^{-5}	0.923×10^{-5}	Yes
71	40.26	5.06	5.47×10^{-6}	0.518×10^{-6}	Yes

Table 3. Comparison of the MCD performance data from MIL 71 and the MCD Performance Prediction Model for specified *STb/No*

Bit rate	*Stb/No*, dB	Bit error rate, MIL 71	Bit error rate, MCD model
7200	1	2.0×10^{-4}	1.438×10^{-4}
	2	9.57×10^{-6}	3.8×10^{-6}
6400	1	5.7×10^{-4}	1.676×10^{-4}
	2	5.45×10^{-5}	0.465×10^{-5}
5600	1	3.98×10^{-4}	2.079×10^{-4}
	2	1.4×10^{-5}	0.6164×10^{-5}
3600	1	2.5×10^{-4}	6.735×10^{-4}
	2	2.5×10^{-5}	3.33×10^{-5}

RF band: S; mod index = 72°; data pattern = PN code.
Receiver: BLK III at 12 Hz Wlo; SDA: BLK III, medium.
SSA: BLK III NARROW/NARROW subcarrier frequency 1.44 MHz

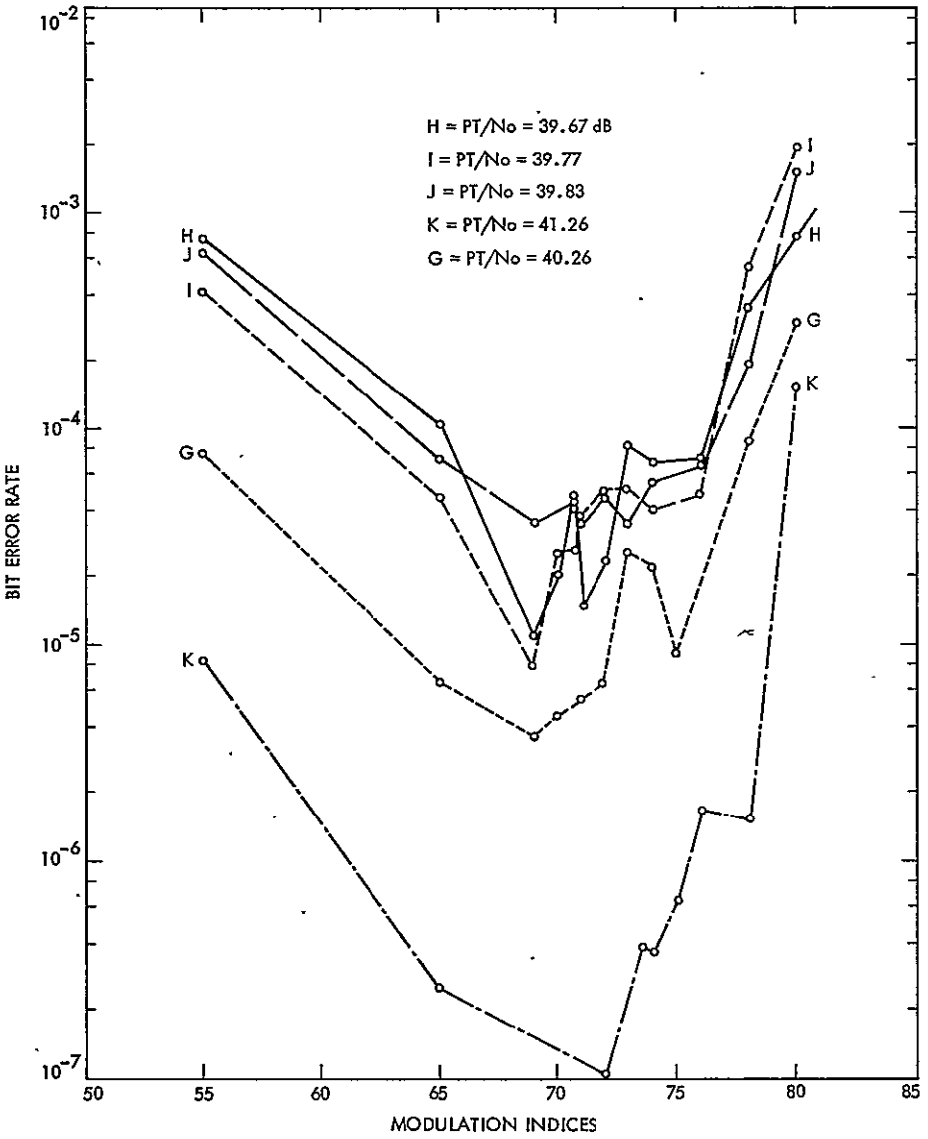

Fig. 1. Bit error rate vs modulation indices

OMIT TO END

Bibliography

Ananda, M. P., "Lunar Gravity: A Mass Point Model," *J. Geophys. Res.*, Vol. 82, No. 20, pp. 3049-3064, July 10, 1977.

Anderson, J. D., Null, G. W., and Thornton, C. T., *The Evaluation of Certain Astronomical Constants from the Radio Tracking of Mariner II*, Technical Report 32-476, Jet Propulsion Laboratory, Pasadena, Calif., reprinted from *Progr. Astronaut. Aeronaut.*, Vol. 14, 1964.

Anderson, J. D., *Determination of the Masses of the Moon and Venus and the Astronomical Unit from Radio Tracking Data of the Mariner II Spacecraft*, Technical Report 32-816, Jet Propulsion Laboratory, Pasadena, Calif., July 1, 1967.

Anderson, J. D., et al., "The Radius of Venus as Determined by Planetary Radar and Mariner V Radio Tracking Data," *J. Atmos. Sci.*, pp. 1171-1174, Sept. 25, 1968.

Anderson, J. D., and Hilt, D. E., "Improvement of Astronomical Constants and Ephemerides from Pioneer Radio Tracking Data," *AIAA J.*, Vol. 7, No. 6, pp. 1048-1054, June 1969.

Anderson, J. D., "Determination of Astrodynamic Constants and a Test of the General Relativistic Time Delay With S-Band Range and Doppler Data From Mariners 6 and 7," *Space Research*, Vol. XI, pp. 105-112, Akademie-Verlag, Berlin, 1971.

Anderson, J. D., et al., "Experimental Test of General Relativity Using Time-Delay Data From Mariner 6 and Mariner 7," *Astrophys. J.*, Vol. 200, No. 1, pp. 221-233, Aug. 15, 1975.

Anderson, J. D., et al., "Tests of General Relativity Using Astrometric and Radio Metric Observations of the Planets," *Acta Astronautica*, Vol. 5, No. 1-2, pp. 43-61, Jan.-Feb. 1978.

Barnum, P. W., et al., *Tracking and Data System Support for the Mariner Mars 1971 Mission: Orbit Insertion Through End of Primary Mission,* Technical Memorandum 33-523, Vol. III, Jet Propulsion Laboratory, Pasadena, Calif., May 15, 1973.

Barnum, P. W., and Renzetti, N. A., *Tracking and Data System Support for the Mariner Mars 1971 Mission: Extended Mission Operations*, Technical Memorandum 33-523, Vol. IV, Jet Propulsion Laboratory, Pasadena, Calif., Dec. 15, 1973.

Barton, W. R., and Miller, R. B., *Tracking and Data System Support for the Pioneer Project: Pioneer 11–Prelaunch Planning Through Second Trajectory Correction: to May 1, 1973*, Technical Memorandum 33-584, Vol. II, Jet Propulsion Laboratory, Pasadena, Calif., Mar. 15, 1975.

Bartos, K. P., et al., *Implementation of the 64-Meter-Diameter Antennas at the Deep Space Stations in Australia and Spain*, Technical Memorandum 33-692, Jet Propulsion Laboratory, Pasadena, Calif., Jan. 15, 1975.

Bathker, D. A., *Radio-Frequency Performance of an 85-ft Ground Antenna: X-Band*, Technical Report 32-1300, Jet Propulsion Laboratory, Pasadena, Calif., July 1, 1968.

Bathker, D. A., *Radio Frequency Performance of a 210-ft Ground Antenna: X-Band*, Technical Report 32-1417, Jet Propulsion Laboratory, Pasadena, Calif., Dec. 15, 1969.

Bathker, D. A., *Predicted and Measured Power Density Description of a Large Ground Microwave System*, Technical Memorandum 33-433, Jet Propulsion Laboratory, Pasadena, Calif., Apr. 15, 1971.

Bathker, D. A., Brown, D. W., and Petty, S. M., *Single- and Dual-Carrier Microwave Noise Abatement in the Deep Space Network*, Technical Memorandum 33-733, Jet Propulsion Laboratory, Pasadena, Calif., Aug. 1, 1975.

Bathker, D. A., *Microwave Performance Characterization of Large Space Antennas*, JPL Publication 77-21, Jet Propulsion Laboratory, Pasadena, Calif., May 15, 1977.

Baumert, L., et al., *Coding Theory and Its Applications to Communications Systems*, Technical Report 32-67, Jet Propulsion Laboratory, Pasadena, Calif., Mar. 31, 1961.

Baumgartner, W. S., *High-Power CW Radar Transmitter*, Technical Report 32-656, Jet Propulsion Laboratory, Pasadena, Calif., Sept. 1, 1964.

Beatty, R. W., and Otoshi, T. Y., "Effect of Discontinuities on the Group Delay of a Microwave Transmission Line," *IEEE Trans. Microwave Theor. Techniq.*, Vol. MTT-23, No. 11, pp. 919-923, Nov. 1975.

Berlekamp, E. R., et al., "On the Inherent Intractability of Certain Coding Problems," *IEEE Trans. Inform. Theor.*, Vol. IT-24, No. 3, pp. 384-386, May 1978.

Berman, A. L., *Tracking System Data Analysis Report, Ranger VII Final Report*, Technical Report 32-719, Jet Propulsion Laboratory, Pasadena, Calif., June 1, 1965.

Berman, A. L., and Rockwell, S. T., *New Optical and Radio Frequency Angular Tropospheric Refraction Models for Deep Space Applications*, Technical Report 32-1601, Jet Propulsion Laboratory, Pasadena, Calif., Nov. 1, 1975.

Berman, A. L., *The Prediction of Zenith Range Refraction From Surface Measurements of Meteorological Parameters*, Technical Report 32-1602, Jet Propulsion Laboratory, Pasadena, Calif., July 15, 1976.

Biber, K. W., and Whittlesey, A. C., *Description and Analysis of 890-MHz Noise-Measuring Equipment*, Technical Report 32-898, Jet Propulsion Laboratory, Pasadena, Calif., Mar. 31, 1966.

Born, G. H., et al., "The Determination of the Satellite Orbit of Mariner 9," *Celest. Mech.*, Vol. 9, No. 3, pp. 395-414, May 1974.

Born, G. H., and Mohan, S. N., "Orbit Determination for Mariner 9 Using Radio and Optical Data," *J. Spacecraft Rockets*, Vol. 12, No. 7, pp. 439-441, July 1975.

Brockman, M. H., et al., *Extraterrestrial Radio Tracking and Communication*, External Publication 808, Jet Propulsion Laboratory, Pasadena, Calif., Nov. 12, 1959. Also available in *Proc. IRE*, Vol. 48, 1960.

Brockman, M. H., and Posner, E. C., *Power Requirements for Deep-Space Telecommunication Links*, Technical Report 32-1395, Jet Propulsion Laboratory, Pasadena, Calif., reprinted from *IEEE Spectrum*, Vol. 6, No. 3, pp. 95-99, Mar. 1969.

Bunce, R. C., *Unified S-Band Receiver-Exciter Subsystem*, Technical Report 32-809, Jet Propulsion Laboratory, Pasadena, Calif., Sept. 15, 1968.

Butman, S., "A General Formulation of Linear Feedback Communication Systems with Solutions," *IEEE Trans. Inform. Theor.*, Vol. IT-15, No. 3, pp. 392-400, May 1969.

Butman, S., "Rate Distortion Over Band-Limited Feedback Channels," *IEEE Trans. Inform. Theor.*, Vol. IT-17, No. 1, pp. 110-112, Jan. 1971.

Butman, S., and Timor, U., "Interplex—An Efficient Multichannel PSK/PM Telemetry System," *IEEE Trans. Commun.*, Vol. COM-20, No. 3, pp. 415-419, June 1972.

Butman, S. A., "Linear Feedback Rate Bounds for Regressive Channels," *IEEE Trans. Inform. Theor.*, Vol. IT-22, No. 3, pp. 363-366, May 1976.

Butman, S. A., et al., "Design Criteria for Noncoherent Gaussian Channels With MFSK Signaling and Coding," *IEEE Trans. Commun.*, Vol. COM-24, No. 10, pp. 1078-1088, Oct. 1976.

Butman, S. A., and Lesh, J.R., "The Effects of Bandpass Limiters on *n*-Phase Tracking Systems," *IEEE Trans. Commun.*, Vol. COM-25, No. 6, pp. 569-576, June 1977.

Cain, D. L., and Hamilton, T. W., *Determination of Tracking Station Locations by Doppler and Range Measurements to an Earth Satellite*, Technical Report 32-534, Jet Propulsion Laboratory, Pasadena, Calif., Feb. 1, 1964.

Carey, C. N., and Sjogren, W. L., *Gravitational Inconsistency in the Lunar Theory: Confirmation by Radio Tracking*, Technical Report 32-1290, Pt. II, Jet Propulsion Laboratory, Pasadena, Calif., reprinted from *Science*, Vol. 160, No. 3830, pp. 875-876, May 24, 1968.

Carpenter, R. L., *Study of Venus by CW Radar–1964 Results*, Technical Report 32-963, Jet Propulsion Laboratory, Pasadena, Calif., reprinted from *Astron. J.*, Vol. 71, No. 2, pp. 142-152, Mar. 1966.

Carr, R. E., *The Jet Propulsion Laboratory Method of Tracking Lunar Probes*, External Publication 793, Jet Propulsion Laboratory, Pasadena, Calif., June 4, 1959.

Chadwick, H. D., and Springett, J. C., "The Design of a Low Data Rate MSFK Communication System" *IEEE Trans. Commun. Technol.*, Vol. COM-18, No. 6, pp. 740-750, Dec. 1970.

Chaney, W. D., *Final Mariner II Tracking System Data Analysis Report*, Technical Report 32-727, Jet Propulsion Laboratory, Pasadena, Calif., Sept. 1, 1965.

Chao, C.-C., "Interstation Frequency Offset Determination Using Differenced 2-Way/3-Way Doppler Data," paper presented at the 1978 Spring Meeting of the American Geophysical Union, Miami, Florida, Apr. 17-20, 1978.

Charles, F. J., and Lindsey, W. C., *Some Analytical and Experimental Phase-Locked Loop Results for Low Signal-to-Noise Ratios*, Technical Report 32-1027, Jet Propulsion Laboratory, Pasadena, Calif., reprinted from *Proc. IEEE*, Vol. 54, No. 9, pp. 1152-1166, Sept. 1966.

Christensen, C. S., and Reinold, S. J., "Navigation of the Mariner 10 Spacecraft to Venus and Mercury," *J. Spacecraft Rockets*, Vol. 12, No. 5, pp. 280-286, May 1975.

Christensen, C. S., et al., "On Achieving Sufficient Dual Station Range Accuracy for Deep Space Navigation at Zero Declination," paper presented at AAS/AIAA Astrodynamics Specialist Conference, Jackson Hole, Wyo., Sept. 7-9, 1977.

Christensen, E. J., et al., "The Mass of Phobos from Viking Flybys," *Geophys. Res. Lett.*, Vol. 4, No. 12, pp. 555-557, Dec. 1977.

Clark, B. G., et al., "High Resolution Observations of Compact Radio Sources at 13 cm," *Astrophys. J.*, Vol. 161, pp. 803-809, Sept. 1970.

Clauss, R. C., et al., *Total System Noise Temperature: 15°K*, Technical Report 32-691, Jet Propulsion Laboratory, Pasadena, Calif., Nov. 1964.

Clauss, R. C., *A 2388-Mc Two-Cavity Maser for Planetary Radar*, Technical Report 32-583, Jet Propulsion Laboratory, Pasadena, Calif., reprinted from *Microwave J.*, Vol. 8, pp. 74-77, May 1965.

Clauss, R. C., *A Traveling Wave Maser for Deep Space Communication at 2295 and 2388 MHz*, Technical Report 32-1072, Jet Propulsion Laboratory, Pasadena, Calif., Feb. 15, 1967.

Clauss, R., Flesner, L. D., and Schultz, S., "Simple Waveguide Reflection Maser with Broad Tunability," *Rev. Sci. Instrum.*, Vol. 48, No. 8, pp. 1104-1105, Aug. 1977.

Cohen, M. H., et al., "Compact Radio Source in the Nucleus of M87," *Astrophys. J.*, Vol. 158, No. 2, Pt. 2, pp. L83-L85, Nov. 1969.

A Collection of Articles on S/X-Band Experiment Zero Delay Ranging Tests, Technical Memorandum 33-747, Vol. I, Jet Propulsion Laboratory, Pasadena, Calif., Nov. 1, 1975.

Coyner, J. V., Jr., *Radial Rib Antenna Surface Deviation Analysis Program*, Technical Memorandum 33-518, Jet Propulsion Laboratory, Pasadena, Calif., Dec. 15, 1971.

Curkendall, D. W., and McReynolds, S. R., "A Simplified Approach for Determining the Information Content of Radio Tracking Data," *J. Spacecraft Rockets*, Vol. 6, No. 5, pp. 520-525, May 1969.

Curkendall, D. W., and Stephenson, R. R., "Earthbased Tracking and Orbit Determination—Backbone of the Planetary Navigation System," *Astronaut. Aeronaut.*, Vol. 7, No. 5, pp. 30-36, May 1970.

Curkendall, D. W., "Planetary Navigation: The New Challenges," *Astronaut. Aeronaut.*, Vol. 7, No. 5, pp. 26-29, May 1970.

Curkendall, D. W., "Algorithms for Isolating Worst Case Systematic Data Errors," *J. Guidance Contr.*, Vol. 1, No. 1, pp. 56-62, Jan.-Feb. 1978.

"The Deep Space Network—An Instrument for Radio Navigation for the Mariner Mission to Mars—1969," *Proceedings of the Second International Conference of STM and AERA*, Reidel Publishing Company, Holland, May 1969.

Description of the Deep Space Network Operational Capabilities as of January 1, 1966, Technical Memorandum 33-255, Jet Propulsion Laboratory, Pasadena, Calif., July 1, 1966.

Description of World Network for Radio Tracking of Space Vehicles, Publication 135, Jet Propulsion Laboratory, Pasadena, Calif., July 1, 1958.

Dickinson, R. M., "The Beamed Power Microwave Transmitting Antenna," *IEEE Trans. Microwave Theor. Tech.*, Vol. MTT-26, No. 5, pp. 335-340, May 1978.

Didday, R. L., and Lindsey, W. C., *Subcarrier Tracking Methods and Communication System Design*, Technical Report 32-1317, Jet Propulsion Laboratory, Pasadena, Calif., reprinted from *IEEE Trans. Commun. Technol.*, Vol. COM-16, No. 4, pp. 541-550, Aug. 1968.

Downs, G. S., and Reichley, P. E., "Observations of Interstellar Scintillations of Pulsar Signals at 2388 MHz," *Astrophys. J.*, Vol. 163, No. 1, Pt. 2, pp. L11-L16, Jan. 1971.

Downs, G. S., et al., "Mars Radar Observation, A Preliminary Report," *Science*, Vol. 174, No. 4016, pp. 1324-1327, Dec. 24, 1971.

Downs, G. S., "Martian Topography and Surface Properties as Seen by Radar. The 1971 Opposition," *Icarus*, Vol. 18, No. 1, pp. 8-21, Jan. 1973.

Downs, G. S., Reichley, P. E., and Morris, G. A., "Pulsar Detections at Frequencies of 8.4 and 15.1 GHz," *Astrophys. J.*, Vol. 181, No. 3, Part 2, pp. L143-L146, May 1, 1973.

Duxbury, T. C., Johnson, T. V., and Matson, D. L., "Galilean Satellite Mutual Occultation Data Processing," *Icarus*, Vol. 25, No. 4, pp. 569-584, Aug. 1975.

Easterling, M., *A Long-Range Precision Ranging System*, Technical Report 32-80, Jet Propulsion Laboratory, Pasadena, Calif., July 10, 1961.

Easterling, M., *Methods for Obtaining Velocity and Range Information from CW Radars*, Technical Report 32-657, Jet Propulsion Laboratory, Pasadena, Calif., Sept. 1, 1964.

Easterling, M., and Goldstein, R., *The Effect of the Interplanetary Medium on S-Band Telecommunications*, Technical Report 32-825, Jet Propulsion Laboratory, Pasadena, Calif., Sept. 1, 1965.

Edelson, R. E. (ed), *Telecommunications Systems Design Techniques Handbook*, Technical Memorandum 33-571, Jet Propulsion Laboratory, Pasadena, Calif., July 15, 1972.

Edelson, R. E., "An Observational Program to Search for Radio Signals From Extraterrestrial Intelligence Through the Use of Existing Facilities," Preprint IAF-A-76-033, Int. Astronaut. Fed. XXVII Congress, Anaheim, Calif., Oct. 10-16, 1976.

Edelson, R. E., and Levy, G. S., "The Search for Extraterrestrial Intelligence: Telecommunications Technology," *Proceedings of the 1976 National Telecommunications Conference*, Vol. I, Dallas, Tex., Nov. 29-Dec. 1, 1976.

Edelson, R. E., "An Experimental Protocol for a Search for Radio Signals of Extraterrestrial Intelligent Origin in the Presence of Man-Made Radio Frequency Sources," paper presented at the XXVIIIth International Astronautical Congress, Prague, Czechoslovakia, Sept. 25-Oct. 1, 1977.

Efron, L., and Solloway, C. B., *Proceedings of the Conference on Scientific Applications of Radio and Radar Tracking in the Space Program*, Technical Report 32-1475, Jet Propulsion Laboratory, Pasadena, Calif., July 1, 1970.

Eimer, M., and Stevens, R., *Tracking and Data Handling for the Pioneer III and Pioneer IV Firings*, External Publication 701, Jet Propulsion Laboratory, Pasadena, Calif., Aug. 14, 1959.

Esposito, P. B., and Wong, S. K., "Geocentric Gravitational Constant Determined from Mariner 9 Radio Tracking Data," paper presented at the International Symposium on Earth Gravity Models (American Geophysical Union, NASA), St. Louis, Aug. 1972.

Estabrook, F. B., and Wahlquist, H. D., "Response of Doppler Spacecraft Tracking to Gravitational Radiation," *Gen. Relat. Grav.*, Vol. 6, No. 5, pp. 439-447, Oct. 1975.

Estacion Espacial de Madrid: Madrid Space Station, Special Publication 43-26, Jet Propulsion Laboratory, Pasadena, Calif., Aug. 31, 1975.

Fearey, J. P., and Renzetti, N. A., "Navigation Results on the Mariner Mars Mission to Mars 1969," International Navigation Conference, Hamburg, Oct. 1969.

Ferrari, A. J., and Ananda, M. P., "Lunar Gravity: A Long-Term Keplerian Rate Method," *J. Geophys. Res.*, Vol. 82, No. 20, pp. 3085-3097, July 10, 1977.

Fjeldbo, G., Kliore, A. J., and Seidel, B. L., "Bistatic Radar Measurements of the Surface of Mars with Mariner 1969," *Icarus*, Vol. 16, No. 3, pp. 502-508, June 1972.

Fjeldbo, G., and Eshleman, V. R., "Radio Occultation Measurements and Interpretations," in *The Atmospheres of Venus and Mars*, p. 225, Gordon and Breach, Science Publishers, Inc., New York, N.Y., 1968.

Fjeldbo, G., "Radio Occultation Experiments Planned for Pioneer and Mariner Missions to the Outer Planets," *Planet. Space Sci.*, Vol. 21, No. 9, pp. 1533-1547, Sept. 1973.

Fjeldbo, G., et al., "Viking Radio Occultation Measurements of the Martian Atmosphere and Topography: Primary Mission Coverage," *J. Geophys. Res.*, Vol. 82, No. 28, pp. 4317-4324, Sept. 30, 1977.

Flanagan, F. M., et al., *Deep Space Network Support of the Manned Space Flight Network for Apollo: 1962-1968*, Technical Memorandum 33-452, Vol. I, Jet Propulsion Laboratory, Pasadena, Calif., July 1970.

Flanagan, F. M., et al., *Deep Space Network Support of the Manned Space Flight Network for Apollo: 1969-1970*, Technical Memorandum 33-452, Vol. II, Jet Propulsion Laboratory, Pasadena, Calif., May 1, 1971.

Fortenberry, J. W., Freeland, R. E., and Moore, D. M., *Five-Meter-Diameter Conical Furlable Antenna*, Technical Report 32-1604, Jet Propulsion Laboratory, Pasadena, Calif., July 15, 1976.

Fredricksen, H., *Error Correction for Deep Space Network Teletype Circuits*, Technical Report 32-1275, Jet Propulsion Laboratory, Pasadena, Calif., June 1, 1968.

Freiley, A. J., Batelaan, P. D., and Bathker, D. A., *Absolute Flux Density Calibrations of Radio Sources: 2.3 GHz*, Technical Memorandum 33-806, Jet Propulsion Laboratory, Pasadena, Calif., Dec. 1, 1977.

Gary, B., Olsen, E. T., and Rosenkranz, P. W., "Radio Observations of Cygnus X-3 and the Surrounding Region," *Nature Phys. Sci.*, Vol. 239, No. 95, pp. 128-130, Oct. 23, 1972.

Gates, C. R., and Johnson, M. S., *A Study of On-Site Computing and Data Processing for a World Tracking Network*, Publication 154, Jet Propulsion Laboratory, Pasadena, Calif., Feb. 9, 1959.

Georgevic, R. M., *Mathematical Model of the Solar Radiation Force and Torques Acting on the Components of a Spacecraft*, Technical Memorandum 33-494, Jet Propulsion Laboratory, Pasadena, Calif., Oct. 1, 1971.

Goldstein, R., Stevens, R., and Victor, W. K., *Radar Exploration of Venus: Goldstone Observatory Report for October-December 1962*, Technical Report 32-396, Jet Propulsion Laboratory, Pasadena, Calif., Mar. 1, 1965.

Goldstein, R. M., *The Analysis of Uncooperative Radar Targets*, Technical Report 32-658, Jet Propulsion Laboratory, Pasadena, Calif., Sept. 1, 1964.

Goldstein, R. M., et al., *The Superior Conjunction of Mariner IV*, Technical Report 32-1092, Jet Propulsion Laboratory, Pasadena, Calif., Apr. 1, 1967.

Goldstein, R. M., "Radar Time-of-Flight Measurements to Venus," *Astron. J.*, Vol. 73, No. 9, Aug. 1968.

Goldstein, R. M., et al., "Preliminary Radar Results of Mars," *Radio Sci.*, Vol. 5, No. 2, pp. 475-478, Feb. 1970.

Goldstein, R. M., and Rumsey, H., "A Radar Snapshot of Venus," *Science*, Vol. 169, Sept. 1970.

Goldstein, R. M., "Radar Observations of Mercury," *Astron. J.*, Vol. 76, No. 10, pp. 1152-1154, Dec. 1971.

Goldstein, R. M., Holdridge, D. B., and Lieske, J. H., "Minor Planets and Related Objects: XII. Radar Observations of (1685) Toro," *Astron J.*, Vol. 78, No. 6, pp. 508-509, Aug. 1973.

Goldstein, R. M., and Morris, G. A., "Ganymede: Observations by Radar," *Science*, Vol. 188, No. 4194, pp. 1211-1212, June 20, 1975.

Goldstein, R. M., Green, R. R., and Rumsey, H., Jr., "Venus Radar Images," *J. Geophys. Res.*, Vol. 81, No. 26, pp. 4807-4817, Sept. 10, 1976.

Golomb, S. W., "New Problems of Space Communications: Part I. Beware of the Tigers," *Astronautics*, Vol. 7, No. 6, p. 19, June 1962.

Golomb, S. W., "New Problems in Space Communications: Part 3," *Astronautics*, Vol. 7, No. 8, p. 26, Aug. 1962.

Golomb, S. W., "Ferreting Signals Out of Noise," *Int. Sci. Technol.*, No. 22, pp. 72-82 and 120, Oct. 1963.

Goodwin, P. S., et al., *Tracking and Data Systems Support for the Helios Project: Project Development Through End of Mission Phase II*, Technical Memorandum 33-752, Vol. I, Jet Propulsion Laboratory, Pasadena, Calif., July 1, 1976.

Gordon, H. J., et al., *The Mariner 6 and 7 Flight Paths and Their Determination From Tracking Data*, Technical Memorandum 33-469, Jet Propulsion Laboratory, Pasadena, Calif., Dec. 1, 1970.

Gottlieb, P., et al., "Lunar Gravity over Large Craters from Apollo 12 Tracking Data," *Science*, Vol. 168, No. 3930, pp. 477-479, Apr. 1970.

Gray, R. M., and Tausworthe, R. C., "Frequency-Counted Measurements, and Phase Locking to Noise Oscillators," *IEEE Trans. Commun. Technol.*, Vol. COM-19, No. 1, pp. 21-30, Feb. 1971.

Gubbay, J., et al., "Variations of Small Quasar Components at 2,300 MHz," *Nature*, Vol. 224, No. 5224, pp. 1094-1095, Dec. 1969.

Gulkis, S., and Gary, B., "Circular Polarization and Total-Flux Measurements of Jupiter at 13.1 cm Wavelength," *Astron. J.*, Vol. 76, No. 1, pp. 12-16, Feb. 1971.

Gulkis, S., et al., "Observations of Jupiter at 13-cm Wavelength During 1969 and 1971," *Icarus*, Vol. 18, No. 2, pp. 181-191, Feb. 1973.

Gulkis, S., et al., "An All-Sky Search for Narrow-Band Radiation in the Frequency Range 1-25 GHz," paper presented at the 1976 U.S. National Commission, International Union of Radio Science, Amherst, Mass., Oct. 10-15, 1976.

Hachenberg, O., et al., "The 100-meter Radio Telescope at Effelsberg," *Proc. IEEE*, Vol. 61, No. 9, pp. 1288-1295, Sept. 1973.

Hall, J. R., and Easterling, M., "The Technology of Ground Stations in the Deep Space Network from 1958 to 1968," *IEEE Conf. Rec.*, Vol. 4, pp. 576-585, 1968.

Hall, J. R., et al., "The General Problem of Data Return from Deep Space," *Space Sci. Rev.*, Vol. 8, pp. 595-664, 1968.

Hall, J. R., *Tracking and Data System Support for Lunar Orbiter*, Technical Memorandum 33-450, Jet Propulsion Laboratory, Pasadena, Calif., Apr. 1970.

Hamilton, T. W., et al., *The Ranger IV Flight Path and Its Determination From Tracking Data*, Technical Report 32-345, Jet Propulsion Laboratory, Pasadena, Calif., Sept. 15, 1962.

Harris, A. W., et al., "2290-MHz Flux Densities of 52 High-Declination Radio Sources," *Astron. J.*, Vol. 81, No. 4, pp. 222-224, Apr. 1976.

Hartop, R. W., *Power Loss Between Arbitrarily Polarized Antennas*, Technical Report 32-457, Jet Propulsion Laboratory, Pasadena, Calif., Sept. 1, 1964.

Havens, W. F., et al., *Scan Pointing Calibration for the Mariner Mars 1971 Spacecraft*, Technical Memorandum 33-556, Jet Propulsion Laboratory, Pasadena, Calif., Aug. 1, 1972.

Heftman, K., and Renzetti, N. A., "Data Return Capabilities of the Deep Space Network in the 1970's," AIAA Paper 67-648, *Proceedings of the AIAA Space Program Issues of the 70's Meeting*, Aug. 1967.

Higa, W. H., *Low-Level Microwave Mixing in Ruby*, Technical Report 32-1016, Jet Propulsion Laboratory, Pasadena, Calif., reprinted from *Proc. IEEE*, Vol. 54, No. 10, p. 1453, Oct. 1966.

Higa, W. H., "Time Synchronization via Lunar Radar," *Proc. IEEE*, Vol. 60, No. 5, pp. 552-557, May 1972.

Higa, W. H., "Spurious Signals Generated by Electron Tunneling on Large Reflector Antennas," *Proc. IEEE*, Vol. 63, No. 2, pp. 306-313, Feb. 1975.

Higa, W. H., *The Superconducting Cavity-Stabilized Maser Oscillator*, Technical Memorandum 33-805, Jet Propulsion Laboratory, Pasadena, Calif., Dec. 15, 1976.

Holmes. J. K., "On a Solution to the Second-Order Phase-Locked Loop," *IEEE Trans. Commun. Technol.*, Vol. COM-18, No. 2, pp. 119-126, Apr. 1970.

Holmes, J. K., "First Slip Times Versus Static Phase Error Offset for the First and Passive Second-Order Phase-Locked Loop," *IEEE Trans. Commun. Technol.*, Vol. COM-19, No. 2, pp. 234-235, Apr. 1971.

Holmes, J. K., and Tegnelia, C. R., *Digital Command System Second-Order Subcarrier Tracking Performance*, Technical Report 32-1540, Jet Propulsion Laboratory, Pasadena, Calif., Oct. 1, 1971.

Holmes J. K., "Performance of a First Order Transition Sampling Digital Phase-Locked Loop Using Random-Walk Models," *IEEE Trans. Commun.*, Vol. COM-20, No. 2, pp. 119-131, Apr. 1972.

Hunter, J. A., "Orbiting Deep Space Relay Station, A Study Report," paper presented at AIAA Conference on Large Space Platforms, Future Needs and Capabilities, Los Angeles, Calif., Sept. 27-29, 1978.

Hurd, W. J., and Anderson, T. O., *Digital Transition Tracking Symbol Synchronizer for Low SNR Coded Systems*, Technical Report 32-1488, Jet Propulsion Laboratory, Pasadena, Calif., reprinted from *IEEE Trans. Commun. Technol.*, Vol. COM-18, No. 2, pp. 141-147, Apr. 1970.

Hurd, W. J., "An Analysis and Demonstration of Clock Synchronization by VLBI," *IEEE Trans. Instr. Meas.*, Vol IM-23, No. 1, pp. 80-89, March 1974.

Jacobson, R. A., McDannel, J. P., and Rinker, G. C., "Use-of Ballistic Arcs in Low Thrust Navigation," *J. Spacecraft Rockets*, Vol. 12, No. 3, pp. 138-145, Mar. 1975.

Jaffe, R., and Rechtin, E., *Design and Performance of Phase-Lock Loops Capable of Near-Optimum Performance over a Wide Range of Input Signal and Noise Levels*, Progress Report 20-243, Jet Propulsion Laboratory, Pasadena, Calif., Dec. 1, 1954; also available in *IRE Trans. Inform. Theory*, No. 1, pp. 66-67, Mar. 1955.

Jordan, J. F., "Orbit Determination for Powered Flight Space Vehicles on Deep Space Missions," *J. Spacecraft Rockets*, Vol. 6, No. 5, pp. 545-550, May 1969.

Jordan, J. F., Melbourne, W. G., and Anderson, J. D., "Testing Relativistic Gravity Theories Using Radio Tracking Data From Planetary Orbiting Spacecraft," *Space Research XIII*, pp. 83-92, Akademie-Verlag, Berlin, 1973.

Jurgens, R. F., and Goldstein, R. M., "Radar Observations at 3.5 and 12.6 cm Wavelength of Asteroid 433 Eros," *Icarus*, Vol. 28, No. 1, pp. 1-15, May 1976.

Jurgens, R. F., and Bender, D. F., "Radar Detectability of Asteroids," *Icarus*, Vol. 31, No. 4, pp. 483-497, Aug. 1977.

Katow, M. S., "Evaluating Computed Distortions of Parabolic Reflectors," *Record of IEEE 1977 Mechanical Engineering in Radar Symposium, Arlington, Virginia, Nov. 8-10, 1977*, IEEE Publication 77CH 1250-0 AES, pp. 91-93.

Kellerman, K. I., et al., "High Resolution Observations of Compact Radio Sources at 13 Centimeters," *Astrophys. J.*, Vol. 161, No. 3, pp. 803-809, Sept. 1970.

Kelly, A. J., *Microwave Probe for Plasma Plumes*, Technical Report 32-625, Jet Propulsion Laboratory, Pasadena, Calif., Feb. 1965.

Kliore, A., Cain, D. L., and Hamilton, T. W., *Determination of Some Physical Properties of the Atmosphere of Mars from Changes in the Doppler Signal of a Spacecraft on an Earth-Occultation Trajectory*, Technical Report 32-674, Jet Propulsion Laboratory, Pasadena, Calif., Oct. 15, 1964.

Kliore, A., and Tito, D. A., *Radio Occultation Investigations of the Atmosphere of Mars*, Technical Report 32-1157, Jet Propulsion Laboratory, Pasadena, Calif., reprinted from *J. Spacecraft Rockets*, Vol. 4, No. 5, pp. 578-582, May 1967.

Kliore, A., "Radio Occultation Measurements of the Atmospheres of Mars and Venus," in *The Atmospheres of Venus and Mars*, edited by J. C. Brandt and M. B. McElrow, p. 205, Gordon and Breach Science Publishers, Inc., New York, N.Y., 1968.

Kliore, A. J., et al., "Summary of Mariner 6 and 7 Radio Occultation Results on the Atmosphere of Mars," *Space Research*, Vol. XI, pp. 165-175, Akademie-Verlag, Berlin, 1971.

Kliore, A. J., et al., "Mariner 9 S-Band Martian Occultation Experiment: Initial Results on the Atmosphere and Topography of Mars," *Science*, Vol. 175, No. 4019, pp. 313-317, Jan. 1972.

Kliore, A. J., et al., "The Atmosphere of Mars From Mariner 9 Radio Occultation Measurements," *Icarus*, Vol. 17, No. 2, pp. 484-516, Oct. 1972.

Kliore, A. J., et al., "S Band Radio Occultation Measurements of the Atmosphere and Topography of Mars with Mariner 9: Extended Mission Coverage of Polar and Intermediate Latitudes " *J. Geophys. Res.*, Vol. 78, No. 20, pp. 4331-4351, July 10, 1973.

Kliore, A. J., "Radio Occultation Exploration of Mars," *Exploration of the Planetary System* (IAU Symposium, No. 65), pp. 295-316, D. Reidel Publishing Co., Dordrecht, Holland, 1974.

Kliore, A. J., Woiceshyn, P. M., and Hubbard, W. P., "Pioneer 10 and 11 Radio Occultations by Jupiter," *COSPAR Space Research*, Vol. XVII, pp. 703-710, Pergamon Press Ltd., Oxford, 1978.

Kuiper, T. B. H., and Morris, M., "Searching for Extraterrestrial Civilizations," *Science*, Vol. 196, pp. 616-621, May 6, 1977.

Labrum, R. G., et al., *The Surveyor V, VI, and VII Flight Paths and Their Determination from Tracking Data*, Technical Report 32-1302, Jet Propulsion Laboratory, Pasadena, Calif., Dec. 1, 1968.

Laeser, R. P., et al., *Tracking and Data System Support for the Mariner Mars 1971 Mission: Prelaunch Phase Through First Trajectory Correction Maneuver*, Technical Memorandum 33-523, Vol. I, Jet Propulsion Laboratory, Pasadena, Calif., Mar. 15, 1972.

Layland, J. W., "On Optimal Signals for Phase-Locked Loops," *IEEE Trans. Commun. Technol.*, Vol. COM-17, No. 5, pp. 526-531, Oct. 1969.

Layland, J. W., and Lushbaugh, W. A., "A Flexible High-Speed Sequential Decoder for Deep Space Channels," *IEEE Trans. Commun. Technol.*, Vol. COM-19, No. 5, pp. 813-820, Oct. 1971.

Layland, J. W., "Buffer Management for Sequential Decoding," *IEEE Trans. Commun.*, Vol. COM-22, No. 10, pp. 1685-1690, Oct. 1974.

Leavitt, R. K., *The Least-Squares Process of MEDIA for Computing DR VID Calibration Polynomials*, Technical Memorandum 33-542, Jet Propulsion Laboratory, Pasadena, Calif., May 15, 1972.

Lesh, J. R., *Signal-to-Noise Ratios in Coherent Soft Limiters*, Technical Report 32-1589, Jet Propulsion Laboratory, Pasadena, Calif., Sept. 15, 1973.

Lesh, J. R., "Signal-to-Noise Ratios in Coherent Soft Limiters," *IEEE Trans. Commun.*, Vol. COM-22, No. 6, pp. 803-811, June 1974.

Lesh, J. R., "Sequential Decoding in the Presence of a Noisy Carrier Reference," *IEEE Trans. Commun.*, Vol. COM-23, No. 11, pp. 1292-1297, Nov. 1975.

Levitt, B. K., "Optimum Frame Synchronization for Biorthogonally Coded Data," *IEEE Trans. Commun.*, Vol. COM-22, No. 8, pp. 1130-1134, Aug. 1974.

Levitt, B. K., "Long Frame Sync Words for Binary PSK Telemetry," *IEEE Trans. Commun.*, COM-23, No. 11, pp. 1365-1367, Nov. 1975.

Levy, G. S., Otoshi, T. Y., and Seidel, B. L., *Ground Instrumentation for Mariner IV Occultation Experiment*, Technical Report 32-984, Jet Propulsion Laboratory, Pasadena, Calif., Sept. 15, 1966.

Levy, G. S., et al., *Lunar Range Radiation Patterns of a 210-Foot Antenna at S-Band*, Technical Report 32-1079, Jet Propulsion Laboratory, Pasadena, Calif., reprinted from *IEEE Trans. Antennas Propagation*, Vol. AP-15, No. 2, pp. 311-313, Mar. 1967.

Levy, G. S., et al., *The Ultra Cone: An Ultra-Low-Noise Space Communication Ground Radio-Frequency System*, Technical Report 32-1340, Jet Propulsion Laboratory, Pasadena, Calif., reprinted from *IEEE Trans. Microwave Theor. Tech.*, Vol. MTT-16, No. 9, pp. 596-602, Sept. 1968.

Levy, G. S., et al., "Pioneer 6: Measurement of Transient Faraday Rotation Phenomena Observed During Solar Occultation," *Science*, Vol. 166, No. 3905, pp. 596-598, Oct. 1969.

Levy, G. S., et al., "Helios-1 Faraday Rotation Experiment: Results and Interpretations of the Solar Occultations in 1975," *J. Geophys.*, Vol. 42, No. 6, pp. 659-672, 1977.

Levy, R., "Computer-Aided Design of Antenna Structures and Components," *Comput. Struc.*, Vol. 6, Nos. 4/5, pp. 419-428, Aug./Oct. 1976.

Levy, R., and McGinness, H., *Wind Power Prediction Models*, Technical Memorandum 33-802, Jet Propulsion Laboratory, Pasadena, Calif., Nov. 15, 1976.

Levy, R., and Katow, M. S., "Implementation of Wind Performance Studies for Large Antenna Structures," *Record of IEEE 1977 Mechanical Engineering in Radar Symposium, Arlington, Virginia, Nov. 8-10, 1977*, IEEE Publication 77CH 1250-0 AES, pp. 27-33.

Levy, R., "Antenna Bias Rigging for Performance Objective," *Record of IEEE 1977 Mechanical Engineering in Radar Symposium, Arlington, Virginia, Nov. 8-10, 1977*, IEEE Publication 77CH 1250-0 AES, pp. 94-97.

Lieske, J. H., and Null, G. W., "Icarus and the Determination of Astronomical Constants," *Astron. J.*, Vol. 74, No. 2, Mar. 1969.

Lieske, J. H., et al., "Simultaneous Solution for the Masses of the Principal Planets from Analysis of Optical Radar and Radio Tracking Data," *Celest. Mech.*, Vol. 4, No. 2, pp. 233-245, Oct. 1971.

Lindsey, W. C., *Optimum and Suboptimum Frequency Demodulation*, Technical Report 32-637, Jet Propulsion Laboratory, Pasadena, Calif., June 15, 1964.

Lindsey, W. C., *Improvements to be Realized Through the Use of Block-Coded Communication Systems*, Technical Report 32-947, Jet Propulsion Laboratory, Pasadena, Calif., reprinted from *IEEE Trans. Aerosp. Electron. Syst.*, Vol. AES-2, No. 3, pp. 364-366, May 1966.

Lindsey, W. C., *Phase-Shift-Keyed Signal Detection with Noisy Reference Signals*, Technical Report 32-968, Jet Propulsion Laboratory, Pasadena, Calif., reprinted from *IEEE Trans. Aerosp. Electron. Syst.*, Vol. AES-2, No. 4, pp. 393-401, July 1966.

Lindsey, W. C., *A Theory for the Design of One-Way and Two-Way Phase-Coherent Communication Systems: Phase-Coherent Tracking Systems*, Technical Report 32-986, Jet Propulsion Laboratory, Pasadena, Calif., July 15, 1969.

Lindsey, W. C., *Optimal Design of One-Way and Two-Way Coherent Communication Links*, Technical Report 32-988, Jet Propulsion Laboratory, Pasadena, Calif., reprinted from *IEEE Trans. Commun. Technol.* Vol. COM-14, No. 4, pp. 418-431, Aug. 1966.

Lindsey, W. C., and Charles. F. J., *A Model Distribution for the Phase Error in Second-Order Phase-Locked Loops*, Technical Report 32-1017, Jet Propulsion Laboratory, Pasadena, Calif., reprinted from *IEEE Trans. Commun. Technol.*, Vol. COM-14, No. 10, pp. 662-664, Oct. 1966.

Lindsey, W. C., *Performance of Phase-Coherent Receivers Preceded by Bandpass Limiters*, Technical Report 32-1162, Jet Propulsion Laboratory, Pasadena, Calif., Sept. 15, 1967.

Lindsey, W. C., "Block Coding for Space Communications," *IEEE Trans. Commun. Technol.* Vol. COM-17, No. 2, pp. 217-225, Apr. 1969.

Lindsey, W. C., *Block-Coded Communications*, Technical Report 32-1380, Jet Propulsion Laboratory, Pasadena, Calif., Aug, 15, 1969.

Lindsey, W. C., *Nonlinear Analysis of Generalized Tracking Systems*, Technical Report 32-1453, Jet Propulsion Laboratory, Pasadena, Calif., reprinted from *Proc. IEEE*, Vol. 57, No. 10, pp. 1705-1722, Oct. 1969.

Lindsey, W. C., and Simon, M. K., "The Effect of Loop Stress on the Performance of Phase-Coherent Communication Systems," *IEEE Trans. Commun. Technol.*, Vol. COM-18, No. 5, pp. 569-588, Oct. 1970.

C-3

Lindsey, W. C., and Simon, M. K., "Carrier Synchronization and Detection of Polyphase Signals," *IEEE Trans. Commun.*, Vol. COM-20, No. 3, pp. 441-454, June 1972.

Lindsey, W. C., and Simon, M. K., "L-Orthogonal Signal Transmission and Detection," *IEEE Trans. Commun.*, Vol. COM-20, No. 5, pp. 953-960, Oct. 1972.

Lindsey, W. C., and Simon, M. K., "On the Detection of Differentially Encoded Polyphase Signals," *IEEE Trans. Commun.*, Vol. COM-20, No. 6, pp. 1121-1128, Dec. 1972.

Lindsey, W. C., *Synchronization Systems in Communication and Control,* Prentice-Hall, Inc., Englewood Cliffs, N.J., 1972.

Lindsey, W. C., and Tausworthe, R. C., *A Bibliography of the Theory and Application of the Phase-Lock Principle,* Technical Report 32-1581, Jet Propulsion Laboratory, Pasadena, Calif., Apr. 1, 1973.

Lindsey, W. C., and Simon, M. K., *Telecommunication Systems Engineering,* Prentice-Hall, Inc., Englewood Cliffs, N.J., 1973.

Liu, A. S., and Pease, G. E., "Spacecraft Ranging From a Ground Digitally Controlled Oscillator," *J. Spacecraft Rockets,* Vol. 12, No. 9, pp. 528-532, Sept. 1975.

Lorell, J., Anderson, J. D., and Sjogren, W. L., *Characteristics and Format of the Tracking Data to Be Obtained by the NASA Deep Space Instrumentation Facility for Lunar Orbiter,* Technical Memorandum 33-230, Jet Propulsion Laboratory, Pasadena, Calif. June 15, 1965.

Lorell, J., Sjogren, W. L., and Boggs, D. *Compressed Tracking Data Used for First Iteration in Selenodesy Experiment, Lunar Orbiters I and II,* Technical Memorandum 33-343, Jet Propulsion Laboratory, Pasadena, Calif., May 1, 1967.

Lorell, J., and Sjogren, W. L., *Lunar Orbiter Data Analysis,* Technical Report 32-1220, Jet Propulsion Laboratory, Pasadena, Calif., Nov. 15, 1967.

Lorell, J., *Lunar Orbiter Gravity Analysis,* Technical Report 32-1387, Jet Propulsion Laboratory, Pasadena, Calif., June 15, 1969.

Lorell, J., et al., "Icarus: Celestial Mechanics Experiment for Mariner," *Int. J. Sol. Sys.*, Vol. 12, Jan. 1970.

Lorell, J., and Laing, P. A., *Compilation of Lunar Orbiter Tracking Data Used for Long-Term Selenodesy,* Technical Memorandum 33-419, Jet Propulsion Laboratory, Pasadena, Calif., Feb. 1, 1970.

Lorell, J., "Estimation of Gravity Field Harmonics in the Presence of Spin-Axis Direction Error Using Radio Tracking Data," *J. Astronaut. Sci.*, Vol. XX, No. 1, pp. 44-54, Aug. 1972.

Ludwig, A. C., et al., *Gain Calibration of a Horn Antenna Using Pattern Integration,* Technical Report 32-1572, Jet Propulsion Laboratory, Pasadena, Calif., Oct. 1, 1972.

Madrid, G. A., et al., *Tracking System Analytic Calibration Activities for the Mariner Mars 1971 Mission,* Technical Report 32-1587, Jet Propulsion Laboratory, Pasadena, Calif., Mar. 1, 1974.

Martin, D. P., *A Combined Radar-Radiometer With Variable Polarization*, Technical Memorandum 33-570, Jet Propulsion Laboratory, Pasadena, Calif., Oct. 15, 1972.

Martin, W. L., and Zygielbaum, A. I., *Mu-II Ranging,* Technical Memorandum 33-768, Jet Propulsion Laboratory, Pasadena, Calif., May 15, 1977.

Mathison, R. P., *Tracking Techniques for Interplanetary Spacecraft,* Technical Report 32-284, Jet Propulsion Laboratory, Pasadena, Calif., Aug. 1, 1962.

McEliece, R. J., *Optimal Communications Nets,* Technical Report 32-697, Jet Propulsion Laboratory, Pasadena, Calif., Apr. 15, 1965.

McNeal, C. E., *Ranger V Tracking Systems Data Analysis Final Report,* Technical Report 32-702, Jet Propulsion Laboratory, Pasadena, Calif., Apr. 15, 1965.

Melbourne, W. G., et al., *Constants and Related Information for Astrodynamical Calculations,* Technical Report 32-1306, Jet Propulsion Laboratory, Pasadena, Calif., July 15, 1968.

Melbourne, W. G., "Planetary Ephemerides," *Astronaut. Aeronaut.,* Vol. 7, No. 5, pp. 38-43, May 1970.

Melbourne, W. G., "Navigation between the Planets," *Sci. Amer.,* Vol. 234, No. 6, pp. 58-74, June 1976.

Merrick, W. D., et al., *Deep Space Communications,* Technical Release 34-10, Jet Propulsion Laboratory, Pasadena, Calif., Jan. 29, 1960; also available in *IRE Trans. Mil. Electron.,* Vol. MIL-4, No. 2-3, pp. 158-163, April-June 1960.

Miller, L., et al., *The Atlas-Centaur VI Flight Path and Its Determination from Tracking Data,* Technical Report 32-911, Jet Propulsion Laboratory, Pasadena, Calif., Apr. 15, 1966.

Miller, R. B., *Tracking and Data System Support for the Pioneer Project: Pioneers 6-9. Extended Missions: July 1, 1972-July 1, 1973,* Technical Memorandum 33-426, Vol. XII, Jet Propulsion Laboratory, Pasadena, Calif., March 1, 1974.

Miller, R. B., *Tracking and Data System Support for the Pioneer Project: Pioneer 10–From April 1, 1972, Through the Jupiter Encounter Period, January 1974,* Technical Memorandum 33-584, Vol. III, Jet Propulsion Laboratory, Pasadena, Calif., June 15, 1975.

Miller, R. B., et al., *Tracking and Data System Support for the Pioneer Project: Pioneer 10–From January 1974 to January 1975; Pioneer 11–From May 1, 1973 Through Jupiter Encounter Period, January 1975,* Technical Memorandum 33-584, Vol. IV, Jet Propulsion Laboratory, Pasadena, Calif., Dec. 1, 1975.

Moyer, T. D., *Mathematical Formulation of the Double-Precision Orbit Determination Program (DPODP),* Technical Report 32-1527, Jet Propulsion Laboratory, Pasadena, Calif., May 17, 1971.

Muhleman, D. O., *Relationship Between the System of Astronomical Constants and the Radar Determinations of the Astronomical Unit,* Technical Report 32-477, Jet Propulsion Laboratory, Pasadena, Calif., Jan. 15, 1964.

Muhleman, D. O., Goldstein, R., and Carpenter, R., *A Review of Radar Astronomy–Parts I, II,* Technical Report 32-824, Jet Propulsion Laboratory, Pasadena, Calif., Jan. 30, 1966, reprinted from *IEEE Spectrum,* Oct. and Nov. 1965.

Muhleman, D. O., et al., *JPL Radar Range and Doppler Observations of Venus, 1961-1966,* Technical Report 32-1123, Jet Propulsion Laboratory, Pasadena, Calif., July 1, 1968.

Muhleman, D. O., et al., "Radio Propagation Measurements of the Solar Corona and Gravitational Field: Applications to Mariner 6 and 7," in *Proceedings of the Conference on Experimental Tests of Gravitational Theories,* California Institute of Technology, Pasadena, Calif., Nov. 1970.

Muhleman, D. O., Esposito, P. B., and Anderson, J. D., "The Electron Density Profile of the Outer Corona and the Interplanetary Medium From Mariner-6 and Mariner-7 Time-Delay Measurements," *Astrophys. J.*, No. 211, No. 3, Part 1, pp. 943-957, Feb. 1, 1977.

Mulhall, B. D., et al., *Tracking System Analytic Calibration Activities for the Mariner Mars 1969 Mission,* Technical Report 32-1499, Jet Propulsion Laboratory, Pasadena, Calif., Nov. 15, 1970.

Mulholland, J. D., and Sjogren, W. L., *Lunar Orbiter Ranging Data,* Technical Report 32-1087, Jet Propulsion Laboratory, Pasadena, Calif., reprinted from *Science,* Vol. 155, No. 3758, pp. 74-76, Jan. 6, 1967.

Mulholland, J. D., *Proceedings of the Symposium on Observation, Analysis and Space Research Applications of the Lunar Motion,* Technical Report 32-1386, Jet Propulsion Laboratory, Pasadena, Calif., Apr. 1969.

Muller, P. M., and Sjogren, W. L., *Consistency of Lunar Orbiter Residuals With Trajectory and Local Gravity Effects,* Technical Report 32-1307, Jet Propulsion Laboratory, Pasadena, Calif., Sept. 1, 1968.

Muller, P. M., and Sjogren, W. L., *Mascons: Lunar Mass Concentrations,* Technical Report 32-1339, Jet Propulsion Laboratory, Pasadena, Calif., reprinted from *Science,* Vol. 161, No. 3842, pp. 680-684, Aug. 16, 1968.

Muller, P. M., Sjogren, W. L., and Wollenhaupt, W. R., "Lunar Gravity: Apollo 15 Doppler Radio Tracking," *The Moon,* Vol. 10, No. 2, pp. 195-205, June 1974.

Murray, B. C., Gulkis, S., and Edelson, R. E., "Extraterrestrial Intelligence: An Observational Approach," *Science,* Vol. 199, No. 4328, pp. 485-492, Feb. 3, 1978.

The NASA/JPL 64-Meter-Diameter Antenna at Goldstone, California: Project Report, Technical Memorandum 33-671, Jet Propulsion Laboratory, Pasadena, Calif., July 15, 1974.

Newburn, R. L., Jr., et al., *Earth-Based Research on the Outer Planets During the Period 1970-1985,* Technical Report 32-1456, Jet Propulsion Laboratory, Pasadena, Calif., Mar. 15, 1970.

Null, G. W., et al., *Mariner IV Flight Path and Its Determination From Tracking Data,* Technical Report 32-1108, Jet Propulsion Laboratory, Pasadena, Calif., Aug. 1, 1967.

Ohlson, J. E., "Polarization Tracking of a Partially Coherent Signal Using a Double Loop," *IEEE Trans. Commun.*, Vol. COM-23, No. 9, pp. 859-866, Sept. 1975.

Ohlson, J. E., and Reid, M. S., *Conical-Scan Tracking With the 64-m-diameter Antenna at Goldstone,* Technical Report 32-1605, Jet Propulsion Laboratory, Pasadena, Calif., Oct. 1, 1976.

O'Neil, W. J., et al., *The Surveyor III and Surveyor IV Flight Paths and Their Determination From Tracking Data,* Technical Report 32-1292, Jet Propulsion Laboratory, Pasadena, Calif., Aug. 15, 1968.

O'Neil, W. J., et al., *Mariner 9 Navigation,* Technical Report 32-1586, Jet Propulsion Laboratory, Pasadena, Calif., Nov. 13, 1973.

Ong., K. M., et al., "A Demonstration of a Transportable Radio Interferometric Surveying System With 3-cm Accuracy on a 307-m Base Line," *J. Geophys. Res.*, Vol. 81, No. 20, pp. 3587-3593, July 10, 1976.

Otoshi, T. Y., *The Effect of Mismatched Components on Microwave Noise-Temperature Calibrations,* Technical Report 32-1345, Jet Propulsion Laboratory, Pasadena, Calif., reprinted from *IEEE Trans. Microwave Theor. Tech.,* Vol. MTT-16, No. 9, pp. 675-686, Sept. 1968.

Otoshi, T. Y., Stelzried, C. T., and Yates, B. C., "Comparisons of Waveguide Losses Calibrated by the DC Potentiometer, AC Ratio Transformer, and Reflectometer Techniques," *IEEE Trans. Microwave Theor. Tech.*, Vol. MTT-18, No. 7, pp. 406-409, July 1970.

Otoshi, T. Y., and Stelzried, C. T., "A Precision Compact Rotary Vane Attenuator," *IEEE Trans. Microwave Theor. Tech.*, Vol. MTT-19, No. 11, pp. 843-854, Nov. 1971.

Otoshi, T. Y., "Precision Reflectivity Loss Measurements of Perforated-Plate Mesh Materials by a Waveguide Technique," *IEEE Trans. Instr. Meas.,* Vol. IM-21, No. 4, pp. 451-457, Nov. 1972.

Otoshi, T. Y., and Stelzried, C. T., "Cosmic Background Noise Temperature Measurement at 13-cm Wavelength," *IEEE Trans. Instr. Meas.,* Vol. IM-24, No. 2, pp. 174-179, June 1975.

Pease, G. E., et al., *The Mariner V Flight Path and Its Determination From Tracking Data,* Technical Report 32-1363, Jet Propulsion Laboratory, Pasadena, Calif., July 1, 1969.

Posner, E. C., *Properties of Error-Correcting Codes at Low Signal-to-Noise Ratios,* Technical Report 32-602, Jet Propulsion Laboratory, Pasadena, Calif., June 15, 1964.

Posner, E. C., "Random Coding Strategies for Minimum Entropy," *IEEE Trans. Inform. Theor.,* Vol. IT-21, No. 4, pp. 388-391, July 1975.

Posner, E. C., "Life Cycle Costing with a Discount Rate," *Utilitas Mathematica,* Vol. 13, pp. 157-188, 1978.

Potter, P. D., *The Design of a Very High Power, Very Low Noise Cassegrain Feed System for a Planetary Radar,* Technical Report 32-653, Jet Propulsion Laboratory, Pasadena, Calif., Aug. 24, 1964.

Potter, P. D., Merrick, W. D., and Ludwig, A. C., *Large Antenna Apertures and Arrays for Deep Space Communications,* Technical Report 32-848, Jet Propulsion Laboratory, Pasadena, Calif., Nov. 1, 1965.

Potter, P. D., *A Computer Program for Machine Design of Cassegrain Feed Systems,* Technical Report 32-1202, Jet Propulsion Laboratory, Pasadena, Calif., Dec. 15, 1967.

Potter, P. D., et al., *A Study of Weather-Dependent Data Links for Deep Space Applications,* Technical Report 32-1392, Jet Propulsion Laboratory, Pasadena, Calif., Oct. 15, 1969.

Powell, R. V., and Hibbs, A. R., "An Entree for Large Space Antennas," *Astronaut. Aeronaut.,* Vol. 15, No. 12, pp. 58-64, Dec. 1977.

Rechtin, E. "Communication Techniques for Space Exploration," *IRE Trans. Space Electron. Telem.,* Vol. SET-5, No. 3, pp. 95-98, Sept. 1959.

Rechtin, E., Stevens, R., and Victor, W. K., *Data Transmission and Communications,* Technical Release 34-55, Jet Propulsion Laboratory, Pasadena, Calif., Apr. 30, 1960.

Rechtin, E., *Space Communications,* Technical Release 34-68, Jet Propulsion Laboratory, Pasadena, Calif., May 1, 1960.

Rechtin, E., et al., *JPL Range and Doppler System,* Technical Memorandum 33-13, Jet Propulsion Laboratory, Pasadena, Calif., Sept. 22, 1961.

Rechtin, E., Rule, B., and Stevens, R., *Large Ground Antennas,* Technical Report 32-213, Jet Propulsion Laboratory, Pasadena, Calif., Mar. 20, 1962.

Rechtin, E., *Lunar Communications,* Technical Memorandum 33-133, Jet Propulsion Laboratory, Pasadena, Calif., June 28, 1963.

Rechtin, E., "Surprises on Venus," *Int. Sci. Technol.,* No. 20, pp. 13-14, Aug. 1963.

Rechtin, E., "Long Range Planning for the Deep Space Network," *Astronaut. Aeronaut.,* Vol. 6, No. 1, pp. 28-35, Jan. 1968.

Reid, M. S., et al., "Low-Noise Microwave Receiving Systems in a Worldwide Network of Large Antennas," *Proc. IEEE,* Vol. 61, No. 9, pp. 1330-1335, Sept. 1973.

Renzetti, N. A., et al., "Radio Tracking Techniques and Performance of the U.S. Deep Space Instrumentation Facility," *Space Research II, Proceedings of the Second International Space Science Symposium,* Florence, Italy, April 1961, North Holland Publishing Company, Amsterdam.

Renzetti, N. A., and Ostermier, B. J., *Communications with Lunar Probes,* Technical Report 32-148, Jet Propulsion Laboratory, Pasadena, Calif., Aug. 23, 1961.

Renzetti, N. A., "DSIF in the Ranger Project," *Astronautics,* Vol. 6, No. 1, pp. 34-37, 70, Sept. 1961.

Renzetti, N. A., *Tracking and Data Acquisition for Ranger Missions I-V,* Technical Memorandum 33-174, Jet Propulsion Laboratory, Pasadena, Calif., July 1, 1964.

Renzetti, N. A., *Tracking and Data Acquisition for Ranger Missions VI-IX,* Technical Memorandum 33-275, Jet Propulsion Laboratory, Pasadena, Calif., Sept. 15, 1966.

Renzetti, N. A., *Tracking and Data Acquisition Support for the Mariner Venus 1962 Mission,* Technical Memorandum 33-212, Jet Propulsion Laboratory, Pasadena, Calif., July 1, 1965.

Renzetti, N. A., *Tracking and Data Acquisition Report, Mariner Mars 1964 Mission: Near-Earth Trajectory Phase,* Technical Memorandum 33-239, Vol. I, Jet Propulsion Laboratory, Pasadena, Calif., Jan. 1, 1965.

Renzetti, N. A., *Tracking and Data Acquisition Report, Mariner Mars 1964 Mission: Cruise to Post-Encounter Phase,* Technical Memorandum 33-239, Vol. II, Jet Propulsion Laboratory, Pasadena, Calif., Oct. 1, 1967.

Renzetti, N. A., *Deep Space Network Support, Atlas/Centaur Missions 1-9,* Technical Memorandum 33-347, Jet Propulsion Laboratory, Pasadena, Calif., Sept. 15, 1967.

Renzetti, N. A., "Tracking and Data Acquisition System for Mariner Missions," *Proceedings of the Seventh International Symposium on Space Technology and Science,* Tokyo, 1967.

Renzetti, N. A., *Tracking and Data Acquisition Report, Mariner Mars 1964 Mission: Extended Mission,* Technical Memorandum 33-239, Vol. III, Jet Propulsion Laboratory, Pasadena, Calif., Dec. 1, 1968.

Renzetti, N. A., and Fearey, J. P., "The Deep Space Network. An Instrument for the Radio Navigation for the Mariner Mission to Mars 1969," IInd International Conference on Space Engineering, Venice, Italy, D. Reidel Publishing Co., Dordrecht, Holland, May 1969.

Renzetti, N. A., *Tracking and Data System Support for Surveyor: Missions I and II,* Technical Memorandum 33-301, Vol. I, Jet Propulsion Laboratory, Pasadena, Calif., July 15, 1969.

Renzetti, N. A., *Tracking and Data System Support for Surveyor: Missions III and IV,* Technical Memorandum 33-301, Vol. II, Jet Propulsion Laboratory, Pasadena, Calif., Sept. 1, 1969.

Renzetti, N. A., *Tracking and Data System Support for Surveyor: Mission V,* Technical Memorandum 33-301, Vol. III, Jet Propulsion Laboratory, Pasadena, Calif., Dec. 1, 1969.

Renzetti, N. A., *Tracking and Data System Support for Surveyor: Mission VI,* Technical Memorandum 33-301, Vol. IV, Jet Propulsion Laboratory, Pasadena, Calif., Dec. 1, 1969.

Renzetti, N. A., *Tracking and Data System Support for Surveyor: Mission VII,* Technical Memorandum 33-301, Vol. V, Jet Propulsion Laboratory, Pasadena, Calif., Dec. 1, 1969.

Renzetti, N. A., *Tracking and Data System Support for the Mariner Venus 67 Mission: Planning Phase Through Midcourse Maneuver,* Technical Memorandum 33-385, Vol. I, Jet Propulsion Laboratory, Pasadena, Calif., Sept. 1, 1969.

Renzetti, N. A., *Tracking and Data System Support for the Mariner Venus 67 Mission: Midcourse Maneuver Through End of Mission,* Technical Memorandum 33-385, Vol. II, Jet Propulsion Laboratory, Pasadena, Calif., Sept. 1, 1969.

Renzetti, N. A., *Tracking and Data System Support for the Pioneer Project: Pioneer VI. Prelaunch to End of Nominal Mission,* Technical Memorandum 33-426, Vol. I, Jet Propulsion Laboratory, Pasadena, Calif., Feb. 1, 1970.

Renzetti, N. A., *Tracking and Data System Support for the Pioneer Project: Pioneer VII. Prelaunch to End of Nominal Mission,* Technical Memorandum 33-426, Vol. II, Jet Propulsion Laboratory, Pasadena, Calif., Apr. 15, 1970.

Renzetti, N. A., *Tracking and Data System Support for the Pioneer Project: Pioneer VIII. Prelaunch Through May 1968,* Technical Memorandum 33-426, Vol. III, Jet Propulsion Laboratory, Pasadena, Calif., July 15, 1970.

Renzetti, N. A., *Tracking and Data System Support for the Pioneer Project: Pioneer IX. Prelaunch Through June 1969,* Technical Memorandum 33-426, Vol. IV, Jet Propulsion Laboratory, Pasadena, Calif., Nov. 15, 1970.

Renzetti, N. A., *Tracking and Data System Support for the Pioneer Project: Pioneer VI. Extended Mission: July 1, 1966-July 1, 1969,* Technical Memorandum 33-426, Vol. V, Jet Propulsion Laboratory, Pasadena, Calif., Feb. 1, 1971.

Renzetti, N. A., *Tracking and Data System Support for the Pioneer Project: Pioneer VII. Extended Mission: February 24, 1967-July 1, 1968,* Technical Memorandum 33-426, Vol. VI, Jet Propulsion Laboratory, Pasadena, Calif., Apr. 15, 1971.

Renzetti, N. A., *Tracking and Data System Support for the Pioneer Project: Pioneer VII. Extended Mission: July 1, 1968-July 1, 1969,* Technical Memorandum 33-426, Vol. VII, Jet Propulsion Laboratory, Pasadena, Calif., Apr. 15, 1971.

Renzetti, N. A., *Tracking and Data System Support for the Pioneer Project: Pioneer VIII. Extended Mission: June 1, 1968-July 1, 1969,* Technical Memorandum 33-426, Vol. VIII, Jet Propulsion Laboratory, Pasadena, Calif., May 1, 1971.

Renzetti, N. A., *Tracking and Data System Support for the Pioneer Project: Pioneers VI-IX. Extended Missions: July 1, 1969-July 1, 1970,* Technical Memorandum 33-426, Vol. IX, Jet Propulsion Laboratory, Pasadena, Calif., Aug. 15, 1971.

Renzetti, N. A., and Siegmeth, A. J., *Tracking and Data System Support for the Pioneer Project: Pioneers 6-9. Extended Missions: July 1, 1971-July 1, 1972,* Technical Memorandum 33-426, Vol. XI, Jet Propulsion Laboratory, Pasadena, Calif., May 1, 1973.

Renzetti, N. A., et al., *Tracking and Data System Support for the Mariner Mars 1969 Mission: Planning Phase Through Midcourse Maneuver,* Technical Memorandum 33-474, Vol. I, Jet Propulsion Laboratory, Pasadena, Calif., May 15, 1971.

Renzetti, N. A., et al., *Tracking and Data System Support for the Mariner Mars 1969 Mission: Midcourse Maneuver Through End of Nominal Mission,* Technical Memorandum 33-474, Vol. II, Jet Propulsion Laboratory, Pasadena, Calif., Sept. 1, 1971.

Renzetti, N. A., Linnes, K. W., and Taylor, T. M., *Tracking and Data System Support for the Mariner Mars 1969 Mission: Extended Operations Mission,* Technical Memorandum 33-474, Vol. III, Jet Propulsion Laboratory, Pasadena, Calif., Sept. 15, 1971.

Renzetti, N. A., *A History of the Deep Space Network: From Inception to January 1, 1969,* Technical Report 32-1533, Vol. I, Jet Propulsion Laboratory, Pasadena, Calif., Sept. 1, 1971.

Renzetti, N. A., "Radio Communications at Planetary Distances," paper presented at the International Convention on Radio Communication, Rome and Bologna, Italy, Mar. 1974.

Richter, H. L., Rechtin, E., and Walter, W. K., *National Ground-Based Surveillance Complex (U),* Publication 146, Jet Propulsion Laboratory, Pasadena, Calif., Feb. 16, 1959 (Confidential).

Rocci, S. A., "The 210-ft Parabolic Fully Steerable Tracking Antennas for a Deep Space Instrumentation Facility," in *Deep Space and Missile Tracking Antennas,* pp. 50-70, ASME, New York, 1966.

Rusch, W. V. T., *Phase Error and Associated Cross-Polarization Effects in Cassegrainian-Fed Microwave Antennas,* Technical Report 32-610, Jet Propulsion Laboratory, Pasadena, Calif., May 30, 1965.

Rusch, W. V. T., and Stelzried, C. T., *Observations of the Lunar Eclipse of December 19, 1964, at a Wavelength of 3.3 MM,* Technical Report 32-1097, Jet Propulsion Laboratory, Pasadena, Calif., reprinted from *Astrophys. J.*, Vol. 148, No. 1, pp. 255-259, Apr. 1967.

Rusch, W. V. T., *Applications of Two-Dimensional Integral-Equation Theory to Reflector-Antenna Analysis,* Technical Memorandum 33-478, Jet Propulsion Laboratory, Pasadena, Calif., May 1, 1971.

Rusch, W. V. T., "Double Aperture Blocking by Two Wavelength-Sized Feed-Support Struts," *Electron. Lett.*, Vol. 10, No. 15, pp. 296-297, July 25, 1974.

Sanger, D. K., *Digital Demodulation with Data Subcarrier Tracking,* Technical Report 32-1314, Jet Propulsion Laboratory, Pasadena, Calif., Aug. 1, 1968.

Siegmeth, A. J., Purdue, R. E., and Ryan, R. E., *Tracking and Data System Support for the Pioneer Project: Pioneers 6-9. Extended Missions: July 1, 1970-July 1, 1971,* Technical Memorandum 33-426, Vol. X, Jet Propulsion Laboratory, Pasadena, Calif., Aug. 15, 1972.

Siegmeth, A. J., et al., *Tracking and Data System Support for the Pioneer Project: Pioneer 10–Prelaunch Planning Through Second Trajectory Correction December 4, 1969 to April 1, 1972,* Technical Memorandum 33-584, Vol. I, Jet Propulsion Laboratory, Pasadena, Calif., Apr. 1, 1973.

Simon, M. K., "Nonlinear Analysis of an Absolute Value Type of an Early-Late Gate Bit Synchronizer," *IEEE Trans. Commun. Technol.*, Vol. COM-18, No. 5, pp. 589-596, Oct. 1970.

Simon, M. K., "Optimization of the Performance of a Digital-Data-Transition Tracking Loop," *IEEE Trans. Commun. Technol.*, Vol. COM-18, No. 5, pp. 686-689, Oct. 1970.

Simon, M. K., and Lindsey, W. C., "Data-Aided Carrier Tracking Loops," *IEEE Trans. Commun. Technol.*, Vol. COM-19, No. 2, pp. 157-168, Apr. 1971.

Simon, M. K., "On the Selection of an Optimum Design Point for Phase-Coherent Receivers Employing Bandpass Limiters," *IEEE Trans. Commun.*, Vol. COM-20, No. 2, pp. 210-214, Apr. 1972.

Simon, M. K., "On the Selection of a Sampling Filter Bandwidth for a Digital Data Detector," *IEEE Trans. Commun.*, Vol..COM-20, No. 3, pp. 438-441, June 1972.

Simon, M. K., and Springett, J. C., "The Performance of a Noncoherent FSK Receiver Preceded by a Bandpass Limiter," *IEEE Trans. Commun.*, Vol. COM-20, No. 6, pp. 1128-1136, Dec. 1972.

Simon, M. K., and Springett, J. C., *The Theory, Design, and Operation of the Suppressed Carrier Data-Aided Tracking Receiver,* Technical Report 32-1583, Jet Propulsion Laboratory, Pasadena, Calif., June 15, 1973.

Simon, M. K., and Smith, J. G., "Hexagonal Multiple Phase-and-Amplitude-Shift-Keyed Signal Sets," *IEEE Trans. Commun.*, Vol. COM-21, No. 10, pp. 1108-1115, Oct. 1973.

Simon, M. K., and Smith, J. G., "Carrier Synchronization and Detection of QASK Signal Sets," *IEEE Trans. Commun.*, Vol. COM-22, No. 2, pp. 98-106, Feb. 1974.

Simon, M. K., *Data-Derived Symbol Synchronization of MASK and QASK Signals,* Technical Memorandum 33-720. Jet Propulsion Laboratory, Pasadena, Calif., Dec. 15, 1974.

Simon, M. K., "A Generalization of Minimum-Shift-Keying (MSK) Type Signaling Based Upon Input Data Symbol Pulse Shaping," *IEEE Trans. Commun.*, Vol. COM-24, No. 8, pp. 845-856, Aug. 1976.

Simon, M. K., "An MSK Approach to Offset QASK," *IEEE Trans. Commun.*, Vol. COM-24, No. 8, pp. 921-923, Aug. 1976.

Simon, M. K., "The False Lock Performance of Costas Loops with Hard-Limited In-Phase Channel," *IEEE Trans. Commun.*, Vol. COM-26, No. 1, pp. 23-34, Jan. 1978.

Simon, M. K., "On the Calculation of Squaring Loss in Costas Loops with Arbitrary Arm Filters," *IEEE Trans. Commun.*, Vol. COM-26, No. 1, pp. 179-184, Jan. 1978.

Simon, M. K., "Tracking Performance of Costas Loops With Hard-Limited In-Phase Channel," *IEEE Trans. Commun.*, Vol. COM-26, No. 4, pp. 420-432, Apr. 1978.

Sjogren, W. L., et al., *The Ranger V Flight Path and Its Determination From Tracking Data,* Technical Report 32-562, Jet Propulsion Laboratory, Pasadena, Calif., Dec. 6, 1963.

Sjogren, W. L., et al., *The Ranger VI Flight Path and Its Determination From Tracking Data,* Technical Report 32-605, Jet Propulsion Laboratory, Pasadena, Calif., Dec. 15, 1964.

Sjogren, W. L., *The Ranger III Flight Path and Its Determination From Tracking Data,* Technical Report 32-563, Jet Propulsion Laboratory, Pasadena, Calif., Sept. 15, 1965.

Sjogren, W. L., et al., *Physical Constants as Determined From Radio Tracking of the Ranger. Lunar Probes,* Technical Report 32-1057, Jet Propulsion Laboratory, Pasadena, Calif., Dec. 30, 1966.

Sjogren, W. L., *Proceedings of the JPL Seminar on Uncertainties in the Lunar Ephemeris,* Technical Report 32-1247, Jet Propulsion Laboratory, Pasadena, Calif., May 1, 1968.

Sjogren, W. L., "Lunar Gravity Estimate: Independent Confirmation," *J. Geophys. Res.,* Vol. 76, No. 29, Oct. 10, 1971.

Sjogren, W. L., et al., "Lunar Gravity via Apollo 14 Doppler Radio Tracking," *Science,* Vol. 175, No. 4018, pp. 165-168, Jan. 14, 1972.

Sjogren, W. L., et al., "Gravity Fields," *IEEE Trans. Geosci. Electron.*, Vol. GE-14, No. 3, pp. 172-183, July 1976.

Slobin, S. D., "Beam Switching Cassegrain Feed System and Its Applications to Microwave and Millimeterwave Radioastronomical Observations," *Rev. Sci. Instr.,* Vol. 41, No. 3, pp. 439-443, Mar. 1970.

Spier, G. W., *Design and Implementation of Models for the Double Precision Trajectory Program (DPTRAJ),* Technical Memorandum 33-451, Jet Propulsion Laboratory, Pasadena, Calif., Apr. 15, 1971.

Springett, J. C., *Telemetry and Command Techniques for Planetary Spacecraft,* Technical Report 32-495, Jet Propulsion Laboratory, Pasadena, Calif., Jan. 15, 1965.

Springett, J. C., and Simon, M. K., "An Analysis of the Phase Coherent-Incoherent Output of the Bandpass Limiter," *IEEE Trans. Commun. Technol.,* Vol. COM-19, No. 1, pp. 42-49, Feb. 1971.

Stelzried, C. T., *Post-Amplifier Noise Temperature Contribution in a Low-Noise Receiving System,* Technical Report 32-446, Jet Propulsion Laboratory, Pasadena, Calif., Jan. 1964.

Stelzried, C. T., Reid, M. S., and Petty, S. M., *A Precision DC-Potentiometer Microwave Insertion-Loss Test Set,* Technical Report 32-887, Jet Propulsion Laboratory, Pasadena, Calif., Mar. 15, 1966.

Stelzried, C. T., Reid, M. S., and Nixon, D., *Precision Power Measurements of Spacecraft CW Signal With Microwave Noise Standards,* Technical Report 32-1066, Jet Propulsion Laboratory, Pasadena, Calif., Feb. 15, 1968.

Stelzried, C. T., and Reid, M. S., *Precision Power Measurements of Spacecraft CW Signal Level With Microwave Noise Standards,* Technical Report 32-1070, Jet Propulsion Laboratory, Pasadena, Calif., reprinted from *IEEE Trans. Instrum. Measurement,* Vol. IM-15, No. 4, pp. 318-324, Dec. 1966.

Stelzried, C. T., Rusch, W. V. T., *Improved Determination of Atmospheric Opacity From Radio Astronomy Measurements,* Technical Report 32-1115, Jet Propulsion Laboratory, Pasadena, Calif., repinted from *J. Geophys. Res.,* Vol. 72, No. 9, pp. 2445-2447, May 1, 1967.

Stelzried, C. T., and Otoshi, T. Y., "Radiometric Evaluation of Antenna-Feed Component Losses," *IEEE Trans. Instrumen. Measurement,* Vol. IM-18, No. 3, pp. 172-183, Sept. 1969.

Stelzried, C. T., "Precision Microwave Waveguide Loss Calibrations," *IEEE Trans. Instrum. Measurement,* Vol. IM-19, No. 1, pp. 23-25, Feb. 1970.

Stelzried, C. T., *A Faraday Rotation Measurement of a 13-cm Signal in the Solar Corona,* Technical Report 32-1401, Jet Propulsion Laboratory, Pasadena, Calif., July 15, 1970.

Stelzried, C. T., et al., "The Quasi-Stationary Coronal Magnetic Field and Electron Density as Determined From a Faraday Rotation Experiment," *Sol. Phys.,* Vol. 14, No. 2, pp. 440-456, Oct. 1970.

Stelzried, C. T., "Operating Noise-Temperature Calibrations of Low-Noise Receiving Systems," *Microwave J.,* Vol. 14, No. 6, pp. 41-46, 48, June 1971.

Stelzried, C. T., et al., "Transformation of Received Signal Polarization Angle to the Plane of the Ecliptic," *J. Spacecraft Rockets,* Vol. 9, No. 2, pp. 69-70, Feb. 1972.

Stevens, R., and Victor, W. K., *The Goldstone Station Communications and Tracking System for Project Echo,* Technical Report 32-59, Jet Propulsion Laboratory, Pasadena, Calif., Dec. 1, 1960.

System Capabilities and Development Schedule of the Deep Space Instrumentation Facility 1963-1967, Technical Memorandum 33-83, Jet Propulsion Laboratory, Pasadena, Calif., Mar. 2, 1962.

Tardani, P. A., *Madrid Site Selection Report,* Technical Memorandum 33-149, Jet Propulsion Laboratory, Pasadena, Calif., July 17, 1963.

Tausworthe, R. C., *A Precision Planetary Range-Tracking Radar,* Technical Report 32-779, Jet Propulsion Laboratory, Pasadena, Calif., reprinted from *IEEE Trans. Space Electron. Telem.,* Vol. SET-11, No. 2, pp. 78-85, June 1965.

Tausworthe, R. C., *Theory and Practical Design of Phase-Locked Receivers,* Technical Report 32-819, Vol. I, Jet Propulsion Laboratory, Pasadena, Calif., Feb. 15, 1966.

Tausworthe, R., *Cycle Slipping in Phase-Locked Loops,* Technical Report 32-1127, Jet Propulsion Laboratory, Pasadena, Calif., reprinted from *IEEE Trans. Commun. Technol.,* Vol. COM-15, No. 3, pp. 417-421, June 1967.

Tausworthe, R. C., Easterling, M. F., and Spear, A. J., *A High-Rate Telemetry System for the Mariner Mars 1969 Mission,* Technical Report 32-1354, Jet Propulsion Laboratory, Pasadena, Calif., Apr. 1, 1969.

Tausworthe, R. C., *DSS Subsystem Implementation by Time-Shared Computer,* Technical Memorandum 33-420, Jet Propulsion Laboratory, Pasadena, Calif., Oct. 1, 1969.

Tausworthe, R. C., "Convergence of Oscillator Spectral Estimators for Counted-Frequency Measurements," *IEEE Trans. Commun.,* Vol. COM-20, No. 2, pp. 213-217, Apr. 1972.

Tausworthe, R. C., "Simplified Formula for Mean-Slip Time of Phase-Locked Loops With Steady-State Phase Error," *IEEE Trans. Commun.,* Vol. COM-20, No. 3, pp. 331-337, June 1972.

Tausworthe, R. C., and Crow, R. B., "Improvements in Deep-Space Tracking by Use of Third-Order Loops," *Proceedings of the 1972 International Telemetering Conference, Los Angeles, California, October 10-12, 1972,* pp. 577-583.

Tausworthe, R. C., *Standard Classifications of Software Documentation,* Technical Memorandum 33-756, Jet Propulsion Laboratory, Pasadena, Calif., Jan. 15, 1976.

Telecommunications Systems Design Techniques Handbook, Technical Memorandum 33-571, edited by R. E. Edelson, Jet Propulsion Laboratory, Pasadena, Calif., July 15, 1972.

Textor, G. P., Kelly, L. B., and Kelly, M., *Tracking and Data System Support for the Mariner Mars 1971 Mission: First Trajectory Correction Maneuver Through Orbit Insertion,* Technical Memorandum 33-523, Vol. II, Jet Propulsion Laboratory, Pasadena, Calif., June 15, 1972.

Thomas, J. B., et al., "A Demonstration of an Independent-Station Radio Interferometry System With 4-cm Precision on a 16-km Base Line" *J. Geophys. Res.,* Vol. 81, No. 5, pp. 995-1005, Feb. 10, 1976.

Thornton, J. H., Jr., *The Surveyor I and Surveyor II Flight Paths and Their Determination From Tracking Data,* Technical Report 32-1285, Jet Propulsion Laboratory, Pasadena, Calif., Aug. 1, 1968.

Timor, U., "Equivalence of Time-Multiplexed and Frequency-Multiplexed Signals in Digital Communications," *IEEE Trans. Commun.,* Vol. COM-20, No. 3, pp. 435-438, June 1972.

Titsworth, R. C., and Welch, L. R., *Power Spectra of Signals Modulated by Random and Pseudorandom Sequences,* Technical Report 32-140, Jet Propulsion Laboratory, Pasadena, Calif., Oct. 10, 1961.

Titsworth, R. C., *The Algebra of Periodic Sequences,* Technical Report 32-381, Jet Propulsion Laboratory, Pasadena, Calif., Jan. 7, 1963.

Titsworth, R. C., *Correlation Properties of Cyclic Sequences,* Technical Report 32-388, Jet Propulsion Laboratory, Pasadena, Calif., July 1, 1963.

Titsworth, R. C., *Optimal Ranging Codes,* Technical Report 32-411, Jet Propulsion Laboratory, Pasadena, Calif., Apr. 15, 1963.

Titsworth, R. C., *Equivalence Classes of Periodic Sequences,* Technical Report 32-568, Jet Propulsion Laboratory, Pasadena, Calif., June 15, 1964, reprinted from *Ill. J. Math.,* Vol. 8, No 2, June 1964.

Titsworth, R. C., *The Role of Pseudorandom Codes in Communications,* Technical Memorandum 33-185, Jet Propulsion Laboratory, Pasadena, Calif., Aug. 3, 1964.

Toukdarian, R. Z., *Final Engineering Report for Goldstone Operations Support Radar,* Technical Memorandum 33-800, Jet Propulsion Laboratory, Pasadena, Calif., Nov. 1, 1976.

"Tracking and Data Acquisition System for Mariner Missions," *Proceedings of the Seventh International Symposium on Space Technology and Science,* Tokyo, May 1967.

Truong, T. K., and Reed, I. S., "Convolutions Over Residue Classes of Quadratic Integers," *IEEE Trans. Inform. Theor.,* Vol. IT-22, No. 4, pp. 468-475, July 1976.

Truong, T. K., and Reed, I. S., "Convolutions over Quartic Integer Residue Classes," *Proceedings of the International Conference on Information Sciences and Systems,* Patras, Greece, Aug. 19-24, 1976.

Truong, T. K., Liu, K. Y., and Reed, I. S., "Fast Number-Theoretic Transforms for Digital Filtering," *Electron, Lett.,* Vol. 12, No. 24, Nov. 1976.

Truong, T. K., et al., "X-Ray Reconstruction by Finite Field Transforms," *IEEE Trans. Nucl. Sci.,* Vol. NS-24, No. 1, pp. 843-849, Feb. 1977.

Truong, T. K., Golomb, S. W., and Reed, I. S., "Integer Convolutions Over the Finite Field $GF(3 \cdot 2^n + 1)$," *SIAM J. Appl. Math.,* Vol. 32, No. 2, pp. 356-365, Mar. 1977.

Truong, T. K., Reed, I. S., and Liu, K. Y., "Fast Algorithm for Computing Complex Number-Theoretic Transforms," *Electron. Lett.*, Vol. 13, No. 10, pp. 278-280, May 12, 1977.

Vegos, C. J., et al., *The Ranger IX Flight Path and Its Determination From Tracking Data,* Technical Report 32-767, Jet Propulsion Laboratory, Pasadena, Calif., Nov. 1, 1968.

Victor, W. K., *Precision Frequency Control–A Communications Requirement of the Space Age,* External Publication 627, Jet Propulsion Laboratory, May 13, 1959.

Victor, W. K., and Stevens, R., "The Role of the Jet Propulsion Laboratory in Project Echo," *IRE Trans.*, Vol. SET-7, pp. 20-29, Mar. 1961.

Victor, W. K., Stevens, R., and Golomb, S. W., *Radar Exploration of Venus: Goldstone Observatory Report for March-May 1961,* Technical Report 32-132, Jet Propulsion Laboratory, Pasadena, Calif., Aug. 1, 1961.

Victor, W. K., Titsworth, R. C., and Rechtin, E., *Telecommunication Aspects of a Manned Mars Mission,* Technical Report 32-501, Jet Propulsion Laboratory, Pasadena, Calif., Aug. 20, 1963.

Viterbi, A. J., *Acquisition Range and Tracking Behavior of Phase-Locked Loops,* External Publication 673, Jet Propulsion Laboratory, Pasadena, Calif., July 14, 1959.

Viterbi, A. J., *On Coded Phase-Coherent Communications,* Technical Report 32-25, Jet Propulsion Laboratory, Pasadena, Calif., Aug. 15, 1960.

Viterbi, A. J., *Classification and Evaluation of Coherent Synchronous Sampled-Data Telemetry Systems,* Technical Report 32-123, Jet Propulsion Laboratory, Pasadena, Calif., June 15, 1961.

Viterbi, A. J., *Phase-Locked Loop Dynamics in the Presence of Noise by Fokker-Planck Techniques,* Technical Report 32-427, Jet Propulsion Laboratory, Pasadena, Calif., Mar. 29, 1963; also reprinted in *IEEE Proc.*, Vol. 51, No. 12, pp. 1737-1753, Dec. 1963.

Viterbi, A. J., *Orthogonal Tree Codes for Communication in the Presence of White Gaussian Noise,* Technical Report 32-1120, Jet Propulsion Laboratory, Pasadena, Calif., reprinted from *IEEE Trans. Commun. Technol.*, Vol. COM-15, No. 2, pp. 238-242, Apr. 1967.

von Roos, O. H., Yip, K. B. W., and Escobal, P. R., "A Global Model of the Earth's Ionosphere for Use in Space Applications," *Astronautica Acta,* Vol. 18 (Supplement), No. 3, pp. 215-232, Aug. 1974.

Weber, W. J., III, "Performance of Phase-Locked Loops in the Presence of Fading Communication Channels," *IEEE Trans. Commun.*, Vol. COM-24, No. 5, pp. 487-499, May 1976.

Weber, W. J., III, Ackerknecht, W. E., and Kollar, F. J., *Viking X-Band Telemetry Experiment Final Report,* Technical Memorandum 33-794, Jet Propulsion Laboratory, Pasadena, California, Sept. 1, 1976.

Winn, F. B., "Selenographic Location of Surveyor VI," in *Surveyor VI Mission Report: Part II. Science Results,* Technical Report 32-1262, Jet Propulsion Laboratory, Pasadena, Calif., Jan. 10, 1968.

Winn, F. B., "Post Landing Tracking Data Analysis," in *Surveyor VII Mission Report: Part II. Science Results,* Technical Report 32-1264, Jet Propulsion Laboratory, Pasadena, Calif., Mar. 15, 1968.

Winn, F. B., "Surveyor Post-Touchdown Analysis of Tracking Data," in *Surveyor Project Final Report: Part II. Science Results,* Technical Report 32-1265, Jet Propulsion Laboratory, Pasadena, Calif., June 15, 1968.

Winn, F. B., *Surveyor Posttouchdown Analyses of Tracking Data,* NASA SP-184, National Aeronautics and Space Administration, Washington, D.C., p. 369.

Wollenhaupt, W. R., *Tracking System Data Analysis Report, Ranger 4 Final Report,* Technical Report 32-523, Jet Propulsion Laboratory, Pasadena, Calif., Mar. 1, 1964.

Wollenhaupt, W. R., et al., *The Ranger VII Flight Path and Its Determination From Tracking Data,* Technical Report 32-694, Jet Propulsion Laboratory, Pasadena, Calif., Dec. 15, 1964.

Wong, S. K., and Reinbold, S. J., "Earth-Moon Mass Ratio From Mariner 9 Radio Tracking Data," *Nature,* Vol. 241, No. 5385, pp. 111-112, Jan. 12, 1973.

Woo, R., and Ishimaru, A., "Remote Sensing of the Turbulence Characteristics of a Planetary Atmosphere by Radio Occultation of a Space Probe," *Radio Sci.,* Vol. 8, No. 2, pp. 103-108, Feb. 1973.

Woo, R. et al., *Effects of Turbulence in the Atmosphere of Venus on Pioneer Venus Radio–Phase I,* Technical Memorandum 33-644, Jet Propulsion Laboratory, Pasadena, Calif., June 30, 1973.

Woo, R., "Measurements of the Solar Wind Using Spacecraft Radio Scattering Observations," in *Study of Traveling Inter-Planetary Phenomena,* pp. 81-100, D. Reidel Publishing Co., Dordrecht, Holland/Boston, 1977.

Woo, R., "Radial Dependence of Solar Wind Properties Deduced from Helios 1/2 and Pioneer 10/11 Radio Scattering Observations," *Astrophys. J.,* Vol. 219, No. 2, Part 1, pp. 727-739, Jan. 15, 1978.

Woo, R. T., "Observations of Turbulence in the Atmosphere of Venus Using Mariner 10 Radio Occultation Measurements," *J. Atmos. Sci.,* Vol. 32, No. 6, pp. 1084-1090, June 1975.

Yuen, J. H., "A Double-Loop Tracking System," *IEEE Trans. Commun.,* Vol. COM-20, No. 6, pp. 1142-1150, Dec. 1972.

Yuen, J. H., *A Practical Statistical Model for Telecommunications Performance Uncertainty,* Technical Memorandum 33-732, Jet Propulsion Laboratory, Pasadena, Calif., June 15, 1975.